# New Ion Mobility-Mass Spectrometry Tools to Characterize and Differentiate Similar Proteins

Theresa A. Gozzo

A dissertation

submitted in partial fulfillment of the

requirements for the degree of

Doctor of Philosophy

University of Washington

2023

Reading Committee:

Matthew F. Bush, Chair

Frantisek Tureček

Robert E. Synovec

Program Authorized to Offer Degree:

Chemistry

University of Washington

## Abstract

New Ion Mobility-Mass Spectrometry Tools to Characterize and Differentiate Similar Proteins

Theresa A. Gozzo

Chair of the Supervisory Committee:

Matthew F. Bush

Department of Chemistry

This dissertation describes new ion mobility-mass spectrometry (IM-MS) approaches for the characterization and differentiation of similar proteins, namely antibodies. Antibodies form the basis of a growing class of biotherapeutics, and they pose an analytical challenge due to their size, flexibility, and heterogeneity. Thorough characterization is required for the safety and efficacy of such therapeutics. IM is a gas-phase separation technique in which charged ions are separated based on their size, shape, and charge, and from IM measurements, ions' collision cross-sections, Ω, can be determined. When IM is paired with MS, which gives a readout of ions' mass-to-charge ($m/z$) ratios, richer structural information can be gained. The new approaches described herein utilize various combinations of solution-phase chemistry, gas-phase chemistry, and collisional activation in conjunction with IM-MS to probe gas-phase ion structures and enhance the ability to distinguish between similar antibodies.

Chapter 1 reviews the effects of charge on ion structures through the discussion of results from gas-phase charge-reduction experiments using cation-to-anion proton-transfer reactions (CAPTR). Comparisons with results from other charge-reduction strategies are also provided. Chapter 2 discusses the differentiation of IgG1$\kappa$ and IgG4$\kappa$ antibodies using combinations of CAPTR, collisional activation, and IM-MS. The novel application of a Jensen-Shannon similarity score for the quantitative comparison of apparent Ω distributions is also introduced. Pre-CAPTR and post-CAPTR activation are applied, and the quantitative comparison of Ω distributions reveals that, relative to established workflows using energy-dependent IM without charge-state manipulation, pre-CAPTR activation and post-CAPTR activation both enhance the differentiation of these antibodies by IM-MS.

Chapters 3 and 4 discuss the use of reducing agents in native IM-MS for the maintenance of redox conditions in electrospray solutions and for the performance of disulfide bond reduction. Chapter 3 investigates the addition of three common reducing agents to protein electrospray ionization solutions and provides needed guidance on which reducing agents and concentrations minimize mass spectral signal interference and protein structural disruption. Chapter 4 introduces a novel programmed-temperature electrospray ionization (ptESI) source and a novel method for performing disulfide bond reduction of proteins with real-time monitoring by MS or IM-MS. The temperature and time resolution allows experimenters to view the onset and progression of bond reduction, rather than just the final product. Four antibody samples are subjected to real-time disulfide bond reduction, and the antibodies are easily distinguished by their reduction profiles, suggesting that this method is sensitive to the stability and disulfide-bond connectivity of these proteins. Overall, the new IM-MS methods presented here could be implemented to enhance current biotherapeutic characterization workflows.

## Dedication

*To Mom and my dear Cody*

**Acknowledgements**

I have many to thank for my success in graduate school. First, I'd like to thank my advisor, Dr. Matt Bush, for guiding me throughout this journey. His scientific advice was invaluable and helped me think through problems in new ways. I truly respect his dedication to high quality work and ethics in science. He is a great role model. I also appreciate the workspace he cultivated; group meetings were a safe place for open discussion and growth. Last, but not least, I want to highlight his mentorship in science communication. Half of being a scientist is disseminating your work and discussing it with others, and his attention to effective communication was so important to my development. I could say so much more, but I will stop there. Thank you, Matt. Next, I need to thank my committee members, past and present, Drs. Rob Synovec, Frank Turecek, Bo Zhang, Al Nelson, and Jim Bruce for testing me, teaching me, and supporting me. Your time and feedback are appreciated.

I also want to thank my undergraduate research advisor, Dr. J.C. Poutsma. His invitation to join the ion lab changed my path forever. And his belief in me gave me the confidence to pursue a PhD. The entire Chemistry Department at The College of William and Mary was, and is, phenomenal, and I am so thankful that I got my chemistry foundations from such talented and dedicated professors. Coming back this year and sharing my graduate research with everyone is one of my proudest moments of graduate school.

To my collaborators, Dr. Ning Zheng and Dr. Baiyun Wang, thank you for including me in such an interesting project. I had fun trying to interpret all of the native mass spectra I collected, and the questions we asked directly inspired my work investigating reducing agents in native mass spectrometry. I am sorry that the answers aren't coming easily, but I hope the documentation I've included in Appendix D will be helpful in your continued endeavors.

To Martin Sadilek in the Mass Spec Facility, thank you for all your help with my students. And thank you for always being such a friendly face whenever I see you; I love chatting with you and laughing at your jokes. I still have the paper hat you made for me from an extra mass spectrum. To Brandon Bol, I couldn't have taught 428 and 321 without you. You always had such a positive attitude when it felt like everything was going wrong, and it made every day so much better. I knew I could rely on you. Congratulations again on your new position! The rest of the chemistry department personnel deserve thanks as well. To those in the front office, the electronics shop, the stockroom, etc., thank you! You contribute to everyone's successes, and you deserve all the recognition for it.

To all of my former students, thank you for enriching my life as a graduate student. When research was taxing, it was so nice to focus on you all and to develop my love for teaching. And it was great to get to know each of you. Thank you for nominating me for my teaching award. It was a beautiful commemoration of my time as TA at UW. I would love to hear all about your future endeavors.

To the Bush lab members, thank you for being my friends in addition to being my colleagues. It has been an absolute joy to collaborate with you all. The feedback, conversations, hangouts, and celebrations are all dear to me, and I am better for having known all of you. To Meagan, thank you for being a wonderful mentor and friend. I am so happy to see you flourishing in your life and career. To Ben, thank you for your friendship and for all of our office discussions during our time in the lab. And thanks for trusting me to watch your boy, Cosmo. To Daniele and Cece, thank you for being great role models in the lab and for providing me with guidance whenever I see you out in the real world. To AnneClaire, thank you for being my first Bush lab contact and for getting beers to catch up here and there. To Alice, it was great to make a

new friend during the isolation of COVID, and I love seeing your growth as a scientist. Thank you for always being ready to chat it up. To May and Chris, thank you for all your work on the temp. controller projects. I can't imagine better mentees. And thank you for livening up the Bush lab and making us more social again. You both are going to do great things in your PhD research and beyond! To Lindsey, thanks for always popping into my office to chat. I have great memories with you, and I can't wait to see where you head next. To Addison, thank you for being a witness for my elopement, and to both Addison and Bruce, good luck with the rest of your doctoral research using the SLIM platforms. To all of you, and the recent Bush lab additions, don't be strangers. I will always be happy to chat and spend time with you all.

Finally, I want to thank all of my friends and family. Thank you to all the new friends I made here in Seattle that made it feel more like home: Rachel, Claudia, Noah, James, Milo, Justin, Ben P., Ben M., Kelly, Devin, and all your partners and pets. I had so much fun at UW and around town with you all, and I couldn't have survived graduate school without your friendship and support. Thank you to all of the hardworking organizers for UAW 4121 as well: Nayon, Brianne, Helen, Ben, and so many more. Keep fighting the good fight. Thank you to all my friends back in RVA who've stuck with me from the other side of the country, especially my best friend, Brittany. I cherish your love and support, and I can't wait to visit with you all more. Thank you to my mom for being an outstanding role model as a teacher and for your unending love and support. And thank you to my sisters for being my friends and cheerleaders. I am proud of you both, and I hope I can host a Seattle visit for you two soon. Last, but not least, I want to thank my husband Cody, for moving all the way across the country with me, persevering through the hard times, and celebrating the good times. Thank you for pushing me when I felt like giving up. I look forward to every additional day I get to spend with you.

## Table of Contents

# Chapter 1. Effects of Charge on Protein Ion Structure: Lessons from Cation-to-Anion, Proton-Transfer Reactions



## 1 Introduction

In cation-to-anion, proton-transfer reactions (CAPTR), gas-phase protein cations are quadrupole-selected and reacted with even-electron monoanions to generate a sequential series of charge-reduced cation products.[1] CAPTR products are then analyzed using ion mobility (IM) mass spectrometry (MS). The precursors and products of CAPTR can also be manipulated using other MS-based techniques, including collisional activation, before mass analysis.[2] We first introduce the foundations and context for these experiments, including charging during electrospray ionization (ESI), IM of ESI-generated protein ions, and methods for manipulating the charge states of protein ions. We then describe various aspects of CAPTR experiments, review the results of our CAPTR-IM-MS studies, and discuss how those results contribute to a deeper understanding of the relationship between protein ion structure and charge state.

### 1.1 ESI and Charge-State Distributions

Inherent to the formation of ions is the acquisition of charge. For example, subjecting proteins in solution to positive-mode ESI generates cations with excess protons. The charge states of proteins in solution, and in vivo, depend on the pH of the solution or cellular environment, amino acid composition, protein structure, and interactions with other molecules. Notably, Figure 1.1A shows that charge states of proteins in solution are uncorrelated with mass.[3]

In contrast, the charge states of ESI-generated ions are strongly correlated with mass for well-folded proteins and uncorrelated with the corresponding charge states in solution.[3] This leads us to consider the factors that influence observed gas-phase charge-state distributions, and additionally, how that charging affects the structures of gas-phase ions relative to their condensed-phase counterparts.

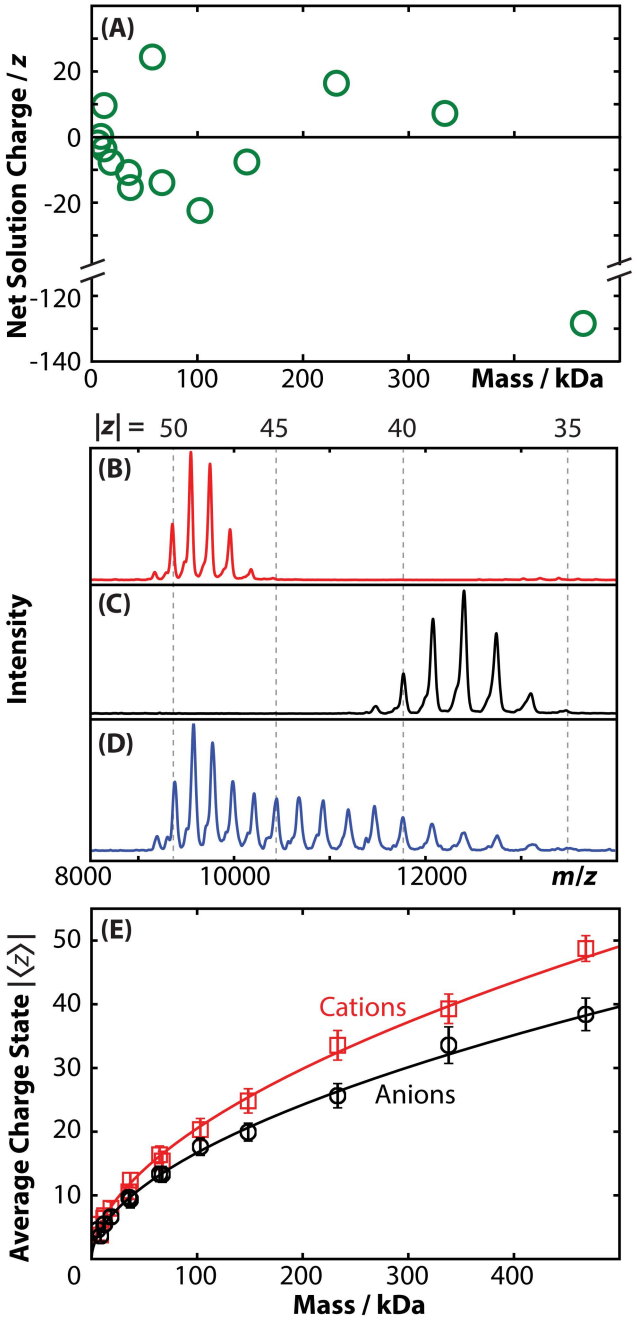

**Figure 1.1.** (A) Net charges of proteins in solution estimated based on the $pK_a$ of constituent amino acids.[4] Nano-ESI of β-galactosidase in 200 mM ammonium acetate at pH 7.0 measured in (B) positive and (C) negative polarities. Spectrum D is similar to spectrum B, but the solution also contained 10 mM triethylamine and additional charge-reduced cations were also observed. (E) Absolute value of the average charge states of selected protein and protein complex ions in positive (red) and negative (black) ion mode as a function of mass. Power functions are fit to the data to serve as a guide to the eye. The bars on those markers span two standard deviations of the observed charge-state distribution. The mean and width of each charge-state distribution varied little between experiments performed over several months. Figure and caption adapted with permission from Allen et al. (2013).[3]

A detailed discussion of proposed ESI mechanisms is beyond the scope of this review, but the ionization process is important to answer these questions. There is no singly agreed upon mechanism to date, but molecular size appears to play a role.[5,6] The charged-residue model is often invoked when discussing the multiple charging of macromolecules;[7,8] however, the charged-residue model alone does not explain all observations.[3,9] For example, it does not explain the polarity dependence of protein ion charge-state distributions: lower average charge states are observed for anions from negative-mode ESI than for cations from positive-mode ESI (Figure 1.1B-E), though anions and cations have been found to be similar in size.[3] These observations and others have been used as evidence to support the combined charged-residue, field-emission model, in which the charge states of many protein ions are limited by competitive

emission of charge carriers during the final stages of analyte desolvation.[3,5] Positive-mode ESI is most used for the study of proteins, so protein cations are the primary focus of this review.

In addition to molecular size, the observed charge-state distributions of macromolecules can depend on solution conditions before ESI.[10–12] Native-like solution conditions seek to preserve noncovalent interactions from the solution environment into the gas phase; these are typically aqueous solutions at neutral pH with similar ionic strength to physiological conditions.[12] Native-like conditions produce narrow charge-state distributions with lower average charge states. In contrast, denaturing solution conditions often contain organic solvent and/or have acidic pH; generating ions from denaturing conditions yields wider charge-state distributions and higher average charge states.[12] Other factors that can affect the observed charge-state distribution in ESI include current and voltage,[13] the position of the ESI emitter relative to the atmospheric-pressure interface to the mass spectrometer,[14] and other IM-MS instrument parameters.[15,16]

### 1.2 IM-MS of Protein Ions

IM-MS is sensitive to the structures of gas-phase ions, and it is increasingly being applied to questions of structural biology.[17] MS is sensitive to the mass and charge of ions, whereas IM is sensitive to the size, shape, and charge of ions. In IM, ions are propelled forward by an applied electric field ($E$) and slowed down by collisions with a background gas. Ions' mobilities ($K$) are calculated from their drift times ($t_d$) through a cell of length, $L$:

$$K = \frac{L}{t_d E} \tag{1.1}$$

Within the low-field limit, the kinetic energy imparted by the drift field is negligible compared to the thermal kinetic energy, and the collision cross-section, Ω, can be calculated using $K$ and the Mason–Schamp equation:[18]

$$\Omega = \frac{3ez}{16N}\left(\frac{2\pi}{\mu k_B T}\right)^{\frac{1}{2}}\frac{1}{K} \quad (1.2)$$

where $e$ is the elementary charge, $z$ is the ion charge state, $N$ is the drift gas number density, $\mu$ is the reduced mass of the ion–drift gas pair, $k_B$ is the Boltzmann constant, and $T$ is temperature of the drift gas.

Since generating gas-phase ions is central to making IM-MS measurements, it is important to consider how charge affects the structures of the analytes. As mentioned previously, ESI of proteins in denaturing solutions yields ions with higher charge than those generated from native-like solutions. IM results show that more highly charged ions also exhibit larger Ω values.[10,12,19,20] IM-MS experiments probing the effect of ESI solution conditions consistently show a strong link between charge and Ω.[19–24] For instance, ubiquitin ions generated by ESI from denaturing conditions of 1:1 water: acetonitrile with 2% acetic acid resulted in charge states 6+ to 13+,[24] whereas 4+ to 6+ were observed under native-like conditions of aqueous 200 mM ammonium acetate at pH 7.[25] Denatured ions exhibited larger Ω values than native-like ions, suggesting unfolding and elongation of the structures. Interestingly, the 6+ ions from denaturing conditions exhibited multimodal Ω distributions: as shown in Figure 1.2, some ions exhibited Ω values similar to native-like 6+ ions and close to values calculated using crystal structures, whereas other ions exhibited larger Ω values indicative of partial unfolding.[24] Such studies provided foundational insights into the contributions of solution conditions and charge state to the structures of gas-phase ions. To investigate these relationships more extensively, a variety of charge-manipulation strategies have been pursued.

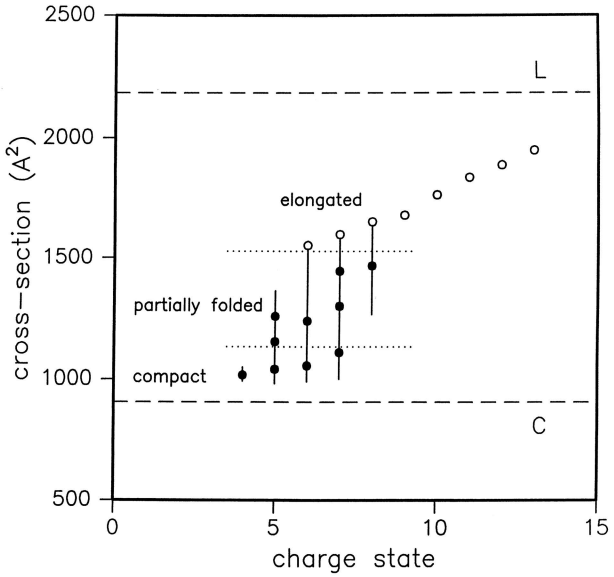


**Figure 1.2.** Experimental collision cross sections for all conformations and charge states observed for ubiquitin, including those produced via charge reduction. 6+ to 13+ charge states were observed directly from electrospray ionization from 1:1 water: acetonitrile with 2% acetic acid. The vertical lines correspond to a distribution of unresolved conformations having a range of collision cross-sections. The filled circles that are superimposed on the lines correspond to reproducible maxima in the unresolved spectra. The horizontal dashed lines correspond to the calculated cross sections for the crystal conformer (C) and the near-linear conformer (L). Horizontal dotted lines are used to divide the data into three conformer types: compact, partially folded, and elongated. Figure and caption adapted with permission from Valentine et al. (1997b).[24]

This review focuses on the effects of charge state on the structures of protein ions. Note that charge state also contributes to the Ω of an ion, even without any changes in structure, because of long-range interactions between the ion and drift gas.[26–28] The magnitude of this

effect increases with the polarizability of the drift gas. Most results described in this review are based on IM measurements performed in helium gas, which has very low polarizability and minimizes this effect.[26]

### 1.3 Charge-State Manipulation

#### 1.3.1 Solution Additives

Supercharging or charge-reducing agents can be added to solution to generate different charge-state distributions after ESI.[3,7,11,29–36] Generating ions from denaturing or supercharging conditions are common approaches to produce broader charge-state distributions,[12,37] but these strategies typically result in greater spectral congestion due to the presence of many different highly charged ions with smaller differences in *m*/*z*, which can make it more challenging to resolve bound species or interfering components. Increasing charge may not produce desirable conditions for maintaining native-like structure; Coulombic repulsion can preferentially favor extended structures relative to compact structures,[38] and supercharging agents are associated with protein unfolding.[11,34,37] Charge reduction is advantageous because it creates additional charge states and can potentially resolve more species at higher *m*/*z*. A drawback to using solution-phase additives is that they can make it more challenging to isolate contributions from solution conditions, ionization, and gas-phase charge state on the structures of the resulting ions. Additionally, the entire sample is exposed to the charge manipulation agent, whereas some gas-phase techniques discussed below may enable the isolation of subpopulations of ions before charge reduction.

#### 1.3.2 Ion/Neutral Chemistry

Gas-phase reactions can decouple ionization and charge modulation, so contributions from changes in charge can be isolated from solution-phase interactions. Gas-phase charge reduction can be accomplished by ion/neutral or ion/ion reactions. Ion/neutral reactions frequently utilize proton transfer. For example, protein cations can be reacted with vapors of neutral basic reagents, and the extent of charge reduction depends on the number of ion/reagent collisions, the thermodynamics of the reaction, and other factors that affect the fraction of ion/reagent collisions that lead to products, *i.e.*, the reaction efficiency.[39–42] Even with strong "proton sponges," this charge reduction strategy is not universal and may compete with ion/neutral clustering.[39–43] As charge state decreases, the reaction efficiency also decreases, which limits the extent of charge reduction.[40,43,44] The low volatility of some reagents also causes persistence in vacuum systems and limits usable pressures.[39,40,45]

### 1.3.3 Ion/Ion Chemistry

Ion/ion reactions benefit from long-range Coulombic attraction, exothermicity at all charge states, and the ability to quickly modulate or purge anions.[43] Ion/ion reactions primarily proceed through electron or proton transfer, though ion exchange or adduction can also occur.[43,46] For reactions of multiply charged cations and singly charged anions, proton transfer, and electron transfer compete. Proton transfer is more likely when even-electron anions are used:[43]

$$[M + xH]^{x+} + A^{-} \rightarrow [M + (x-1)H]^{(x-1)+} + AH \quad (1.3)$$

This reaction yields a charge-reduced cation that is also even electron; fragmentation of these products is rare.[47,48] Electron transfer is more likely when a radical anion is used:[43]

$$[M + xH]^{x+} + A^{\bullet -} \rightarrow [M + xH]^{\bullet (x-1)+} + A \quad (1.4)$$

This reaction yields a charge-reduced cation that is odd electron, *i.e.*, a radical cation. When electron transfer yields products that have the *m*/*z* of the expected charge-reduced product, it is

also possible that radical-induced cleavages occurred, but that fragments remain bound through noncovalent interactions.[47,49,50] Therefore, Reactions 1.3 and 1.4 may yield charge-reduced products that have very different structures. Although beyond the scope of this review, ion/ion chemistry enables many other exciting reactions,[51] including the ability to invert the polarity of protein ions[52] and form crosslinks that are sensitive to the gas-phase structures of protein ions.[53]

The advent of electron-capture dissociation (ECD)[54], and electron-transfer dissociation (ETD)[55], techniques helped motivate additional electron-based charge-transfer studies.[56–59] In ECD, low-energy electrons are captured, forming odd-electron species, which frequently undergo fragmentation at the backbone N–$C_\alpha$ bonds.[60–62] In ETD, instead of free electrons, anions are used to transfer electrons to cations; ETD has been found to produce similar fragments to ECD.[55,58] Charge-reduced products are also observed from both ECD and ETD,[54,55,58] but ETD has been used more extensively to intentionally generate those products.[36,49,58,63] Both charge-reduction ETD (crETD) and electron transfer with no dissociation, i.e., ETnoD, are used to describe the use of ETD as a charge-reduction technique. For ease of discussion, we will use crETD to refer to both implementations for the remainder of the review. Some reagents that have been used for crETD are fluoranthene, azobenzene, 1,3-dicyanobenzene, 1,4-dicyanobenzene, and p-nitrotoluene.[36,49,56,63,64]

Perfluorocarbons have several properties that are beneficial for proton transfer.[43] Foundational studies using perfluoro-1,3-dimethylcyclohexane (PDCH) as an anion source were particularly useful for reactions with protein cations. Many of these experiments were performed on a modified 3D quadrupole ion trap.[65] An ESI source produced peptide and protein cations, and an atmospheric-sampling, glow-discharge interface produced anions from vapors of PDCH. The ion trap was floated at a negative voltage for the accumulation of cations, a precursor ion

isolation step followed,[66] and then the trap offset was switched to a positive voltage for the subsequent injection of anions. A period of mutual storage followed during which the voltage was held at or near zero, and ions were permitted to react. Anions were often removed, and then cations were detected. High-*m*/*z* measurements were made using resonance ejection.[67]

Using this setup, ions of insulin, ubiquitin, cytochrome *c*, myoglobin, albumin, transferrin, phosphorylase B, and more were reacted with PDCH anions.[44,65] From these experiments, key aspects of these reactions were revealed. For one, anions derived from PDCH formed no adducts with peptide and protein cations, but, for other anions studied, adduction to high-mass cations was observed.[44] Furthermore, no evidence of product cation fragmentation was observed, despite the net exothermicity of the reactions.[43] It was additionally found that PDCH-derived anions resist electron transfer, likely due to their high electron affinity and the instability of radical products.[47] Finally, favorable reaction kinetics were demonstrated under pseudo-first-order conditions; rates increase with the square of the charge state, and the reaction efficiency is constant for all charge states.[44,68] This work also highlighted the utility of proton-transfer reactions for assigning the charge state and mass of protein analytes as well as for resolving interfering signals.[43,46]

### 1.3.4 Atmospheric-pressure Analogues

As mentioned previously, it is useful to perform reactions within the mass spectrometer, but charge reduction can be performed at the instrument interface, for example, by positioning a corona-discharge ionization source[69,70] or an α emitter[71] adjacent to the ESI emitter induces charge reduction. The first reported implementation of gas-phase ion/ion reactions of multiply charged ions used a y-tube reactor at atmospheric pressure coupled with a quadrupole mass filter.[72,73] In these cases, the reactant ion species are not specifically identified because they are

formed by discharge or α particle reactions with air or bath gas at near-atmospheric pressure. The chemistry of the reactions is less clear. Ion/neutral reactions have also been performed at atmospheric pressure by exposure of generated ions to nebulized base.[29]

### 1.4 Combining Charge-state Manipulation and IM-MS

IM-MS has been combined with the full catalog of charge-manipulation strategies to achieve a range of goals including increasing the information content of experiments and probing the effects of charge on ion structure. For example, Clemmer and coworkers performed groundwork in incorporating IM after ion/neutral proton-transfer reactions of protein ions, investigating the effects of multiple different reagents.[24,42,74] The first instrument integrating an IM separation of charge-reduced products following ion/ion reactions was reported by Badman and coworkers; it included three ion sources, a 3D ion trap where ion/ion chemistry was performed, an IM drift tube, and a quadrupole-time-of-flight mass spectrometer.[75] The implementation of CAPTR with IM-MS is described in the following section. Selected results from IM-MS studies using different charge-reduction strategies will be discussed in the *Comparison to Other Charge Reduction Strategies* section.

## 2 CAPTR Implementation and Effects on Mass Spectral Analysis

### 2.1 Instrumentation

CAPTR experiments were performed on a Waters Synapt G2 HDMS modified with a radio frequency-confining drift cell[76] and a glow-discharge ionization source to generate monoanions for ion/ion chemistry,[77] as shown in Figure 1.3A. In collaboration with František Tureček, this instrument has also been used to characterize the structures of peptide ions and their ETD products.[78–82] A nanoESI source was used to generate protein cations from borosilicate

capillaries with inner diameters of 0.78 mm pulled to a 1–3 μm tip for all studies. By inserting a platinum wire into the wide end of the capillary, electrical contact with the solution was established. The atmospheric–pressure interface was held at an elevated temperature of 120 °C for the duration of experiments to prevent fouling of the ion optics; some experiments used a temperature-controlled source for independent control of the temperatures of the sample capillary and MS interface since heat transfer to the capillary had been observed.[83] PDCH was placed in the solvent reservoir at room temperature, and nitrogen gas seeded with the headspace vapor was introduced to a stainless-steel discharge needle positioned after the sampling cone. $[PDCH–F]^-$ monoanions were generated by glow discharge, quadrupole selected at $m/z$ 381, and accumulated in the stacked-ring ion trap cell for 100 ms. The instrument was then switched to positive polarity, and cations, the whole population or a quadrupole-selected population, were transmitted through the cloud of anions for 1–10 s. During transmission, the traveling-wave amplitude in the trap remained at 0 V for maximum spatial overlap of cations and anions. Figure 1.3B shows the relative potentials applied to ion optics during anion fill and cation transmission under minimal-activation conditions. Figure 1.3C shows the relative potentials during experiments that activate cations before or after CAPTR. Residual precursor ions and charge-reduced products were sent on to the drift cell, the collision cell, and then to the time-of-flight analyzer. Unless otherwise stated, the drift gas was helium for the discussed experiments. The use of this platform for characterizing the relationship between charge and gas-phase ion structure is discussed in Section 3.

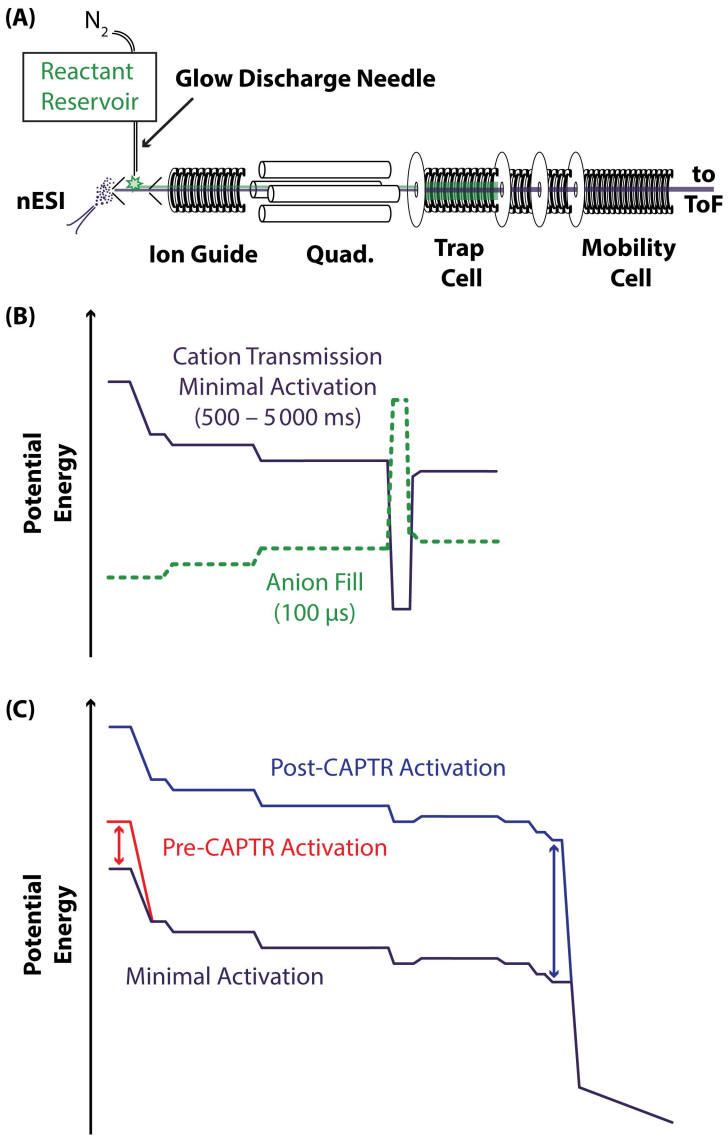


**Figure 1.3.** (A) Diagram of the modified Waters Synapt G2 HDMS used in these experiments. Anions (green) are generated by glow-discharge ionization and accumulated in the trap cell. Cations (purple) are generated by nanoESI and are trapped with anions for CAPTR. Residual precursor and CAPTR product ions are separated using IM in a radio-frequency confining drift cell before mass analysis. (B) Relative potentials applied to selected ion optics during cation transmission (*solid purple line*) and anion fill (*dashed green line*). (C) Representative potential-

energy diagrams for cation transmission during minimal activation, pre-CAPTR activation, and post-CAPTR activation experiments. Panels (A) and (C) and associated caption adapted with permission from Laszlo et al. (2016).[2] Panel (B) and associated caption adapted with permission from Laszlo and Bush (2015).[1]

The instrument geometry used for CAPTR is most similar to that of Badman and coworkers.[75] Our implementation differs from previous approaches in that ion/ion chemistry is performed in a stacked-ring ion guide, and the anion population is depleted significantly during most experiments, so pseudo-first order conditions are not maintained.[1] In previous approaches, the reaction time was tuned to preferentially form a specific charge-reduced product of interest, but with CAPTR a wider range of *z* values for charge-reduced products are observed simultaneously.[1]

**2.2 Charge-state Determination, Mass Assignment, and Resolution**

Although this review is focused on the effects of charge on protein ion structure, we also want to comment on the utility of CAPTR to aid in the interpretation of native mass spectra, which often exhibit congestion and narrow charge-state distributions that challenge charge-state assignments and determination of mass.[84] Creating additional charge states helps alleviate the uncertainty in this process. Figure 1.4 shows a native mass spectrum of pyruvate kinase and the CAPTR mass spectrum of the isolated *m*/*z* 7200 ions.[1] Simulated mass spectra corresponding to charge state assignments of 31+, 32+, and 33+ for the precursor ion are plotted over the experimental spectra. Each of the simulated native mass spectra provides a reasonable representation of the experimental native mass spectrum, but only the simulated CAPTR mass spectrum for the charge-state assignment of 32+ agrees well with the experimental CAPTR

spectrum. With CAPTR, the ambiguity in charge state was virtually eliminated. Adjacent mass spectral peaks that differ by one charge have increased spacing at higher *m*/*z*, so, for example, a 12+ ion of neutral mass 223.1 kDa, a 13+ ion of neutral mass 230.1 kDa, and a 14+ ion of neutral mass 237.3 kDa can be resolved in *m*/*z* space. Additionally, increasing the number of mass spectral peaks provides more observations for mass determination. This is a benefit of any strategy that increases the available charge-state observations, but CAPTR both increases the number of observations and the spacing between peaks. The accuracy of the mass analyzer and the mass heterogeneity of the analytes stemming from incomplete desolvation, nonspecific adduction, covalent modifications, and so on, become the main contributing factors to mass uncertainty.

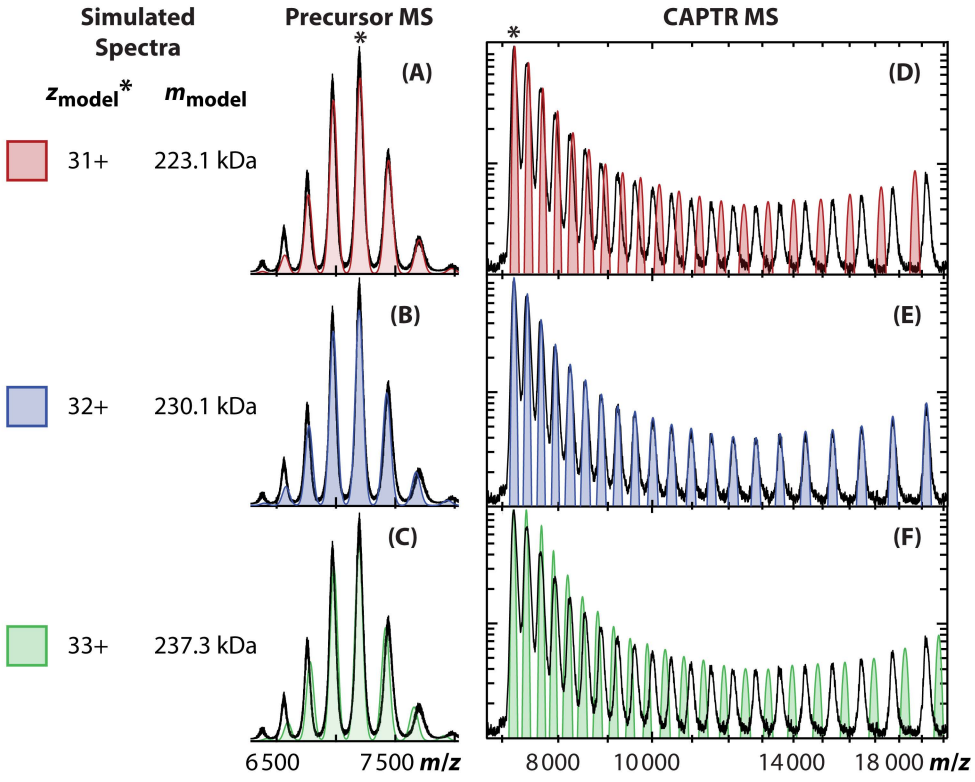


**Figure 1.4.** (A)–(C) Each shows a simulated spectrum (*blue, red*, and *green)* modeling the experimental native mass spectrum of pyruvate kinase (*black*).

Assigning the base peak at *m*/*z* 7200 a charge of 31+ (A, *red*), 32+ (B, *blue*), or 33+ (C, *green*) results in apparent masses of 223.1, 230.3, and 237.3 kDa, respectively; (D)–(F) Each shows a simulated spectrum modeling the experimental CAPTR spectrum for the *m*/*z* 7200 peak of pyruvate kinase. These spectra were simulated using the mass determined for the corresponding model of the native mass spectrum. Intensities were set manually to resemble the intensities in the experimental spectrum. Figure and caption adapted with permission from Laszlo and Bush (2015).[1]

CAPTR can also increase the resolution of interfering species in congested mass spectra, analogous to previous approaches by McLuckey and coworkers in ion traps.[44,68,85,86] The improved resolution was demonstrated using yeast enolase and bovine serum albumin.[1] In the native mass spectra, peak overlap was observed, but after isolating an overlapped peak and performing CAPTR, the products were well resolved. After 12 CAPTR events, the mass spectral resolution was 54 compared to 0.016 for the precursors. The change in resolution with charge reduction depends on the effect of each CAPTR event on the peak width and centroid values of product ion distributions. The following equation predicts the resolution of two peaks as a function of the number of CAPTR events (*n*):

$$R_{CAPTR}(n) = \frac{\frac{m_x}{(z_x^*-n)} - \frac{m_y}{(z_y^*-n)}}{2\left[\sigma_x^*\left(\frac{z_x^*}{z_x^*-n}\right)+\sigma_y^*\left(\frac{z_y^*}{z_y^*-n}\right)\right]} \quad (1.5)$$

where *m, z*, and *σ* are mass, charge, and standard deviation of species *x* and *y. z** and *σ** signify the charge state and standard deviations of the initial precursor ion specifically. The relationship between charge and peak width is based on fundamental time-of-flight equations;[87] this equation

assumes that centroid values shift only because of the changes in charge state. In sum, CAPTR provides a facile way to resolve components in high-mass, heterogeneous samples.

## 3 Effects of CAPTR on the Structure of Protein Ions

Observations of CAPTR with PDCH-derived monoanions support previous findings that proton transfer is the predominant charge-transfer pathway, rather than anion adduction or electron transfer.[1] Unlike electron transfer, no evidence for fragmentation has been observed during CAPTR experiments.[1,11,28,83,88]These properties of CAPTR, in addition to the wide range of charge states produced for structural characterization and mass assignment, support its utility as an analytical platform. In this section, we review the results of CAPTR-IM-MS of various protein cations generated from different solutions.

### 3.1 CAPTR of Protein Ions from Denaturing Solutions

As discussed previously, ions generated from denaturing solutions yield more highly charged ions with larger Ω values, indicating varying degrees of protein unfolding. By monitoring changes in Ω, we used CAPTR to investigate whether charge reduction can mitigate some of the structural effects associated with denaturing conditions. Studies also helped investigate the relationship between protein mass, Ω, and the extent of refolding with charge reduction. Ions of ubiquitin (8.6 kDa, monomer), cytochrome *c* (12 kDa, monomer), lysozyme (14.3 kDa, monomer), bovine serum albumin (BSA, 66 kDa, monomer), and antibodies, IgG1 (149 kDa, heterotetramer) and IgG4 (156 kDa, heterotetramer), were probed using various denaturing conditions. Ubiquitin and cytochrome *c* ions were both generated from 70:30 water:methanol acidified with trifluoroacetic acid to a pH of 2.[83] Ubiquitin ions with charge states of 5+ to 13+ were observed from ESI, and from each precursor ion, CAPTR products as

low as 3+ in charge were observed.[2] For ease of discussion CAPTR ions will be represented by "$P \rightarrow C$" for the remainder of the review where "$P$" is the precursor ion charge state and "$C$" is the product ion charge state. For example, ubiquitin 13 → 3 specifies the 3+ CAPTR product ion generated from the 13+ precursor.

Figure 1.5A shows the Ω distributions for the 13 → $C$ ubiquitin ions. With increasing numbers of CAPTR events (i.e., decreasing $C$), the distributions shift to smaller Ω values. The distributions appear relatively symmetric for large and small values of $C$, whereas the distributions appear multimodal for intermediate values of $C$. The largest compaction for denatured ubiquitin was observed for the 13 → 3 ions; this corresponds to a 50% decrease in Ω, indicating significant refolding upon reduction in charge by 10 CAPTR events.[2] Figure 1.5B shows the Ω values found for all $P \rightarrow C$ ubiquitin ions—these values depend strongly on $C$ and weakly on $P$. Differences between selected $P \rightarrow C$ ubiquitin ions will be discussed in Section 4.

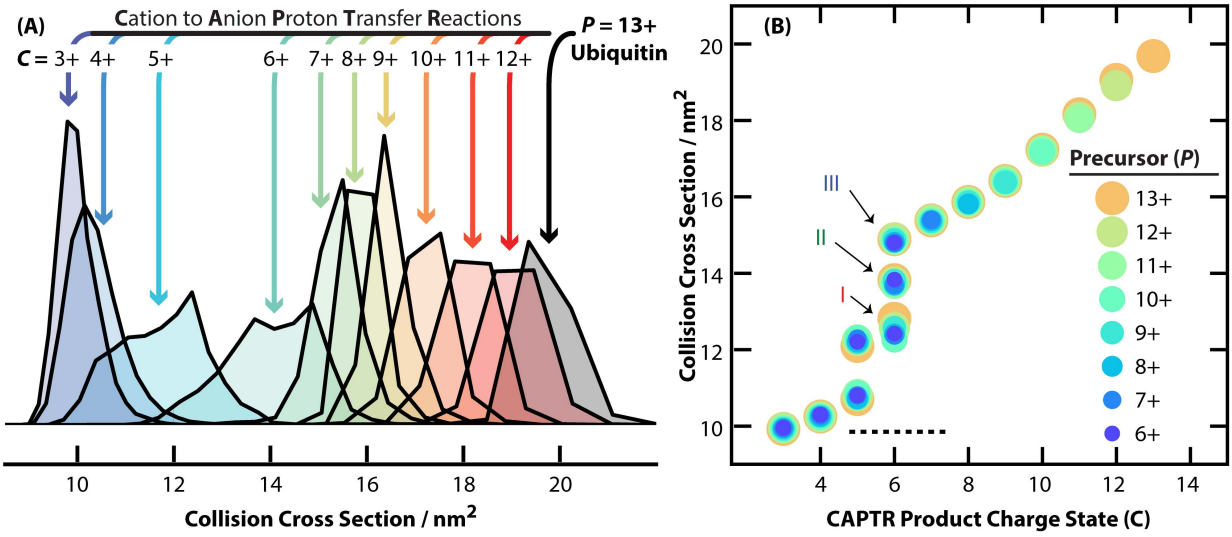


**Figure 1.5**. (A) Normalized Ω distributions of all 13 → $C$ ions of ubiquitin. All ions except 13 → 6 and 13 → 5 exhibit monomodal Ω distributions. 13 → 6 and 13 → 5 exhibit trimodal and bimodal Ω distributions, respectively. (B) Ω of

precursor (*P*) and CAPTR product ions (*P* → *C*) of ubiquitin. The lowest charge state product detected for each precursor ion was 3+. Precursor charge states are represented by differently colored circles, which were selected to facilitate visualization of the data. Average Ω of 4+ to 6+ ubiquitin from a native-like solution[25] is shown with a dotted line for comparison. Figure and caption adapted with permission from Laszlo et al. (2016).[2] CAPTR, cation-to-anion, proton-transfer reaction.

Generated from the same solution conditions, cytochrome *c* cations as high as 18+ in charge were observed.[83] Figure 1.6A shows the Ω distributions for the 18 → *C* cytochrome *c* ions; these distributions follow the general trends with decreasing *C* that were described for the 13 → *C* ubiquitin ions. The 18+ precursor ions exhibited a near 56% decrease in Ω on charge reduction to 4+ and 3+, corresponding to 14 or 15 CAPTR events. To compare with ubiquitin after 10 CAPTR events, cytochrome *c* 18 → 8 compacted by 30%. Interestingly, cytochrome *c* 13 → 3 ions, also produced by 10 CAPTR events, compacted by 49%. Lysozyme ions were generated by ESI from 1:1 water:acetonitrile with 0.2% acetic acid.[28] Under these conditions, 8+ to 13+ ions were produced. The 13 → 3 ions were the lowest-*z* CAPTR products observed with a corresponding 37% decrease in Ω. BSA ions, which are much larger in mass than lysozyme ions, were generated from 70:30 water:methanol with 0.2% formic acid.[11] Ions up to 45+ in charge were subjected to CAPTR. Following 35 CAPTR events, the 45 → 10 ions decreased 48% in Ω from that of the precursor (Figure 1.7C). After 10 CAPTR events, Ω decreased by only 10%. IgG1 and IgG4 ions were generated by ESI from aqueous 0.1% acetic acid; these ions are over twice as large in mass as BSA ions (Gozzo & Bush, manuscript submitted). 49+ ions were the

ions of highest *z* subjected to CAPTR, yielding products as low in *z* as 15+ and 16+ for IgG1 and IgG4, respectively (33–34 CAPTR events). The parallel decrease in Ω was 21% for IgG1 and 17% for IgG4. After 10 CAPTR events, 49 → 39 ions had only decreased by 5.4% and 4.3% in Ω for IgG1 and IgG4, respectively.

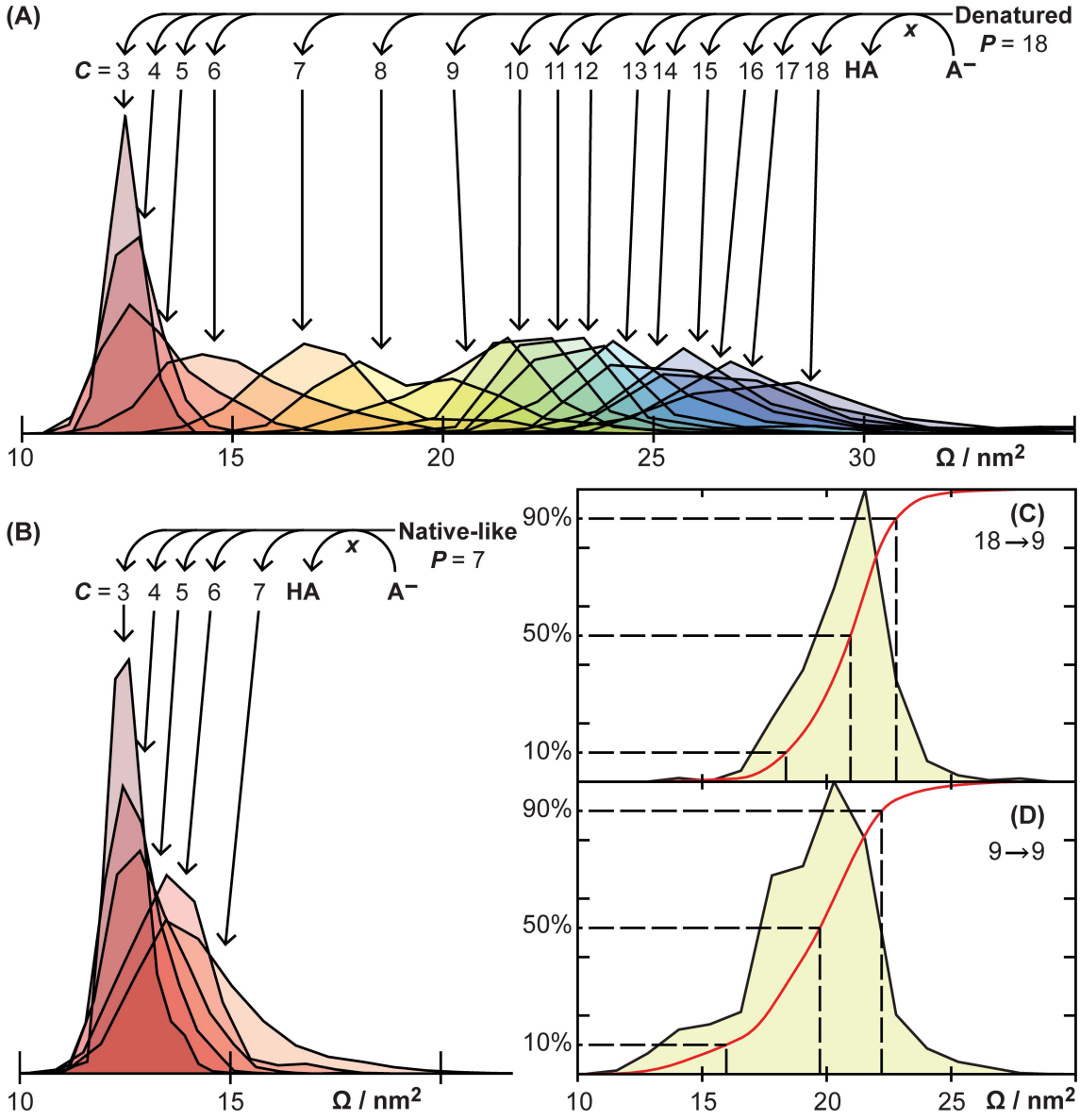


**Figure 1.6**. (A) Apparent Ω distributions for all 18 → C ions of cytochrome c from denaturing conditions. (B) Ω distributions for all 7 → C ions of cytochrome c from native-like conditions. The Ω distribution (black solid lines), cumulative

distribution (red lines), and critical Ω values (black dashed lines) for the (C) 18 → 9 and (D) 9 → 9 ions from denaturing conditions. All experiments probed ions generated using a temperature-controlled, electrospray ionization source set to 25°C. Figure and caption adapted with permission from Laszlo et al. (2017a).[83]

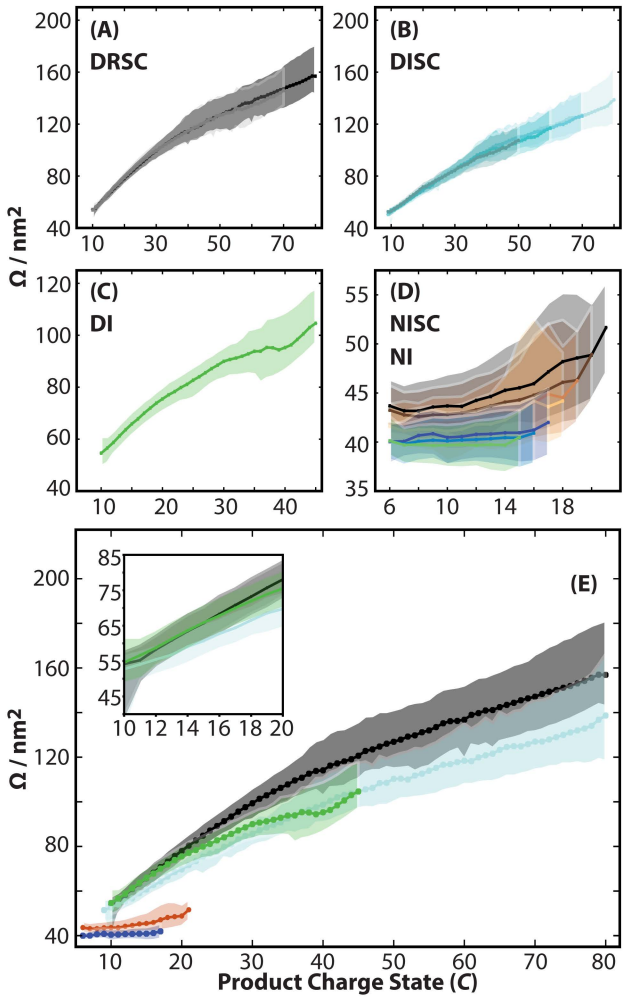


**Figure 1.7**. Results from IM-MS of CAPTR products of bovine serum albumin ions generated from various solution conditions. Markers correspond to the $\widetilde{\Omega}$ (median) values and the shaded regions span from 10% to 90% of the cumulative distribution function of each apparent Ω distribution. Results for (A) the

$^{DRSC}P\rightarrow C$, $P = 70$ and 80, ions, (B) the $^{DISC}P\rightarrow C$, $P = 50$, 60, 70, and 80, ions, (C) the $^{DI}45\rightarrow C$ ions, and (D) the $^{NISC}P\rightarrow C$, $P = 18$ to 21 (*copper tones*), and the $^{NI}P\rightarrow C$, $P = 15$ to 17 (*cool tones*), ions. (E) Summary of results for the highest P from each solution condition, that is, the $^{DRSC}80\rightarrow C$, $^{DISC}80\rightarrow C$, $^{DI}45\rightarrow C$, $^{NISC}21\rightarrow C$, and $^{NI}17\rightarrow C$ ions. The inset of E shows the results for $^{DRSC}80\rightarrow C$, $^{DISC}80\rightarrow C$, $^{DI}45\rightarrow C$ ions for $20 \geq C \geq 10$. Figure and caption adapted with permission from Gadzuk-Shea and Bush (2018).[11] CAPTR, cation-to-anion, proton-transfer reaction; DI, denaturing, disulfide-intact; DISC, denaturing, disulfide-intact, supercharging; DRSC, denaturing, disulfide-reducing, supercharging; IM, ion mobility; MS, mass spectrometry; NI, native-like, disulfide-intact; NISC, native-like, disulfide-intact, supercharging.

A summary of the results for CAPTR of denatured protein ions can be viewed in Figure 1.8A,C. Across the board, protein cations generated from denaturing solutions all refolded to some extent following CAPTR. The extent to which, if at all, removing excess charges may enable protein ions to form new interactions that are also present in the corresponding native structures is unclear. For example, molecular dynamics simulations of 13+ ubiquitin in the gas phase following sequential proton stripping results in the formation of increasingly compact structures that yield calculated Ω values that are qualitatively similar to many of our experimental observations for the CAPTR products of 13+ ubiquitin generated from a denaturing solution.[89] The proton-stripped 3+ ions from the simulations had calculated Ω values similar to those measured for native-like ubiquitin ions[20,25] and similar to those previously calculated for native structures of ubiquitin.[90,91] However, the molecular-dynamics structures were “inside-out,”

with new electrostatic interactions on the interior and hydrophobic residues on the exterior, as shown in Figure 1.9.[89] Additional simulations would benefit our understanding of the specific structural changes that occur at the molecular level following individual CAPTR events, especially for ions that exhibit Ω distributions that depend strongly on how they were formed (e.g., 7+ ions from different solution conditions or from different numbers of CAPTR events). A trend between the degree of compaction and mass was also observed. As the ions increased in mass, the level of collapse in Ω from precursor ions to CAPTR products tended to decrease. This trend will be discussed further in Section 3.4.

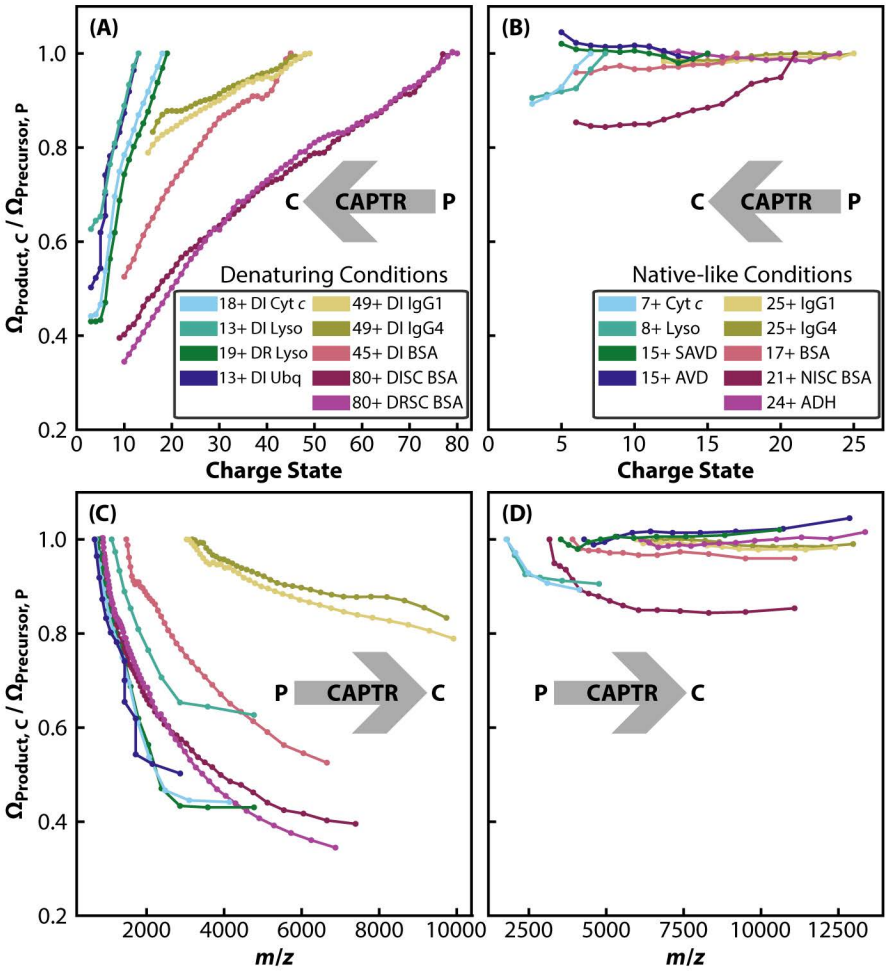

**Figure 1.8**. Summary of CAPTR results across different studies. Ω values used to determine $\Omega_{Product}/\Omega_{Precursor}$ correspond to either the centroid values of the Gaussian fits of the Ω distributions or to the 50% critical value calculated from cumulative distributions functions (integrations of apparent Ω distributions), depending on the study. (A) and (C) Results from protein ions generated by ESI from denaturing conditions. (B) and (D) Results from protein ions generated from native-like conditions. (A) and (B) Represent $\Omega_{Product}/\Omega_{Precursor}$ as a function of charge state, so precursors are of the highest charge and have $\Omega_{Product}/\Omega_{Precursor}$ equal to 1.0. (C) and (D) Represent $\Omega_{Product}/\Omega_{Precursor}$ as a function of *m*/*z*, so precursors are of the lowest *m*/*z*. Protein abbreviations are as follows: cytochrome *c* (cyt *c*), lysozyme (lyso), ubiquitin (ubq), bovine serum albumin (BSA), streptavidin (SAVD), avidin (AVD), and alcohol dehydrogenase (ADH). CAPTR, cation-to-anion, proton-transfer reaction; ESI, electrospray ionization.

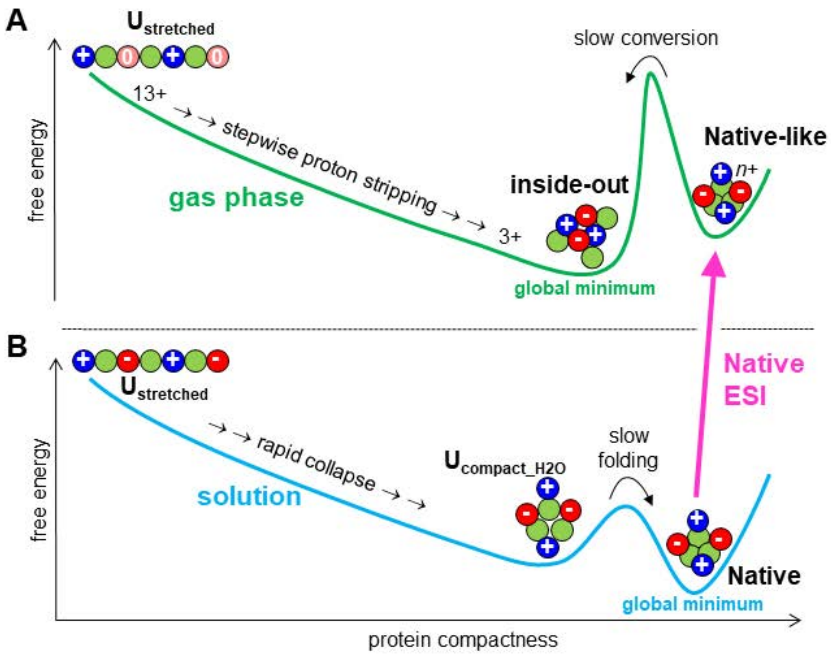


**Figure 1.9**. Cartoon summary of protein folding (A) in the gas phase and (B) in aqueous solution. Native ESI provides a connection between the two energy landscapes. Protein chains are shown in hydrophobic (green) and hydrophilic (positive/blue, negative/red) residues. An extended $U_{stretched}$ conformation was included in (B) to facilitate comparisons with the gas-phase behavior; we do not suggest that folding in solution generally starts from $U_{stretched}$. Figure and caption adapted with permission from Sever and Konermann (2020).[89] ESI, electrospray ionization.

### 3.2 CAPTR of Protein Ions from Native-Like Solutions

CAPTR was also applied to investigate the relationship between Ω and charge for protein ions generated from native-like conditions. Native-like solution conditions were the same for all protein cations probed: aqueous 200 mM ammonium acetate at pH 7. Cytochrome *c*, lysozyme,

BSA, and IgG proteins were probed under both denaturing and native-like conditions, so they will be discussed first. The observed charge states were lower overall when compared to denaturing conditions, as expected. The most-intense charge states observed directly from electrospray were 6+ to 8+ for both cytochrome *c* and lysozyme. The 7+ cytochrome *c* precursor ions gave rise to CAPTR products as low as 3+ in *z*, corresponding to four CAPTR events.[83] The 7 → 3 ions were observed to be 11% smaller than their 7+ precursors (Figure 1.6B). Lysozyme 8+ precursor ions yielded lowest-*z* CAPTR products of 3+ as well; these were 8.4% smaller than their precursors.[28] For comparison, lysozyme 7 → 3 products were only about 6.3% smaller than the 7+ precursors.

CAPTR of the native-like ions of BSA yielded a maximum compaction of 6% for the 17 → 6 ions, corresponding to 11 CAPTR events[11] as shown in Figure 1.7D. From recent work probing IgG1 and IgG4 ions, maximum relative decreases in Ω of 2.3% and 2.2% were observed for the IgG1 25 → 13 ions and IgG4 26 → 14 ions, respectively (Gozzo & Bush, submitted). Twelve CAPTR events occurred in both cases. Additional native-like proteins probed by CAPTR included avidin (64 kDa, homotetramer), streptavidin (53 kDa, homotetramer), and alcohol dehydrogenase (147 kDa, homotetramer). Relative to their precursor ions, the maximum decreases in Ω values of the product ions were 2.9%, 2.3%, and 3.6% for avidin, streptavidin, and alcohol dehydrogenase, respectively, which occurred within the first few CAPTR events (Figure 1.10).

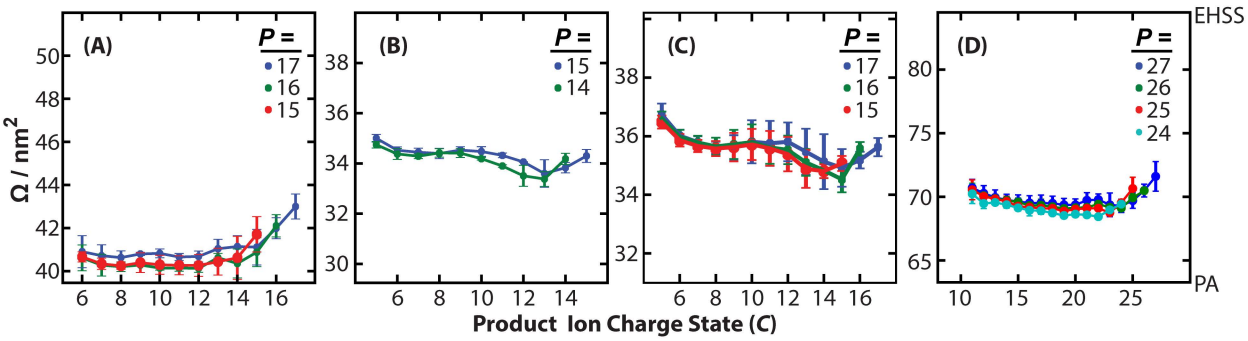


**Figure 1.10**. Ω values of the $P \rightarrow C$ ions of (A) serum albumin, (B) streptavidin, (C) avidin, and (D) alcohol dehydrogenase, where "*P*" is the charge state of the precursor and "*C*" is the charge state of the CAPTR product. The bars span the 95% confidence interval for each value, and the upper and lower limits of each panel correspond to the Ω values calculated using the projection approximation, PA, and exact hard spheres scattering, EHSS, methods. The different colors indicate ions from different *P*. Figure and caption adapted with permission from Laszlo and Bush (2017).[88] CAPTR, cation-to-anion, proton-transfer reaction.

A summary of the results for CAPTR of native-like protein ions is shown in Figure 8B,D. Overall, minimal compaction was observed with charge reduction by CAPTR indicating that the excess charges on native-like ions have a relatively small impact on Ω. Less charge-state dependence was observed than for the unfolded ions generated from denaturing solutions. Ω values of cytochrome *c* and lysozyme exhibited a stronger dependence on *C* than those of the other proteins studied. Trends in this data and comparisons to those for denatured ions will be discussed in Section 3.4.

### 3.3 Comparing Solution Conditions for Single Proteins

In addition to examining the effect of charge state on protein ions spanning a range of masses and Ω values, CAPTR-IM-MS was used to investigate the relationship between Ω and charge reduction for gas-phase ion structures of a single protein generated from different solution conditions. Our broadest study of the relationship between solution conditions, charge state, and Ω was one in which bovine serum albumin, BSA, ions were generated from five different solutions ranging from native-like to very disruptive.[11] These conditions are referred to as native-like, disulfide-intact (NI); native-like, disulfide-intact, supercharging (NISC); denaturing, disulfide-intact (DI); denaturing, disulfide-intact, supercharging, (DISC); and denaturing, disulfide-reducing, supercharging (DRSC), as described in the original work.[11] The more disruptive the original solution, the higher the charge states, the wider the charge-state distributions, and the larger the initial Ω values. Despite some overlap in the observed charge states produced (DISC and DRSC), none of the observed Ω values overlapped, indicating that ion structure depended strongly on the original solution conditions.

A subset of BSA ions from each condition was selected and subjected to CAPTR (Figure 1.7). Ω values of $P \rightarrow C$ ions from both DRSC ($P = 70$ and 80) and DISC ($P = 50$, 60, 70, and 80) conditions depended weakly on $P$ and decreased monotonically with decreasing $C$. Ions from DI conditions exhibited lower charge states than those from DISC conditions, so the selected precursor was 45+. A steady decrease in Ω was observed for most $45 \rightarrow C$ ions, except for 35+ to 40+ products, which all had similar Ω values. Compared to ions from native-like conditions, ions from denaturing conditions exhibited more significant compaction with decreasing $C$ due to refolding. From NISC conditions, precursors of charge 18+ to 21+ were selected. For $P = 19$ to 21, a steeper decrease in Ω was observed for the first CAPTR event with smaller decreases in Ω

for the remaining charge reduction down to $C = 6$. $18 \rightarrow C$ ions from NISC conditions were all similar in Ω. Some ions from NISC conditions exhibited weak dependence on $P$, for example, the $P \rightarrow 14$ ions increase in Ω with increasing $P$, but the lowest $C$ ions (6+) exhibited no trend in Ω with $P$. From NI conditions, $P = 15$ to 17, and Ω values for the $P \rightarrow C$ ions were all similar to each other, suggesting no significant dependence on the charge state of the precursor or product. When comparing ions across conditions, $P \rightarrow C$ ions from denaturing conditions were all larger than the corresponding $P \rightarrow C$ ions from NISC conditions, which were all larger than those from NI conditions. $P \rightarrow C$ ions of the same $C$ from DISC and DI conditions were similar in Ω. Ions from DRSC conditions were larger for high $C$, but the difference decreased with decreasing $C$. The rate of compaction with each CAPTR event was similar for ions from both DISC and DRSC conditions for $C \geq 36$, but both rates of compaction increased for $C < 36$. The DRSC compaction rate increased more, leading to the convergence of Ω values at low $C$. The difference between these two conditions was the presence or absence of disulfide bonds. Ions from DRSC conditions were more able to extend to larger structures than ions from DISC or DI conditions and were also able to refold more with each CAPTR event, emphasizing the constraining nature of disulfide bonding on the structures of these ions.

Another notable observation was that $P \rightarrow C$ ions from denaturing conditions with $C$ values also observed from native-like conditions did not compact down to similar Ω values to the $P \rightarrow C$ ions from NI conditions—they remained about 30% larger. This result suggests that these ions retained some aspects of their solution-phase structures, even as they folded to smaller Ω with each CAPTR event. Finally, even though ions from NISC conditions decreased in Ω with decreasing charge state, they remained larger than ions from NI conditions for all charge states, indicating that protein structure is perturbed with supercharging by sulfolane. These structural

changes were not mitigated by CAPTR, that is, supercharging can cause irreversible changes to the structures of protein ions.

In summary, these results suggest that gas-phase ions retain some aspects of their solution-phase structure in the gas phase. CAPTR revealed that the Ω values of product ions can depend simultaneously on the original solution conditions, *P*, and *C*. These experiments suggest that protein ions have a memory of their prior structures from solution, and their gas-phase structures respond to charge reduction and collisional activation accordingly.

### 3.4 Effects of Charge Density on Ion Structure

Together, the results discussed above suggest that charge density, as represented by *m*/*z*, is a significant factor governing the overall impact of charge on gas-phase ion structures. CAPTR-IM-MS experiments showed that, without exception, the Ω values of protein cations generated from denaturing solution conditions had a stronger dependence on charge than protein cations generated from native-like conditions. Denatured ions experienced significant refolding with charge reduction by CAPTR. Smaller protein ions with lower masses, lower initial *m*/*z* values, and lower initial Ω generally compacted more significantly with *C* than larger ions, as evidenced by larger percent decreases in Ω with CAPTR, even over the same number of CAPTR events (Figure 1.8A,C).

An exception to this trend was observed when comparing 18 → 8 ions of cytochrome *c* to 13 → 3 ions of lysozyme from DI conditions. Although these both correspond to 10 CAPTR events, and the charge density is greater for 18+ ions of cytochrome *c* when compared to 13+ ions of lysozyme from DI conditions, lysozyme ions exhibited greater compaction in Ω (37% vs. 30%). When we instead compare 13 → 3 ions from both proteins, cytochrome *c* ions exhibited the greater compaction in Ω. There was a steeper decrease in Ω when subjecting the 13+

cytochrome *c* precursor ions to 10 CAPTR events than when subjecting the 18+ ions to the same extent of CAPTR. This may suggest that, up to a certain point, excess protons limit the formation of additional noncovalent interactions because the Coulombic strain is still too high. Additionally, 13 → *C* cytochrome *c* ions were similar in Ω to the 18 → *C* ions where *C* = 13 to 3. An increase in the rate of compaction with CAPTR was also observed for BSA ions from DISC and DRSC conditions below *C* = 36, supporting this hypothesis. 18+ DI lysozyme ions were not observed from denaturing conditions, so 18 → *C* ions are not available for comparison; however, disulfide-reduced (DR) lysozyme 18+ ions were produced and subjected to CAPTR. 18 → *C* ions exhibited similar extents of compaction to cytochrome *c* 18 → *C* ions across all *C*. This observation suggests that, in addition to charge density, other aspects of structure, for example, disulfide-bonding, impact the relationship between Ω and charge.

The Ω values of native-like ions depended relatively weakly on charge (Figure 1.8B,D). Compared to denatured ions, the percent decrease in Ω values with CAPTR was minimal, but a similar trend between charge density and the extent of compaction was observed. These experiments suggest that the amount of charging resulting from ESI is generally well-accommodated by large, native-like protein ions, but it can still have a modest effect on Ω. The structures of smaller protein ions appear to be far more sensitive to the excess charges associated with ESI.

Altogether, these observations reveal that excess charges can have a larger effect on smaller protein ions, which may be the result of higher charge density, lower surface-to-volume ratios, and a more limited ability to self-solvate those excess charges. These results are in agreement with recent work investigating the charge-state distributions of protein ions formed by ESI and their relationships with Ω.[38] Smaller protein ions exhibited more positive slopes in Ω

with increasing charge across their charge-state distributions. The increase in Ω with charge was attributed to the limited ability of these smaller proteins to undergo surface compaction and self-solvation, leading to Coulombic repulsion that stabilized larger conformations.[38] This is consistent with the stronger relationship observed between Ω and *z* for smaller proteins using CAPTR-IM-MS. This suggests that smaller, native-like ions have significant Coulombic strains, which are associated with more significant decreases in Ω upon charge reduction, whereas larger, native-like ions initially have lower Coulombic strains, and concomitantly, exhibit less compaction upon charge reduction.

## 4 Probing Energy Landscapes

Energy-dependent IM is used to study the stability and conformational space of ions in the gas phase.[92] For example, in collision-induced unfolding (CIU), native-like ions are activated as a function of collision energy and then analyzed by IM. Activation enables ions to overcome the energy barriers to isomerization and often results in the formation of new, stable structures that have larger Ω values.[93] CIU results have been used to study the stabilities of proteins,[94] modes of ligand binding,[95] and to differentiate similar biotherapeutics.[96] Applying collisional activation before or after CAPTR enables us to probe different regions of the energy landscapes of gas-phase ions.

### 4.1 Pre-CAPTR Activation

Pre-CAPTR activation is performed on precursor ions before subjecting them to CAPTR for charge reduction. This will be represented with an asterisk by the precursor charge state: $P^* \rightarrow C$. Pre-CAPTR activation can be accomplished at the atmospheric-pressure interface by increasing the bias between the sampling cone voltage and the extraction cone (Figure 1.3C).

Pre-CAPTR activation has also been accomplished by increasing the bias between the quadrupole and the trap cell.[2] These methods allow for the investigation of the effects of precursor activation on product ion structures and have been proposed to provide an indirect probe of precursor ion structure. For example, in studying denatured ubiquitin ions with CAPTR, the 8* → 8 (activated precursor ions that did not undergo reaction) Ω distributions were independent of the voltage applied,[2] but the Ω distributions of the 8* → 6 ions changed with increasing energy (Figure 1.11E). The 8* → 6 ions display features I, II, and III, with I being the most intense at low energies. Features II and III grow in intensity, whereas feature I decreases in intensity, with increasing activation. It is possible that the 8* → 8 ions isomerize to different conformations that have indistinguishable Ω, but form structures with resolvable Ω for the 8* → 6 ions. For the highest energies tested (70–100 V), the 8* → 6 distributions were similar. This may reflect a quasi-equilibrium[92] of structures formed in the 8* → 8 populations at those energies.

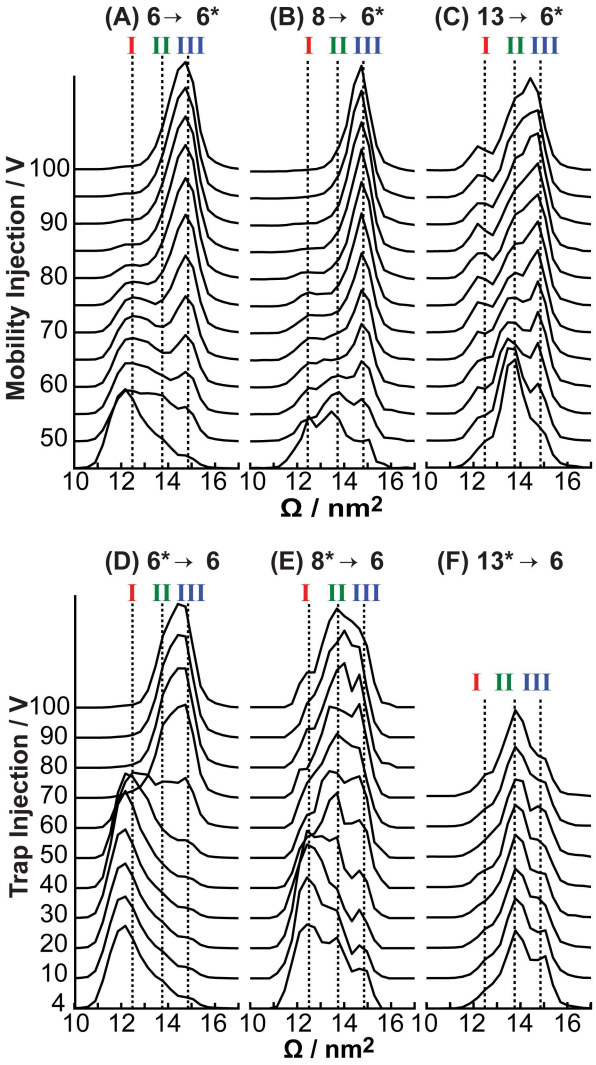


**Figure 1.11**. Post-CAPTR activation of (A) 6 → 6*, (B) 8 → 6*, and (C) 13 → 6* ubiquitin ions. Pre-CAPTR activation of (D) 6* → 6, (E) 8* → 6, and (F) 13* → 6 ubiquitin ions. Vertical lines corresponding to the average Ω for the three features of the Ω distribution of 6+ (I–III) from Figure 1.5B are included for comparison. These mobility experiments used a field of 6.4 $V \cdot cm^{-1}$. Figure and caption adapted with permission from Laszlo et al. (2016).[2] CAPTR, cation-to-anion, proton-transfer reaction.

Recently, pre-CAPTR activation was used to differentiate IgG1$\kappa$ and IgG4$\kappa$ from human myeloma (Gozzo & Bush, submitted). These antibodies have high sequence similarity and have the same number of interchain disulfide bonds, but they differ in connectivity of said bonds.[97] They are difficult to differentiate by IM-MS alone.[96] The 25* → 25 ions of IgG1 and IgG4 displayed indistinguishable or very similar Ω distributions at all the pre-CAPTR activation voltages tested, but with charge reduction, the Ω distributions of the 25* → 12 ions were more resolved. At 75 V precursor activation, for example, IgG4 did not compact as much as IgG1 with charge reduction, creating differences in the Ω distributions with decreasing charge that reflect the subtle differences in their structures. These results suggest that pre-CAPTR activation and IM-MS may be useful for differentiating similar biomolecules and biotherapeutics, even in cases where activation and IM-MS alone (i.e., CIU) are inadequate.

### 4.2 Post-CAPTR Activation

Post-CAPTR activation is performed on residual precursor and CAPTR product ions after exiting the trap cell and before analysis by IM-MS. This is represented with an asterisk by the product charge state: $P \rightarrow C^*$. Post-CAPTR activation can be performed as a function of the dc bias between the trap cell and mobility cell, which increases the kinetic energy of ions during injection to the mobility cell (Figure 1.3C). Collisional activation after CAPTR has also been accomplished by establishing a region analogous to the helium cell on the unmodified Synapt G2,[98] but pressurizing it with argon for more energetic collisions.[88] This region is located just before the drift region. Post-CAPTR activation is used to directly probe the stabilities and structures of product ions.

Post-CAPTR activation was applied to the 6+ ions generated from various precursors ($P$ = 6, 8, and 13) of denatured ubiquitin.[2] The 6* → 6 and 6 → 6* results were similar, indicating

similar activation mechanisms for pre- and post-CAPTR activation in the experiments (Figure 1.11A,D). Features I, II, and III were observed in the Ω distributions, with feature I being the most compact and feature III being the most unfolded. At low energies, 6 → 6* displayed mainly feature I, with low intensity for the other two features. 8 → 6* ions also exhibited the highest intensity for feature I, but presented significant intensities for features II and III as well. With increasing activation voltage, both the 6 → 6* and 8 → 6* ions unfolded to predominantly feature III, though 8 → 6* ions completed the transition 10 V earlier than 6 → 6* ions (Figure 1.11A,B). In contrast, 13 → 6* ions populate feature II mainly, with low intensities of I and III at low energies (Figure 1.11C). The intensity of feature I do not change significantly with increasing energy but feature II gives way slightly and feature III increases in intensity until they are about equivalent at the highest voltages. The persistence of features I and II contrasts observations for the 6 → 6* and 8 → 6* ions, which suggests that 13 → 6* ions exhibit different structures than those ions. They do not appear to interconvert in these experiments, indicating that different regions of the energy landscape were probed.

Post-CAPTR activation was also applied to 15+ ions of BSA generated from different solution conditions.[11] In this case, nitrogen was used as the drift gas, so, as ions were injected into the mobility cell with increasing voltage, more efficient energy deposition occurred than with a helium-filled drift cell. 15 → 15* ions from NI conditions, 60 → 15* ions from DISC conditions, and 70 → 15* ions from DRSC were tested. The apparent Ω distributions and their median values are presented in Figure 1.12. At low energies, Ω distributions of ions from DRSC and DISC conditions overlapped significantly, while the Ω distributions of ions from NI conditions were distinct and appeared at smaller Ω. With increasing activation, the populations from DRSC and DISC conditions began to compact while the ions from NI conditions got larger.

At the highest injection voltages, ions generated from all three conditions exhibited similar Ω values and their Ω distributions largely overlapped, providing evidence for population of similar areas of their energy landscapes. The distributions of ions from DRSC were slightly shifted to larger Ω compared to distributions of ions from NI and DISC conditions. This is different from the results observed using post-CAPTR activation on ubiquitin 6+ ions generated from the same solution conditions, but from different precursors.[2] In this case, a quasi-equilibrium[92] of structures may have been reached before the energy required for dissociation was reached. On the other hand, these ions could have different structures that just happen to coincide in Ω. The initial population of 15+ ions from NI conditions is significantly different than the other populations based on its response to increasing energy; the ions from NI conditions overcome energy barriers to isomerize to larger structures while the other ions decrease in size. This reflects the disintegration of intramolecular interactions that prevent such expansion, whereas the compaction of ions from DISC and DRSC conditions may be credited to the formation of initially absent intramolecular interactions. This provides additional support for the generation of kinetically trapped structures via ESI; ions from different solution conditions retain aspects of condensed-phase structure, but gas-phase equilibrium structures may be significantly different.

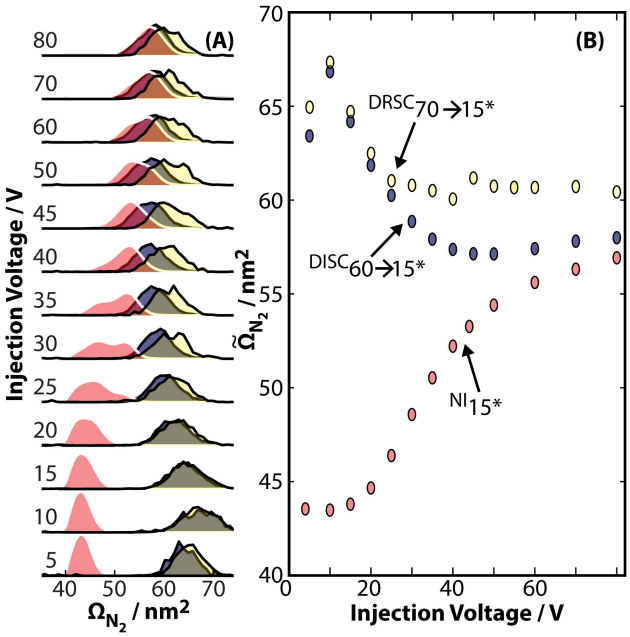


**Figure 1.12**. (A) Apparent $\Omega_{N_2}$ distributions of the $^{NI}15^*$ (*magenta*), $^{DISC}60 \rightarrow 15^*$ (*purple*), and $^{DISC}70 \rightarrow 15^*$ (*yellow*) BSA ions as a function of the injection voltage used to transfer the ions into a drift cell containing 1.2 Torr nitrogen gas. (B) $\widetilde{\Omega}_{N_2}$ values of the distributions in (A) as a function of the injection voltage. Figure and caption adapted with permission from Gadzuk-Shea and Bush (2018).[11]

## 5 Comparison to Results from Other Charge-Reduction Strategies

The following section compares the IM-MS results from studies using CAPTR with those using other methods to manipulate charge. As discussed in Section 1.3, these methods include the addition of solution modifiers before ESI, atmospheric-pressure methods, gas-phase ion/neutral chemistry, and gas-phase ion/ion chemistry. Some methods include the isolation of precursors of a specific charge state, but others simultaneously affect all precursors. This

discussion focuses on studies of ubiquitin, cytochrome *c*, lysozyme, alcohol dehydrogenase, and pyruvate kinase. Although many of these studies used drift tubes[99] or radio-frequency confining drift tubes[100] containing helium gas, some used traveling-wave IM in $N_2$ gas and external calibration with helium-based Ω values. We will not discuss potential bias in the values determined using the latter, but the challenges and potential errors associated with calibration are discussed elsewhere.[101,102]

### 5.1 Effects of Charge on Small, Single-Domain Proteins

Ubiquitin and cytochrome *c* are widely used as models of single-domain proteins. Results from the following experiments were selected for comparison to results from CAPTR of these protein ions: ion/neutral proton transfer of denatured ubiquitin,[24] crETD of denatured ubiquitin,[103] and crETD of native-like and denatured cytochrome *c*.[49] CAPTR was performed on quadrupole-selected 6+ to 13+ ubiquitin ion populations generated from denaturing solution conditions, as discussed in Section 3.1 and shown in Figure 1.5.[2] Clemmer and coworkers generated ubiquitin ions from a different denaturing solution and performed ion/neutral proton-transfer reactions broadly, on the whole population of observed ions, 6+ to 13+.[24] Results of ion/neutral proton-transfer reactions are shown in Figure 1.2. $^{DT}\Omega_{He}$ values of the precursor ions in these two studies were similar, with some differences observed for 6+ to 8+ distributions. After CAPTR, all $P \rightarrow C$ ions exhibited smaller Ω values than their precursors.[2] The product ions of a particular *C* formed from different *P* had very similar Ω values, pointing to a strong dependence on *P* and a weak dependence on *C*. These results are also consistent with an earlier study of ion/ion proton transfer of ubiquitin ions.[75]

The 4+ and 5+ products of ion/neutral proton transfer from ubiquitin cations to different bases exhibited either compact or partially folded, rather than elongated conformers.[24] More-

compact populations were depleted preferentially; this effect was stronger with stronger bases. More-elongated populations exhibited no evidence for folding, which was attributed to the larger gas-phase acidities of elongated protein ions (i.e., removing a proton from those ions is more endergonic) and the preferential depletion of compact ions that are expected to have smaller gas-phase acidities[24] (i.e., removing a proton from those ions is less endergonic). In contrast, CAPTR appears to charge reduce all conformers of ubiquitin,[2] which is consistent with the large exergonicity of ion/ion proton-transfer reactions. Despite these differences, both studies report Ω values that depend strongly on *z*.

CAPTR[2] and crETD[103] of selected ubiquitin ions generated from denaturing solutions both resulted in folding and compaction in Ω with charge reduction. crETD was performed on quadrupole-selected ubiquitin ions with 1,4-dicyanobenzene radical anions;[103] this reagent yields both proton-transfer and electron-transfer products.[43,47,64] In this case, the apparent ratio of proton-transfer to electron-transfer products was determined, and, in contrast to ion/neutral studies, preferential depletion of certain conformations was not observed, which was attributed to the more homogenous sizes of the precursor ions. In both the crETD and CAPTR studies, the charge-reduced products exhibited similar Ω values to those for the identically charged ions generated directly from ESI, indicating that Ω depends on *z*. With increasing post-reduction collisional activation, the Ω distributions of $6 \rightarrow 6^*$ and $8 \rightarrow 6^*$ ions evolved qualitatively similarly in the two studies, suggesting similar structures may have been probed.

CAPTR was performed on quadrupole-selected cytochrome *c* ions generated from both native-like and denaturing solution conditions as discussed earlier and shown in Figure 1.6.[83] crETD was performed on quadrupole-selected cytochrome *c* ions from similar solution conditions using 1,3-dicyanobenzene radical anions.[49] That study reports that proton transfer was

not a major pathway in those crETD experiments. Like the ion/neutral studies of denatured ubiquitin, the most compact features of denatured cytochrome *c* were preferentially depleted by charge-reduction reactions; the remaining precursor ions exhibited more extended populations. In CAPTR experiments, preferential depletion was not observed. Despite some differences in precursor and product distributions, both studies observed that Ω depended on *z*. For instance, 10+ products of crETD from 10+, 11+, and 12+ precursor ions all exhibited similar Ω distributions.[49] For the intermediate-charged CAPTR products ($P \rightarrow C,\ C = 9$ to 5), the Ω of the product ions also depended weakly on *P*.[83] Ω distributions of native-like ions generated for CAPTR experiments were significantly smaller and exhibited fewer features than the corresponding native-like ions in crETD studies. To perform crETD in this case, the optimized instrument conditions were activating. When crETD was performed on the native-like 7+ ions for example, the resulting 6+ ions compacted to sizes closer to native-like 6+ ions measured under non-crETD conditions.[49] As a result, compaction was more significant than was observed with CAPTR. Overall, these studies suggest that Ω can depend strongly on *z* for small, single-domain protein cations.

### 5.2 Effects of Charge on Proteins with Internal Disulfide Bonds

Lysozyme is a 14 kDa protein whose native structure contains four internal disulfide bonds. The charge states of lysozyme ions from denaturing, disulfide-intact (DI) and denaturing, disulfide-reducing (DR) conditions have been manipulated using ion/neutral proton transfer reactions[42] and CAPTR.[28] Both studies reported similar $^{DT}\Omega_{He}$ values for ions from DR conditions and the presence of a slightly unfolded population for ions from DI conditions, but the earlier study also reported a more-folded population for ions from DI conditions. For the ion/neutral proton-transfer experiments, the full populations of lysozyme ions from DI or DR

conditions were transmitted through a gas cell containing a vapor of either n-butylamine or 7-methyl-1,5,7-triazobicyclo[4.4.0]dec-5-ene.[42] For ions from both conditions that were subjected to ion/neutral proton-transfer reactions, $^{DT}\Omega_{He}$ distributions were more compact than those of the originating ions.[42] CAPTR of selected precursors from both conditions also yielded charge-reduced product ions that were more compact than their precursors.[28]

Energy-dependent experiments were used to probe stabilities of charge-reduced lysozyme ions. For ions from DI conditions, collisional activation of 6+ lysozyme ions from ion/neutral proton transfer resulted in $^{DT}\Omega_{He}$ values that appeared to be independent of the applied activation voltage.[42] In contrast, the $^{DT}\Omega_{He}$ values of 12 → 6* CAPTR products decreased with increasing energy.[28] At low energies, the 12 → 6* ions exhibited $^{DT}\Omega_{He}$ values that were larger than those of the 6+ ions from ion/neutral proton transfer, and at the highest energies, 12 → 6* ions exhibited $^{DT}\Omega_{He}$ values that were indistinguishable from those of the 6+ ions from ion/neutral proton transfer.[28,42] The results are consistent with the formation of fully annealed products following ion/neutral proton-transfer reactions and kinetically trapped products following CAPTR; with increasing energy the CAPTR products anneal and have similar structures to those formed directly by ion/neutral proton-transfer reactions. Potential factors that may contribute to these results include: (1) the CAPTR product was generated from a 12+ precursor, whereas the ion/neutral proton-transfer products were generated from a full distribution of charge states that did not extend to the 12+ ion, (2) ion/neutral proton-transfer products may have preferentially reacted with more compact precursors and yielded more compact products,[24] and (3) ion/neutral proton transfer may result in greater heating (and preannealing) than CAPTR.

For ions from DR conditions, collisional activation of 6+ lysozyme ions from ion/neutral proton transfer resulted in $^{DT}\Omega_{He}$ values that increased with increasing energy.[42] At low energies,

the 12 → 6* CAPTR products exhibited larger $^{DT}\Omega_{He}$ values than those for the 6+ ions from ion/neutral proton transfer. With increasing energy, structures with smaller $^{DT}\Omega_{He}$ values became populated, but larger structures near 17.5 $nm^2$ persisted over all energies. Although the results from these two studies using identical DR conditions indicate that Ω can depend strongly on *z* and the presence of disulfide bond, the significant differences in the energy-dependent IM analysis of ions from ion/neutral proton-transfer reactions and CAPTR suggest that those two charge-reduction methods can yield products that populate very different regions of the energy landscape of a protein.

### 5.3 Effects of Charge on Native-Like Ions of Larger Proteins

Alcohol dehydrogenase (ADH) and pyruvate kinase (PK), which are homotetramers with masses of 147 and 237 kDa, respectively, have been used to study the effects of charge on the structures of native-like protein ions. In addition to CAPTR,[88] the charge states of ADH and PK have been manipulated using solution-phase additives of triethylamine[3] or 1,5-diazabicyclo[4,3,0]non-5-ene (DBU),[29] and ion/neutral proton transfer with nebulized DBU.[29] In addition, the charge states of ADH have been manipulated using crETD with 1,4-dicyanobenzene radical anions[63] and those of PK have been manipulated using corona-discharge.[69] CAPTR and crETD were applied to quadrupole-selected ions, whereas other charge-reduction methods were applied to all ions simultaneously.

Figure 1.13A shows Ω values of ADH as a function of charge state. Overall, CAPTR yielded the widest range of product-ion charge states. The products compacted slightly following the first few CAPTR events and the maximum decrease in Ω relative to the precursor was 3.6%.[88] Ω values of ions generated from solutions with triethylamine were nearly identical to those of ions of the same *z* from native-like conditions.[3] Below 24+, ions generated from

triethylamine solution increased in Ω modestly with decreasing charge.[3] A similar trend was observed for ions exposed to nebulized DBU at atmospheric pressure.[29] When DBU was added to solution, instead of introduced in the gas phase, addition activation was required to knock off proton-bound base molecules and accomplish the desired charge reduction.[29] This also resulted in slightly unfolded ions that were significantly larger than native-like ions from ESI at charge states 21+ to 27+. These ions exhibited a significant decrease in Ω with decreasing charge state. The observation that solution modifiers often complex with protein cations during ESI—thus requiring supplemental activation to release the protein ion of interest—illustrates some of the challenges associated with using solution modifiers and using the resulting data to understand the relationship between charge and protein ion structure. The Ω values of crETD products of ADH depended more strongly on charge state than those for the CAPTR products, for example, the 26+ precursor yielded a 15+ product that was 6.4% smaller.[63] The comparatively large decrease in Ω when 26+ ADH is subjected to crETD is consistent with heating and annealing of those products; the arrival times of 25 → 17* ADH ions decrease with increasing post-CAPTR collision energy.[88] The products generated from crETD may be different than those produced from CAPTR; charge reduction with 1,4-dicyanobenzene radical anions can proceed through either nondissociative electron transfer or proton transfer. All studies of the charge reduction of native-like ions of ADH indicate the Ω values of these ions depend less strongly on charge than smaller, single-domain proteins.

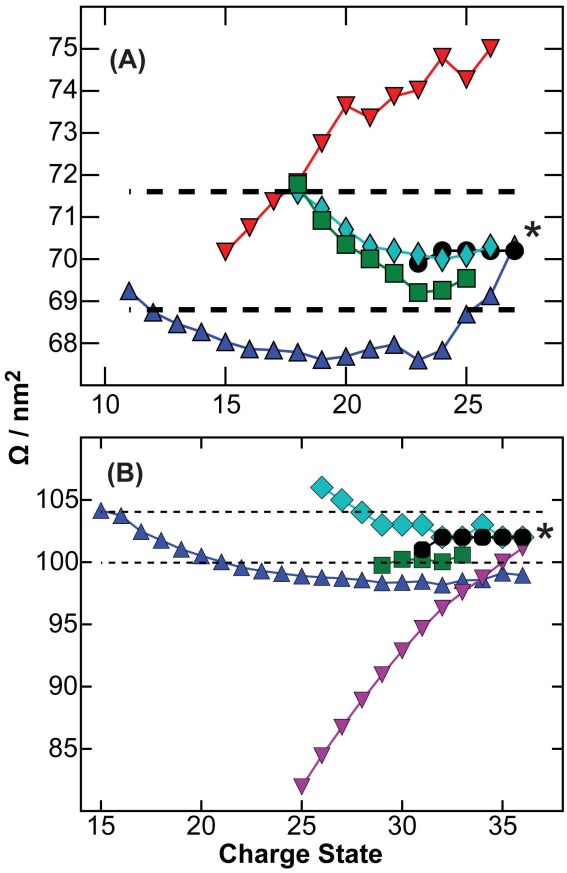


**Figure 1.13**. Ω values for (A) alcohol dehydrogenase and (B) pyruvate kinase ions. Results from CAPTR (*blue triangles*) are based on the average of values for the products from each precursor.[88] For comparison, values are also plotted for ions generated from ESI of solutions containing 200 mM ammonium acetate at pH 7.0, *black circles*,[3] 200 mM ammonium acetate with 10 mM triethylamine at pH 7.0, *cyan diamonds*,[3] 100 mM ammonium acetate at pH 6.9 with exposure to nebulized 1,5-diazabicyclo[4,3,0]non-5-ene, DBU, *green squares*,[29] 100 mM ammonium acetate at pH 6.9 and reacted with 1,4-dicyanobenzene radical anions, *red inverted triangles*,[63] and 100 mM ammonium acetate in close proximity to a corona discharge probe, *purple inverted triangles*.[69] Dashed horizontal lines indicate ±2% of the data point marked with an asterisk (*). Figure and caption

adapted with permission from Laszlo and Bush (2017).[88] CAPTR, cation-to-anion, proton-transfer reaction; ESI, electrospray ionization.

Figure 1.13B shows Ω values as a function of charge state for PK. For experiments with DBU and triethylamine, similar challenges were reported as described above for ADH.[3,29] Incorporating triethylamine into the electrospray solution and exposing ions to nebulized DBU both yielded ions with Ω values that were similar to those generated from solutions without those modifiers.[3,29] These results support the claim that the structure of native-like PK ions does not depend strongly on charge state. Another study generated PK ions from native-like conditions in close proximity to a corona-discharge probe using $N_2$ gas.[69] Contrary to results using the other approaches discussed, the application of the corona-discharge probe yields ions whose Ω values decrease significantly with decreasing *z*, for example, the Ω values of the 25+ ions were 19% smaller than the 36+ ions.[69] These differences may be attributable to factors inherent to the charge-reduction method, for example, generation of new species by corona discharge or activation in the high fields of the discharge region. Alternatively, the larger changes reported for these experiments could be a consequence of the IM measurement, which used traveling-wave IM with ramped amplitudes.

**6 Energetics**

As discussed in Section 1.3.3, ion–ion reactions like CAPTR (Reaction 1.3) are expected to be highly exothermic. These expectations originate from comparison of the proton affinities of the monoanion and the protein cations.[43] Here, we will expand on energetics by quantifying the change in free energy of these reactions, and we will discuss implications for interpreting

CAPTR data. Reaction 1.3 can be separated into reactions for extracting a proton from a protein polycation:

$$[M + xH]^{x+} \rightarrow [M + (x-1)H]^{(x-1)+} + H^+ \quad (1.6)$$

and adding a proton to the monoanion:

$$[PDCH - F]^- + H^+ \rightarrow [PDCH - F + H] \quad (1.7)$$

The change in free energy for a proton-transfer reaction in the gas phase is usually expressed using the gas-phase basicity (GB) of the proton acceptor, which is the negative of the change in free energy that occurs when the proton acceptor and a proton combine to form product. Therefore, the change in free energies for Reactions (1.6) and (1.7) are:

$$\Delta G_{Reaction\ 5} = GB([M + (x-1)H]^{(x-1)+}) \quad (1.8)$$

$$\Delta G_{Reaction\ 6} = -GB([PDCH - F]^-) \quad (1.9)$$

Experimental measurements of the apparent GB of cytochrome *c* ions generated from denaturing solutions range from 801 kJ mol$^{-1}$ (for the 15+ ion) to 980 kJ mol$^{-1}$ (for the 3+ ion);[104] GB values increase with decreasing charge state. Based on experimental measurements of the GB of lysine-containing peptide ions[104,105] and the relative GB of lysine and arginine,[106] we proposed an upper limit for the GB of a protein ion of 1080 kJ mol$^{-1}$.[1] Based on electronic structure calculations, the diabatic GB of the lowest-energy conformer of [PDCH–F]$^-$ was 1310 kJ mol$^{-1}$. Many conformers of the reactant and product were also considered, but this was the smallest GB found for this reaction.[1]

These comparisons suggest that each CAPTR event is exergonic by at least 230 kJ mol$^{-1}$, as shown in Figure 1.14. A protein ion has far more degrees of freedom than the PDCH–containing product, therefore statistical partitioning of the energy from a series of CAPTR events would result in significant heating of the protein ion. However, no significant fragmentation has

been observed during CAPTR experiments,[1] which is consistent with analogous reactions performed under different conditions.[107] Furthermore, activation and re-thermalization of CAPTR products can result in the formation of new structures (see Section 4.2). Those results indicate that the structures of CAPTR products depend strongly on kinetic trapping, that is, energy deposition during CAPTR is insufficient to anneal the products and form the equilibrium distribution of structures.

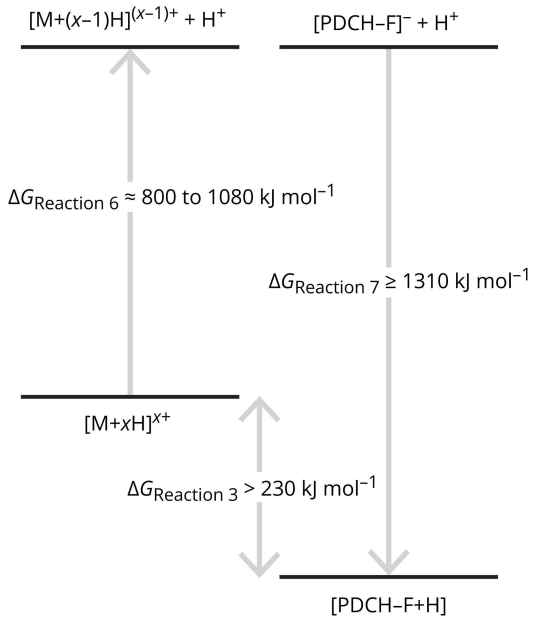


**Figure 1.14**. Partial reactions that were used to estimate the exergonicity of each cation-to-anion, proton-transfer reaction event (Reaction 1.3). See text for a discussion of these estimates.

Although the total change in free energy resulting from each CAPTR event is highly exergonic, it is possible that the energy does not partition statistically between the products. For example, Uggerud and coworkers reported results from ab initio direct dynamics of proton transfer from the hydronium cation to neutral ammonia.[108] In some trajectories, the proton

transferred directly and deposited a “high and nonstatistical fraction of the reaction enthalpy into the product ammonium ion.” In trajectories exhibiting long-lived interaction complexes, the reaction enthalpy partitioned statistically between the products.[109] Because the rate-limiting step of ion/ion reactions in the gas phase is the formation of a long-range interaction complex,[47] direct proton transfer and nonstatistical partitioning may be even more likely for ion/ion reactions than for the ion/neutral reaction considered by Uggerud and coworkers.

Based on the evidence and discussion above, we propose that nonstatistical partitioning of energy into the neutralized monoanion is a significant process during CAPTR experiments, which would result in significantly less heating of charge-reduced protein ions than suggested by the large total change in free energy associated with each CAPTR event. Although some interpretations of ECD and ETD data invoke nonstatistical partitioning of energy after the polycation combines with an electron,[110,111] all models are consistent with the bulk of that recombination energy being available to the reduced cation.[60–62] Note that in ECD, a free electron combines with a polycation; without fragmentation the entire recombination energy must partition into the protein. In ETD, extracting an electron from a monoanion is endergonic and combining that electron with the polycation is exergonic; it is challenging to envision a mechanism for the exergonicity of that reaction to preferentially partition into the electron donor. Therefore, relative to CAPTR, electron-based, charge-reduction methods result in greater energy deposition into the charge-reduced protein ions. The extent of ion heating from this energy deposition will be mitigated by the large number of degrees of freedom of protein ions and competition with relaxation via radiative emission and collisional cooling.

## 7 Conclusions

Foundational IM-MS studies demonstrated that protein ions with different charge states can exhibit very different Ω values (Figure 1.2). However, the charge states observed for a given protein can depend on many factors (Figure 1.1), not all of which affect their Ω values. Combining charge manipulation and IM-MS has furthered our understanding of the relationship between the charge states and structures of protein ions in the gas phase. Results from CAPTR-IM-MS experiments on a variety of protein ions suggest that charge density plays a crucial role in this relationship. Protein ions with higher charge densities, that is, smaller $m/z$ values, generally experience significant decreases in Ω values following each CAPTR event (Figure 1.8C). For these protein ions, the charge state appears to be a predominant factor affecting their gas-phase structure (Figures 1.5, 1.6, 1.7A-C). On the other hand, protein ions with low charge densities tend to have Ω values that depend weakly on charge state (Figure 1.8D), suggesting that their gas-phase structure is not primarily determined by charge state and corroborating their ability to retain many structural characteristics from solution (Figures 1.6,1.7,1.10). Other factors influencing the magnitude of the decreases in Ω values following CAPTR events include the original solution conditions before ESI and the presence of disulfide bonds (Figure 1.7). Compared to other charge-manipulation strategies, CAPTR-IM-MS experiments offer the advantage of precursor isolation (Figure 1.3) and the ability to analyze a large series of charge-reduced products in parallel (Figure1.4).

Activating CAPTR precursors, that is, pre-CAPTR activation, or CAPTR products, that is, post-CAPTR activation (Figure 1.3C), often results in the formation of new structures that have different Ω values (Figures 1.11 and 1.12). This indicates that CAPTR products are kinetically trapped and can retain a memory of their solution-phase structures. The observed

kinetic trapping and lack of fragmentation, despite the high net exergonicity of each CAPTR event (Figure 1.14), suggests that energy partitions preferentially into the neutralized monoanion. This may limit the structural changes to the portions that interacted with the extracted charge. Compared to other charge-reduction strategies, CAPTR-IM-MS appears to offer more independent control over the extent of charge reduction and energy deposition during experiments. CAPTR also exhibits no signs of selective reaction with certain precursor conformations over others.

CAPTR-IM-MS has proven to be an effective method for unraveling the complex relationship between the charge state and structure of protein ions. With the ability to isolate the contributions of charge from other factors, this technique offers a valuable addition to the current suite of tools for structural biology and biophysics research. Its ability to resolve charge-state ambiguities (Figure 1.4) and enhance the resolution of ions with similar $m/z$ values (Equation 1.5) provides a clear advantage for native mass spectrometry. We suggest that researchers consider incorporating CAPTR into their workflows when exploring the structures of proteins and their complexes.

## 8 Acknowledgements

This work was supported by the National Science Foundation through award 2203513 from the Division of Chemistry, with partial cofunding from the Division of Molecular and Cellular Biosciences. The entire Bush lab and its alumni want to thank and gratefully acknowledge Prof. František Tureček. As a collaborator and colleague, he helped inspire our interest in combining ion-ion chemistry and IM-MS, facilitated the integration of ion-ion chemistry on our first IM-MS system, and most importantly, helped us all do our best science.

## 9 References

(1) Laszlo, K. J.; Bush, M. F. Analysis of Native-Like Proteins and Protein Complexes Using Cation to Anion Proton Transfer Reactions (CAPTR). *J. Am. Soc. Mass Spectrom.* **2015**, *26* (12), 2152–2161. https://doi.org/10.1007/s13361-015-1245-4.

(2) Laszlo, K. J.; Munger, E. B.; Bush, M. F. Folding of Protein Ions in the Gas Phase after Cation-to-Anion Proton-Transfer Reactions. *J. Am. Chem. Soc.* **2016**, *138* (30), 9581–9588. https://doi.org/10.1021/jacs.6b04282.

(3) Allen, S. J.; Schwartz, A. M.; Bush, M. F. Effects of Polarity on the Structures and Charge States of Native-Like Proteins and Protein Complexes in the Gas Phase. *Anal. Chem.* **2013**, *85* (24), 12055–12061. https://doi.org/10.1021/ac403139d.

(4) Putnam, C. Protein Calculator, 2006. https://protcalc.sourceforge.net/.

(5) Hogan, C. J.; Carroll, J. A.; Rohrs, H. W.; Biswas, P.; Gross, M. L. Combined Charged Residue-Field Emission Model of Macromolecular Electrospray Ionization. *Anal. Chem.* **2009**, *81* (1), 369–377. https://doi.org/10.1021/ac8016532.

(6) Kaltashov, I. A.; Mohimen, A. Estimates of Protein Surface Areas in Solution by Electrospray Ionization Mass Spectrometry. *Anal. Chem.* **2005**, *77* (16), 5370–5379. https://doi.org/10.1021/ac050511+.

(7) Iavarone, A. T.; Williams, E. R. Mechanism of Charging and Supercharging Molecules in Electrospray Ionization. *J. Am. Chem. Soc.* **2003**, *125* (8), 2319–2327. https://doi.org/10.1021/ja021202t.

(8) Kebarle, P.; Verkerk, U. H. Electrospray: From Ions in Solution to Ions in the Gas Phase, What We Know Now. *Mass Spectrom. Rev.* **2009**, *28* (6), 898–917. https://doi.org/10.1002/mas.20247.

(9) Konermann, L.; Ahadi, E.; Rodriguez, A. D.; Vahidi, S. Unraveling the Mechanism of Electrospray Ionization. *Anal. Chem.* **2013**, *85* (1), 2–9. https://doi.org/10.1021/ac302789c.

(10) Bohrer, B. C.; Merenbloom, S. I.; Koeniger, S. L.; Hilderbrand, A. E.; Clemmer, D. E. Biomolecule Analysis by Ion Mobility Spectrometry. *Annu. Rev. Anal. Chem.* **2008**, *1* (1), 293–327. https://doi.org/10.1146/annurev.anchem.1.031207.113001.

(11) Gadzuk-Shea, M. M.; Bush, M. F. Effects of Charge State on the Structures of Serum Albumin Ions in the Gas Phase: Insights from Cation-to-Anion Proton-Transfer Reactions, Ion Mobility, and Mass Spectrometry. *J. Phys. Chem. B* **2018**, *122* (43), 9947–9955. https://doi.org/10.1021/acs.jpcb.8b08427.

(12) Kafader, J. O.; Melani, R. D.; Schachner, L. F.; Ives, A. N.; Patrie, S. M.; Kelleher, N. L.; Compton, P. D. Native vs Denatured: An in Depth Investigation of Charge State and Isotope Distributions. *J. Am. Soc. Mass Spectrom.* **2020**, *31* (3), 574–581. https://doi.org/10.1021/jasms.9b00040.

(13) Han, Z.; Chen, L. C. High-Pressure nanoESI of Highly Conductive Volatile and Non-Volatile Buffer Solutions from a Large Taylor Cone: Effect of Spray Current on Charge State Distribution. *Int. J. Mass Spectrom.* **2022**, *476*, 116845. https://doi.org/10.1016/j.ijms.2022.116845.

(14) Benesch, J. L. P.; Ruotolo, B. T.; Sobott, F.; Wildgoose, J.; Gilbert, A.; Bateman, R.; Robinson, C. V. Quadrupole-Time-of-Flight Mass Spectrometer Modified for Higher-Energy Dissociation Reduces Protein Assemblies to Peptide Fragments. *Anal. Chem.* **2009**, *81* (3), 1270–1274. https://doi.org/10.1021/ac801950u.

(15) Bush, M. F.; Hall, Z.; Giles, K.; Hoyes, J.; Robinson, C. V.; Ruotolo, B. T. Collision Cross Sections of Proteins and Their Complexes: A Calibration Framework and Database for Gas-Phase Structural Biology. *Anal. Chem.* **2010**, *82* (22), 9557–9565. https://doi.org/10.1021/ac1022953.

(16) Wang, G.; Cole, R. B. Solution, Gas-Phase, and Instrumental Parameter Influences on Charge-State Distributions in Electrospray Ionization Mass Spectrometry. In *Electrospray ionization mass spectrometry: fundamentals, instrumentation, and applications*; Cole, R. B., Ed.; Wiley: New York, 1997; pp 137–174.

(17) Barth, M.; Schmidt, C. Native Mass Spectrometry—A Valuable Tool in Structural Biology. *J. Mass Spectrom.* **2020**, *55* (10). https://doi.org/10.1002/jms.4578.

(18) Mason, E.; McDaniel, W. *Transport Properties of Ions in Gases*; Wiley, 1988.

(19) Clemmer, D. E.; Hudgins, R. R.; Jarrold, M. F. Naked Protein Conformations: Cytochrome c in the Gas Phase. *J. Am. Chem. Soc.* **1995**, *117* (40), 10141–10142. https://doi.org/10.1021/ja00145a037.

(20) Wyttenbach, T.; Bowers, M. T. Structural Stability from Solution to the Gas Phase: Native Solution Structure of Ubiquitin Survives Analysis in a Solvent-Free Ion Mobility–Mass Spectrometry Environment. *J. Phys. Chem. B* **2011**, *115* (42), 12266–12275. https://doi.org/10.1021/jp206867a.

(21) Bleiholder, C.; Liu, F. C. Structure Relaxation Approximation (SRA) for Elucidation of Protein Structures from Ion Mobility Measurements. *J. Phys. Chem. B* **2019**, *123* (13), 2756–2769. https://doi.org/10.1021/acs.jpcb.8b11818.

(22) Shelimov, K. B.; Jarrold, M. F. Conformations, Unfolding, and Refolding of Apomyoglobin in Vacuum: An Activation Barrier for Gas-Phase Protein Folding. *J. Am. Chem. Soc.* **1997**, *119* (13), 2987–2994. https://doi.org/10.1021/ja962914k.

(23) Valentine, S. J.; Clemmer, D. E. H/D Exchange Levels of Shape-Resolved Cytochrome *c* Conformers in the Gas Phase. *J. Am. Chem. Soc.* **1997**, *119* (15), 3558–3566. https://doi.org/10.1021/ja9626751.

(24) Valentine, S. J.; Counterman, A. E.; Clemmer, D. E. Conformer-Dependent Proton-Transfer Reactions of Ubiquitin Ions. *J. Am. Soc. Mass Spectrom.* **1997**, *8* (9), 954–961. https://doi.org/10.1016/S1044-0305(97)00085-8.

(25) Salbo, R.; Bush, M. F.; Naver, H.; Campuzano, I.; Robinson, C. V.; Pettersson, I.; Jørgensen, T. J. D.; Haselmann, K. F. Traveling-Wave Ion Mobility Mass Spectrometry of Protein Complexes: Accurate Calibrated Collision Cross-Sections of Human Insulin Oligomers: Traveling-Wave IM-MS of Protein Complexes. *Rapid Commun. Mass Spectrom.* **2012**, *26* (10), 1181–1193. https://doi.org/10.1002/rcm.6211.

(26) Canzani, D.; Laszlo, K. J.; Bush, M. F. Ion Mobility of Proteins in Nitrogen Gas: Effects of Charge State, Charge Distribution, and Structure. *J. Phys. Chem. A* **2018**, *122* (25), 5625–5634. https://doi.org/10.1021/acs.jpca.8b04474.

(27) Hogan, C. J.; Ruotolo, B. T.; Robinson, C. V.; Fernandez de la Mora, J. Tandem Differential Mobility Analysis-Mass Spectrometry Reveals Partial Gas-Phase Collapse of the GroEL Complex. *J. Phys. Chem. B* **2011**, *115* (13), 3614–3621. https://doi.org/10.1021/jp109172k.

(28) Laszlo, K. J.; Munger, E. B.; Bush, M. F. Effects of Solution Structure on the Folding of Lysozyme Ions in the Gas Phase. *J. Phys. Chem. B* **2017**, *121* (13), 2759–2766. https://doi.org/10.1021/acs.jpcb.7b00783.

(29) Bornschein, R. E.; Hyung, S.-J.; Ruotolo, B. T. Ion Mobility-Mass Spectrometry Reveals Conformational Changes in Charge Reduced Multiprotein Complexes. *J. Am. Soc. Mass Spectrom.* **2011**, *22* (10), s13361-011-0204-y. https://doi.org/10.1007/s13361-011-0204-y.

(30) Kaldmäe, M.; Österlund, N.; Lianoudaki, D.; Sahin, C.; Bergman, P.; Nyman, T.; Kronqvist, N.; Ilag, L. L.; Allison, T. M.; Marklund, E. G.; Landreh, M. Gas-Phase Collisions with Trimethylamine- *N* -Oxide Enable Activation-Controlled Protein Ion Charge Reduction. *J. Am. Soc. Mass Spectrom.* **2019**, *30* (8), 1385–1388. https://doi.org/10.1007/s13361-019-02177-8.

(31) Lomeli, S. H.; Peng, I. X.; Yin, S.; Ogorzalek Loo, R. R.; Loo, J. A. New Reagents for Increasing ESI Multiple Charging of Proteins and Protein Complexes. *J. Am. Soc. Mass Spectrom.* **2010**, *21* (1), 127–131. https://doi.org/10.1016/j.jasms.2009.09.014.

(32) Lyu, J.; Liu, Y.; McCabe, J. W.; Schrecke, S.; Fang, L.; Russell, D. H.; Laganowsky, A. Discovery of Potent Charge-Reducing Molecules for Native Ion Mobility Mass Spectrometry Studies. *Anal. Chem.* **2020**, *92* (16), 11242–11249. https://doi.org/10.1021/acs.analchem.0c01826.

(33) Pacholarz, K. J.; Barran, P. E. Use of a Charge Reducing Agent to Enable Intact Mass Analysis of Cysteine-Linked Antibody-Drug-Conjugates by Native Mass Spectrometry. *EuPA Open Proteomics* **2016**, *11*, 23–27. https://doi.org/10.1016/j.euprot.2016.02.004.

(34) Sterling, H. J.; Daly, M. P.; Feld, G. K.; Thoren, K. L.; Kintzer, A. F.; Krantz, B. A.; Williams, E. R. Effects of Supercharging Reagents on Noncovalent Complex Structure in

Electrospray Ionization from Aqueous Solutions. *J. Am. Soc. Mass Spectrom.* **2010**, *21* (10), 1762–1774. https://doi.org/10.1016/j.jasms.2010.06.012.

(35) Townsend, J. A.; Keener, J. E.; Miller, Z. M.; Prell, J. S.; Marty, M. T. Imidazole Derivatives Improve Charge Reduction and Stabilization for Native Mass Spectrometry. *Anal. Chem.* **2019**, *91* (22), 14765–14772. https://doi.org/10.1021/acs.analchem.9b04263.

(36) Yang, Y.; Niu, C.; Bobst, C. E.; Kaltashov, I. A. Charge Manipulation Using Solution and Gas-Phase Chemistry to Facilitate Analysis of Highly Heterogeneous Protein Complexes in Native Mass Spectrometry. *Anal. Chem.* **2021**, *93* (7), 3337–3342. https://doi.org/10.1021/acs.analchem.0c05249.

(37) Sterling, H. J.; Prell, J. S.; Cassou, C. A.; Williams, E. R. Protein Conformation and Supercharging with DMSO from Aqueous Solution. *J. Am. Soc. Mass Spectrom.* **2011**, *22* (7), s13361-011-0116–x. https://doi.org/10.1007/s13361-011-0116-x.

(38) Rolland, A. D.; Biberic, L. S.; Prell, J. S. Investigation of Charge-State-Dependent Compaction of Protein Ions with Native Ion Mobility–Mass Spectrometry and Theory. *J. Am. Soc. Mass Spectrom.* **2022**, *33* (2), 369–381. https://doi.org/10.1021/jasms.1c00351.

(39) Ikonomou, M. G.; Kebarle, P. An Ion Source with Which Ions Produced by Electrospray Can Be Subjected to Ion/Molecule Reactions at Intermediate Pressures (10–100 Torr). Deprotonation of Polyprotonated Peptides. *Int. J. Mass Spectrom. Ion Process.* **1992**, *117*, 283–298. https://doi.org/10.1016/0168-1176(92)80099-M.

(40) McLuckey, S. A.; Glish, G. L.; Van Berkel, G. J. Charge Determination of Product Ions Formed from Collision-Induced Dissociation of Multiply Protonated Molecules via Ion/Molecule Reactions. *Anal. Chem.* **1991**, *63* (18), 1971–1978. https://doi.org/10.1021/ac00018a014.

(41) Ogorzalek Loo, R. R.; Smith, R. D. Investigation of the Gas-Phase Structure of Electrosprayed Proteins Using Ion-Molecule Reactions. *J. Am. Soc. Mass Spectrom.* **1994**, *5* (4), 207–220. https://doi.org/10.1016/1044-0305(94)85011-9.

(42) Valentine, S. J.; Anderson, J. G.; Ellington, A. D.; Clemmer, D. E. Disulfide-Intact and -Reduced Lysozyme in the Gas Phase: Conformations and Pathways of Folding and Unfolding. *J. Phys. Chem. B* **1997**, *101* (19), 3891–3900. https://doi.org/10.1021/jp970217o.

(43) McLuckey, S. A.; Stephenson, J. L. Ion/Ion Chemistry of High-Mass Multiply Charged Ions. *Mass Spectrom. Rev.* **1998**, *17* (6), 369–407. https://doi.org/10.1002/(SICI)1098-2787(1998)17:6<369::AID-MAS1>3.0.CO;2-J.

(44) Stephenson, J. L.; McLuckey, S. A. Ion/Ion Reactions in the Gas Phase: Proton Transfer Reactions Involving Multiply-Charged Proteins. *J. Am. Chem. Soc.* **1996**, *118* (31), 7390–7397. https://doi.org/10.1021/ja9611755.

(45) Herron, W. J.; Goeringer, D. E.; McLuckey, S. A. Product Ion Charge State Determination via Ion/Ion Proton Transfer Reactions. *Anal. Chem.* **1996**, *68* (2), 257–262. https://doi.org/10.1021/ac950895b.

(46) Pitteri, S. J.; McLuckey, S. A. Recent Developments in the Ion/Ion Chemistry of High-Mass Multiply Charged Ions. *Mass Spectrom. Rev.* **2005**, *24* (6), 931–958. https://doi.org/10.1002/mas.20048.

(47) Gunawardena, H. P.; He, M.; Chrisman, P. A.; Pitteri, S. J.; Hogan, J. M.; Hodges, B. D. M.; McLuckey, S. A. Electron Transfer versus Proton Transfer in Gas-Phase Ion/Ion Reactions of Polyprotonated Peptides. *J. Am. Chem. Soc.* **2005**, *127* (36), 12627–12639. https://doi.org/10.1021/ja0526057.

(48) Herron, W. J.; Goeringer, D. E.; McLuckey, S. A. Gas-Phase Electron Transfer Reactions from Multiply-Charged Anions to Rare Gas Cations. *J. Am. Chem. Soc.* **1995**, *117* (46), 11555–11562. https://doi.org/10.1021/ja00151a021.

(49) Jhingree, J. R.; Beveridge, R.; Dickinson, E. R.; Williams, J. P.; Brown, J. M.; Bellina, B.; Barran, P. E. Electron Transfer with No Dissociation Ion Mobility–Mass Spectrometry (ETnoD IM-MS). The Effect of Charge Reduction on Protein Conformation. *Int. J. Mass Spectrom.* **2017**, *413*, 43–51. https://doi.org/10.1016/j.ijms.2016.08.006.

(50) Riley, N. M.; Westphall, M. S.; Coon, J. J. Activated Ion-Electron Transfer Dissociation Enables Comprehensive Top-Down Protein Fragmentation. *J. Proteome Res.* **2017**, *16* (7), 2653–2659. https://doi.org/10.1021/acs.jproteome.7b00249.

(51) McLuckey, S. A.; Huang, T.-Y. Ion/Ion Reactions: New Chemistry for Analytical MS. *Anal. Chem.* **2009**, *81* (21), 8669–8676. https://doi.org/10.1021/ac9014935.

(52) He, M.; Emory, J. F.; McLuckey, S. A. Reagent Anions for Charge Inversion of Polypeptide/Protein Cations in the Gas Phase. *Anal. Chem.* **2005**, *77* (10), 3173–3182. https://doi.org/10.1021/ac0482312.

(53) Cheung See Kit, M.; Webb, I. K. Application of Multiple Length Cross-Linkers to the Characterization of Gaseous Protein Structure. *Anal. Chem.* **2022**, *94* (39), 13301–13310. https://doi.org/10.1021/acs.analchem.2c03044.

(54) Zubarev, R. A.; Kelleher, N. L.; McLafferty, F. W. Electron Capture Dissociation of Multiply Charged Protein Cations. A Nonergodic Process. *J. Am. Chem. Soc.* **1998**, *120* (13), 3265–3266. https://doi.org/10.1021/ja973478k.

(55) Syka, J. E. P.; Coon, J. J.; Schroeder, M. J.; Shabanowitz, J.; Hunt, D. F. Peptide and Protein Sequence Analysis by Electron Transfer Dissociation Mass Spectrometry. *Proc. Natl. Acad. Sci.* **2004**, *101* (26), 9528–9533. https://doi.org/10.1073/pnas.0402700101.

(56) Abzalimov, R. R.; Kaltashov, I. A. Electrospray Ionization Mass Spectrometry of Highly Heterogeneous Protein Systems: Protein Ion Charge State Assignment via Incomplete Charge Reduction. *Anal. Chem.* **2010**, *82* (18), 7523–7526. https://doi.org/10.1021/ac101848z.

(57) Geels, R. B. J.; van der Vies, S. M.; Heck, A. J. R.; Heeren, R. M. A. Electron Capture Dissociation as Structural Probe for Noncovalent Gas-Phase Protein Assemblies. *Anal. Chem.* **2006**, *78* (20), 7191–7196. https://doi.org/10.1021/ac060960p.

(58) Pitteri, S. J.; Chrisman, P. A.; Hogan, J. M.; McLuckey, S. A. Electron Transfer Ion/Ion Reactions in a Three-Dimensional Quadrupole Ion Trap: Reactions of Doubly and Triply Protonated Peptides with $SO_2^{\bullet -}$. *Anal. Chem.* **2005**, *77* (6), 1831–1839. https://doi.org/10.1021/ac0483872.

(59) Xia, Y.; Han, H.; McLuckey, S. A. Activation of Intact Electron-Transfer Products of Polypeptides and Proteins in Cation Transmission Mode Ion/Ion Reactions. *Anal. Chem.* **2008**, *80* (4), 1111–1117. https://doi.org/10.1021/ac702188q.

(60) Syrstad, E. A.; Turecček, F. Toward a General Mechanism of Electron Capture Dissociation. *J. Am. Soc. Mass Spectrom.* **2005**, *16* (2), 208–224. https://doi.org/10.1016/j.jasms.2004.11.001.

(61) Turecček, F.; Chen, X.; Hao, C. Where Does the Electron Go? Electron Distribution and Reactivity of Peptide Cation Radicals Formed by Electron Transfer in the Gas Phase. *J. Am. Chem. Soc.* **2008**, *130* (27), 8818–8833. https://doi.org/10.1021/ja8019005.

(62) Tureček, F.; Julian, R. R. Peptide Radicals and Cation Radicals in the Gas Phase. *Chem. Rev.* **2013**, *113* (8), 6691–6733. https://doi.org/10.1021/cr400043s.

(63) Lermyte, F.; Williams, J. P.; Brown, J. M.; Martin, E. M.; Sobott, F. Extensive Charge Reduction and Dissociation of Intact Protein Complexes Following Electron Transfer on a Quadrupole-Ion Mobility-Time-of-Flight MS. *J. Am. Soc. Mass Spectrom.* **2015**, *26* (7), 1068–1076. https://doi.org/10.1007/s13361-015-1124-z.

(64) Liu, J.; McLuckey, S. A. Electron Transfer Dissociation: Effects of Cation Charge State on Product Partitioning in Ion/Ion Electron Transfer to Multiply Protonated Polypeptides. *Int. J. Mass Spectrom.* **2012**, *330–332*, 174–181. https://doi.org/10.1016/j.ijms.2012.07.013.

(65) Stephenson, J. L.; McLuckey, S. A. Adaptation of the Paul Trap for Study of the Reaction of Multiply Charged Cations with Singly Charged Anions. *Int. J. Mass Spectrom. Ion Process.* **1997**, *162* (1–3), 89–106. https://doi.org/10.1016/S0168-1176(96)04510-7.

(66) McLuckey, S. A.; Goeringer, D. E.; Glish, G. L. Selective Ion Isolation/Rejection over a Broad Mass Range in the Quadrupole Ion Trap. *J. Am. Soc. Mass Spectrom.* **1991**, *2* (1), 11–21. https://doi.org/10.1016/1044-0305(91)80056-D.

(67) Kaiser, R. E.; Louris, J. N.; Amy, J. W.; Cooks, R. G.; Hunt, D. F. Extending the Mass Range of the Quadrupole Ion Trap Using Axial Modulation. *Rapid Commun. Mass Spectrom.* **1989**, *3* (7), 225–229. https://doi.org/10.1002/rcm.1290030706.

(68) McLuckey, S. A.; Stephenson, J. L.; Asano, K. G. Ion/Ion Proton-Transfer Kinetics: Implications for Analysis of Ions Derived from Electrospray of Protein Mixtures. *Anal. Chem.* **1998**, *70* (6), 1198–1202. https://doi.org/10.1021/ac9710137.

(69) Campuzano, I. D. G.; Schnier, P. D. Coupling Electrospray Corona Discharge, Charge Reduction and Ion Mobility Mass Spectrometry: From Peptides to Large Macromolecular

Protein Complexes. *Int. J. Ion Mobil. Spectrom.* **2013**, *16* (1), 51–60. https://doi.org/10.1007/s12127-013-0120-x.

(70) Ebeling, D. D.; Westphall, M. S.; Scalf, M.; Smith, L. M. Corona Discharge in Charge Reduction Electrospray Mass Spectrometry. *Anal. Chem.* **2000**, *72* (21), 5158–5161. https://doi.org/10.1021/ac000559h.

(71) Scalf, M.; Westphall, M. S.; Smith, L. M. Charge Reduction Electrospray Mass Spectrometry. *Anal. Chem.* **2000**, *72* (1), 52–60. https://doi.org/10.1021/ac990878c.

(72) Loo, R. R. O.; Udseth, H. R.; Smith, R. D. Evidence of Charge Inversion in the Reaction of Singly Charged Anions with Multiply Charged Macroions. *J. Phys. Chem.* **1991**, *95* (17), 6412–6415. https://doi.org/10.1021/j100170a006.

(73) Ogorzalek Loo, R. R.; Udseth, H. R.; Smith, R. D. A New Approach for the Study of Gas-Phase Ion-Ion Reactions Using Electrospray Ionization. *J. Am. Soc. Mass Spectrom.* **1992**, *3* (7), 695–705. https://doi.org/10.1016/1044-0305(92)87082-A.

(74) Shelimov, K. B.; Clemmer, D. E.; Hudgins, R. R.; Jarrold, M. F. Protein Structure *in Vacuo* : Gas-Phase Conformations of BPTI and Cytochrome *c*. *J. Am. Chem. Soc.* **1997**, *119* (9), 2240–2248. https://doi.org/10.1021/ja9619059.

(75) Zhao, Q.; Soyk, M. W.; Schieffer, G. M.; Fuhrer, K.; Gonin, M. M.; Houk, R. S.; Badman, E. R. An Ion Trap-Ion Mobility-Time of Flight Mass Spectrometer with Three Ion Sources for Ion/Ion Reactions. *J. Am. Soc. Mass Spectrom.* **2009**, *20* (8), 1549–1561. https://doi.org/10.1016/j.jasms.2009.04.014.

(76) Allen, S. J.; Giles, K.; Gilbert, T.; Bush, M. F. Ion Mobility Mass Spectrometry of Peptide, Protein, and Protein Complex Ions Using a Radio-Frequency Confining Drift Cell. *The Analyst* **2016**, *141* (3), 884–891. https://doi.org/10.1039/C5AN02107C.

(77) Williams, J. P.; Brown, J. M.; Campuzano, I.; Sadler, P. J. Identifying Drug Metallation Sites on Peptides Using Electron Transfer Dissociation (ETD), Collision Induced Dissociation (CID) and Ion Mobility-Mass Spectrometry (IM-MS). *Chem. Commun.* **2010**, *46* (30), 5458. https://doi.org/10.1039/c0cc00358a.

(78) Marek, A.; Pepin, R.; Peng, B.; Laszlo, K. J.; Bush, M. F.; Tureček, F. Electron Transfer Dissociation of Photolabeled Peptides. Backbone Cleavages Compete with Diazirine Ring Rearrangements. *J. Am. Soc. Mass Spectrom.* **2013**, *24* (11), 1641–1653. https://doi.org/10.1007/s13361-013-0630-0.

(79) Marek, A.; Shaffer, C. J.; Pepin, R.; Slováková, K.; Laszlo, K. J.; Bush, M. F.; Tureček, F. Electron Transfer Reduction of the Diazirine Ring in Gas-Phase Peptide Ions. On the Peculiar Loss of [NH $_4$ O] from Photoleucine. *J. Am. Soc. Mass Spectrom.* **2015**, *26* (3), 415–431. https://doi.org/10.1007/s13361-014-1047-0.

(80) Pepin, R.; Laszlo, K. J.; Peng, B.; Marek, A.; Bush, M. F.; Tureček, F. Comprehensive Analysis of Gly-Leu-Gly-Gly-Lys Peptide Dication Structures and Cation-Radical Dissociations Following Electron Transfer: From Electron Attachment to Backbone Cleavage, Ion–Molecule Complexes, and Fragment Separation. *J. Phys. Chem. A* **2014**, *118* (1), 308–324. https://doi.org/10.1021/jp411100c.

(81) Pepin, R.; Laszlo, K. J.; Marek, A.; Peng, B.; Bush, M. F.; Lavanant, H.; Afonso, C.; Tureček, F. Toward a Rational Design of Highly Folded Peptide Cation Conformations. 3D Gas-Phase Ion Structures and Ion Mobility Characterization. *J. Am. Soc. Mass Spectrom.* **2016**, *27* (10), 1647–1660. https://doi.org/10.1007/s13361-016-1437-6.

(82) Pepin, R.; Petrone, A.; Laszlo, K. J.; Bush, M. F.; Li, X.; Tureček, F. Does Thermal Breathing Affect Collision Cross Sections of Gas-Phase Peptide Ions? An Ab Initio

Molecular Dynamics Study. *J. Phys. Chem. Lett.* **2016**, *7* (14), 2765–2771. https://doi.org/10.1021/acs.jpclett.6b01187.

(83) Laszlo, K. J.; Buckner, J. H.; Munger, E. B.; Bush, M. F. Native-Like and Denatured Cytochrome *c* Ions Yield Cation-to-Anion Proton Transfer Reaction Products with Similar Collision Cross-Sections. *J. Am. Soc. Mass Spectrom.* **2017**, *28* (7), 1382–1391. https://doi.org/10.1007/s13361-017-1620-4.

(84) McKay, A. R.; Ruotolo, B. T.; Ilag, L. L.; Robinson, C. V. Mass Measurements of Increased Accuracy Resolve Heterogeneous Populations of Intact Ribosomes. *J. Am. Chem. Soc.* **2006**, *128* (35), 11433–11442. https://doi.org/10.1021/ja061468q.

(85) McLuckey, S. A.; Goeringer, D. E. Ion/Molecule Reactions for Improved Effective Mass Resolution in Electrospray Mass Spectrometry. *Anal. Chem.* **1995**, *67* (14), 2493–2497. https://doi.org/10.1021/ac00110a026.

(86) Stephenson, J. L.; McLuckey, S. A. Ion/Ion Proton Transfer Reactions for Protein Mixture Analysis. *Anal. Chem.* **1996**, *68* (22), 4026–4032. https://doi.org/10.1021/ac9605657.

(87) Guilhaus, M. Special Feature: Tutorial. Principles and Instrumentation in Time-of-Flight Mass Spectrometry. Physical and Instrumental Concepts. *J. Mass Spectrom.* **1995**, *30* (11), 1519–1532. https://doi.org/10.1002/jms.1190301102.

(88) Laszlo, K. J.; Bush, M. F. Interpreting the Collision Cross Sections of Native-like Protein Ions: Insights from Cation-to-Anion Proton-Transfer Reactions. *Anal. Chem.* **2017**, *89* (14), 7607–7614. https://doi.org/10.1021/acs.analchem.7b01474.

(89) Sever, A. I. M.; Konermann, L. Gas Phase Protein Folding Triggered by Proton Stripping Generates Inside-Out Structures: A Molecular Dynamics Simulation Study. *J. Phys. Chem. B* **2020**, *124* (18), 3667–3677. https://doi.org/10.1021/acs.jpcb.0c01934.

(90) Bleiholder, C.; Johnson, N. R.; Contreras, S.; Wyttenbach, T.; Bowers, M. T. Molecular Structures and Ion Mobility Cross Sections: Analysis of the Effects of He and $N_2$ Buffer Gas. *Anal. Chem.* **2015**, *87* (14), 7196–7203. https://doi.org/10.1021/acs.analchem.5b01429.

(91) Jurneczko, E.; Barran, P. E. How Useful Is Ion Mobility Mass Spectrometry for Structural Biology? The Relationship between Protein Crystal Structures and Their Collision Cross Sections in the Gas Phase. *The Analyst* **2011**, *136* (1), 20–28. https://doi.org/10.1039/C0AN00373E.

(92) Pierson, N. A.; Valentine, S. J.; Clemmer, D. E. Evidence for a Quasi-Equilibrium Distribution of States for Bradykinin $[M + 3H]^{3+}$ Ions in the Gas Phase. *J. Phys. Chem. B* **2010**, *114* (23), 7777–7783. https://doi.org/10.1021/jp102478k.

(93) Dixit, S. M.; Polasky, D. A.; Ruotolo, B. T. Collision Induced Unfolding of Isolated Proteins in the Gas Phase: Past, Present, and Future. *Curr. Opin. Chem. Biol.* **2018**, *42*, 93–100. https://doi.org/10.1016/j.cbpa.2017.11.010.

(94) Freeke, J.; Bush, M. F.; Robinson, C. V.; Ruotolo, B. T. Gas-Phase Protein Assemblies: Unfolding Landscapes and Preserving Native-like Structures Using Noncovalent Adducts. *Chem. Phys. Lett.* **2012**, *524*, 1–9. https://doi.org/10.1016/j.cplett.2011.11.014.

(95) Rabuck, J. N.; Hyung, S.-J.; Ko, K. S.; Fox, C. C.; Soellner, M. B.; Ruotolo, B. T. Activation State-Selective Kinase Inhibitor Assay Based on Ion Mobility-Mass Spectrometry. *Anal. Chem.* **2013**, *85* (15), 6995–7002. https://doi.org/10.1021/ac4012655.

(96) Tian, Y.; Han, L.; Buckner, A. C.; Ruotolo, B. T. Collision Induced Unfolding of Intact Antibodies: Rapid Characterization of Disulfide Bonding Patterns, Glycosylation, and

Structures. *Anal. Chem.* **2015**, *87* (22), 11509–11515. https://doi.org/10.1021/acs.analchem.5b03291.

(97) Vidarsson, G.; Dekkers, G.; Rispens, T. IgG Subclasses and Allotypes: From Structure to Effector Functions. *Front. Immunol.* **2014**, *5*. https://doi.org/10.3389/fimmu.2014.00520.

(98) Giles, K.; Williams, J. P.; Campuzano, I. Enhancements in Travelling Wave Ion Mobility Resolution: Enhancements in Travelling Wave Ion Mobility Resolution. *Rapid Commun. Mass Spectrom.* **2011**, *25* (11), 1559–1566. https://doi.org/10.1002/rcm.5013.

(99) Gabelica, V.; Shvartsburg, A. A.; Afonso, C.; Barran, P.; Benesch, J. L. P.; Bleiholder, C.; Bowers, M. T.; Bilbao, A.; Bush, M. F.; Campbell, J. L.; Campuzano, I. D. G.; Causon, T.; Clowers, B. H.; Creaser, C. S.; De Pauw, E.; Far, J.; Fernandez-Lima, F.; Fjeldsted, J. C.; Giles, K.; Groessl, M.; Hogan, C. J.; Hann, S.; Kim, H. I.; Kurulugama, R. T.; May, J. C.; McLean, J. A.; Pagel, K.; Richardson, K.; Ridgeway, M. E.; Rosu, F.; Sobott, F.; Thalassinos, K.; Valentine, S. J.; Wyttenbach, T. Recommendations for Reporting Ion Mobility Mass Spectrometry Measurements. *Mass Spectrom. Rev.* **2019**, *38* (3), 291–320. https://doi.org/10.1002/mas.21585.

(100) Allen, S. J.; Bush, M. F. Radio-Frequency (Rf) Confinement in Ion Mobility Spectrometry: Apparent Mobilities and Effective Temperatures. *J. Am. Soc. Mass Spectrom.* **2016**, *27* (12), 2054–2063. https://doi.org/10.1007/s13361-016-1479-9.

(101) Bush, M. F.; Campuzano, I. D. G.; Robinson, C. V. Ion Mobility Mass Spectrometry of Peptide Ions: Effects of Drift Gas and Calibration Strategies. *Anal. Chem.* **2012**, *84* (16), 7124–7130. https://doi.org/10.1021/ac3014498.

(102) Zhong, Y.; Hyung, S.-J.; Ruotolo, B. T. Characterizing the Resolution and Accuracy of a Second-Generation Traveling-Wave Ion Mobility Separator for Biomolecular Ions. *The Analyst* **2011**, *136* (17), 3534. https://doi.org/10.1039/c0an00987c.

(103) Lermyte, F.; Łącki, M. K.; Valkenborg, D.; Gambin, A.; Sobott, F. Conformational Space and Stability of ETD Charge Reduction Products of Ubiquitin. *J. Am. Soc. Mass Spectrom.* **2017**, *28* (1), 69–76. https://doi.org/10.1007/s13361-016-1444-7.

(104) Schnier, P. D.; Gross, D. S.; Williams, E. R. Electrostatic Forces and Dielectric Polarizability of Multiply Protonated Gas-Phase Cytochrome c Ions Probed by Ion/Molecule Chemistry. *J. Am. Chem. Soc.* **1995**, *117* (25), 6747–6757. https://doi.org/10.1021/ja00130a015.

(105) Sterner, J. L.; Johnston, M. V.; Nicol, G. R.; Ridge, D. P. Apparent Proton Affinities of Highly Charged Peptide Ions. *J. Am. Soc. Mass Spectrom.* **1999**, *10* (6), 483–491. https://doi.org/10.1016/S1044-0305(99)00020-3.

(106) Bouchoux, G. Gas Phase Basicities of Polyfunctional Molecules. Part 3: Amino Acids. *Mass Spectrom. Rev.* **2012**, *31* (3), 391–435. https://doi.org/10.1002/mas.20349.

(107) Stephenson, J. L.; Van Berkel, G. J.; McLuckey, S. A. Ion-Ion Proton Transfer Reactions of Bio-Ions Involving Noncovalent Interactions: Holomyoglobin. *J. Am. Soc. Mass Spectrom.* **1997**, *8* (6), 637–644. https://doi.org/10.1016/S1044-0305(97)00023-8.

(108) Bueker, H.-H.; Helgaker, T.; Ruud, K.; Uggerud, E. Energetics and Dynamics of Intermolecular Proton-Transfer Processes. 2. Ab Initio Direct Dynamics Calculations of the Reaction $H_3O^+ + NH_3 \rightarrow NH_4^+ + H_2O$. *J. Phys. Chem.* **1996**, *100* (38), 15388–15392. https://doi.org/10.1021/jp960943b.

(109) Bueker, H.-H.; Helgaker, T.; Ruud, K.; Uggerud, E. Energetics and Dynamics of Intermolecular Proton-Transfer Processes. 2. Ab Initio Direct Dynamics Calculations of the Reaction $H_3O^+ + NH_3 \rightarrow NH_4^+ + H_2O$. *J. Phys. Chem.* **1996**, *100* (38), 15388–15392. https://doi.org/10.1021/jp960943b.

(110) Breuker, K.; Oh, H.; Lin, C.; Carpenter, B. K.; McLafferty, F. W. Nonergodic and Conformational Control of the Electron Capture Dissociation of Protein Cations. *Proc. Natl. Acad. Sci.* **2004**, *101* (39), 14011–14016. https://doi.org/10.1073/pnas.0406095101.

(111) Leib, R. D.; Donald, W. A.; Bush, M. F.; O'Brien, J. T.; Williams, E. R. Nonergodicity in Electron Capture Dissociation Investigated Using Hydrated Ion Nanocalorimetry. *J. Am. Soc. Mass Spectrom.* **2007**, *18* (7), 1217–1231. https://doi.org/10.1016/j.jasms.2007.03.033.

# Chapter 2. Differentiating Antibodies Using Charge-State Manipulation, Collisional Activation, and Ion Mobility – Mass Spectrometry

This chapter has been submitted to Analytical Chemistry and ChemRxiv. Gozzo, T.A., Bush, M.F. "Differentiating Antibodies Using Charge-State Manipulation, Collisional Activation, and Ion Mobility – Mass Spectrometry." *Manuscript Submitted* **2023**.

## 1 Abstract

Antibody-based therapeutics continue to expand both in the number of products and their use in patients. These heterogeneous proteins challenge traditional drug characterization strategies, but ion mobility (IM) – mass spectrometry (MS) approaches have eased the challenge of higher-order structural characterization. Energy-dependent IM-MS, e.g., collision-induced unfolding (CIU), has been demonstrated to be sensitive to subtle differences in structure. In the present study, we combine a charge-reduction method, cation-to-anion proton-transfer reactions (CAPTR), with energy-dependent IM-MS and varied solution conditions to probe their combined effects on the gas-phase structures of IgG1κ and IgG4κ from human myeloma. CAPTR paired with MS-only analysis improves the confidence of charge-state assignments and the resolution of interfering protein species. Collision cross-section distributions were determined for each of the charge-reduced products. Similarity scoring was used to quantitively compare distributions determined from matched experiments analyzing samples of the two antibodies. Relative to workflows using energy-dependent IM-MS without charge-state manipulation, combining CAPTR and energy-dependent IM-MS enhanced the differentiation of these antibodies. Combined, these results indicate that CAPTR can benefit many aspects of antibody characterization and differentiation.

## 2 Introduction

Monoclonal antibodies (mAbs) constituted 4 out of 10 of the top drugs by sales in 2021[1] and the list of approved mAbs therapeutics continues to expand.[2] All currently approved mAb therapeutics are based on Immunoglobulin Gammas (IgGs).[3,4] Relative to small-molecule therapeutics, mAbs have resisted general strategies for characterization and quality control. They are large, flexible molecules rich with post-translational modifications, making them heterogeneous.[5,6] These properties challenge high-resolution structural techniques and only a few atomic-resolution structures for full-length, intact antibodies have been reported.[7–10] These challenges have motivated the use of complementary techniques.[11,12] Ion mobility (IM) mass spectrometry (MS) is fast, sensitive, and tolerant of heterogeneity and dynamics. In IM, ions are separated by size, shape, and charge by collisions with background gas molecules in the presence of an electric field; their mobilities can be used to determine what is commonly referred to as a collision cross-section (Ω). This can be used in conjunction with native MS, which provides information about the mass and noncovalent interactions of analytes. Protein ions generated by electrospray ionization (ESI) from native-like solution conditions can have similar Ω values to those predicted based on condensed-phase structures, consistent with the retention of aspects of native structure in the gas phase.[13,14] Complementary methods have corroborated these conclusions, e.g., GroEL ions were soft-landed following MS, and the resulting electron microscopy images were consistent with the retention of solution-phase structures.[15,16]

IM-MS has been used to characterize multispecific antibodies,[17,18] differentiate disulfide variants,[19,20] glycosylation variants,[21] and IgG subclasses,[19] measure the drug-to-antibody ratios of antibody-drug conjugates,[22,23] and more. The subjects of the present study, IgG1 and IgG4, share more than 90% sequence identity, and they differ not in terms of number, but in

connectivity of their disulfide bonds.[4] The apparent Ω distributions for IgG1 and IgG4 have been reported to be similar to each other,[24,25] but centered at Ω values that are more than 30% smaller than those calculated for the few existing crystal structures of IgGs.[24–27] Furthermore, the apparent Ω distributions are wider than those for other protein complexes of similar masses.[24,25] The small magnitude and large widths of the apparent Ω distributions have been attributed to the flexibility of IgGs in solution, specifically that of the hinge region,[24] and the structural collapse upon entry into the gas phase.[24–27] Collision-induced unfolding (CIU) has been demonstrated to be sensitive to subtle differences in gas-phase IgG structures. In CIU, ions are subjected to increasing collisional activation, their arrival times are monitored via IM, and the resulting unfolding patterns can be used to distinguish ion populations. Although IgG1 and IgG4 are difficult to differentiate based on IM-MS measurements alone, they do show distinct unfolding patterns with CIU.[19,28]

The charge states of gas-phase protein ions depend on the size and structure of the protein, the properties of the solvent and other solutes, the ionization mechanism, and other factors.[29–33] Charge-state manipulation of protein ions can help probe the effects of charge on the properties of those ions.[34] Several charge-reduction methods have been implemented with MS,[35–38] and with IM, it is also possible to probe structural changes in relation to charge state. Building upon the pioneering contributions of McLuckey and coworkers,[39] we introduced Cation-to-Anion Proton-Transfer Reactions (CAPTR) to generate a series of charge-reduced protein ions that can be analyzed in parallel.[37] For example, we used CAPTR to investigate the effects of charge state, solution conditions, and internal disulfide bonding on Ω for a large, multidomain protein, bovine serum albumin (BSA).[31] BSA ions were generated from five different solution conditions that perturbed the native-like structure to varying extents.[31] Ions generated from

denaturing conditions exhibited Ω values that depended strongly on *z*, whereas ions from native-like conditions depended weakly on *z*. The CAPTR products of single domain proteins from denaturing conditions and native-like ions of the same charge states can exhibit similar Ω values,[40,41] but the lowest-*z* CAPTR products of BSA from denaturing conditions exhibited Ω values that were significantly larger those for the corresponding native-like ions.[31] CAPTR results for BSA[31] and lysozyme[41] from denaturing, disulfide-reducing conditions indicate that those ions compact more per CAPTR event than the corresponding ions from disulfide-intact conditions. These results suggest that disulfide bonds limit expansion to larger Ω at high *z*, but also limit compaction at low *z*. Collisional activation in combination with CAPTR, i.e., pre- or post-CAPTR activation, has aided in differentiating ions with similar apparent Ω distributions. For example, Ω distributions of 8+ ubiquitin appeared to be independent of applied activation voltage, but Ω distributions of 6+ ions generated by CAPTR of the activated 8+ precursors depended on the extent of activation; these differences provided indirect evidence for unresolved, energy-dependent structural changes in the precursor.[42] Additional results from CAPTR-based experiments and comparisons with results from other charge-reduction methods have been reviewed recently.[34] Overall, these results support the ideas that solution conditions and disulfide bonding impact gas-phase protein ion structure and suggest that charge should be considered when using IM-MS to study biomolecular structure.

Based on CIU of IgGs,[19,28] CAPTR of BSA,[31] and pre-CAPTR activation of ubiquitin,[42] we hypothesized that combining charge-state manipulation and energy-dependent IM may enable better differentiation of antibodies than either technique alone. Here, we tested that hypothesis using a combination of experiments and quantitative comparisons of results for IgG1 and IgG4 using similarity scoring[43] implemented with the Jensen-Shannon distance metric.[44–46]

## 2 Methods

**2.1 Samples**. Samples of IgG1$\kappa$ and IgG4$\kappa$ (product/lot numbers: I5154/SLCB8124 and I4639/SLBR4231V, respectively) from human myeloma were purchased from Sigma-Aldrich (St. Louis, MO). For native-like conditions, 20 μL samples with a concentration of 1 mg $mL^{-1}$ (~7 μM) antibody were exchanged into aqueous 200 mM ammonium acetate at pH 7.0 using Micro Bio-Spin 6 columns (Bio-Rad, Hercules, CA). For denaturing conditions, the same procedure was used, but the samples were instead exchanged into aqueous 0.1% acetic acid.

**2.2 Experiments**. All experiments were conducted on a Waters Synapt G2 HDMS modified with a glow-discharge ionization source[47] and a radio-frequency confining drift cell (Figure 2.1a).[48] Cations were generated using electrokinetic electrospray ionization, as described previously.[49] The sample capillary was inserted into a copper block that was maintained at 25 °C using a Peltier device. The atmospheric-pressure interface was maintained at 120 °C for the duration of CAPTR experiments to reduce fouling of the source and ion optics; the temperature of the sample capillary and atmospheric-pressure interface are independent in these experiments.[40] To perform CAPTR, perfluoro-1,3-dimethylcyclohexane (PDCH, Sigma-Aldrich, St. Louis, MO) was introduced as a vapor in nitrogen gas. After glow-discharge ionization, the fragments, the monoanion $[PDCH–F]^-$ at $m/z$ 381, were quadrupole selected and accumulated in the trap for 100 ms. The instrument polarity was then switched to positive mode to allow selected cations of IgG1 or IgG4 to be transmitted through the trap cell of accumulated anions for 1 to 5 s.[37] Product ions and residual precursor ions were then pulsed into the mobility cell for 200 μs every 36.4 ms. The sampling cone voltage was varied between 25 and 125 V to probe the effects of pre-CAPTR activation, and the trap bias was varied between 5 and 100 V to probe the

effects of post-CAPTR activation (Figure 2.1b). For collision-induced unfolding (CIU) experiments without CAPTR, cations of a single charge state were selected, and the trap collision voltage was ramped from 5 to 200 V (Figure 2.1b).

IM arrival-time distributions were measured using an RF-confining drift cell[48] filled with approximately 1.5 Torr helium for most experiments. For post-CAPTR activation experiments, 0.9 Torr nitrogen drift gas was used instead. Field-dependent measurements at eight to ten drift voltages between 104 and 354 V were used to determine the *m*/*z*-dependent and *m*/*z*-independent transport times from the end of the mobility cell to the time-of-flight (TOF) analyzer. The arrival-time distributions collected for CAPTR product ions from measurements at a single field strength (7.3 $V \cdot cm^{-1}$) were corrected with transport times, translated into mobility (*K*) distributions, and finally transformed into apparent Ω distributions using the Mason-Schamp equation.[50] Additional details are described in the Supporting Information.

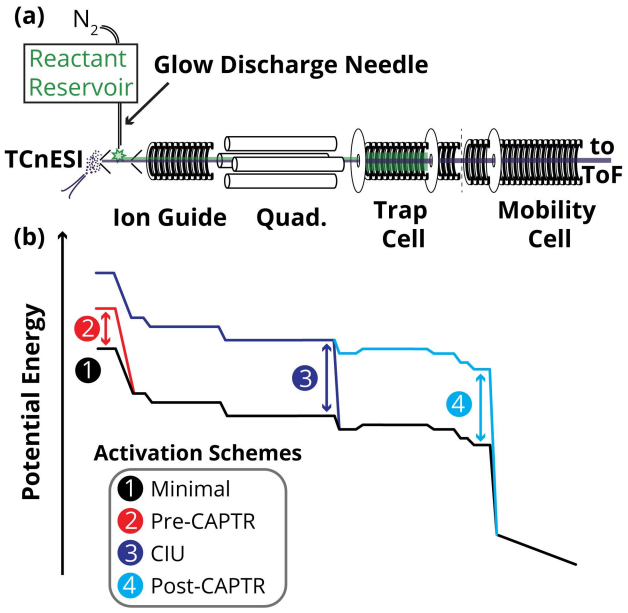


**Figure 2.1**. (a) Diagram of the modified Waters Synapt G2 HDMS with radio-frequency confining drift cell. Anions (green) are generated by glow-discharge ionization and accumulated in the trap cell. Cations (purple) are generated by

nanoelectrospray ionization and transmitted through the anion population in the trap cell for CAPTR. Residual precursor and CAPTR product ions are separated by IM prior to mass analysis. (b) Representative potential-energy diagrams for cation transmission during minimal activation, pre-CAPTR activation, collision-induced unfolding (CIU), and post-CAPTR activation experiments. Figure adapted with permission from *J. Am. Chem. Soc*. **2016**, *138*, 9581−9588.[42] Copyright 2016 American Chemical Society.

## 3 Results and Discussion

The goal of this study was to probe the relationship between solution conditions, charge state, and Ω for highly flexible macromolecules and to determine whether their responses to activation could be used to rapidly differentiate similar proteins. To achieve this goal, we characterized the gas-phase structures of IgG1κ and IgG4 κ from human myeloma, which will be referred to as IgG1 and IgG4, using CAPTR and IM-MS as a function of solution conditions and energy. Ions originating from electrospray of two different solution conditions will be analyzed by MS and IM-MS experiments. Selected ions will be subjected to CAPTR to probe the relationship between charge and Ω. And finally, results from collisional activation in combination with CAPTR will be used to compare IgG1 and IgG4 ion stabilities and structures.

### 3.1 Differentiation of IgGs by Charge State Assignment and Mass Determination.

Figures 2.2a-d show the mass spectra of IgG1 and IgG4 from native-like conditions of samples held at 25 °C; similar mass spectra were also obtained without temperature control of the sample (Figure A1). Ions generated from native-like conditions will be denoted with a

superscript "N", e.g., $^{N}$IgG1. Like other large proteins, the mass spectra of $^{N}$IgG1 and $^{N}$IgG4 display a narrow charge-state distribution with high *m/z* values. The degree of similarity between these spectra should also be noted; it is challenging to distinguish IgG1 and IgG4 from these results alone. Simulated mass spectra are overlayed on top of the experimental native mass spectra based on the charge-state assignment of the peaks at 6195 *m/z* ($^{N}$IgG1) and 6227 *m/z* ($^{N}$IgG4) as either 24+ or 25+; the simulated native mass spectra agree reasonably well with the experimental native mass spectra for both sets of charge-state assignments.

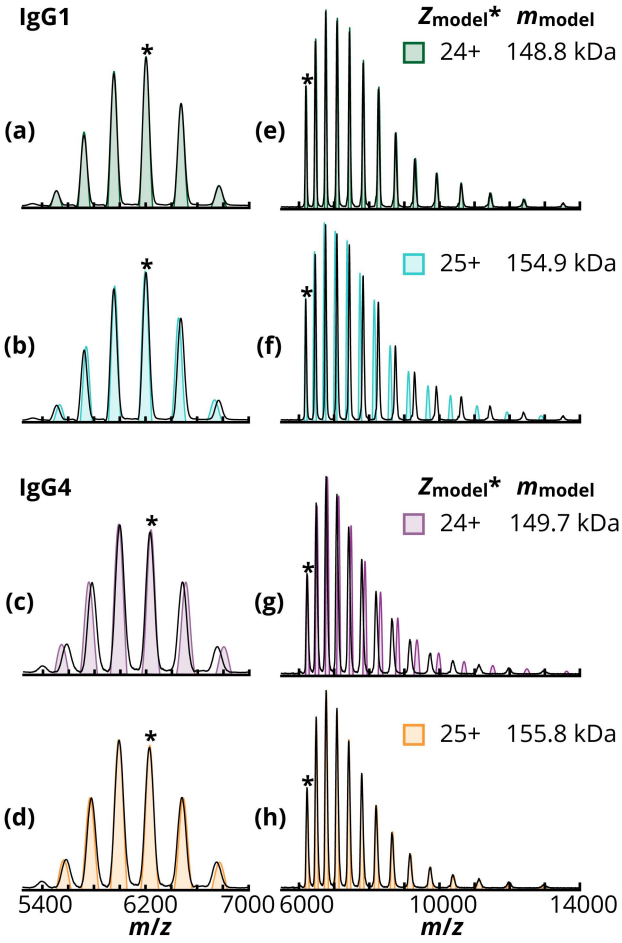


**Figure 2.2**. (a-d) The IgG1 (a, b) and IgG4 (c, d) experimental mass spectra of ions from native-like conditions (black) are overlayed with simulated mass spectra based on the charge assignment of the peaks centered near 6195 *m/z*

(IgG1) and 6227 *m*/*z* (IgG4). Assignment of the indicated IgG1 peak as 24+ (a, green) or 25+ (b, blue) results in mass determinations of 148.8 and 154.9 kDa, respectively. Assignment of the indicated IgG4 peak as 24+ (c, purple) or 25+ (d, orange) results in mass determinations of 148.7 and 155.7 kDa, respectively. (e)-(h) show the experimental mass spectra (black) of the CAPTR products generated after quadrupole of the indicated ions; corresponding CAPTR mass spectra were simulated using the masses determined from the models of the native mass spectra.

The ions near 6200 *m*/*z* were also quadrupole-isolated and subjected to CAPTR; the experimental CAPTR spectra are shown in Figure 2.2e-h. CAPTR mass spectra were also simulated based on the masses determined from the 24+ and 25+ models of the native mass spectra. The experimental and simulated CAPTR spectra agree only when the peaks near 6200 *m*/*z* are assigned to 24+ for $^{N}$IgG1 and 25+ for $^{N}$IgG4. Some mass spectra of $^{N}$IgG1 and $^{N}$IgG4 from the same source have been assigned so that peaks with similar *m*/*z* for both proteins have the same charge state.[19,24] For the IgG samples used in this investigation, the additional peaks generated by CAPTR reveal that these two analytes have different charge-state distributions and different masses. Figures A2 and A3 show the standard deviations associated with propagating mass through various charge-state assignments of the precursor and charge-reduced ion peaks. The analysis resulted in average masses of 148,714 ± 58 Da and 155,826 ± 61 Da (95% confidence interval) for IgG1 and IgG4, respectively, under these minimally activating conditions. This analysis suggests that some previously reported charge-state assignments for $^{N}$IgG4*κ* may be incorrect. Different post-translational modifications on IgG1 and IgG4 may

contribute to the observed mass difference between these two samples. IgG glycosylation can represent 2% to 3% of the total antibody molecular weight.[3,51] With minimal applied activation, incomplete desolvation could contribute to the overall masses as well, but this likely affected both analytes similarly. With increased collisional activation in the source (up to 125 V sampling cone voltage), the mass difference decreased to 6.7 kDa from 7.1 kDa. Regardless, this analysis highlights the potential ambiguity in interpreting native mass spectra of high mass ions and showcases the application of CAPTR to increase the confidence in native MS charge-state and mass assignments.[37] In this case, despite exhibiting similar native mass spectra, CAPTR also enabled the rapid differentiation of $^{N}$IgG1 and $^{N}$IgG4 ions by mass alone.

IgG1 and IgG4 ions generated from aqueous 0.1% acetic acid display a much wider charge-state distribution and higher charge states overall than those from native-like conditions. Ions generated from these denaturing conditions will be denoted with a superscript "D", e.g., $^{D}$IgG1. Figures A5 and A6 show mass spectra of $^{D}$IgG1 and $^{D}$IgG4 from ESI. The highest resolved charge states observed for $^{D}$IgG1 and $^{D}$IgG4 were 50+ and 58+, respectively. The lowest charge state observed for both $^{D}$IgG1 and $^{D}$IgG4 was 27+. Bimodal charge-state distributions were observed for each sample: one at lower *m*/*z* and one at higher *m*/*z*. The presence of higher *m*/*z* distributions, like those observed for $^{N}$IgG1 and $^{N}$IgG4, suggest that these conditions were only partially denaturing, but will be referred to as denaturing for simplicity.

The $^{D}$IgG1 and $^{D}$IgG4 ions were also subjected to CAPTR prior to mass analysis. Ions are identified by "$^{\text{Condition}}P \rightarrow C$" where "*P*" is the charge state of the precursor ion, "*C*" is the charge state of the CAPTR product, and "Condition" is the solution conditions ("N" or "D"). When CAPTR was performed on either all ions (no precursor selection), $P = 47$ or 49 for $^{D}$IgG1, or $P = 49$ for $^{D}$IgG4, a single series of products were generated (Figures A5 to A10). The masses of

these products are consistent with the analysis of native-like ions discussed above. Interestingly, when CAPTR was performed on $P = 47$ for $^{D}$IgG4, two series of product ions were generated that have masses 155.6 kDa and 158.9 kDa (Figure A5). These species were unresolved in the spectra of both the full population of ESI-generated ions and the CAPTR products of that full population (Figure A8). The 155.6 kDa species is predominant in this spectrum, consistent with the other spectra of this sample (Figures A5 to A10) and that form being predominant in solution. No evidence for a 3.3 kDa fragment ion was observed, consistent the presence of the 155.6 kDa species in solution and the absence of fragmentation in CAPTR experiments.[34] These two species represent different antibody proteoforms in the original sample, and may differ in both sequence, glycosylation, and other properties. Resolving interfering populations is another benefit of CAPTR that could aid in the analysis of challenging biopharmaceutical samples.

### 3.2 Collision Cross-Section (Ω) Values and Solution Conditions

Ω with helium ($^{DT}\Omega_{He}$) were determined from field-dependent measurements of drift time as a function of reciprocal drift voltage. Arrival-time distributions were found to be unimodal for electrospray-generated $^{N}$IgG ions. The centroid of each distribution was estimated from that of the best-fit normal distribution, as described previously.[52] Figure A4 shows CCS values calculated based on different charge-state assignments. When the charge states are assigned based on the CAPTR mass spectra, the $^{DT}\Omega_{He}$ values of the $^{N}$IgG1 and $^{N}$IgG4 ions differ by less than 2%. The 24+ and 23+ populations are most similar in size with a <0.6% difference. With such small differences in Ω, IgG1 and IgG4 cannot be differentiated by Ω alone. Within samples, the Ω values ranged from 67.6 to 69.6 nm$^2$ (3% difference) for 22+ to 27+ IgG1 and 67.9 to 72.1 nm$^2$ (6% difference) for 23+ to 28+ IgG4. For comparison, 24+ to 27+ alcohol dehydrogenase

(mass of 147 kDa) exhibited $^{DT}\Omega_{He}$ that differed by up to 3.5%.[53] If IgG1 and IgG4 are assumed to have more similar masses, *i.e.*, peaks at similar *m*/*z* in both spectra are both incorrectly assigned the same charge state (Figure 2.2), the apparent maximum difference in Ω grows to 3.9% for the 22+ or 23+ populations, depending on the misassignment (Figure A4). These results illustrate how charge-state assignment can impact the interpretation of ion mobility results.

The $^{DT}\Omega_{He}$ values for ions from denaturing conditions ranged from 69.2 to 112.2 nm$^2$ (47% difference) for $^{D}$IgG1 and 72.6 to 132.0 nm$^2$ (58% difference) for $^{D}$IgG4. For comparison to $^{D}$IgG1, 50+ ions of $^{D}$IgG4 had a Ω value of 114.0 nm$^2$. Ions of charge states also observed under native-like conditions exhibited similar centroid Ω values to their native-like counterparts (Figure A10). Relative to $^{N}$IgG1 and $^{N}$IgG4 ions, Ω values depended more strongly on charge state, which is consistent with results for other protein ions generated from denaturing conditions.[31,40,41] For most charge states, larger differences in Ω values were observed between $^{D}$IgG1 and $^{D}$IgG4 ions than for $^{N}$IgG1 and $^{N}$IgG4. The largest difference was observed for the 31+ charge state (7.8%).

### 3.3 Relationship Between Charge and Ω

Three $^{N}$IgG1 and $^{N}$IgG4 precursors, 26+, 25+, and 24+, and two $^{D}$IgG1 and $^{D}$IgG4 precursors, 49+ and 47+, were selected for analysis based on their intensities and subjected to CAPTR. The CAPTR products originating from each of the precursors were characterized by IM-MS. Arrival-time distributions were converted to median collision-cross sections ($^{DT}\tilde{\Omega}_{He}$) with helium as described in the Supporting Information. For the $^{N}P{\rightarrow}C$ ions, the $\tilde{\Omega}$ values depended weakly on both *P* and *C* (Figure 2.3). Although there were small, systematic differences between the $\tilde{\Omega}$ values of IgG1 and IgG4, but those differences were comparable in

magnitude to those for the precursor ions that were not subjected to CAPTR. The Supporting Information includes a more detailed discussion of these values. Compared to other native-like proteins of similar mass, $^{N}$IgG1 and $^{N}$IgG4 undergo slightly less compaction with charge reduction, which may be the result of the compaction these molecules have undergone upon entrance into the gas phase, consistent with previous work.[23–26] The small magnitude of these differences in Ω are consistent with those for the CAPTR products of other large, native-like protein ions,[31,53] as shown for $^{N}$BSA in Figure 2.3. Overall, the results of these experiments suggest that the excess positive charges on these native-like antibody ions have a small effect on their structures as monitored by CAPTR and IM, which is consistent with our observations for large, well-folded proteins.[31,53]

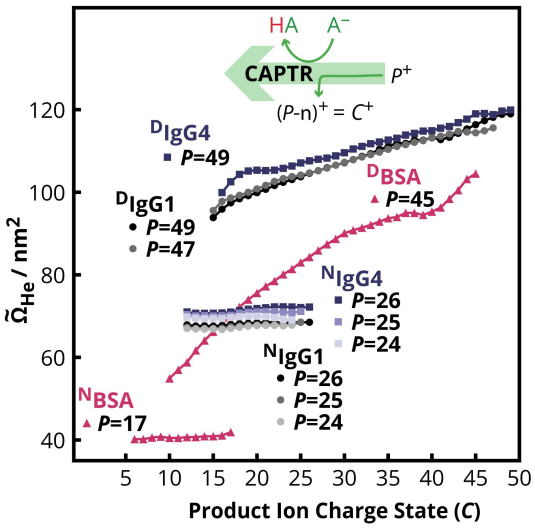


**Figure 2.3.** $^{DT}\tilde{\Omega}_{He}$ values of IgG1, IgG4, and BSA ions produced from electrospray from native-like and denaturing solution conditions and subjected to CAPTR. Denaturing conditions used for BSA experiments were comprised of 70:30 water/methanol with 0.2% formic acid; native-like conditions were the same as those used for IgGs. Precursors 26+, 25+, and 24+ were selected for CAPTR of $^{N}$IgGs, and precursors 47+ and 49+ were selected for CAPTR of

$^{D}$IgGs. Note that CAPTR of $^{D}$IgG4 47+ ions revealed the presence of two species within the sample (Figure A4); these IM results are not shown. The 45+ and 17+ precursors were selected for CAPTR of $^{D}$BSA and $^{N}$BSA, respectively.

For the $^{D}P\rightarrow C$ ions, the $\widetilde{\Omega}$ values depended weakly on $P$ and strongly on $C$ (Figure 2.3). For a given $P$ and $C$, the Ω values for the IgG4 ion was between 0.5 and 5.9% larger than the corresponding IgG1 ion. The Supporting Information includes a more detailed discussion of these values. Although the Ω decreased significantly after each CAPTR event, the Ω value for each $^{D}P\rightarrow C$ ions was considerably larger that for all $^{N}P\rightarrow C$ ions. For each $C$, the Ω values for the CAPTR products of $^{D}$IgG1 and $^{D}$IgG4 were larger than those for $^{D}$BSA. However, relative to $^{D}$BSA ions, the $^{D}$IgG ions compacted less per CAPTR event. Linear regression of the results in Figure 2.3 suggests that $^{D}$BSA ions exhibited a maximum change of 1.97 $nm^2 \cdot z^{-1}$, whereas $^{D}$IgG ions exhibited a maximum of 0.92 and 0.88 $nm^2 \cdot z^{-1}$ for $^{D}$IgG1 and $^{D}$IgG4, respectively. This finding may be a consequence of the denaturing conditions. The condition used for the IgGs were less disruptive than that used for $^{D}$BSA; the Ω and charge states and Ω observed for the $^{D}$IgGs may have been limited by decreased extents of structural disruption in solution and charging during ionization.

**3.4 Pre-CAPTR Activation of Ions from Native-Like Conditions.**

To investigate the relationship between the structures of the precursors and their CAPTR products, $^{N}$IgG ions were analyzed as a function of sampling cone voltage (Figure 2.1b). Increasing this voltage increases the extent of collisional activation in the atmospheric-pressure interface, which occurs prior to quadrupole selection and CAPTR. Note that collision activation

can also result in the loss of charge,[54] which may also contribute to these results. An asterisk is used to indicate the activated species, i.e., "$^{N}P^{*}\rightarrow C$." The 26+ and 25+ precursor ions of IgG1 and IgG4 were selected for these experiments and were probed at sampling cone voltages of 25, 50, 75, 100, and 125 V.

Generally, with increasing sampling cone voltage, the apparent $^{DT}\Omega_{He}$ distributions for all observed $^{N}P^{*}\rightarrow C$ ions tended to shift to larger values, increase in width, and exhibit more multimodal character. Figure 2.4 illustrates these trends for the $^{N}25^{*}\rightarrow C$ ions of IgG1 and IgG4. With decreasing $C$, the apparent Ω distributions tended to shift to smaller values, decrease in width, and exhibit more unimodal character. These trends are generally consistent with results from pre-CAPTR activation of other native-like ions of proteins.[53] For a given $C$ and sampling cone voltage, the apparent Ω distributions for IgG1 and IgG4 exhibited varying extents of overlap. The extent of that overlap was greatest for the two highest sampling cone voltages. For example, with a sampling cone voltage of 100 V, the distributions for IgG1 and IgG4 exhibited significant overlap and the extent of overlap depended weakly on $C$. By comparison, with a sampling cone voltage of 75 V, there were greater differences between the distributions for IgG1 and IgG4, and those differences increased with the number of CAPTR events. These results all indicate that the apparent Ω distributions of these antibody ions can depend on the pre-CAPTR activation voltage, $C$, and the identity of the antibody.

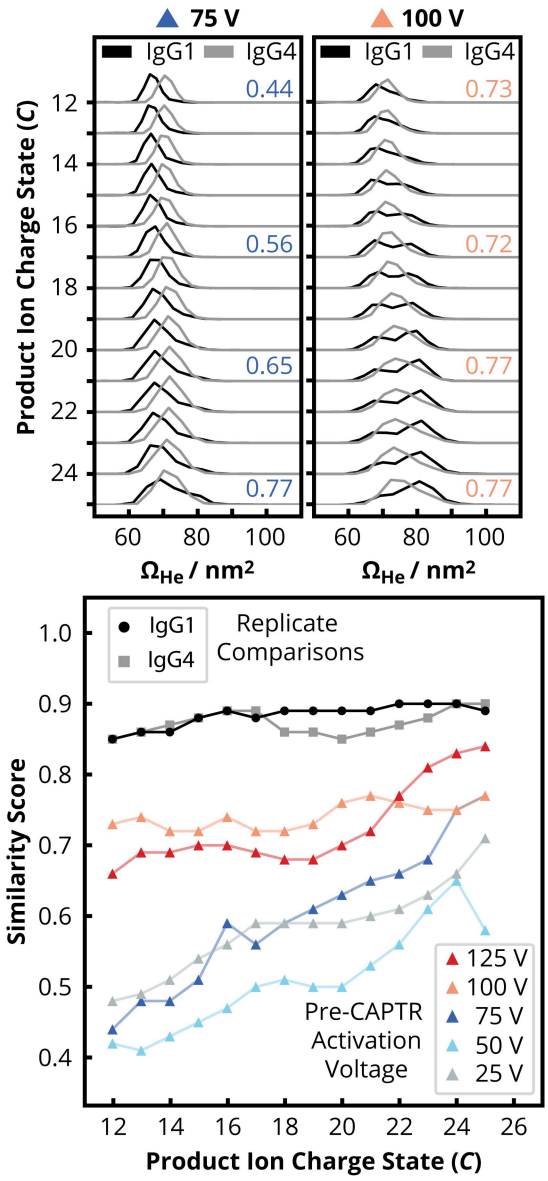


**Figure 2.4.** (Left) The apparent $^{DT}\Omega_{He}$ distributions of CAPTR products and residual precursor ions generated after activation (75 V and 100 V, pre-CAPTR activation) of 25+ precursors. Similarity scores are provided for representative distribution comparisons. (Right) The similarity scores for comparison of the apparent $^{DT}\Omega_{He}$ distributions of replicates of IgG1 and IgG4 $^{N}25 \rightarrow C$ versus charge state (triangles) and the similarity scores for the comparison of the apparent $^{DT}\Omega_{He}$ distributions of IgG1 and IgG4 at different pre-CAPTR activation

voltages versus charge state (circles). For most pre-CAPTR activation voltages, the $^{DT}\Omega_{He}$ distributions of the lower charged ions are more distinguishable (lower similarity scores) than those of their activated precursors.

Next, we quantified these differences using similarity scoring. We previously introduced the use of similarity scores to quantify the differences between arrival-time distributions and evaluate the significance of those differences relative to the variance of the underlying measurements.[43] Here, we calculated the Jensen-Shannon distance metric, which scores the difference between two probability distributions[44–46] and has been applied across many fields, including bioinformatics, genomics, proteomics, machine learning, and linguistics.[55–59] We define the similarity as 1 minus the Jensen-Shannon distance, which is the square root of the Jensen-Shannon divergence. A more detailed description of this similarity score metric and how it was calculated is available in the Supporting Information.

Figure 2.4 helps identify the most dissimilar Ω distributions for $^{N}$IgG1 and $^{N}$IgG4 ions formed from 25+* precursors. The apparent Ω distributions at 75 V and 100 V pre-CAPTR activation are shown as examples, and similarity scores comparing Ω distributions at all pre-CAPTR activation voltages are plotted. At most levels of pre-CAPTR activation, the Ω distributions of charge-reduced products exhibit less similarity than the corresponding precursors. For example, using 75 V, the Ω distributions of the 25+* precursor of $^{N}$IgG1 and $^{N}$IgG4 yield a similarity score of 0.81, whereas that for the $^{N}$25*→12 ions is 0.53. For reference, scores comparing replicates of $^{N}$25→*C* at 25 V are all 0.87 or higher (Ω distributions of replicates shown in Figures A11 and A12). *Therefore, the low similarity determined for the $^{N}$25*→12 ions from the two samples provides unambiguous evidence that the samples are*

*different, at a higher level of confidence than possible for the 25+* ions from those samples*. $^{N}$IgG1 and $^{N}$IgG4 activated precursors display similar Ω distributions, but their 12+ products are extremely sensitive to their differences. Similar trends in similarity scores are seen for $^{N}$26*→C Ω, as shown in Figures A13 and A14. These results provide further evidence that ions with similar Ω values don't necessarily have similar structures.

Collisional activation without charge-state manipulation, i.e., CIU, has been used applied previously to differentiate $^{N}$IgG1 and $^{N}$IgG4 from the same source.[19] To directly compare CIU with pre-CAPTR activation, 25+ and 26+ ions of both antibodies were probed as a function of collision energy using methods as indicated in Figure 2.1b. Figures A16 and A17 show representative Ω distributions. Figure 2.5 shows the similarity score between the distributions obtained for each charge state as a function of the collision voltages. The lowest similarity score calculated for $^{N}$IgG1 and $^{N}$IgG4 Ω distributions is 0.66, which was for the 26+ ions that were analyzed using a 70 V trap injection voltage with a value of 0.66. This aligns well with the low collision voltage range in which large CIU differences were observed previously for 23+ ions of IgG1$\kappa$ and IgG4$\kappa$.[19] For comparison, the similarity scores for $^{N}$25*→*C* and $^{N}$26*→*C* ions at 50 V pre-CAPTR activation are plotted as a function of *C*. The lowest score achieved from pre-CAPTR activation experiments is 0.41, which was for the 25*→13 ions. The apparent Ω distributions resulting from pre-CAPTR activation of the two samples are less similar, i.e., the two samples are better differentiated by pre-CAPTR activation than CIU.

Note that we previously compared Ω distributions using a similarity score that depended on dot products.[43] Analyzing the current results using either that similarity score or the Jensen-Shannon similarity score results in similar trends and identical conclusions (Figure A15). However, in other ongoing projects, we identified edge cases for which the dot-product-based

similarity score yields values outside of the expected bounds from zero to one. Based on that finding, we now recommend using the Jensen-Shannon similarity score for comparing distributions from IM experiments.

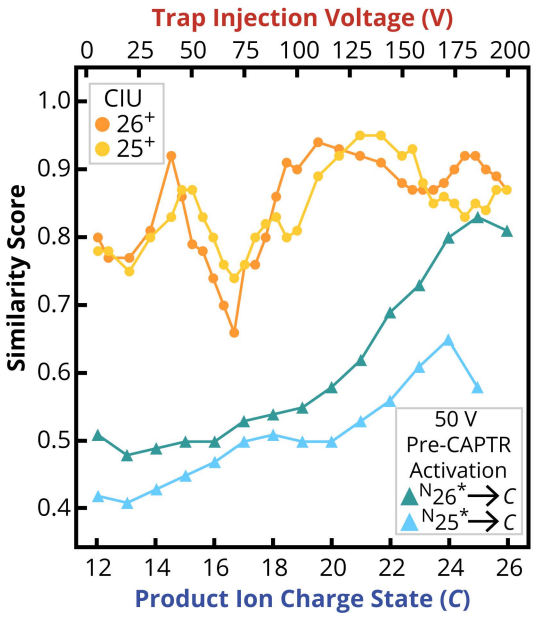


**Figure 2.5.** The similarity scores of the apparent $^{DT}\Omega_{He}$ distributions of $^{N}$IgG1 and $^{N}$IgG4 CAPTR products and residual precursor (25+ and 26+) ions at 50 V pre-CAPTR activation versus charge state (cool colors, bottom axis), and the similarity scores of apparent $^{DT}\Omega_{He}$ distributions of $^{N}$IgG1 and $^{N}$IgG4 precursor ions (25+ and 26+) subjected to collision-induced unfolding versus trap collision energy (warm colors, top axis). The distributions of charge-reduced products are more distinguishable (lower similarity scores) than those of the precursor ions subjected to CIU.

### 3.5 Post-CAPTR Activation of IgG1 and IgG4

To further probe the gas-phase structures of $^{N}$IgG ions and their CAPTR products, those ions were analyzed as a function of the injection voltage into a nitrogen-filled mobility cell

(Figure 2.1b). This will be referred to as post-CAPTR activation and the activated species are noted with an asterisk, i.e., "$^{N}P \rightarrow C^{*}$." Only the 26+ precursor ions of IgG1 and IgG4 were selected for these experiments. Note, the temperature of the sample capillary was not controlled independently of the atmospheric-pressure interface for the post-CAPTR activation experiments.

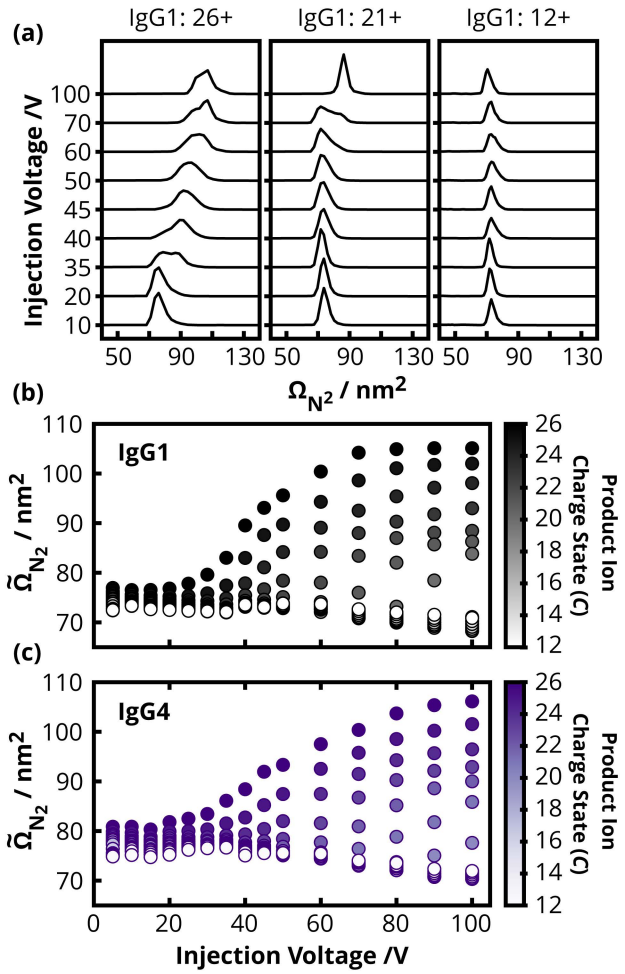


**Figure 2.6**. Post-CAPTR activation of $^{N}$IgG1 and $^{N}$IgG4. (a) Apparent $\Omega_{N2}$ distributions of $^{N}26 \rightarrow 26^{*}$, $^{N}26 \rightarrow 21^{*}$, and $^{N}26 \rightarrow 12^{*}$ ions of IgG1 at selected mobility cell injection voltages. (b) $\widetilde{\Omega}_{N2}$ values of each IgG1 $^{N}26 \rightarrow C^{*}$ ion population as a function of mobility cell injection voltage. (c) $\widetilde{\Omega}_{N2}$ values of each IgG4 $^{N}26 \rightarrow C^{*}$ ion population as a function of mobility cell injection voltage.

Figure 2.6a shows apparent $^{DT}\Omega_{N_2}$ distributions of $^{N}26\rightarrow26^*$, $^{N}26\rightarrow21^*$, and $^{N}26\rightarrow12^*$ ions of IgG1 at selected mobility cell injection voltages; corresponding distributions for IgG4 are shown in Figure A18. $\widetilde{\Omega}_{N_2}$ values of IgG1 and IgG4 $^{N}26\rightarrow C^*$ ions are shown in Figure 2.6b at all post-CAPTR activation voltages tested. IgG1 and IgG4 $^{N}26\rightarrow C^*$ ions exhibited very similar trends. Notably, ions of lower *C* exhibited a collapse in **Ω** with increasing injection voltage, whereas ions of intermediate *C* exhibited an initial collapse, and then expanded in Ω at higher injection voltages. Ions of highest *C* did not exhibit any evidence for collapse prior to expanding in **Ω** with increasing injection voltage. As discussed in the Introduction, IgGs are hypothesized to undergo significant collapse upon transition to the gas phase.[24–27] Some charge-reduced ions in these experiments exhibited evidence for collapse, suggesting that the initial ions from were not fully collapsed. Previous work investigating charge-state dependent compaction of protein complexes with and without internal cavities showed that ions of lower charge with internal cavities accessed compact conformations at low activation voltages prior to undergoing unfolding at higher voltages.[60] The post-CAPTR activation results for IgGs qualitatively resemble those for charge-reduced complexes with internal cavities. This suggests ion flexibility can contribute to similar charge-state dependent compaction.

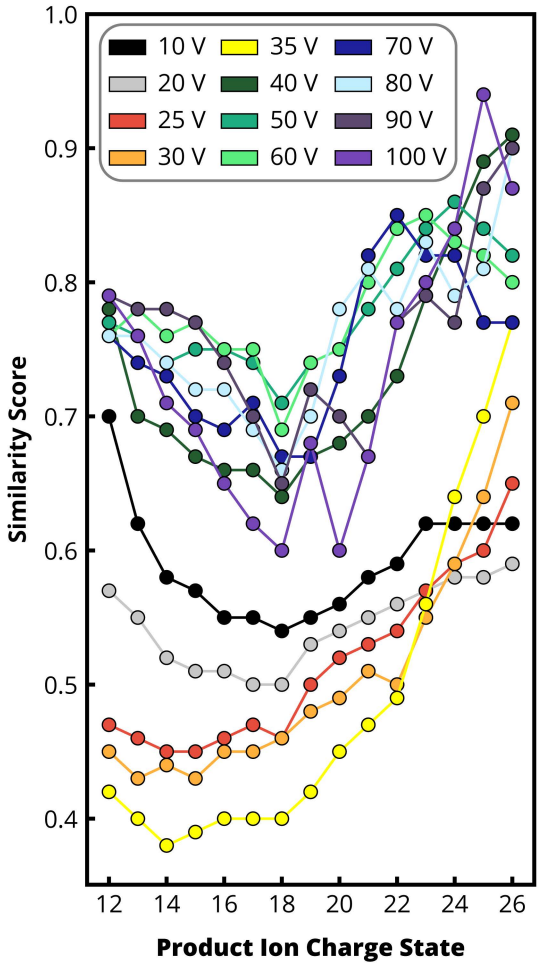


**Figure 2.7**. Similarity scores comparing the apparent $\Omega_{N2}$ distributions of $^{N}26 \rightarrow C^{*}$ ions of IgG1 and IgG4 at different post-CAPTR activation voltages.

Figure 2.7 shows similarity scores calculated for apparent Ω distributions of the $^{N}26 \rightarrow C^{*}$ ions of IgG1 and IgG4 at selected post-CAPTR activation voltages. These results show that many combinations of *C* and activation voltage yielded similar apparent Ω distributions for IgG1 and IgG4, notably when the values of *C* and the activation voltage were both large. However, other combinations yield very different apparent Ω distributions. For example, data for the $^{N}26 \rightarrow C^{*}$ ions, where $C = 13$ to 18, acquired using a post-CAPTR activation of 35 V yielded

similarity scores near 0.4. Those scores are amongst the lowest found in this study (Figures 2.4, 2.5, and 2.7) and demonstrate that post-CAPTR activation can also provide compelling evidence that these two samples are different.

## 4 Conclusions

This study used CAPTR, pre- and post-CAPTR activation, and IM-MS (Figure 2.1) to characterize and compare samples of IgG1 and IgG4 from human myeloma. Consistent with previous studies,[19,24] it was challenging to distinguish between IgG1 and IgG4 using native MS or native IM-MS alone (Figures 2.2a-d and Figure A4). Combining CAPTR and native MS enabled more confident charge state and mass assignments, which revealed a significant mass difference between the two antibodies (Figure 2.2e-h). Combining CAPTR and denaturing MS, revealed intrasample heterogeneity that would have otherwise gone undetected (Figure A5D). Combining CAPTR and IM-MS reveals that for ions from native-like conditions (Figure 2.3), the initial ions and their charge-reduced products all have similar Ω values. For ions from denaturing conditions, each consecutive CAPTR event results in a charge-reduced product that has a smaller Ω value, but values for all products were significantly larger than those for all CAPTR products of ions from native-like conditions. In general, these trends suggest that native-like IgGs ions share many properties with other native-like protein ions that have high masses.[31,34,53]

These samples were also analyzed using pre-CAPTR or post-CAPTR activation. With increasing pre-CAPTR activation, the Ω distributions for all ions tended to shift to larger values, increase in width, and exhibit more multimodal character. With decreasing *C*, the apparent Ω distributions tended to shift to smaller values, decrease in width, and exhibit more unimodal character. These trends are generally consistent with results from pre-CAPTR activation of other

native-like ions of proteins.[31,53] With increasing post-CAPTR activation, the changes in the Ω distributions depended on the number of CAPTR events. Products with the lowest charge state exhibited a collapse in Ω with increasing injection voltage, products with the intermediate charge state exhibited an initial collapse, and then expanded in Ω at higher injection voltages, and products with the highest charge state only expanded in Ω with increasing injection voltage. This relationship between charge state and the effect of activation qualitatively resembles that reported based on CIU of charge-reduced complexes with internal cavities.[60] This suggests the IgGs ions did not fully collapse during transfer to the gas-phase. Similarity scoring was used to quantitively compare Ω distributions determined from matched experiments analyzing samples of the two antibodies, which aided in identifying experiments that maximized sample differentiation. Relative to workflows using energy-dependent IM without charge-state manipulation (Figure 2.5), pre-CAPTR activation (Figure 2.4) and post-CAPTR activation (Figure 2.7) both enhanced the differentiation of these antibodies by IM. In sum, CAPTR enhanced many aspects of our ability to characterize and differentiate these antibody samples. We suggest that researchers consider incorporating CAPTR into their workflows for characterizing biotherapeutics.

**Supporting Information**: Additional description of data analysis procedures and similarity score calculations, as well as figures of additional experimental results.

## 5 Acknowledgements

This work was supported by the National Science Foundation through awards 1807382 and 2203513 from the Division of Chemistry, with partial co-funding from the Division of Molecular and Cellular Biosciences.

## 6 References

(1) Urquhart, L. Top Companies and Drugs by Sales in 2021. *Nat. Rev. Drug Discov.* **2022**, *21* (4), 251–251. https://doi.org/10.1038/d41573-022-00047-9.

(2) Kaplon, H.; Crescioli, S.; Chenoweth, A.; Visweswaraiah, J.; Reichert, J. M. Antibodies to Watch in 2023. *mAbs* **2023**, *15* (1), 2153410. https://doi.org/10.1080/19420862.2022.2153410.

(3) Beck, A.; Sanglier-Cianférani, S.; Van Dorsselaer, A. Biosimilar, Biobetter, and Next Generation Antibody Characterization by Mass Spectrometry. *Anal. Chem.* **2012**, *84* (11), 4637–4646. https://doi.org/10.1021/ac3002885.

(4) Vidarsson, G.; Dekkers, G.; Rispens, T. IgG Subclasses and Allotypes: From Structure to Effector Functions. *Front. Immunol.* **2014**, *5*, 520. https://doi.org/10.3389/fimmu.2014.00520.

(5) Roux, K. H.; Strelets, L.; Michaelsen, T. E. Flexibility of Human IgG Subclasses. *J. Immunol.* **1997**, *159* (7), 3372–3382.

(6) Boune, S.; Hu, P.; Epstein, A. L.; Khawli, L. A. Principles of N-Linked Glycosylation Variations of IgG-Based Therapeutics: Pharmacokinetic and Functional Considerations. *Antibodies* **2020**, *9* (2), 22. https://doi.org/10.3390/antib9020022.

(7) Harris, L. J.; Larson, S. B.; Hasel, K. W.; McPherson, A. Refined Structure of an Intact IgG2a Monoclonal Antibody. *Biochemistry* **1997**, *36* (7), 1581–1597. https://doi.org/10.1021/bi962514+.

(8) Harris, L. J.; Skaletsky, E.; McPherson, A. Crystallographic Structure of an Intact IgG1 Monoclonal Antibody. *J. Mol. Biol.* **1998**, *275* (5), 861–872. https://doi.org/10.1006/jmbi.1997.1508.

(9) Saphire, E. O.; Parren, P. W. H. I.; Pantophlet, R.; Zwick, M. B.; Morris, G. M.; Rudd, P. M.; Dwek, R. A.; Stanfield, R. L.; Burton, D. R.; Wilson, I. A. Crystal Structure of a Neutralizing Human IgG Against HIV-1: A Template for Vaccine Design. *Science* **2001**, *293* (5532), 1155–1159. https://doi.org/10.1126/science.1061692.

(10) Scapin, G.; Yang, X.; Prosise, W. W.; McCoy, M.; Reichert, P.; Johnston, J. M.; Kashi, R. S.; Strickland, C. Structure of Full-Length Human Anti-PD1 Therapeutic IgG4 Antibody Pembrolizumab. *Nat. Struct. Mol. Biol.* **2015**, *22* (12), 953–958. https://doi.org/10.1038/nsmb.3129.

(11) Beck, A.; Wagner-Rousset, E.; Bussat, M.-C.; Lokteff, M.; Klinguer-Hamour, C.; Haeuw, J.-F.; Goetsch, L.; Wurch, T.; Dorsselaer, A.; Corvaia, N. Trends in Glycosylation, Glycoanalysis and Glycoengineering of Therapeutic Antibodies and Fc-Fusion Proteins. *Curr. Pharm. Biotechnol.* **2008**, *9* (6), 482–501. https://doi.org/10.2174/138920108786786411.

(12) Xu, Y.; Wang, D.; Mason, B.; Rossomando, T.; Li, N.; Liu, D.; Cheung, J. K.; Xu, W.; Raghava, S.; Katiyar, A.; Nowak, C.; Xiang, T.; Dong, D. D.; Sun, J.; Beck, A.; Liu, H. Structure, Heterogeneity and Developability Assessment of Therapeutic Antibodies. *mAbs* **2019**, *11* (2), 239–264. https://doi.org/10.1080/19420862.2018.1553476.

(13) Barth, M.; Schmidt, C. Native Mass Spectrometry—A Valuable Tool in Structural Biology. *J. Mass Spectrom.* **2020**, *55* (10). https://doi.org/10.1002/jms.4578.

(14) Tamara, S.; den Boer, M. A.; Heck, A. J. R. High-Resolution Native Mass Spectrometry. *Chem. Rev.* **2022**, *122* (8), 7269–7326. https://doi.org/10.1021/acs.chemrev.1c00212.

(15) Westphall, M. S.; Lee, K. W.; Salome, A. Z.; Lodge, J. M.; Grant, T.; Coon, J. J. Three-Dimensional Structure Determination of Protein Complexes Using Matrix-Landing Mass

Spectrometry. *Nat. Commun.* **2022**, *13* (1), 2276. https://doi.org/10.1038/s41467-022-29964-4.

(16) Esser, T. K.; Böhning, J.; Fremdling, P.; Agasid, M. T.; Costin, A.; Fort, K.; Konijnenberg, A.; Gilbert, J. D.; Bahm, A.; Makarov, A.; Robinson, C. V.; Benesch, J. L. P.; Baker, L.; Bharat, T. A. M.; Gault, J.; Rauschenbach, S. Mass-Selective and Ice-Free Electron Cryomicroscopy Protein Sample Preparation via Native Electrospray Ion-Beam Deposition. *PNAS Nexus* **2022**, *1* (4), pgac153. https://doi.org/10.1093/pnasnexus/pgac153.

(17) Debaene, F.; Wagner-Rousset, E.; Colas, O.; Ayoub, D.; Corvaïa, N.; Van Dorsselaer, A.; Beck, A.; Cianférani, S. Time Resolved Native Ion-Mobility Mass Spectrometry to Monitor Dynamics of IgG4 Fab Arm Exchange and "Bispecific" Monoclonal Antibody Formation. *Anal. Chem.* **2013**, *85* (20), 9785–9792. https://doi.org/10.1021/ac402237v.

(18) Deslignière, E.; Ollivier, S.; Ehkirch, A.; Martelet, A.; Ropartz, D.; Lechat, N.; Hernandez-Alba, O.; Menet, J.-M.; Clavier, S.; Rogniaux, H.; Genet, B.; Cianférani, S. Combination of IM-Based Approaches to Unravel the Coexistence of Two Conformers on a Therapeutic Multispecific mAb. *Anal. Chem.* **2022**, *94* (22), 7981–7989. https://doi.org/10.1021/acs.analchem.2c00928.

(19) Tian, Y.; Han, L.; Buckner, A. C.; Ruotolo, B. T. Collision Induced Unfolding of Intact Antibodies: Rapid Characterization of Disulfide Bonding Patterns, Glycosylation, and Structures. *Anal. Chem.* **2015**, *87* (22), 11509–11515. https://doi.org/10.1021/acs.analchem.5b03291.

(20) Deslignière, E.; Botzanowski, T.; Diemer, H.; Cooper-Shepherd, D. A.; Wagner-Rousset, E.; Colas, O.; Béchade, G.; Giles, K.; Hernandez-Alba, O.; Beck, A.; Cianférani, S. High-

Resolution IMS–MS to Assign Additional Disulfide Bridge Pairing in Complementarity-Determining Regions of an IgG4 Monoclonal Antibody. *J. Am. Soc. Mass Spectrom.* **2021**, *32* (10), 2505–2512. https://doi.org/10.1021/jasms.1c00151.

(21) Upton, R.; Migas, L. G.; Pacholarz, K. J.; Beniston, R. G.; Estdale, S.; Firth, D.; Barran, P. E. Hybrid Mass Spectrometry Methods Reveal Lot-to-Lot Differences and Delineate the Effects of Glycosylation on the Tertiary Structure of Herceptin®. *Chem. Sci.* **2019**, *10* (9), 2811–2820. https://doi.org/10.1039/C8SC05029E.

(22) Marcoux, J.; Champion, T.; Colas, O.; Wagner-Rousset, E.; Corvaïa, N.; Van Dorsselaer, A.; Beck, A.; Cianférani, S. Native Mass Spectrometry and Ion Mobility Characterization of Trastuzumab Emtansine, a Lysine-Linked Antibody Drug Conjugate: Native MS and IM-MS for Trastuzumab Emtansine Analysis. *Protein Sci.* **2015**, *24* (8), 1210–1223. https://doi.org/10.1002/pro.2666.

(23) Pacholarz, K. J.; Barran, P. E. Use of a Charge Reducing Agent to Enable Intact Mass Analysis of Cysteine-Linked Antibody-Drug-Conjugates by Native Mass Spectrometry. *EuPA Open Proteomics* **2016**, *11*, 23–27. https://doi.org/10.1016/j.euprot.2016.02.004.

(24) Pacholarz, K. J.; Porrini, M.; Garlish, R. A.; Burnley, R. J.; Taylor, R. J.; Henry, A. J.; Barran, P. E. Dynamics of Intact Immunoglobulin G Explored by Drift-Tube Ion-Mobility Mass Spectrometry and Molecular Modeling. *Angew. Chem. Int. Ed.* **2014**, *53* (30), 7765–7769. https://doi.org/10.1002/anie.201402863.

(25) Campuzano, I. D. G.; Larriba, C.; Bagal, D.; Schnier, P. D. Ion Mobility and Mass Spectrometry Measurements of the Humanized IgGk NIST Monoclonal Antibody. In *ACS Symposium Series*; Schiel, J. E., Davis, D. L., Borisov, O. V., Eds.; American Chemical

Society: Washington, DC, 2015; Vol. 1202, pp 75–112. https://doi.org/10.1021/bk-2015-1202.ch004.

(26) Hansen, K.; Lau, A. M.; Giles, K.; McDonnell, J. M.; Struwe, W. B.; Sutton, B. J.; Politis, A. A Mass-Spectrometry-Based Modelling Workflow for Accurate Prediction of IgG Antibody Conformations in the Gas Phase. *Angew. Chem. Int. Ed.* **2018**, *57* (52), 17194–17199. https://doi.org/10.1002/anie.201812018.

(27) Devine, P. W. A.; Fisher, H. C.; Calabrese, A. N.; Whelan, F.; Higazi, D. R.; Potts, J. R.; Lowe, D. C.; Radford, S. E.; Ashcroft, A. E. Investigating the Structural Compaction of Biomolecules Upon Transition to the Gas-Phase Using ESI-TWIMS-MS. *J. Am. Soc. Mass Spectrom.* **2017**, *28* (9), 1855–1862. https://doi.org/10.1007/s13361-017-1689-9.

(28) Deslignière, E.; Ollivier, S.; Beck, A.; Ropartz, D.; Rogniaux, H.; Cianférani, S. Benefits and Limitations of High-Resolution Cyclic IM-MS for Conformational Characterization of Native Therapeutic Monoclonal Antibodies. *Anal. Chem.* **2023**, acs.analchem.2c05265. https://doi.org/10.1021/acs.analchem.2c05265.

(29) Wang, G.; Cole, R. B. Solution, Gas-Phase, and Instrumental Parameter Influences on Charge-State Distributions in Electrospray Ionization Mass Spectrometry. In *Electrospray ionization mass spectrometry: fundamentals, instrumentation, and applications*; Cole, R. B., Ed.; Wiley: New York, 1997; pp 137–174.

(30) Allen, S. J.; Schwartz, A. M.; Bush, M. F. Effects of Polarity on the Structures and Charge States of Native-Like Proteins and Protein Complexes in the Gas Phase. *Anal. Chem.* **2013**, *85* (24), 12055–12061. https://doi.org/10.1021/ac403139d.

(31) Gadzuk-Shea, M. M.; Bush, M. F. Effects of Charge State on the Structures of Serum Albumin Ions in the Gas Phase: Insights from Cation-to-Anion Proton-Transfer Reactions,

Ion Mobility, and Mass Spectrometry. *J. Phys. Chem. B* **2018**, *122* (43), 9947–9955. https://doi.org/10.1021/acs.jpcb.8b08427.

(32) Kafader, J. O.; Melani, R. D.; Schachner, L. F.; Ives, A. N.; Patrie, S. M.; Kelleher, N. L.; Compton, P. D. Native vs Denatured: An in Depth Investigation of Charge State and Isotope Distributions. *J. Am. Soc. Mass Spectrom.* **2020**, *31* (3), 574–581. https://doi.org/10.1021/jasms.9b00040.

(33) Han, Z.; Chen, L. C. High-Pressure nanoESI of Highly Conductive Volatile and Non-Volatile Buffer Solutions from a Large Taylor Cone: Effect of Spray Current on Charge State Distribution. *Int. J. Mass Spectrom.* **2022**, *476*, 116845. https://doi.org/10.1016/j.ijms.2022.116845.

(34) Gozzo, T. A.; Bush, M. F. Effects of Charge on Protein Ion Structure: Lessons from Cation-to-Anion Proton-Transfer Reactions. *Mass Spectrom. Rev.* **2023**, DOI: 10.1002/mas.21847.

(35) Stephenson, J. L.; McLuckey, S. A. Ion/Ion Proton Transfer Reactions for Protein Mixture Analysis. *Anal. Chem.* **1996**, *68* (22), 4026–4032. https://doi.org/10.1021/ac9605657.

(36) Abzalimov, R. R.; Kaltashov, I. A. Electrospray Ionization Mass Spectrometry of Highly Heterogeneous Protein Systems: Protein Ion Charge State Assignment via Incomplete Charge Reduction. *Anal. Chem.* **2010**, *82* (18), 7523–7526. https://doi.org/10.1021/ac101848z.

(37) Laszlo, K. J.; Bush, M. F. Analysis of Native-Like Proteins and Protein Complexes Using Cation to Anion Proton Transfer Reactions (CAPTR). *J. Am. Soc. Mass Spectrom.* **2015**, *26* (12), 2152–2161. https://doi.org/10.1007/s13361-015-1245-4.

(38) Huguet, R.; Mullen, C.; Srzentić, K.; Greer, J. B.; Fellers, R. T.; Zabrouskov, V.; Syka, J. E. P.; Kelleher, N. L.; Fornelli, L. Proton Transfer Charge Reduction Enables High-Throughput Top-Down Analysis of Large Proteoforms. *Anal. Chem.* **2019**, *91* (24), 15732–15739. https://doi.org/10.1021/acs.analchem.9b03925.

(39) McLuckey, S. A.; Stephenson, J. L. Ion/Ion Chemistry of High-Mass Multiply Charged Ions. *Mass Spectrom. Rev.* **1998**, *17* (6), 369–407. https://doi.org/10.1002/(SICI)1098-2787(1998)17:6<369::AID-MAS1>3.0.CO;2-J.

(40) Laszlo, K. J.; Buckner, J. H.; Munger, E. B.; Bush, M. F. Native-Like and Denatured Cytochrome c Ions Yield Cation-to-Anion Proton Transfer Reaction Products with Similar Collision Cross-Sections. *J. Am. Soc. Mass Spectrom.* **2017**, *28* (7), 1382–1391. https://doi.org/10.1007/s13361-017-1620-4.

(41) Laszlo, K. J.; Munger, E. B.; Bush, M. F. Effects of Solution Structure on the Folding of Lysozyme Ions in the Gas Phase. *J. Phys. Chem. B* **2017**, *121* (13), 2759–2766. https://doi.org/10.1021/acs.jpcb.7b00783.

(42) Laszlo, K. J.; Munger, E. B.; Bush, M. F. Folding of Protein Ions in the Gas Phase after Cation-to-Anion Proton-Transfer Reactions. *J. Am. Chem. Soc.* **2016**, *138* (30), 9581–9588. https://doi.org/10.1021/jacs.6b04282.

(43) Hong, S.; Bush, M. F. Collision-Induced Unfolding Is Sensitive to the Polarity of Proteins and Protein Complexes. *J. Am. Soc. Mass Spectrom.* **2019**, *30* (11), 2430–2437. https://doi.org/10.1007/s13361-019-02326-z.

(44) Lin, J. Divergence Measures Based on the Shannon Entropy. *IEEE Trans. Inf. Theory* **1991**, *37* (1), 145–151. https://doi.org/10.1109/18.61115.

(45) Endres, D. M.; Schindelin, J. E. A New Metric for Probability Distributions. *IEEE Trans. Inf. Theory* **2003**, *49* (7), 1858–1860. https://doi.org/10.1109/TIT.2003.813506.

(46) Österreicher, F.; Vajda, I. A New Class of Metric Divergences on Probability Spaces and Its Applicability in Statistics. *Ann. Inst. Stat. Math.* **2003**, *55* (3), 639–653. https://doi.org/10.1007/BF02517812.

(47) Williams, J. P.; Brown, J. M.; Campuzano, I.; Sadler, P. J. Identifying Drug Metallation Sites on Peptides Using Electron Transfer Dissociation (ETD), Collision Induced Dissociation (CID) and Ion Mobility-Mass Spectrometry (IM-MS). *Chem. Commun.* **2010**, *46* (30), 5458. https://doi.org/10.1039/c0cc00358a.

(48) Allen, S. J.; Giles, K.; Gilbert, T.; Bush, M. F. Ion Mobility Mass Spectrometry of Peptide, Protein, and Protein Complex Ions Using a Radio-Frequency Confining Drift Cell. *Analyst* **2016**, *141* (3), 884–891. https://doi.org/10.1039/C5AN02107C.

(49) Davidson, K. L.; Oberreit, D. R.; Hogan, C. J.; Bush, M. F. Nonspecific Aggregation in Native Electrokinetic Nanoelectrospray Ionization. *Int. J. Mass Spectrom.* **2017**, *420*, 35–42. https://doi.org/10.1016/j.ijms.2016.09.013.

(50) Gabelica, V.; Shvartsburg, A. A.; Afonso, C.; Barran, P.; Benesch, J. L. P.; Bleiholder, C.; Bowers, M. T.; Bilbao, A.; Bush, M. F.; Campbell, J. L.; Campuzano, I. D. G.; Causon, T.; Clowers, B. H.; Creaser, C. S.; De Pauw, E.; Far, J.; Fernandez-Lima, F.; Fjeldsted, J. C.; Giles, K.; Groessl, M.; Hogan, C. J.; Hann, S.; Kim, H. I.; Kurulugama, R. T.; May, J. C.; McLean, J. A.; Pagel, K.; Richardson, K.; Ridgeway, M. E.; Rosu, F.; Sobott, F.; Thalassinos, K.; Valentine, S. J.; Wyttenbach, T. Recommendations for Reporting Ion Mobility Mass Spectrometry Measurements. *Mass Spectrom. Rev.* **2019**, *38* (3), 291–320. https://doi.org/10.1002/mas.21585.

(51) Thompson, N. J.; Rosati, S.; Heck, A. J. R. Performing Native Mass Spectrometry Analysis on Therapeutic Antibodies. *Methods* **2014**, *65* (1), 11–17. https://doi.org/10.1016/j.ymeth.2013.05.003.

(52) Bush, M. F.; Campuzano, I. D. G.; Robinson, C. V. Ion Mobility Mass Spectrometry of Peptide Ions: Effects of Drift Gas and Calibration Strategies. *Anal. Chem.* **2012**, *84* (16), 7124–7130. https://doi.org/10.1021/ac3014498.

(53) Laszlo, K. J.; Bush, M. F. Interpreting the Collision Cross Sections of Native-like Protein Ions: Insights from Cation-to-Anion Proton-Transfer Reactions. *Anal. Chem.* **2017**, *89* (14), 7607–7614. https://doi.org/10.1021/acs.analchem.7b01474.

(54) Sobott, F.; McCammon, M. G.; Robinson, C. V. Gas-Phase Dissociation Pathways of a Tetrameric Protein Complex. *Int. J. Mass Spectrom.* **2003**, *230* (2–3), 193–200. https://doi.org/10.1016/j.ijms.2003.09.008.

(55) Itzkovitz, S.; Hodis, E.; Segal, E. Overlapping Codes within Protein-Coding Sequences. *Genome Res.* **2010**, *20* (11), 1582–1589. https://doi.org/10.1101/gr.105072.110.

(56) Sims, G. E.; Jun, S.-R.; Wu, G. A.; Kim, S.-H. Alignment-Free Genome Comparison with Feature Frequency Profiles (FFP) and Optimal Resolutions. *Proc. Natl. Acad. Sci.* **2009**, *106* (8), 2677–2682. https://doi.org/10.1073/pnas.0813249106.

(57) Mehri, A.; Jamaati, M.; Mehri, H. Word Ranking in a Single Document by Jensen–Shannon Divergence. *Phys. Lett. A* **2015**, *379* (28–29), 1627–1632. https://doi.org/10.1016/j.physleta.2015.04.030.

(58) Zhang, S.; Li, X.; Fan, C.; Wu, Z.; Liu, Q. Application of Machine Learning Techniques to Predict Protein Phosphorylation Sites. *Lett. Org. Chem.* **2019**, *16* (4), 247–257. https://doi.org/10.2174/1570178615666180907150928.

(59) Martins, A.; Smith, N.; Xing, E.; Aguiar, P.; Figueiredo, M. Nonextensive Information Theoretic Kernels on Measures. *J. Mach. Learn. Res.* **2009**, *10*, 935–975.

(60) Hall, Z.; Politis, A.; Bush, M. F.; Smith, L. J.; Robinson, C. V. Charge-State Dependent Compaction and Dissociation of Protein Complexes: Insights from Ion Mobility and Molecular Dynamics. *J. Am. Chem. Soc.* **2012**, *134* (7), 3429–3438. https://doi.org/10.1021/ja2096859.

# Chapter 3. Recommendations for the Use of Reducing Agents in Native Mass Spectrometry

## 1 Introduction

Maintenance of cellular redox homeostasis is critical for proper function, and redox imbalance is implicated in various diseases.[1,2] Relative to extracellular spaces, the cytoplasm in cells is reducing and different organelles and compartments maintain different redox conditions to carry out important biological functions; these conditions can even change in conjunction with the cell cycle.[3,4] The mitochrondria, which relies on electron transfer chains in order to generate ATP, is the most redox-active locale and maintains a lower steady-state redox potential than the cytosol.[3] Within the cell, glutathione (GSH), a tripeptide, serves as a key reducer or antioxidant.[5]

In laboratory protocols for protein science, reducing agents are often added during the purification and storage of protein solutions; these additions are useful in cases where the protein, its cofactors, or ligands are sensitive to oxidative stress. For proteins with free cysteines, this prevents unwanted cysteine modifications, including the formation of non-native disulfide bonds, that can cause protein aggregation.[6] For example, proteins that utilize iron-sulfur clusters are typically sensitive to oxygen. Fumarate and Nitrate Reduction Protein (FNR) in *E. coli* is a regulator for the switch between anaerobic and aerobic respiration; FNR binds a [4Fe-4S] cluster that acts as an oxygen sensor, and once oxidized to [2Fe-2S], FNR can no longer form the dimer necessary to bind to DNA.[7] In many studies of FNR, anaerobic chambers have been used to protect the protein from oxygen during protein purification and sample preparation, and common reducing agent, dithiothreitol (DTT), has been added to purification buffers in concentrations of 1-2.5 mM.[7,8] Sodium dithionite has been used for this purpose as well.[9,10] Both of these agents have been added in investigations of the anerobic restoration of the protein from the [2Fe-2S] state to the [4Fe-4S] state.[8,10] Native MS studies of FNR, and other iron-sulfur proteins, may

control exposure to oxygen, but the reducing agent, dithiothreitol, DTT, has also been added in concentrations up to 20 mM before MS measurements, in order to remove any stray persulfides, or after MS measurements, in order to investigate reversibility of protein modifications.[7,11] Other agents, GSH and tris(2-carboxyethyl)phosphine (TCEP), have also been used in native MS studies of iron-sulfur cluster proteins.[12] Reducing agents are also used to reduce native or non-native disulfide bonds in bottom-up proteomics experiments, in which proteins are digested with enzymes prior to primary structural analyses by LC-MS,[13] or for protein unfolding/refolding experiments.[14]

β-mercaptoethanol (βME), DTT, and TCEP are some of the most commonly used reducing agents in protein science.[13,15,16] βME is a monothiol and under standard conditions, the reaction of βME to reduce disulfide bonds is reversible, so an excess must be added to drive the reduction reactions to completion.[16,17] Of the three reducing agents to be discussed here, βME is the most volatile and will readily evaporate from solution.[16,18] As βME concentration decreases, the equilibrium effects, i.e., the reoxidation of products, need to be considered. Thiol-containing reducers will also reduce metals in solution, so the presence of metals will decrease the long term stability of βME and DTT, a dithiol reducer.[15,19] Metal chelates can be added to improve stability, but only in the case that metal-containing cofactors are unimportant to the native structure and function of the protein-of-interest.[15] βME is foul-smelling, is the most toxic of these common reducing agents,[13,16] forms hydrogen gas in the presence of strong acids or alkali metals, and releases toxic fumes on heating.[20]

DTT is a dithiol and is converted to a stable cyclic disulfide on oxidation, preventing reoxidation of products by the reverse reaction, so a lower concentration of DTT is required compared to reduction with βME.[17] In-solution, DTT is readily oxidized by air, so it has a shorter

half-life than βME or TCEP, but solid DTT is more shelf stable than liquid βME.[15,19] It is less foul-smelling, less volatile, and less hazardous than βME, so it is easier to handle safely.[17] Regarding the useful pH ranges of DTT and βME, the pKa values of the thiol groups are above 9.[16,19,21] Because of the decreased nucleophilicity of thiol groups versus thiolates, they are less effective at acidic pH.[16,22]

TCEP is a phosphine-based reducing agent, rather than a thiol, and it is nonvolatile and odorless.[16] It also is less susceptible to oxidation by air, so TCEP solutions are more stable than βME or DTT solutions.[16] It has a higher reducing capacity and performs faster than the thiol compounds as well, and due to the stability of the phosphine oxide product, the reaction is essentially irreversible.[15,23] TCEP is also effective over a much wider pH range of 1.5 to 8.5.[23] TCEP is not as sensitive to metal ions in solution as DTT, but it is sensitive to oxidation by metal chelators, and its stability is reduced in phosphate buffers.[15] Like DTT, TCEP has been shown to be competitive with protein sulfhydryls for labeling with maleimide or iodoacetamide, which is sometimes performed after disulfide bond reduction.[15] A final caveat of reduction by TCEP is that it should be performed at room temperature, rather than with heating like βME or DTT; with heating, TCEP can convert cysteine to alanine.[24]

In the pursuit of protein studies using native mass spectrometry (MS), it may be desirable to maintain reducing conditions throughout the analysis in order to preserve aspects of solution-phase structure. As mentioned before, some protein complexes are particularly sensitive to redox conditions, so oxidation can compromise native MS investigations of their structures, like in the prior example of iron-sulfur proteins.[7] There is, however, a lack of consensus in the literature regarding the compatibility of reducing agents with mass spectrometric analyses. Some studies have mentioned the use of reducing agents in native MS,[25,26] but different agents are chosen

depending on the study, and for most, there is no discussion of the choice of agent or concentration. Two protocols provide suggestions, but one lacks mention of TCEP,[27] while the other recommends TCEP or DTT over βME.[28] The protocols also recommend different ranges of reducing agent concentration (1-2 mM versus 1-5 mM) without much discussion of the origin of these recommendations. Additionally, there is evidence for βME or DTT covalent binding in non-native MS following purification or SDS-PAGE separation,[29–31] making the ideal choice of reducing agent unclear.

This study seeks to evaluate effects of the addition of βME, DTT, or TCEP on the resulting mass spectra of proteins standards in order to provide recommendations for their use. Reducing agents were included at various concentrations over a pH range common to native MS experiments (pH 6-8), and IM-MS results were analyzed for effects like adduction and disruption to protein structure.

## 2 Methods

Cytochrome *c* (horse heart, C7752), ribonuclease A (bovine pancreas, R6513), and dithiothreitol (D0632) were purchased from Sigma-Aldrich (St. Louis, MO). B-mercaptoethanol (AC125470100) was purchased from Fisher Scientific (Palatine, IL). TCEP•HCl was a gift from Prof. Ning Zheng (University of Washington). Protein stock solutions were prepared at 100 μM in aqueous 200 mM ammonium acetate at pH 6, 7, or 8 and buffer exchanged (final concentration 50 μM) into fresh aqueous ammonium acetate solutions using either Sartorius Vivaspin 500 Centrifugal Concentrators (MWCO 5kDa, Fisher Scientific) or Micro Bio-Spin 6 columns (Bio-Rad, Hercules, CA) in order to desalt. TCEP, DTT, and βME were prepared at stock concentrations of 20 mM, 150 mM, and 150 mM, respectively, in 200 mM ammonium

acetate and adjusted to pH 6, 7, and 8 with acetic acid or ammonium hydroxide. TCEP was also prepared at a stock concentration of 5 mM in 200 mM ammonium acetate and not pH adjusted (measured pH 5.74) in order to investigate impacts of improper sample preparation on protein mass spectra. The final concentration of protein was 10 μM in all solutions subjected to IM-MS analysis. Reducing agent concentrations were varied. For reduction experiments, DTT or βME was added to ribonuclease A solutions and incubated at 70–80 °C for 7 minutes. For reduction with TCEP, incubation was performed for 10 minutes at ~40 °C.

Mass Spectrometry experiments were performed on a Waters SELECT SERIES Cyclic IMS system[32] or a modified Waters Synapt G2 HDMS.[33] As described previously, nanoelectrospray ionization was performed from borosilicate capillaries with inner diameters of 0.78 mm pulled to tip of 1-3 μM with a Sutter Instruments P-97 micropipette puller (Novato, CA).[34] Ion mobility arrival time distributions were measured using the traveling wave cyclic ion mobility cell filled with 2 mBar nitrogen. All mobility experiments were performed on the same day. Driftscope v2.8 was used to extract ion mobility data, and all arrival time distributions were normalized to an integral of 1.

**3 Results and Discussion**

The goal of this study was to determine if and under what conditions intact protein ions can be generated by electrospray ionization from solutions containing common reducing agents, βME, DTT, or TCEP, without negative impacts on the ionization process or protein structure. For most experiments, cytochrome *c* was chosen. The mass of cytochrome *c* (equine heart, Cyt *c*) is about 12 kDa, making isotopic resolution feasible on both mass spectrometers used in this study. In its native state, no cysteine-cysteine disulfide bonds are present, but Cyt *c* does contain two

cysteine residues, which are covalently bound to a heme c group via thioether bonds.[35] Because the cysteines of Cyt *c* are already in a reduced state in coordination with the heme group, no further reduction can occur by the addition of reducing agents; however, the iron center of the heme can be reduced to the $Fe^{2+}$ form (neutral heme) from $Fe^{3+}$ form (+1-charged heme).[35,36] As a follow-up test-case, ribonuclease A was chosen. RbA is often used as model system to characterize the effectiveness of disulfide reduction.[37] The mass of ribonuclease A (bovine pancreas, RbA) is about 13.6 kDa, and four cysteine-cysteine disulfide bonds are present in its native structure.[38] Due to high thermal stability, it was hypothesized that no shifts to lower mass, corresponding to reduction chemistry, should be observed on the addition of reducing agents at moderate concentration without incubation at high temperature prior to MS analyses.

### 3.1 Effects of Reducing Agents on Mass Spectra of Cytochrome *c*

The range of pKa values of TCEP (phosphorus: 7.68, carboxyl groups: 4.31, 3.59, 2.87),[39] and the differences between the reducing efficiencies of TCEP, DTT, and βME at different pH also motivated investigations of pH effects. Each agent was tested with Cyt *c* at pH 6, 7, and 8. TCEP is commonly available as a hydrochloride salt, which will lower the pH of prepared protein solutions if no adjustment is performed, so TCEP was also added to protein solutions without pH adjustment. TCEP was tested over the range of 50 μM to 5 mM, whereas DTT and βME were tested over a range of 1 mM to 100 mM. In biochemical and mass spectrometric protocols, TCEP is typically used in concentrations up to 2 mM, DTT in concentrations up to 20 mM, and βME in concentrations up to 100 mM or more, depending on the application.[13,18,27,28,31,40,41]

Figure 3.1 shows selected mass spectra of native-like Cyt *c* electrospray-generated from aqueous 200 mM ammonium acetate at pH 7 with and without the addition of reducing agents;

these spectra were acquired on a Cyclic IMS system. The expected average mass of neutral, oxidized Cyt *c* is 12,360.95 Da, including the heme c group, and considering common modifications to the protein: the N-terminal methionine is not likely present, and the new N-terminal amino acid, glycine, is likely acetylated.[42] The experimental mass at pH 7, 12,360.87 Da, was determined by taking the weighted average of the isotopic peaks and is in good agreement with the predicted mass. Note that in the preparation of Cyt *c* from Sigma, there are contaminant peaks and remaining salt that were not fully removed by buffer exchange. At concentrations of 5 and 10 mM, no mass spectral effects are observed for reducing agents DTT and βME, as shown in Figure 3.1. The addition of 1 mM TCEP•HCl resulted in the observation of adducts of TCEP, primarily on charge states 6+ and below, as well as the presence of +1-charged clusters of TCEP, oxidized TCEP, sodium, and potassium in the lower *m*/*z* range. The presence of adducts on lower charge states, but not higher charge states, of Cyt *c* suggests that activation results in “collisional-induced cleaning” of TCEP adducts.[43]

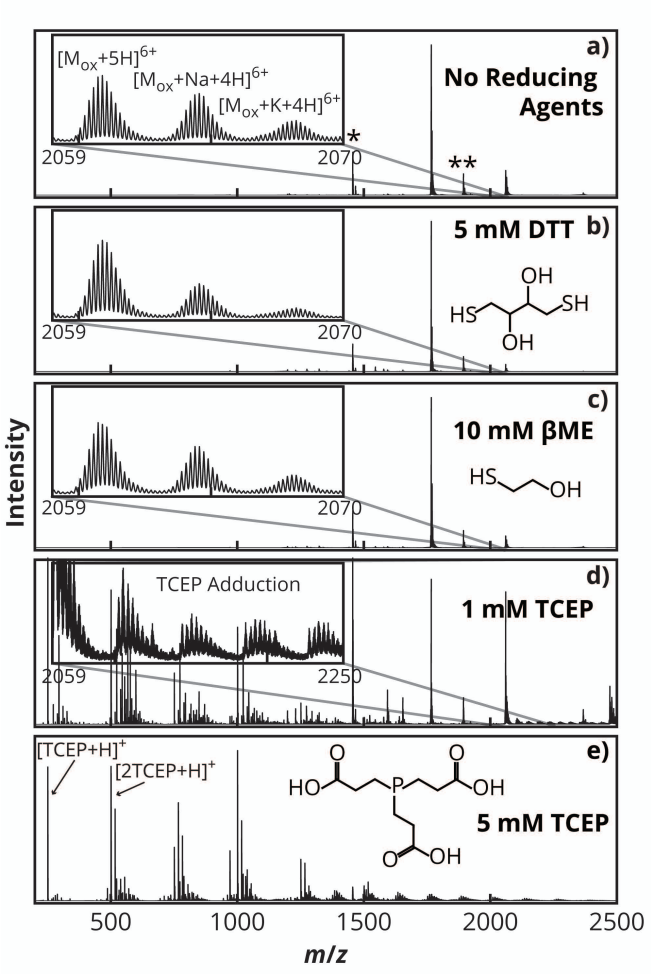


**Figure 3.1**. Mass spectra of Cytochrome *c* (Cyt *c*) in aqueous 200 mM ammonium acetate at pH 7 a) without reducing agents, b) with 5 mM DTT, c)10 mM βME, d) 1 mM TCEP, and e) 5 mM TCEP collected on a Waters Cyclic Select Series instrument. Insets of a), b), and c) show 7+ Cyc *c*. The inset of d) shows adduction of 1, 2, 3, and 4 TCEP molecules to 6+ Cyt *c*. Contaminant peaks are labeled with * (2910 Da) and ** (9460 Da).

Collisional activation was performed in the trap region of the Cyclic IMS system to determine whether activation could effectively mitigate TCEP adduction. At 4 V trap injection voltage, TCEP adduction was observed on the 6+ ions, but adduct peaks decreased in intensity

with increasing trap collision energy. At 40 V, adduction of TCEP to Cyt *c* was no longer visible for the 6+ charge state population (Figure B1).The application of collision energy also decreased the signals observed for the TCEP clusters. For example, for pH 6, 1 mM TCEP, the application of 15 V of trap injection voltage reduced interference by TCEP and enabled the observation of the 8+ charge state (Figure B2). The ESI current was also varied to test its impact on salt cluster and adduct signals; increasing the ESI current results in initial droplets that have larger diameters.[34] Increasing the ESI current caused more interference by TCEP. At 132 nA, increased TCEP clustering was observed, and the signal for all observed cytochrome *c* peaks decreased in intensity as compared to 25 nA (Figure B3).

At 5mM, the presence of TCEP results in significant interference with Cyt *c* ion signal, with protein peaks becoming barely discernable, and the major observed peaks are assigned to clusters of TCEP instead. No signal corresponding to free heme c was observed with any of the reducing agent additions shown in Figure 3.1. Figure 3.2 shows a comparison of spectra collected on a Waters Cyclic instrument and a Waters Synapt G2 instrument, with and without the addition of TCEP•HCl. The pH of the solution without TCEP was adjusted to pH 7, and the pH of solutions with TCEP were not adjusted in this case. While the unadjusted pH had little effect on the observed clustering and adduction of TCEP, the choice of instrumentation did have an effect. Spectra from the Synapt G2 display adduction of TCEP on both observed charge states (6 and 7+) even at TCEP•HCl concentrations as low as 50 μM (Figure B4). On the Cyclic instrument, at 1 mM, the intensity ratio of the nonadducted 6+ Cyt *c* peak to its 1 TCEP adduct peak was 49:1, whereas the same ratio for a 1 mM TCEP addition on the Synapt G2 was about 1.5 to 1. These differences suggest a greater baseline level of ion activation on the Cyclic IMS than on the Synapt G2 systems. In addition to differences in devices used for ion mobility, the

Synapt G2 uses a stacked-ring ion guide to transmit ions from the atmospheric-pressure interface, whereas the Cyclic IMS system used a conjoined ion guide, which has been associated with increased ion activation.[44]

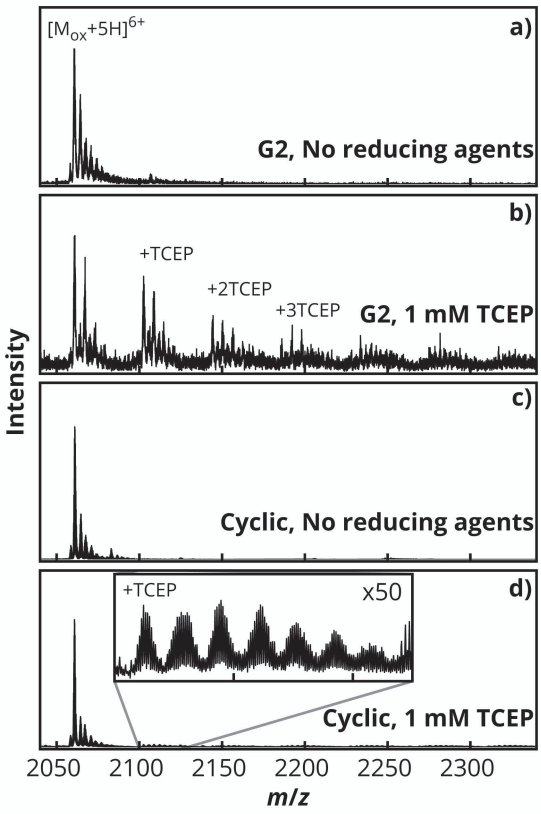


**Figure 3.2**. Comparison of mass spectra acquired on a Waters Synapt G2 (a, b) with those acquired on a Waters Cyclic Select Series (c,d).a) and c) show spectra of Cyt *c* in 200 mM ammonium acetate adjusted to pH 7. b) and d) show spectra of Cyt *c* in 200 mM ammonium acetate with TCEP added to a concentration of 1 mM without pH adjustment of the added TCEP solution.

Because of the negative impacts on ionization and the extent of adduction observed, TCEP was not tested at concentrations higher than 5 mM; however, DTT and βME showed little effect on Cyt *c* mass spectra when added in concentrations up to 10 mM and 20 mM,

respectively. Although no adduct formation or significant protein signal interference was observed at concentrations of even 100 mM (Figure B5) significant shifts to higher charge states were observed. Figure 3.3 shows the average charge state observed at pH 7 with increasing concentration of the three different reducing agents. The *m*/*z* ranges defined for each charge state are available in Table B1; they were held the same for DTT and βME analyses, but the range was broadened in TCEP analyses in order to include contributions from adduct peaks. At pH 7, the average charge state without the addition of agents was calculated to be 6.8. At 100 mM DTT, the average increased to 8.4, at 100 mM BME the average increased to 7.5, and at 1 mM TCEP, the average decreased to 5.7. The charge state distribution can be affected by solution constituents,[45] but also by differences in ESI tip shape and orifice size,[46] tip positioning,[47] and current.[48] For IM-MS experiments performed on the Cyclic, the current was maintained between 30 and 60 nA for the majority of experiments. The tip position was not measured, but a camera was used to visually inspect the tip position. These factors contribute to a small variance in charge-state distributions between technical replicates., The large shifts to higher charge states associated with high βME and DTT concentrations is therefore attributed to unfolding of the protein in solution. Additionally, similar charge state shifts were observed with the addition of DTT on different days (Figure B6)

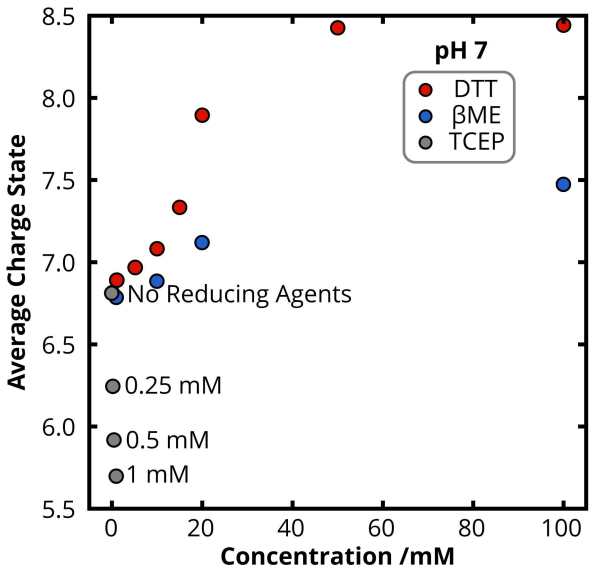


**Figure 3.3**. Average charge state of Cytochrome *c* in 200 mM ammonium acetate with increasing concentrations of reducing agents at pH 7.

Without the addition of a reducing agent, the average charge state of Cyt *c* was about 6.8 for pH 6, 7, and 8. Additionally, the average charge state decreased similarly at all pH values with the addition of TCEP to 1 mM (Figure B7). The addition of TCEP resulted in a significant increase in signal for 5 and 6+ cytochrome *c*, so overall interference by TCEP could be the result of multiple processes, including adduction, ion suppression, and charge reduction. The addition of DTT to 100 mM raised the average charge state to 8.4 and 8.5 at pH 6 and 7, respectively, but only to 8.1 at pH 8 (Figure B8). For additions of βME to a 100 mM concentration, the average charge state increased to 7.3 at pH 6, to 7.5 at pH 7, and to 8.3 at pH 8. (Figure B9). Between pH 6 and pH 7, the effect was minimal, but increasing to pH 8 from pH 6 increased the maximum average charge state by an entire charge.

Based on the results from mass spectral analyses, DTT and βME are more compatible with native MS than TCEP, likely due to their superior volatility. At concentrations higher than

10 mM of DTT and 20 mM of βME the observed charge-state distribution of Cyt *c* shifts significantly to higher charge, consistent with unfolding in solution. These effects are not associated with reduction of the heme. The addition of alcohols, or other organic solvents, to electrospray solutions can result in a similar increase in the average charge state of proteins.[45] This has been attributed to structural destabilization or denaturation in solution.[45] Based on mass spectral observations, denaturation of Cyt *c* likely occurs as a result of the addition of high concentrations of DTT and βME and is more significant with DTT, a diol, than with βME.

### 3.2 Effects of Reducing Agents on the Ion Mobility of Cytochrome *c*

Because shifts to higher charge state likely indicate structural disruption in solution, ion mobility data was collected to investigate shifts in protein ion structure concomitant with reducing agent addition. The 7+ charge state was observed under all reducing agent concentrations, so it was chosen for mobility analysis, though it decreased in intensity significantly at high concentrations of DTT and βME. Figure 3.4 shows the arrival time distributions of 7+ Cyt *c* at pH 7 at various concentrations of reducing agent; TCEP adduct peaks were excluded from this analysis. Surprisingly, no large shifts in arrival time distributions were observed, even at high reducing agent concentrations. A small decrease in arrival time is observed with increasing reducing agent concentration, but no indication of unfolding is present. Similar results for 7+ Cyt *c* were observed at pH 6, 7, and 8 (Figure B10, B11). At pH 6 and pH 8, some shifts to longer arrival times were observed with reducing agent addition, but the shifts were minimal. No evidence for significant unfolding was observed.

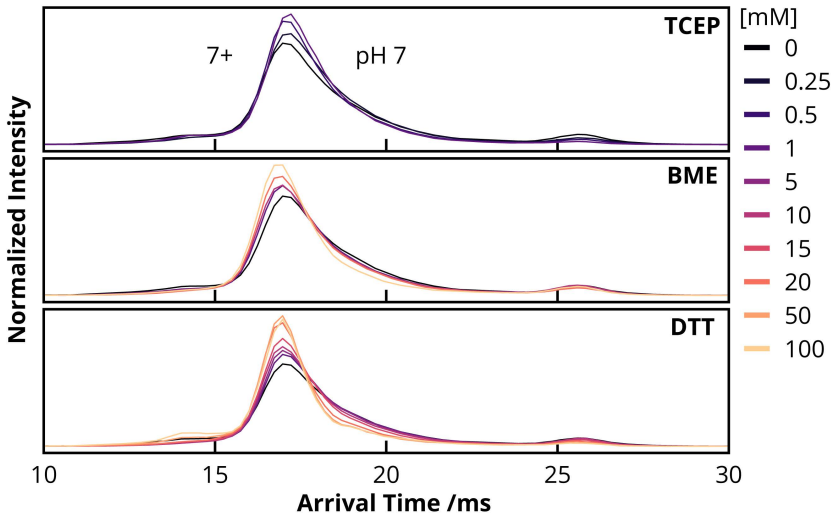


**Figure 3.4**. Cyclic ion mobility arrival time distributions of 7+ Cyt *c* (1760 to 1800 *m*/*z*) in 200 mM ammonium acetate, pH 7, with and without reducing agents.

The 6+ charge state was also analyzed, though it almost entirely disappeared from spectra at 100 mM concentrations of DTT and βME. 6+ arrival time distributions at pH7 are shown in Figure 3.5. At 20, 50, and 100 mM DTT, the peak at longer arrival times grew in intensity, suggesting that Cyt *c* experienced some unfolding. Similar results are observed at pH 6 and pH 8 for DTT, and at pH 8, the same shift is observed upon addition of 100 mM βME as well (Figure B12, B13). The low intensity of 6+ Cyt *c* at high DTT and βME concentration impacts interpretation of these results. Charge states, 5, 8, 9, and 10+ were not present, or not of significant intensity, without the addition of reducing agents, so their mobility data is not included here.

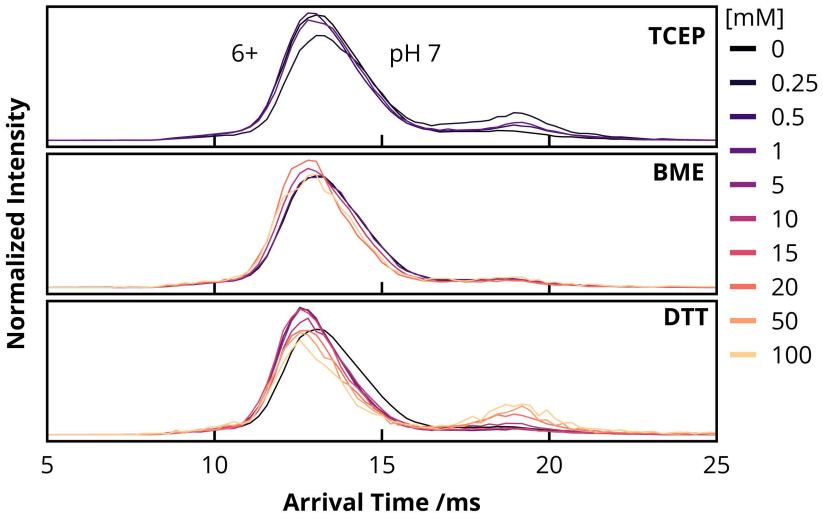


**Figure 3.5**. Cyclic ion mobility arrival time distributions of 6+ Cyt *c* (2055 to 2100 *m*/*z*) in 200 mM ammonium acetate, pH 7, with and without reducing agents.

As mentioned before, excess charging from ESI often associated with protein denaturation in solution. The lack of significant shifts in the arrival time distributions of 6 and 7+ Cyt *c* suggests that a native-like population of Cyt *c* may still be present in solution, even at higher reducing agent concentrations. As more Cyt *c* experiences unfolding in solution, the populations of 6 and 7+ Cyt *c* become depleted, and the majority of Cyt *c* instead takes on additional charge.

### 3.3 Incubation of Cytochrome *c* and Ribonuclease A with Reducing Agents

As a final set of experiments, Cytochrome *c* (Cyt *c* ) and Ribonuclease A (RbA) were subjected to a modified disulfide bond reduction procedure[37] and the resulting mass spectra were analyzed for completeness of reduction. Because the addition of TCEP resulted in poorer quality

mass spectra at most concentrations, it was only tested at 500 uM at pH 7, and it was evaluated for utility at this low concentration. DTT was added to a concentration of 5 mM and βME was added to a concentration of 10 mM, and the protein solutions were incubated between 70 and 80 °C for 7 minutes prior to analysis. Protein solutions containing TCEP were instead incubated at 40 °C for 10 minutes to prevent unwanted chemical modification resulting from heat.[24] Figure 3.6 shows mass spectral results from incubations of RbA with reducing agents.

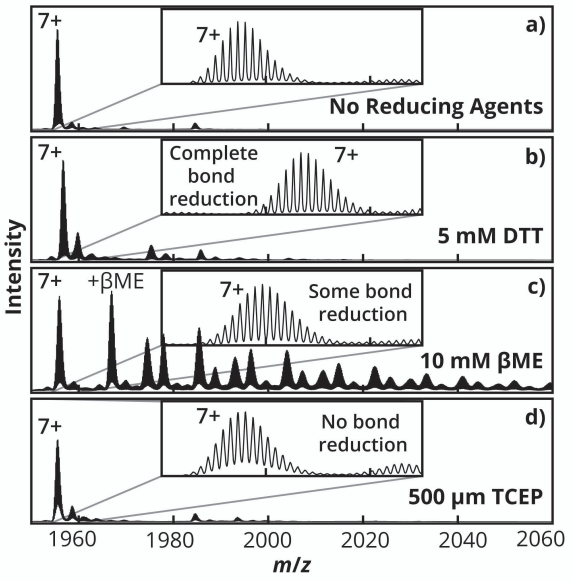


**Figure 3.6**. Disulfide bond reduction of RbA. The 7+ charge state of RbA a) without reducing agents or incubation, b) incubated with 5 mM DTT, c) incubated with 10 mM βME, d) incubated with 500 µM TCEP.

After performing incubation with TCEP, no changes in the resulting mass spectra of Cyt *c* or RbA were observed. The protocol could be modified by increasing the temperature or increasing the duration of incubation. Increasing the concentration of TCEP is another option, but a corresponding increase in salt clusters and TCEP adduction may occur.

After incubation with βME for 7 minutes at high temperature, reduction was not completed. At pH 6 the 7+ charge state increased in mass by 4.2 Da, at pH 7 the 7+ charge state increased in mass by 2.6 Da, and at pH 8 the 7+ charge state increased in mass by 1.2 Da. These results are surprising, considering the high pKa of the thiol group of βME. For complete reduction, the mass shift should be equivalent to the addition of 8 protons. RbA also displayed significant features assigned to covalent modification by βME resulting from incomplete reduction. After incubation with DTT for 7 minutes at high temperature, reduction of the 8 disulfide bonds of RbA was complete at all pH values with no observed covalent modification by DTT.

Cyt *c* incubation was only performed at pH 7 for reference because no reduction of the protein can occur. No βME molecules were observed to be attached to Cyt *c* after incubation, which is what we expect. βME and DTT have the ability to reduce metals in solution, and a small shift to higher *m*/*z* is observed (Figure B14). The oxidized heme carries a +1 charge, so the 7+ population of Cyt *c* only carries 6 excess protons. A reduction of the heme (neutral) would mean that the 7+ population of Cyt *c* now carries 7 excess protons. We hypothesize that heme reduction is the source of this shift. A similar shift is observed post-incubation with DTT.

## 4 Conclusion

We evaluated common reducing agents for compatibility with native and disulfide-bond reduced IM-MS in order to provide a clear set of recommendations for their use. For native MS, reducing agents can help prevent unwanted oxidation of proteins, and for disulfide bond reduction, it is helpful to choose a reducing agent that doesn't have to be removed prior to analysis. Of the three reducing agents, TCEP affected the mass spectral results the most at

concentrations under 5 mM. The use of TCEP resulted in signal interference that could complicate protein studies (Figures 3.1 and 3.2). The observed interference results from nonvolatility and ion adduction, but potentially ion suppression or charge reduction as well. The stability of proteins can be affected by other solutes, including reducing agents. For example, DTT and βME did not adduct to protein ions, but the addition of either in concentrations higher than 20 mM was associated with changes in the charge-state distribution of Cyt *c* that are consistent with the destabilization of protein in solution (Figure 3.3) We recommend avoiding the use of TCEP, if possible. Lowering electrospray currents and increasing collisional activation, to the extent possible without significantly disrupting protein structure, can help if the use of TCEP cannot be avoided. Ultimately, the system-of-interest should be the strongest consideration in choosing which reducing agent is most appropriate. Sensitivity to one agent or another, e.g., insolubility or aggregation, should be taken into consideration.[25] The choice of buffer and the presence of metals or metal chelators should also be considered.

For disulfide bond reduction, DTT worked best for RbA (Figure 3.6). The addition of 5 mM DTT resulted in the reduction of all 8 disulfide bonds of RbA at pH 6, 7, and 8. The addition of 10 mM βME resulted in incomplete reduction and covalent attachment of βME to the protein, which increased spectral congestion. Increased βME concentration or extended incubation should improve bond reduction. The protocol performed for TCEP addition resulted in no reduction at all. Heat is not recommended for reduction with TCEP due to the potential for unwanted chemical modification of proteins, so extended incubation times may be required. Sensitivity of the system-of-interest to heat should be taken into consideration for the particular incubation protocol used. Heat can result in protein unfolding, making internal disulfide bonds more accessible to reducing agents, but aggregation could also occur, depending on the protein.

For highly flexible proteins, excessive heating may not even be necessary, e.g. antibodies can undergo reduction at room temperature.[49] Overall, DTT and βME are the most suitable reducing agents for native mass spectrometry due to their high volatility, and DTT was best overall because of its performance for disulfide bond reduction. Due to increased safety concerns when using βME, we opt for DTT over βME whenever possible. We hope this work provides a better starting point for investigators considering adding reducing agents to native or top-down IM-MS experiments of proteins.

## 5 Acknowledgements

This work was supported by the National Science Foundation through award 2203513 from the Division of Chemistry, with partial co-funding from the Division of Molecular and Cellular Biosciences.

## 6 References

(1) Le Gal, K.; Schmidt, E. E.; Sayin, V. I. Cellular Redox Homeostasis. *Antioxidants* **2021**, *10* (9), 1377. https://doi.org/10.3390/antiox10091377.

(2) Tretter, V.; Hochreiter, B.; Zach, M. L.; Krenn, K.; Klein, K. U. Understanding Cellular Redox Homeostasis: A Challenge for Precision Medicine. *Int. J. Mol. Sci.* **2021**, *23* (1), 106. https://doi.org/10.3390/ijms23010106.

(3) Go, Y.-M.; Jones, D. P. Redox Compartmentalization in Eukaryotic Cells. *Biochim. Biophys. Acta BBA - Gen. Subj.* **2008**, *1780* (11), 1273–1290. https://doi.org/10.1016/j.bbagen.2008.01.011.

(4) Meng, J.; Lv, Z.; Zhang, Y.; Wang, Y.; Qiao, X.; Sun, C.; Chen, Y.; Guo, M.; Han, W.; Ye, A.; Xie, T.; Chu, B.; Shi, C.; Yang, S.; Chen, C. Precision Redox: The Key for Antioxidant Pharmacology. *Antioxid. Redox Signal.* **2021**, *34* (14), 1069–1082. https://doi.org/10.1089/ars.2020.8212.

(5) Couto, N.; Wood, J.; Barber, J. The Role of Glutathione Reductase and Related Enzymes on Cellular Redox Homoeostasis Network. *Free Radic. Biol. Med.* **2016**, *95*, 27–42. https://doi.org/10.1016/j.freeradbiomed.2016.02.028.

(6) Remans, K.; Lebendiker, M.; Abreu, C.; Maffei, M.; Sellathurai, S.; May, M. M.; Vaněk, O.; De Marco, A. Protein Purification Strategies Must Consider Downstream Applications and Individual Biological Characteristics. *Microb. Cell Factories* **2022**, *21* (1), 52. https://doi.org/10.1186/s12934-022-01778-5.

(7) Crack, J. C.; Thomson, A. J.; Le Brun, N. E. Mass Spectrometric Identification of Intermediates in the $O_2$ -Driven [4Fe-4S] to [2Fe-2S] Cluster Conversion in FNR. *Proc. Natl. Acad. Sci.* **2017**, *114* (16). https://doi.org/10.1073/pnas.1620987114.

(8) Khoroshilova, N.; Popescu, C.; Münck, E.; Beinert, H.; Kiley, P. J. Iron-Sulfur Cluster Disassembly in the FNR Protein of *Escherichia Coli* by $O_2$ : [4Fe-4S] to [2Fe-2S] Conversion with Loss of Biological Activity. *Proc. Natl. Acad. Sci.* **1997**, *94* (12), 6087–6092. https://doi.org/10.1073/pnas.94.12.6087.

(9) Lazazzera, B. A.; Beinert, H.; Khoroshilova, N.; Kennedy, M. C.; Kiley, P. J. DNA Binding and Dimerization of the Fe−S-Containing FNR Protein from Escherichia Coli Are Regulated by Oxygen. *J. Biol. Chem.* **1996**, *271* (5), 2762–2768. https://doi.org/10.1074/jbc.271.5.2762.

(10) Kiley, P. J.; Beinert, H. Oxygen Sensing by the Global Regulator, FNR: The Role of the Iron-Sulfur Cluster. *FEMS Microbiol. Rev.* **1998**, *22* (5), 341–352. https://doi.org/10.1111/j.1574-6976.1998.tb00375.x.

(11) Crack, J. C.; Le Brun, N. E. Native Mass Spectrometry of Iron-Sulfur Proteins. In *Fe-S proteins: methods and protocols*; Santos, P. C. dos, Ed.; Methods in molecular biology; Humana Press: New York, NY, 2021.

(12) Lin, C.-W.; McCabe, J. W.; Russell, D. H.; Barondeau, D. P. Molecular Mechanism of ISC Iron–Sulfur Cluster Biogenesis Revealed by High-Resolution Native Mass Spectrometry. *J. Am. Chem. Soc.* **2020**, *142* (13), 6018–6029. https://doi.org/10.1021/jacs.9b11454.

(13) Müller, T.; Winter, D. Systematic Evaluation of Protein Reduction and Alkylation Reveals Massive Unspecific Side Effects by Iodine-Containing Reagents. *Mol. Cell. Proteomics MCP* **2017**, *16* (7), 1173–1187. https://doi.org/10.1074/mcp.M116.064048.

(14) Li, Y.-J.; Rothwarf, D. M.; Scheraga, H. A. Mechanism of Reductive Protein Unfolding. *Nat. Struct. Mol. Biol.* **1995**, *2* (6), 489–494. https://doi.org/10.1038/nsb0695-489.

(15) Burmeister Getz, E.; Xiao, M.; Chakrabarty, T.; Cooke, R.; Selvin, P. R. A Comparison between the Sulfhydryl Reductants Tris(2-Carboxyethyl)Phosphine and Dithiothreitol for Use in Protein Biochemistry. *Anal. Biochem.* **1999**, *273*, 73–80. https://doi.org/10.1006/abio.1999.4203.

(16) Mthembu, S. N.; Sharma, A.; Albericio, F.; de la Torre, B. G. Breaking a Couple: Disulfide Reducing Agents. *ChemBioChem* **2020**, *21* (14), 1947–1954. https://doi.org/10.1002/cbic.202000092.

(17) Cleland, W. W. Dithiothreitol, a New Protective Reagent for SH Groups *. *Biochemistry* **1964**, *3* (4), 480–482. https://doi.org/10.1021/bi00892a002.

(18) *Bio-Rad Technical Support FAQs: FAQ268440261 on SDS-PAGE*. https://www.bio-rad.com/webroot/web/html/lsr/tech_support_faqs/FAQ268440261.html (accessed 2023-04-19).

(19) Stevens, R.; Stevens, L.; Price, N. The Stabilities of Various Thiol Compounds Used in Protein Purifications. *Biochem. Educ.* **1983**, *11* (2), 70. https://doi.org/10.1016/0307-4412(83)90048-1.

(20) 2-Mercaptoethanol SDS M3148. https://www.sigmaaldrich.com/PT/pt/sds/sigma/m3148.

(21) *Ionisation Constants of Organic Acids in Aqueous Solution*; International Union of Pure and Applied Chemistry, Serjeant, E. P., Dempsey, B., International Union of Pure and Applied Chemistry, Eds.; IUPAC chemical data series; Pergamon Press: Oxford ; New York, 1979.

(22) Nagy, P. Kinetics and Mechanisms of Thiol–Disulfide Exchange Covering Direct Substitution and Thiol Oxidation-Mediated Pathways. *Antioxid. Redox Signal.* **2013**, *18* (13), 1623–1641. https://doi.org/10.1089/ars.2012.4973.

(23) Han, J. C.; Han, G. Y. A Procedure for Quantitative Determination of Tris(2-Carboxyethyl)Phosphine, an Odorless Reducing Agent More Stable and Effective than Dithiothreitol. *Anal. Biochem.* **1994**, *220*, 5–10. https://doi.org/10.1006/abio.1994.1290.

(24) Wang, Z.; Rejtar, T.; Zhou, Z. S.; Karger, B. L. Desulfurization of Cysteine-Containing Peptides Resulting from Sample Preparation for Protein Characterization by Mass Spectrometry. *Rapid Commun. Mass Spectrom.* **2010**, *24*, 267–275. https://doi.org/10.1002/rcm.4383.

(25) Walker, L. R.; Marty, M. T. Revealing the Specificity of a Range of Antimicrobial Peptides in Lipid Nanodiscs by Native Mass Spectrometry. *Biochemistry* **2020**, *59* (23), 2135–2142. https://doi.org/10.1021/acs.biochem.0c00335.

(26) Marzahn, M. R.; Marada, S.; Lee, J.; Nourse, A.; Kenrick, S.; Zhao, H.; Ben-Nissan, G.; Kolaitis, R.; Peters, J. L.; Pounds, S.; Errington, W. J.; Privé, G. G.; Taylor, J. P.; Sharon, M.; Schuck, P.; Ogden, S. K.; Mittag, T. Higher-order Oligomerization Promotes Localization of SPOP to Liquid Nuclear Speckles. *EMBO J.* **2016**, *35* (12), 1254–1275. https://doi.org/10.15252/embj.201593169.

(27) Hernández, H.; Robinson, C. V. Determining the Stoichiometry and Interactions of Macromolecular Assemblies from Mass Spectrometry. *Nat. Protoc.* **2007**, *2* (3), 715–726. https://doi.org/10.1038/nprot.2007.73.

(28) Vimer, S.; Ben-Nissan, G.; Sharon, M. Direct Characterization of Overproduced Proteins by Native Mass Spectrometry. *Nat. Protoc.* **2020**, *15* (2), 236–265. https://doi.org/10.1038/s41596-019-0233-8.

(29) Klarskov, K.; Roecklin, D.; Bouchon, B.; Sabatie, J.; Vandorsselaer, A.; Bischoff, R. Analysis of Recombinant Schistosoma Mansoni Antigen rSmp28 by On-Line Liquid

Chromatography-Mass Spectrometry Combined with Sodium Dodecyl Sulfate Polyacrylamide Gel Electrophoresis. *Anal. Biochem.* **1994**, *216* (1), 127–134. https://doi.org/10.1006/abio.1994.1016.

(30) Schuhmacher, M.; Glocker, M. O.; Wunderlin, M.; Przybylski, M. Direct Isolation of Proteins from Sodium Dodecyl Sulfate-Polyacrylamide Gel Electrophoresis and Analysis by Electrospray-Ionization Mass Spectrometry. *Electrophoresis* **1996**, *17* (5), 848–854. https://doi.org/10.1002/elps.1150170506.

(31) Begg, G. E.; Speicher, D. W. Mass Spectrometry Detection and Reduction of Disulfide Adducts between Reducing Agents and Recombinant Proteins with Highly Reactive Cysteines. *J. Biomol. Tech.* **1999**, *10* (1), 17–20.

(32) Giles, K.; Ujma, J.; Wildgoose, J.; Pringle, S.; Richardson, K.; Langridge, D.; Green, M. A Cyclic Ion Mobility-Mass Spectrometry System. *Anal. Chem.* **2019**, *91* (13), 8564–8573. https://doi.org/10.1021/acs.analchem.9b01838.

(33) Allen, S. J.; Giles, K.; Gilbert, T.; Bush, M. F. Ion Mobility Mass Spectrometry of Peptide, Protein, and Protein Complex Ions Using a Radio-Frequency Confining Drift Cell. *The Analyst* **2016**, *141* (3), 884–891. https://doi.org/10.1039/C5AN02107C.

(34) Davidson, K. L.; Oberreit, D. R.; Hogan, C. J.; Bush, M. F. Nonspecific Aggregation in Native Electrokinetic Nanoelectrospray Ionization. *Int. J. Mass Spectrom.* **2017**, *420*, 35–42. https://doi.org/10.1016/j.ijms.2016.09.013.

(35) Kranz, R. G.; Richard-Fogal, C.; Taylor, J.-S.; Frawley, E. R. Cytochrome *c* Biogenesis: Mechanisms for Covalent Modifications and Trafficking of Heme and for Heme-Iron Redox Control. *Microbiol. Mol. Biol. Rev.* **2009**, *73* (3), 510–528. https://doi.org/10.1128/MMBR.00001-09.

(36) He, F.; Hendrickson, C. L.; Marshall, A. G. Unequivocal Determination of Metal Atom Oxidation State in Naked Heme Proteins: Fe(III)Myoglobin, Fe(III)Cytochrome *c* , Fe(III)Cytochrome B5, and Fe(III)Cytochrome B5 L47R. *J. Am. Soc. Mass Spectrom.* **2000**, *11* (2), 120–126. https://doi.org/10.1016/S1044-0305(99)00132-4.

(37) Scigelova, M.; Green, P. S.; Giannakopulos, A. E.; Rodger, A.; Crout, D. H. G.; Derrick, P. J. A Practical Protocol for the Reduction of Disulfide Bonds in Proteins Prior to Analysis by Mass Spectrometry. *Eur. J. Mass Spectrom.* **2001**, *7* (1), 29–34. https://doi.org/10.1255/ejms.385.

(38) Raines, R. T. Ribonuclease A. *Chem. Rev.* **1998**, *98* (3), 1045–1066. https://doi.org/10.1021/cr960427h.

(39) Krężel, A.; Latajka, R.; Bujacz, G. D.; Bal, W. Coordination Properties of Tris(2-Carboxyethyl)Phosphine, a Newly Introduced Thiol Reductant, and Its Oxide. *Inorg. Chem.* **2003**, *42* (6), 1994–2003. https://doi.org/10.1021/ic025969y.

(40) Scopes, R. K. Stabilizing Factors for Enzymes. In *Protein Purification: Principles and Practice*; Springer Advanced Texts in Chemistry; Springer-Verlag, 1987; pp 246–252.

(41) Jocelyn, P. C. Chemical Reduction of Disulfides. In *Methods in Enzymology*; Academic Press, 1987; Vol. 143, pp 246–256.

(42) Margoliash, E. PRIMARY STRUCTURE AND EVOLUTION OF CYTOCHROME C. *Proc. Natl. Acad. Sci.* **1963**, *50* (4), 672–679. https://doi.org/10.1073/pnas.50.4.672.

(43) Benesch, J. L. P. Collisional Activation of Protein Complexes: Picking up the Pieces. *J. Am. Soc. Mass Spectrom.* **2009**, *20* (3), 341–348. https://doi.org/10.1016/j.jasms.2008.11.014.

(44) Guttman, M.; Wales, T. E.; Whittington, D.; Engen, J. R.; Brown, J. M.; Lee, K. K. Tuning a High Transmission Ion Guide to Prevent Gas-Phase Proton Exchange During H/D Exchange MS Analysis. *J. Am. Soc. Mass Spectrom.* **2016**, *27* (4), 662–668. https://doi.org/10.1007/s13361-015-1330-8.

(45) Kafader, J. O.; Melani, R. D.; Schachner, L. F.; Ives, A. N.; Patrie, S. M.; Kelleher, N. L.; Compton, P. D. Native vs Denatured: An in Depth Investigation of Charge State and Isotope Distributions. *J. Am. Soc. Mass Spectrom.* **2020**, *31* (3), 574–581. https://doi.org/10.1021/jasms.9b00040.

(46) Li, Y.; Cole, R. Shifts in Peptide and Protein Charge State Distributions with Varying Spray Tip Orifice Diameter in Nanoelectrospray Fourier Transform Ion Cycltron Resonance Mass Spectrometry. *Anal. Chem.* **2003**, *75* (21), 5739–5746. https://doi.org/10.1021/ac0301402.

(47) Benesch, J. L. P.; Ruotolo, B. T.; Sobott, F.; Wildgoose, J.; Gilbert, A.; Bateman, R.; Robinson, C. V. Quadrupole-Time-of-Flight Mass Spectrometer Modified for Higher-Energy Dissociation Reduces Protein Assemblies to Peptide Fragments. *Anal. Chem.* **2009**, *81* (3), 1270–1274. https://doi.org/10.1021/ac801950u.

(48) Han, Z.; Chen, L. C. High-Pressure nanoESI of Highly Conductive Volatile and Non-Volatile Buffer Solutions from a Large Taylor Cone: Effect of Spray Current on Charge State Distribution. *Int. J. Mass Spectrom.* **2022**, *476*, 116845. https://doi.org/10.1016/j.ijms.2022.116845.

(49) Song, Y.; Cai, H.; Tan, Z.; Mussa, N.; Li, Z.-J. Mechanistic Insights into Inter-Chain Disulfide Bond Reduction of IgG1 and IgG4 Antibodies. *Appl. Microbiol. Biotechnol.* **2022**, *106* (3), 1057–1066. https://doi.org/10.1007/s00253-022-11778-5.

# Chapter 4. Real-Time Disulfide Bond Reduction using Programmed-Temperature Electrospray Ionization (ptESI)

## 1 Introduction

As touched on in Chapter 3, disulfide bonding is an important aspect of higher order protein structure. Cysteine, though one of the least abundant amino acids in proteins, is highly conserved and is often present in functional sites.[1] Cysteine can be post-translationally modified to form disulfide bonds with other cysteines or sulfur-containing molecules, like heme. The formation of a disulfide bond is an oxidation process that converts two free sulfhydryl groups to an S-S linkage, releasing two electrons. Disulfide bonds contribute to proper protein folding, stabilize tertiary and quaternary structure, and can confer functional redox sensitivity.[1–5] Cleavage can lead to collapse of native structures while improper bond formation can lead to aggregation.[2] Genetic substitution of cysteine residues[6] or improper disulfide formation is linked to diseases like prion diseases, ALS, cancer, Parkinson's, and HIV.[4]

Monoclonal antibodies (mAbs) are proteins of particular interest due to their enabling role in a growing class of biotherapeutics.[7,8] All currently approved therapeutics have been developed based on Immunglobulin gamma (IgG), primarily IgG1, IgG2, and IgG4.[9] IgG1 and IgG4 consist of two heavy and two light chains held together by disulfide bonds: two in the hinge region binding heavy chains together and one in each arm binding light and heavy chains together.[10] They also possess 12 additional intrachain disulfide bonds.[10] For safety and efficacy, it is imperative to characterize the disulfide linkages present in these therapeutics and to maintain strict quality control in long term production.[11] Wild-type IgG4 has the propensity to form half-mAbs (HL pairs) and bispecific mAbs. Bispecific mAbs form by fab-arm exchange (FAE), in

which two half-mAbs from different IgG4s come together to form an IgG4 with two different antigen binding regions.[12] The hinge region of IgG1 mAbs contain the amino acid motif CPPC, and the two proline residues provide enough steric hindrance to prevent the facile formation of intra-heavy chain disulfide bonds in place of the interchain disulfide bonds that link the half mAbs together.[10,13] IgG4 mAbs instead possesses a CPSC sequence in the hinge region, resulting in more labile disulfide bonds and imparting an intrachain/interchain equilibrium.[10,13,14] R409 also weakens noncovalent interactions in the CH3 (third constant heavy domain) region contributing to this phenomenon.[15] For biotherapeutic development, bispecificity can be useful, but the hinge amino acids of IgG4 can also be mutated to provide stability and prevent unwanted aggregation, disassembly, or arm exchange.[16,17]

Disulfide bond reduction is a common laboratory procedure used for mass spectrometric analyses of proteins as well as for protein folding/unfolding studies,[18,19] as suggested in Chapter 3. It is also commonly performed for SDS-PAGE[20] and Western blotting[21] procedures for protein analysis. For mAb characterization, disulfide bonds are reduced for primary sequence analysis and intact mass analysis of light and heavy chains.[22,23] Disulfide bond reduction is most often performed by the addition of reducing agents like β-mercaptoethanol (βME), dithiothreitol (DTT), and tris(2-carboxyethyl)phosphine (TCEP).[18,24,25] Glutathione has also been used as a mild reducing agent to induce FAE *in vitro*.[26] Studies have revealed differential susceptibility of disulfide bonds of IgG1 to reduction, as well as differences in the susceptibility based on the type of light chain incorporated in the molecules.[27–29] Additionally, studies have shown that IgG1 and IgG4 molecules, despite their high sequence similarity and equivalent number of disulfide bonds, respond differently to the addition of reducing agents; the order in which disulfide bonds are

reduced with increasing reducing agent concentration, as monitored by capillary electrophoresis, can be related to differences in disulfide bond connectivity, solvent accessibility, and lability.[30]

Chromatography, capillary electrophoresis, and mass spectrometry-based methods are commonly used for antibody characterization.[31–33] Ion mobility-mass spectrometry (IM-MS) methods are also gaining interest as a number of studies have shown their utility for intact, higher order structural assessments.[34–38] Time-resolved experiments have been used to determine equilibrium constants for the formation of half-mAbs and to monitor FAE kinetics.[39–41] As mentioned previously, the introduction of different concentrations of reducing agents has been used to investigate the disulfide bond reduction pathways for different antibodies with capillary electrophoresis, gel electrophoresis, or LC-MS.[27,28,30] The implementation of time-dependent studies can help reduce sample preparation needs.[29] Online or in-source electrochemical reduction in combination with LC-MS or IM-MS also show promise for more rapid analyses;[22,42–46] however, progressive reduction has not been achieved in all cases. The investigator may need to adjust the capillary voltage or electrochemical potential and perform separate acquisitions. Additionally, electrochemical processes can alter solution pH in ESI[47] or produce gases that affect ESI spray stability.[45] And the range of applicable capillary voltages can be affected by the ESI tip size.[48] In nanoESI, high voltages can result in discharge and damage to borosilicate capillary tips, preventing further analyses.[48]

Temperature-controlled ESI sources have been used to set the temperature of samples in the ESI capillary and probe the stability of noncovalent complexes via MS.[49] Variable-temperature ESI (vtESI) has been used to investigate unfolding and disassembly of protein complexes in mixtures and cell lysates,[50] the transition state thermochemistry of IgG antibodies,[51] and more.[52,53] The majority of vtESI sources use resistive heating or thermoelectric

devices, and experiments are usually performed in a stepped-temperature mode, in which incubation is performed at selected temperatures and spectra are acquired after each incubation.[53–59] Two more rapid vtESI sources have been demonstrated. One uses a $CO_2$ laser to heat the tips of sample capillaries, and the temperature is indirectly estimated.[60] The other is a segmented source that has been used to "temperature-jump" flowing samples.[61]

Here, we introduce a programmed-temperature, electrospray ionization (ptESI) source capable of rapid temperature cycling with high fidelity between the solution temperature and the programmed temperature, and we apply it to monitor disulfide bond reduction of proteins in real time via MS. With the addition of DTT just prior to analysis, controlled temperature application, akin to benchtop incubation, allows the disulfide bond reduction reactions to proceed while mass spectra are collected. Reactions performed in small volumes or microdroplets increase the speed with which antibody structural characterization can be performed, and the introduction of enzymes and reducing agents to electrospray solutions has been performed previously.[62] We propose that the addition of real-time monitoring will allow unique insights into reduction pathways and aid in antibody differentiation. We first apply this technique to Ribonuclease A (RbA), a small protein with four disulfide bonds. Following demonstration with RbA, we apply the approach to four different IgG antibodies to investigate the potential to rapidly differentiate these large proteins by their reduction profiles.

## 2 Methods

### 2.1 Sample Preparation and Ion Mobility-Mass Spectrometry

Ribonuclease A (bovine pancreas, R6513) and dithiothreitol (D0632) were purchased from Sigma-Aldrich (St. Louis, MO). Samples of polyclonal IgG1$\kappa$ and IgG4$\kappa$ (product/lot numbers: I5154/SLCB8124 and I4639/SLBR4231V, respectively) from human myeloma and

Silu Lite SigmaMAb K4 Universal Antibody Standard Human (MSQC14), an IgG4κ mAb, were also purchased from Sigma-Aldrich. Samples of NIST IgG1κ monoclonal antibody (NISTmAb, RM 8671) were a gift from Associate Professor Miklos Guttman (University of Washington). The RbA stock solution was prepared at 100 μM in aqueous 200 mM ammonium acetate at pH 7 and buffer exchanged (final concentration 50 μM) into fresh aqueous ammonium acetate using Micro Bio-Spin 6 columns (Bio-Rad, Hercules, CA) in order to desalt. DTT was prepared at a stock concentration of 20 mM in aqueous 200 mM ammonium acetate at pH 7. The final concentration of RbA was 10 μM and the final concentration of DTT was 5 mM in solutions subjected to IM-MS analysis.

All antibody samples were also buffer exchanged into aqueous 200 mM ammonium acetate using Micro Bio-Spin 6 columns. Aliquots of polyclonal IgG1$\kappa$ and IgG4$\kappa$ (1 mg $mL^{-1}$) were buffer-exchanged from a storage solution of aqueous 20 mM tris-buffered saline, pH 8. The final concentration of polyclonal IgG1$\kappa$ or IgG4$\kappa$ was ~3 μM in solutions analyzed by MS. Aliquots of NISTmAb (10 mg $mL^{-1}$) were buffer-exchanged from a storage solution of aqueous 6 mM L-histidine, 12.5 mM L-histidine HCl at pH 6.0. The final concentration of NISTmAb was ~8 μM in solutions analyzed by MS. SigmaMAb K4 was received as a lyophilized powder and was dissolved in 200 mM ammonium acetate at pH 7 to a concentration of 1.25 mg $mL^{-1}$. It was desalted by buffer-exchanging into fresh aqueous ammonium acetate. The final concentration of SigmaMAb K4 was ~4 μM in solutions analyzed by MS.

Antibody samples were aliquoted into 5 uL portions for analysis. 0.5 μL of cold 20 mM DTT was added to a 5 uL antibody sample (final concentration of ~2 mM). The sample was mixed using a cold syringe, and the solution was loaded into a borosilicate glass capillary (1.00 mm O.D., 0.78 mm I.D.) that was pulled to a 1-3 μm tip (Sutter Instruments P-97), then

immediately inserted into the ptESI source held at 10 °C. A platinum wire was used to make electrical contact with the solution for electrokinetic ESI.[48] A temperature gradient of ±30 °C $min^{-1}$ gradient from 10 to 90 to 25 °C was used for disulfide bond reduction of RbA. Programs tested with peak temperatures of 75 °C were insufficient to instigate bond reduction, even with a slower gradient (±15 ° C $min^{-1}$). A temperature gradient of ±9 °C $min^{-1}$ from 10 to 65 to 25 °C was chosen for disulfide bond reduction of antibodies, which took ~11 minutes. Faster gradients, ±15 ° C $min^{-1}$ and ±30 °C $min^{-1}$, also resulted in disulfide bond reduction, but slower gradients improved the temperature resolution.

Ion mobility–mass spectrometry experiments were performed on a Waters SELECT SERIES Cyclic IMS system.[63] Ion mobility data was not collected during antibody experiments due to low signal intensity. Ion mobility arrival time distributions of RbA were measured using the traveling wave cyclic ion mobility cell filled with 2 mBar nitrogen. All mobility experiments were performed on the same day. Driftscope v2.8 was used to extract ion mobility data, and all arrival time distributions were normalized to an integral of 1.

## 3 Results and Discussion

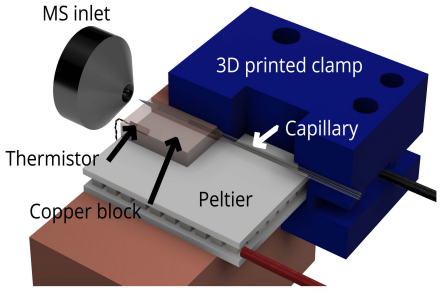


**Figure 3.1**. Render of the programmed-temperature, electrospray ionization (ptESI) source.

### 3.1 Programmed-Temperature, Nanoelectrospray Ionization (ptESI)

The home-built ptESI source (Figure 3.1) consists of a copper block, into which the sample capillary is inserted, a thermoelectric device (Peltier) to heat and cool the copper block, a thermistor to measure the temperature of the copper block, and a 3D-printed clamp to maximize thermal conductivity between the copper block and the Peltier. The Peltier is interfaced with a bipolar temperature controller. To characterize the performance of this source, we used three different temperatures: the *programmed temperature* (the set point for the Peltier temperature controller), the *block temperature* (the measured temperature of the copper block that holds the sample capillary), and the *solution temperature* (the measured temperature of the solution inside the capillary). For characterization experiments, the solution temperature was measured using a microscale thermocouple inserted into a sample capillary containing an aqueous ammonium acetate solution.

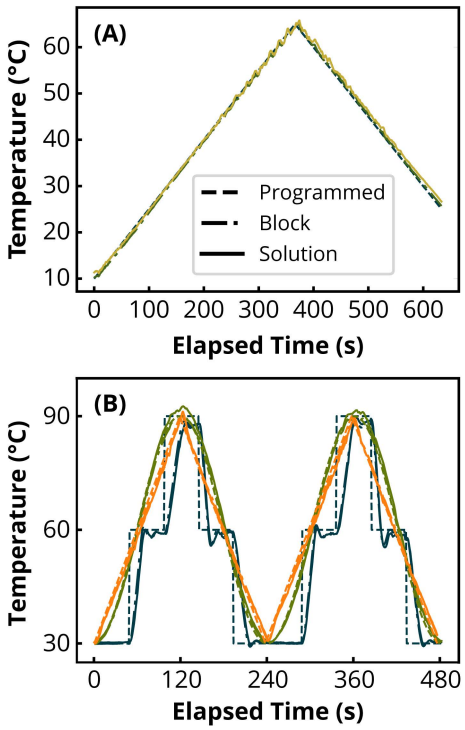


**Figure 3.2**. Comparison of programmed, block, and solution temperatures over the course of three different temperature program profiles. Block temperatures

were measured using a thermistor inserted into the copper block, and solution temperatures were measured using a thermocouple inside the sample capillary. Block and solution temperatures were logged simultaneously for characterization of the source. The ramp rate of the saw tooth program (orange) was ±30 °C $min^{-1}$.

Figure 3.2A shows a comparison of programmed, block, and solution temperatures for the temperature cycle used for antibody characterization (±9 °C $min^{-1}$ from 10 to 65 to 25 °C), and Figure 3.2B shows a similar comparison for three different temperature profiles. For all four programs, the solution temperature was very similar to the block temperature. This high fidelity suggests that there is high thermal conductivity between the copper block and the sample capillary and that the copper block temperature is a good proxy for the sample temperature during thermal cycling experiments. Thermal contact between the copper block and the Peltier was achieved by the application of thermal paste and the 3D-printed clamp. The low thermal mass of the copper block also helped maximize the thermal conductivity between the copper block and the Peltier. The snug fit of the sample capillary within the copper block helped maximize heat transfer between the block and the solution as well. These three design elements contribute to the excellent agreement between the programmed, block, and solution temperatures.

Figure 3.3 shows the solution temperature measured as a function of the applied gradient. For all temperature gradients, the solution temperature was also very similar to the block temperature. For gradients up to +30 °C $min^{-1}$, the solution temperature and the block temperature exhibited a systematic lag of a couple seconds behind the programmed temperature, and for the most rapid gradients, larger differences were observed between the programmed

temperature and the solution/block temperature, especially at peak temperatures. This is primarily attributed to insufficient power delivery to the Peltier. The maximum power in this prototype version of the ptESI source was limited by the maximum current of the power supply (3 amps), not by the limits of the Peltier (8 amps) or the temperature controller (20 amps). Second generation designs are in-process to improve on the current implementation and expand the compatibility of the source with instruments of different manufacturers. These characterization experiments indicate that the ptESI source can change sample temperatures with gradients of at least ±30 °C·min$^{-1}$, which is more rapidly than other temperature-controlled ESI sources.

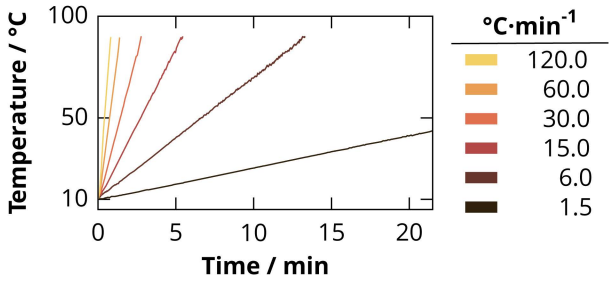


**Figure 3.3**. Solution temperatures measured during selected temperature programs using a thermocouple inside the sample capillary. (A) Solution temperatures measured using temperature gradients as indicated. (B) Three complete cycles of a modified sawtooth function that has a gradient of ±30 °C·min$^{-1}$ (ptESI, *blue*), and for comparison, a program with 7 steps that mimics a vtESI experiment (*green*).

### 3.2 Real–Time Disulfide Bond Reduction of Ribonuclease A

RbA was chosen as a test case for this method because its disulfide bond reduction is well-studied.[64] RbA is also low in mass and able to be isotopically resolved to confirm the reduction of all four disulfide bonds. No disulfide bond reduction was observed following sample capillary loading and handling at room temperature. Figure 3.4 shows selected spectra from the temperature cycle with 5 mM DTT. DTT was chosen based on results from previous experiments (Ch. 3). βME was also tested, but covalent modifications to the protein were observed. The bond reduction of RbA doesn't become evident until the peak of the cycle at 90 °C, and RbA becomes fully reduced near the end of the cycle at 35 °C.

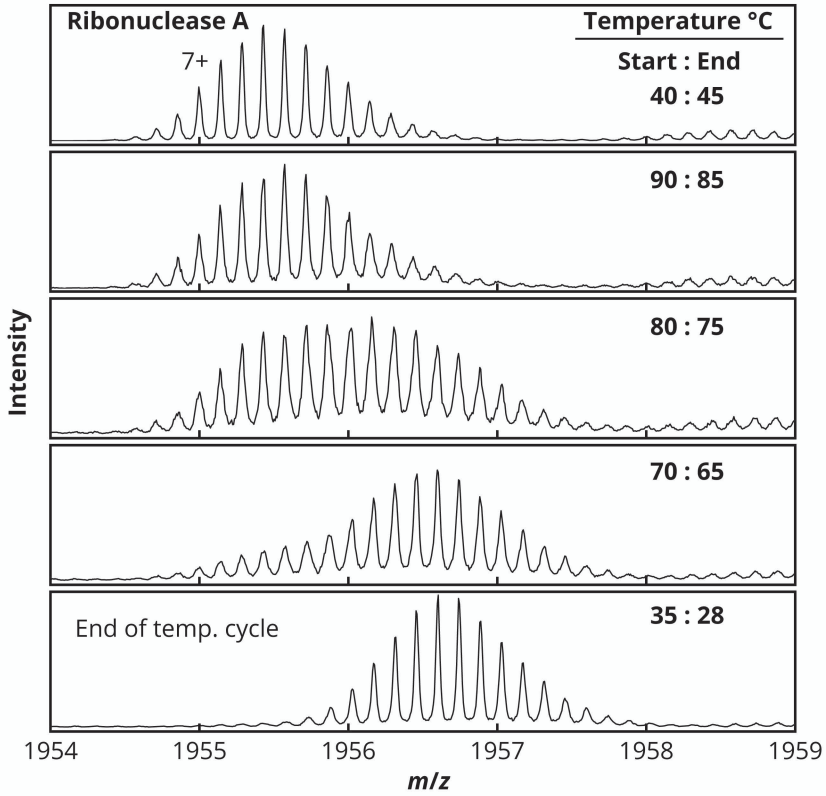


**Figure 3.4**. Selected spectra of the 7+ species from a ±30 °C $min^{-1}$ temperature cycle of Ribonuclease A (RbA) with 5 mM DTT. Start and end temperatures indicate the range of temperatures over which mass spectra were signal-averaged. The onset of bond reduction occurs at 90 °C and reduction of all four disulfide

bonds is complete by ~35 °C. The shift in isotope distribution corresponds to the addition of 8H.

Figure 3.5 shows representative IM arrival time distributions of 7+ RbA over the course of the temperature cycle. Small shifts towards longer arrival times begin to occur during heating starting at 70 °C. By 85-90 °C, a second peak is observed at significantly longer arrival times. In the mass spectra, shifts aren't observed until between 90 and 85 °C during the temperature cycle's cooling phase, but the IM data suggests that reduction is preceded by slight unfolding at a lower temperature. The appearance of the second arrival time peak likely reflects the onset of disulfide bond reduction. As more of the 7+ RbA population experiences reduction during the cooling phase, the second arrival time peak becomes more populated, indicating unfolding. At 40 to 35 °C, the majority of the 7+ population exhibits longer arrival times, but there is still a small population that is more compact. The same temperature cycle was also performed on RbA in the absence of reduction agents, and the corresponding MS data are shown in Appendix C (Figure C1).

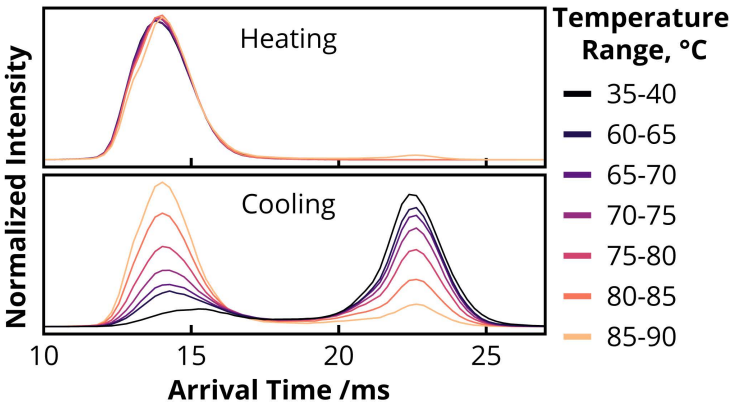

**Figure 3.5**. Representative IM arrival time distributions of 7+ RbA during a ±30 °C $min^{-1}$ temperature cycle with 5 mM DTT. Arrival time distributions exhibited during (A) heating and (B) cooling.

### 3.3 Real–Time Disulfide Bond Reduction of Antibodies

Antibodies were found to be susceptible to disulfide-bond reduction at room temperature, so samples were kept cold during DTT addition and tip loading using an insulated container and chilled beads. A control experiment was performed in which a NISTmAb sample was held at 10 °C for 15 minutes; the low temperature didn't stop bond reduction entirely, but it effectively slowed down reduction prior to temperature cycling (Figure C2). All samples were also subjected to a temperature cycle (identical to that used for disulfide reduction) in the absence of reducing agents (Figures C3-C6). Figure 3.6 shows potential pathways and products for disulfide bond reduction of the interchain disulfide bonds of IgG antibodies. For the remainder of this discussion light chain will be referred to as L, heavy chain will be referred to as H, half molecules will be referred to as HL, and other products will be referred to similarly.

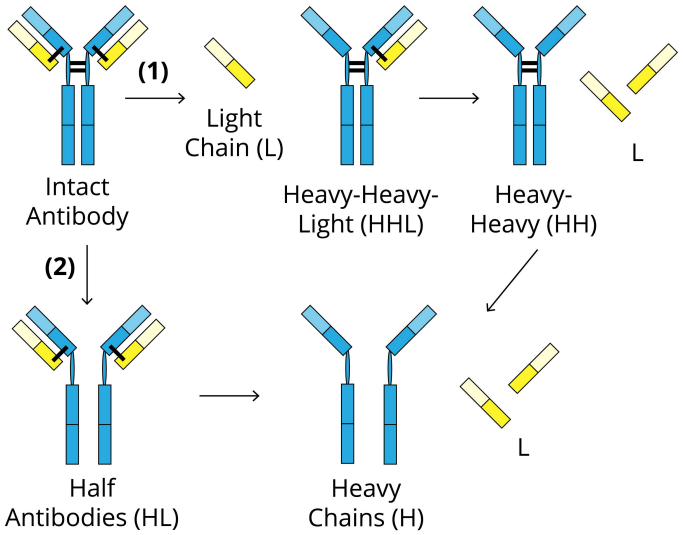


**Figure 3.6**. Reduction products of IgG antibodies. Complete reduction of interchain disulfide bonds will result in freed intact heavy (H) and light chains (L). Pathway (1) occurs if the disulfide bonds between the heavy and light chains are preferentially reduced. Pathway (2) occurs if the disulfide bonds between heavy chains (hinge region) are preferentially reduced. The relative abundances of the reduction products can be used to determine whether one pathway is dominant for a particular antibody.

Studies have suggested that IgG1 antibodies tend to experience pathway (1) as the dominant reduction pathway, in which the disulfide bonds between L and H chains are reduced first,[28,30] whereas wild-type IgG4 antibodies tend to experience pathway (2) as the dominant reduction pathway, in which hinge disulfide bonds are reduced first.[30] Therapeutic IgG4 antibodies with hinge stabilization were suggested to undergo a more hybrid pathway, with hinge disulfide reduction as the primary pathway and L-H bond reduction as the secondary pathway.[30]

### 3.3.1 Monoclonal Antibodies

Monoclonal antibodies are produced from a single line of cells in a laboratory, so within a sample, the antigen-binding regions, and other aspects of structure, should be the same. NISTmAb is a recombinant humanized IgG1κ monoclonal antibody standard, and SigmaMAb K4 is a recombinant humanized IgG4κ monoclonal antibody standard. Both are well-characterized in terms of primary sequence, disulfide bonding, and glycosylation. Figure 3.7 shows NISTmAb mass spectra at various points in a temperature program with DTT. The first reduction products appear simultaneously in the temperature cycle of NISTmAb. HL and L products are present at low intensities even at 10 °C. Evidence for HH or HHL (loss of two light chains) products are also present at the beginning of the cycle; they overlap with the highest charge states of the intact mAb. The peaks are broad and of low intensity, and are no longer evident by ~40 °C. No additional peaks corresponding to these products become resolved during the cycle. Fragments close to 50 kDa in mass were observed in spectra of NISTmAb, SigmaMAb K4, and polyclonal IgG1$\kappa$ in the absence of reducing agents, but these fragments do not likely correspond to intact heavy chains. For example, NISTmAb is expected to have abundant heavy chain populations with G0F or G1F glycosylation, corresponding to average masses of ~50,907 and 51,069 Da, respectively, including pyroglutamic acid and lysine clipping modifications.[65] The masses determined from the most abundant fragment peaks of NISTmAb are ~47,043 Da, 47,145 Da, 47,259 Da, and 47,628 Da. These fragments will be referred to as H-like fragments.

Both L and HL products increased in intensity gradually until, between 47-50 °C, they begin to increase in intensity more steeply. From 45 to 65 °C, the intensities of these two products were in competition. At the onset of the cycle's descent, the HL product became dominant and remains the most intense product until the end of the cycle. Higher charge states of all species were observed, with maximum intensity occurring during the peak of the cycle

between 45 °C and 45 °C. High charge states of HL and H were still present at low intensity post-cycle, even after cooling to 10 °C. Sufficient resolution of the isotopic distributions was not achieved for antibodies in these experiments, so the occurrence of intrachain disulfide bond reduction cannot be confirmed. Partly due to spectral congestion, peaks corresponding to H do not become apparent until later in the cycle, when higher charge states are formed. Glycoforms are resolved for these H peaks (Figure C7). During the cycle's descent, between 55 and 40 °C, the signal for HL overtakes that of the intact NISTmAb as well.

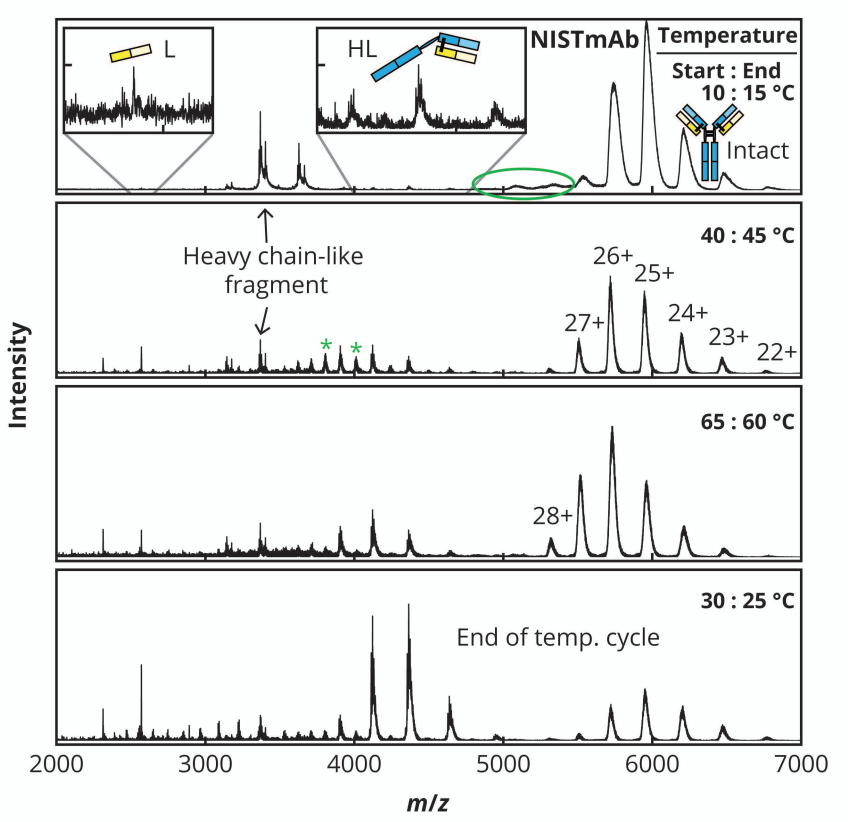


**Figure 3.7**. Selected spectra from a ±9 °C $min^{-1}$ temperature cycle of NISTmAb with 2 mM DTT. The y-axis absolute intensity maxima are the same for all four plots so that differences in intensity over the course of the temperature cycle can be appreciated. Insets at 10-15 °C show the presence of L (x50 zoom) and HL (x25 zoom) at the beginning of the cycle. The H-like fragment decreases in

intensity slightly over the course of a cycle. The *green circle* highlights a region in which there is overlap with intact mAb; these peaks could represent HH or HHL chains, but the low intensity and poor resolution prevents extensive characterization. These products are also short-lived. The *green asterisks* highlight peaks that could suggest additional fragmentation pathways beyond disulfide bond reduction; they are similar in mass to HL, but they do not line up with the expected intact mass of NISTmAb. H products are observed at low intensity lower *m*/*z* (to the left of L). H-products aren't highlighted here.

SigmaMAb K4 displayed a significantly different disulfide bond reduction pattern than NISTmAb. The hinge region of SigmaMAb K4 contains a single amino acid S to P mutation to add stability relative to wild-type IgG4 antibodies and prevent HL formation.[17] Figure 3.8 shows SigmaMAb K4 mass spectra at various points in the temperature program with DTT. During the temperature cycle in the presence of DTT, very minimal amounts of HL were detected. The primary observed product was L, which was even present after a temperature cycle in the absence of DTT. The expected mass of the freed light chain with intact intrachain disulfide bonds is ~23,254 Da, and the experimental mass was 23,253.6 Da. There are additional high intensity species present in the L region of the mass spectra which diminish over the course of the cycle, but they represent the dominant peaks until ~40 °C (Figure C8). The additional species have experimental masses of 23,272 and 23,561 Da. These may represent modifications of L or fragments, potentially of H. Similar species were not observed during the reduction of NISTmAb. The L population of SigmaMAb K4 increased steadily over the course of the temperature cycle, overtaking the intact mAb by the top of the cycle at 65 °C. The H-like

fragment was also observed to decrease in intensity over the course of a cycle, similar to NISTmAb. Intact H was present in the spectra but overlapped with the H-like fragment and was poorly resolved. HH and HHL products were not observed. Unlike NISTmAb, only minor shifts in the average charge state of the products were observed over the course of the temperature cycle, and no highly charged H products were detected.

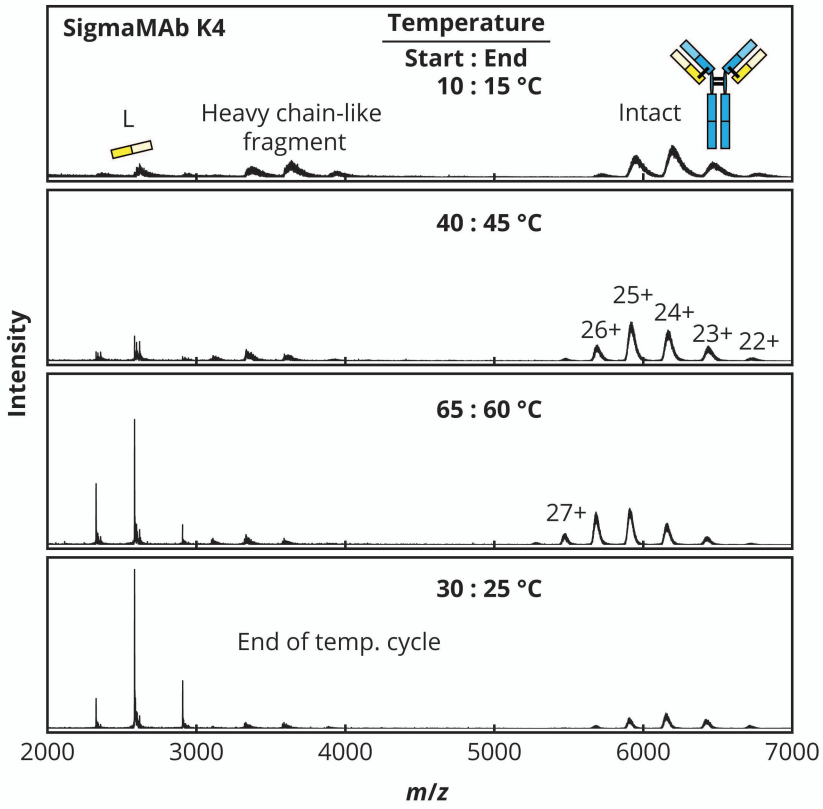


**Figure 3.8**. Selected spectra from a ±9 °C $min^{-1}$ temperature cycle of SigmaMAb K4 with 2 mM DTT. The y-axis absolute intensity maxima are the same for all four plots so that differences in intensity over the course of the temperature cycle can be appreciated. A heavy chain-like fragment is present in this antibody sample as well, and its intensity decreases only slightly over the course of the temperature cycle. The light chain (L) is the only observed reduction product.

The pathways of reduction of these two antibodies were clearly different, and they could easily be distinguished from each other. The hinge amino acid sequences and lengths of NISTmAb and SigmaMAb K4 differ (*EPKSCDKTHTCPPCP* and *ESKYGPPCPPCP*, respectively) as well as the connectivity of their disulfide bonds.[66,67] The stabilization of the hinge region of SigmaMAb IgG4, and the decreased flexibility of the hinge compared to IgG1 antibodies, likely contributed to these results.[68] Because of the absence of HL products from the SigmaMAb IgG4 spectra, it is likely that the L-H bond was reduced first, whereas NISTmAb may have experienced a hybrid or sequential pathway in which L-H and hinge bond reduction happened on a similar timescale. The absence of HHL fragments from the spectra is discussed in section 3.3.3.

### 3.3.2 Polyclonal Antibodies

Polyclonal antibodies are produced from different lines of cells in response to the same antigen. Antibodies within a sample may differ in terms of their antigen-binding region, as well as other aspects of their structure. Both IgG1κ and IgG4κ were purified from human plasma and documentation only verifies a single subclass and light chain type. These two samples are more heterogenous than the monoclonal standards discussed above. L and H sequences are not documented, and neither are glycoforms types or abundances.

IgG1κ followed a similar disulfide bond reduction pattern to NISTmAb (Figure 3.9). Again, broad, low-intensity peaks were observed overlapping with the intact antibody at the beginning of the cycle. They also diminished by ~40 °C. HL and L reduction products arose simultaneously, but they were not present at the beginning of the cycle. Intensities of these products grew very slowly, and appreciable intensity wasn't observed until 47-50 °C. At ~ 55 °C, the intensities of L and HL began rising more quickly. The intensities of the HL peaks didn't

exceed those of the intact IgG1κ until ~30 °C in the temperature cycle's descent, and the intensity of the L never exceeded that of the HL. Two L peaks are present throughout the cycle corresponding to masses of 23,420 and 23,580 Da. H peaks are not well resolved throughout the cycle, but there is some evidence for them at the end of the cycle. H-like fragments decrease in intensity slightly over the duration of the cycle.

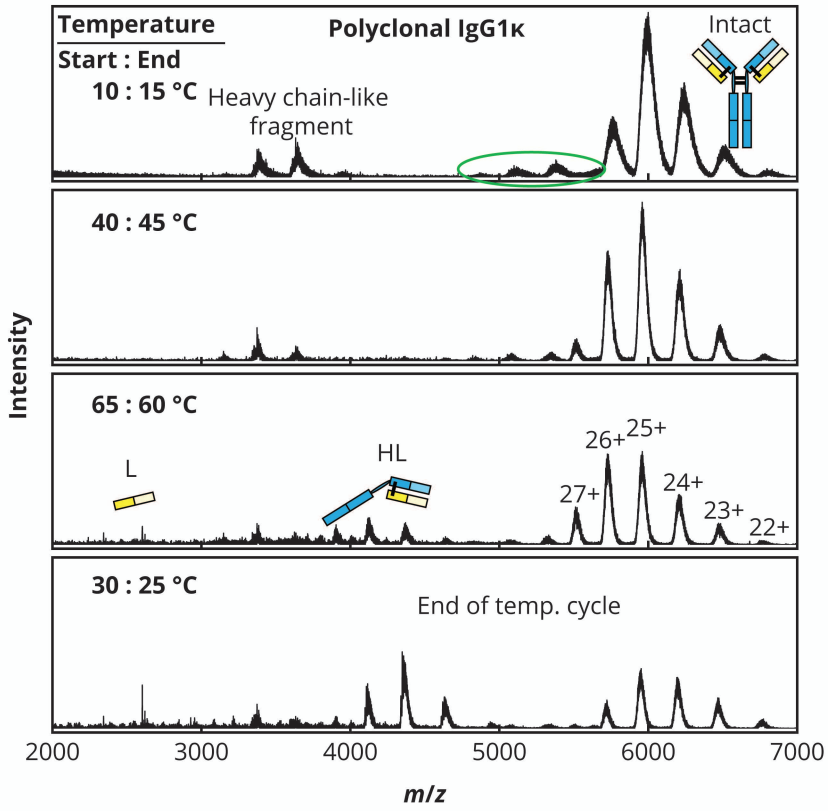


**Figure 3.9**. Selected spectra from a ±9 °C $min^{-1}$ temperature cycle of IgG1κ from human myeloma with 2 mM DTT. The y-axis absolute intensity maxima are the same for all four plots so that differences in intensity over the course of the temperature cycle can be appreciated. H-like fragments are present in this sample as well. The *green circle* highlights a region in which there is overlap of fragments with the intact antibody peaks. The low intensity prevents extensive characterization of these short-lived products. The L and HL products don't

appear until around 47 °C and rise in intensity during the temperature cycle's descent.

The polyclonal IgG4κ sample was the most heterogeneous of the antibody samples within this study. At least two distinct populations of HL species were observed in the spectra in the absence of reducing agent (Figure C6). This is not surprising given previous work in which CAPTR resolved multiple populations of antibodies within this sample (Ch. 2). These are also wild-type IgG4 antibodies, which are known to undergo half molecule formation.[12] At the beginning of the temperature cycle with DTT, peaks corresponding to HL are already present in the spectra of IgG4κ, and the intact antibody peaks are particularly poorly resolved compared to spectra collected in the absence of reducing agents (Figure 3.10). L peaks are also present at the beginning of the cycle, though at a much lower intensity. By 40°C, the L peaks exceeded the intensity of the HL peaks. Both products rose in intensity, with the HL exceeding that of the L again (40-45 °C), and then as reduction proceeded, the L peaks became the dominant peaks in the spectra by 60 °C. Only one population of L is evident with a mass of 23,659 Da. H, or smaller H fragments, are likely present by 55 °C, though it is difficult to distinguish contributions from more highly charged HL and to determine how many populations of H are present. HH and HHL peaks were not observed over the duration of a cycle.

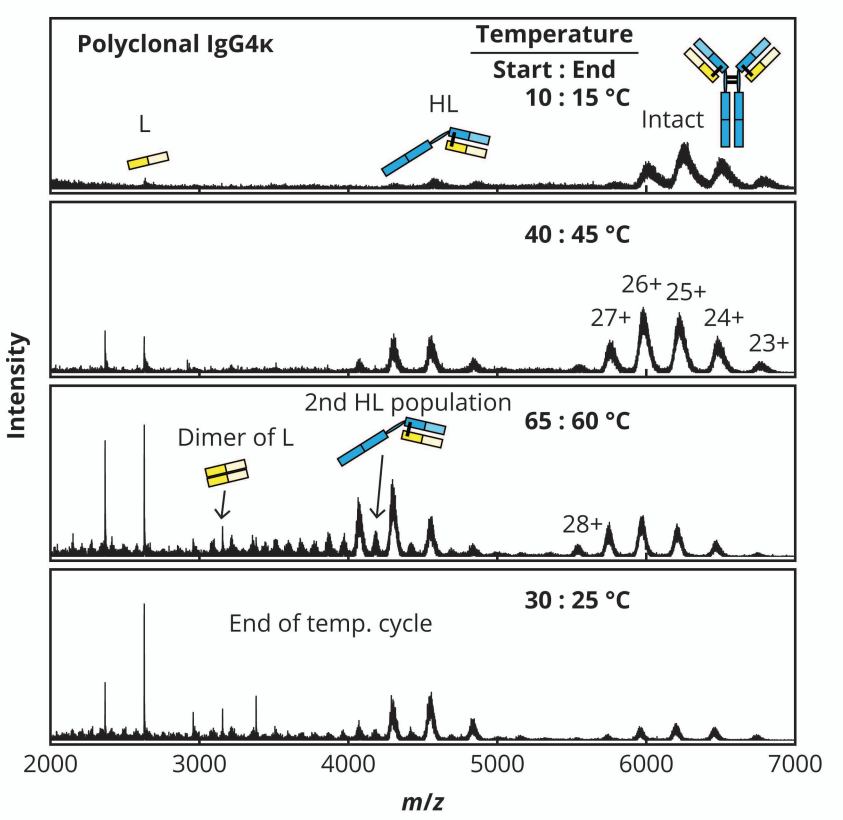


**Figure 3.10**. Selected spectra from a ±9 °C $min^{-1}$ temperature cycle of IgG4κ from human myeloma with 2 mM DTT. The y-axis absolute intensity maxima are the same for all four plots so that differences in intensity over the course of the temperature cycle can be appreciated. No heavy chain-like fragment is present in this sample. The light chain (L) and half antibody (HL) products are observed at the beginning of the cycle. Two populations of half antibody (HL) products were resolved with masses of ~77,471 and 79,493 Da (glycoforms were not well resolved). These align reasonably well with the determined intact IgG4κ masses of 155.6 and 158.9 kDa from a previous study utilizing charge reduction (Ch. 2). Nonspecific dimerization of L is observed later in the temperature cycle.

### 3.3.3 Discussion of All Antibody Samples

As suggested previously, all antibodies were also subjected to temperature cycles in the absence of DTT. Shifts in average charge state were observed over the duration of cycles, but the mass spectra collected at 10 °C before and after a cycle were not significantly different for NISTmAb or polyclonal IgG1$\kappa$ (Figures C4 and C6). For these samples, no bond reduction was attributable to temperature cycling in the absence of reducing agents. SigmaMAb K4 and IgG4$\kappa$ were particularly susceptible to disulfide bond reduction; a slight increase in freed light chain was observed for SigmaMAb K4 (Figure C4) and a slight increase in half molecule was observed for polyclonal IgG4 after heating in the absence of reducing agents (Figure C6). All intact antibody peaks are significantly broader at the beginning of temperature cycles in the presence of DTT; this may be due to the presence of HH or HHL products that are poorly resolved from the intact antibody. Incomplete desolvation at 10 °C is another potential source of this peak broadening; it is unclear whether DTT has an effect on the desolvation process at low temperatures.

Fragments similar in mass to H products were observed in the spectra of NISTmAb, SigmaMAb K4, and polyclonal IgG1$\kappa$ in the absence of reducing agents. Studies have shown that hinge fragmentation can occur during storage of mAbs, specifically nonenzymatic cleavage of the upper hinge region of heavy chains.[69,70] Cleavages of this nature result in Fab arm fragments comprised of an intact light chain connected to a heavy chain fragment.[69] Predicted masses for these fragments are of similar mass to the fragments observed in the present study. Similar fragments have also been observed in other MS studies of intact mAbs, though they've not been a subject of discussion.[51,71] The fragments observed in the present study decreased in intensity slightly over the course of the temperature cycles, but evidence for a corresponding H fragment was not observed.

All of the antibody samples could be distinguished by real-time disulfide bond reduction. Reduction performed in this manner also gives unique insights into the reduction pathways of each antibody. Comparing the IgG1 antibodies, despite the similarity of the spectra at certain points in the cycle (65-60 °C, Figures 3.7 and 3.9), NISTmAb appeared to be more susceptible to disulfide bond reduction with 2 mM DTT. The intensities of the L and HL products relative to the intact NISTmAb were higher at a lower temperature compared to the polyclonal IgG1κ antibody products relative to its intact form. This can even be seen at the beginning of the cycle at 10 °C. Additionally, more of the intact NISTmAb was depleted by the end of the cycle at 25 °C. The HL and L products appear simultaneously, and, at the end of the cycle, the HL products are more abundant than the L products for both NISTmAb and polyclonal IgG1. This was surprising compared to results from other studies that suggest that the L-H disulfide bond is more easily reduced.[28,30] Interestingly, an experiment on a different day, with a more rapid temperature cycle (15 °C $min^{-1}$), showed clear resolution of the HH product of NISTmAb and higher intensities of the H product with lower charge (Figure C9). This was not observed in any other experiments, but the results provide evidence that HH and H are able to be ionized and detected following reaction in the sample capillary. These results are discussed more in Appendix C. Based on the combined results, we hypothesize that there may have been difficulty detecting HHL species, which were also absent in IgG4 spectra. Thermal cycling experiments using temperature-controlled ESI and MS have been performed on another IgG1κ standard, and the investigators hypothesized that the HHL product aggregated, preventing its detection.[51] We observed no significant disruption to spray stability, but this is one possibility for the absence of HHL from the spectra. If aggregation of HHL were to occur, this could bias the L and HL relative populations because the L of the HHL aggregate would no longer be available for reduction or

detection. It is also possible that the HHL product rapidly reduced and dissociated to form H and HL populations in these experiments, suggesting a sequential reduction pathway. It is possible that once one L-H disulfide bond is reduced, hinge reduction occurs before the second L-H bond is reduced. Earlier in the temperature cycles the HL and L populations are more similar before the HL population increases beyond that of the L.

The IgG4 antibodies were more easily differentiable by reduction than the IgG1 antibodies. SigmaMAb K4 produced mostly L over the duration of the run, while polyclonal IgG4κ produced significant levels of both HL and L. At some points during the cycle of the polyclonal IgG4, the HL and L products seemed to be in competition, similar to the IgG1 antibodies, but the L product was dominant at the end of the cycle. The hinge stabilization of SigmaMAb K4 likely contributed to these differences. We hypothesize that the L-H disulfide bond was preferentially reduced during temperature cycles of SigmaMAb K4. If hinge disulfide bonds were not often reduced under these conditions, and the HHL products were not available for reduction or detection, then it would follow that no HL species would be observed. Compared to the hinge-stabilized monoclonal antibody, wild-type IgG4 experiences more hinge flexibility.[30] The polyclonal IgG4 displayed a significant intensity of the HL products at the beginning of the cycle, and considering a small amount of these species were observed in the spectra in the absence of DTT as well, we hypothesize that hinge reduction occurred more readily. Based on the relative abundance of reduction products and intact antibodies at the end of the cycles, we also hypothesize that both IgG4 antibodies were more susceptible to disulfide bond reduction under these conditions than the IgG1 antibodies.

## 4 Conclusion

We introduced ptESI and showed that this source design results in fast, high-fidelity temperature control of the sample within a sample capillary. With the versatility of the programming, ptESI opens the door to real-time reaction monitoring and more detailed thermochemical studies of proteins and other biomolecules with MS. The automation and speed decreases experimenter workload and increases the throughput of these analyses. Initial experiments with RbA showcase the abilities of real-time disulfide bond reduction monitoring. The temperature resolution allows experimenters to view the onset and progression of bond reduction, rather than just the final product (Figure 3.4). With the addition of ion mobility, more detailed information can be gained about the onset of unfolding and the initiation of the reactions (Figure 3.5).

Real-time disulfide bond reduction of monoclonal and polyclonal antibody standards demonstrated that ptESI can be used to differentiate complex biomolecules with similar structures. NISTmAb and polyclonal IgG1κ samples experienced similar reduction pathways, but the ability to temperature- and time-resolve their reduction reactions revealed differences in the onset and rate of the appearance of their reaction products (Figures 3.7 and 3.9). For SigmaMAb K4, the effect of the amino acid mutation on the stability of the hinge disulfide bonds was readily apparent, and it was easily distinguished from the other three antibody samples (Figure 3.8). Polyclonal IgG4κ appeared to undergo a hybrid pathway between that of the IgG1 antibodies and SigmaMAb K4, and the dominant L product, as well as its heterogeneity, distinguished it from the rest (Figure 3.10). Clear differences were observed between all antibody samples without extensive temperature program optimization, highlighting the sensitivity of this method to the stability and disulfide-bond connectivity of these antibodies. Future experiments will investigate a larger variety of temperature programs and DTT concentrations, as well as compare

biotherapeutic biosimilars, which are even more alike in disulfide-bond connectivity. Further investigation is also necessary to understand the absence of HHL products and the influence of its aggregation or dissociation on the resulting reduction profiles. This technology shows potential for a variety of thermochemical applications, and improvements to the source design are underway to enable its broader use.

## 5 Acknowledgements

This work was supported by the National Science Foundation through award 2203513 from the Division of Chemistry, with partial co-funding from the Division of Molecular and Cellular Biosciences.

## 6 References

(1) Marino, S. M.; Gladyshev, V. N. Cysteine Function Governs Its Conservation and Degeneration and Restricts Its Utilization on Protein Surfaces. *J. Mol. Biol.* **2010**, *404* (5), 902–916. https://doi.org/10.1016/j.jmb.2010.09.027.

(2) Wiedemann, C.; Kumar, A.; Lang, A.; Ohlenschläger, O. Cysteines and Disulfide Bonds as Structure-Forming Units: Insights From Different Domains of Life and the Potential for Characterization by NMR. *Front. Chem.* **2020**, *8*, 280. https://doi.org/10.3389/fchem.2020.00280.

(3) Arolas, J. L.; Aviles, F. X.; Chang, J.-Y.; Ventura, S. Folding of Small Disulfide-Rich Proteins: Clarifying the Puzzle. *Trends Biochem. Sci.* **2006**, *31* (5), 292–301. https://doi.org/10.1016/j.tibs.2006.03.005.

(4) Bechtel, T. J.; Weerapana, E. From Structure to Redox: The Diverse Functional Roles of Disulfides and Implications in Disease. *PROTEOMICS* **2017**, *17* (6), 1600391. https://doi.org/10.1002/pmic.201600391.

(5) Bosnjak, I.; Bojovic, V.; Segvic-Bubic, T.; Bielen, A. Occurrence of Protein Disulfide Bonds in Different Domains of Life: A Comparison of Proteins from the Protein Data Bank. *Protein Eng. Des. Sel.* **2014**, *27* (3), 65–72. https://doi.org/10.1093/protein/gzt063.

(6) Wu, H.; Ma, B.-G.; Zhao, J.-T.; Zhang, H.-Y. How Similar Are Amino Acid Mutations in Human Genetic Diseases and Evolution. *Biochem. Biophys. Res. Commun.* **2007**, *362* (2), 233–237. https://doi.org/10.1016/j.bbrc.2007.07.141.

(7) Urquhart, L. Top Companies and Drugs by Sales in 2021. *Nat. Rev. Drug Discov.* **2022**, *21* (4), 251–251. https://doi.org/10.1038/d41573-022-00047-9.

(8) Kaplon, H.; Crescioli, S.; Chenoweth, A.; Visweswaraiah, J.; Reichert, J. M. Antibodies to Watch in 2023. *mAbs* **2023**, *15* (1), 2153410. https://doi.org/10.1080/19420862.2022.2153410.

(9) Tang, Y.; Cain, P.; Anguiano, V.; Shih, J. J.; Chai, Q.; Feng, Y. Impact of IgG Subclass on Molecular Properties of Monoclonal Antibodies. *mAbs* **2021**, *13* (1), 1993768. https://doi.org/10.1080/19420862.2021.1993768.

(10) Liu, H.; May, K. Disulfide Bond Structures of IgG Molecules: Structural Variations, Chemical Modifications and Possible Impacts to Stability and Biological Function. *mAbs* **2012**, *4* (1), 17–23. https://doi.org/10.4161/mabs.4.1.18347.

(11) Moritz, B.; Stracke, J. O. Assessment of Disulfide and Hinge Modifications in Monoclonal Antibodies. *ELECTROPHORESIS* **2017**, *38* (6), 769–785. https://doi.org/10.1002/elps.201600425.

(12) Aalberse, R. C.; Schuurman, J. IgG4 Breaking the Rules. *Immunology* **2002**, *105* (1), 9–19. https://doi.org/10.1046/j.0019-2805.2001.01341.x.

(13) Schuurman, J.; Perdok, G. J.; Gorter, A. D.; Aalberse, R. C. The Inter-Heavy Chain Disulfide Bonds of IgG4 Are in Equilibrium with Intra-Chain Disulfide Bonds. *Mol. Immunol.* **2001**, *38* (1), 1–8. https://doi.org/10.1016/S0161-5890(01)00050-5.

(14) Labrijn, A. F.; Buijsse, A. O.; Van Den Bremer, E. T. J.; Verwilligen, A. Y. W.; Bleeker, W. K.; Thorpe, S. J.; Killestein, J.; Polman, C. H.; Aalberse, R. C.; Schuurman, J.; Van De Winkel, J. G. J.; Parren, P. W. H. I. Therapeutic IgG4 Antibodies Engage in Fab-Arm Exchange with Endogenous Human IgG4 in Vivo. *Nat. Biotechnol.* **2009**, *27* (8), 767–771. https://doi.org/10.1038/nbt.1553.

(15) Labrijn, A. F.; Rispens, T.; Meesters, J.; Rose, R. J.; Den Bleker, T. H.; Loverix, S.; Van Den Bremer, E. T. J.; Neijssen, J.; Vink, T.; Lasters, I.; Aalberse, R. C.; Heck, A. J. R.; Van De Winkel, J. G. J.; Schuurman, J.; Parren, P. W. H. I. Species-Specific Determinants in the IgG CH3 Domain Enable Fab-Arm Exchange by Affecting the Noncovalent CH3–CH3 Interaction Strength. *J. Immunol.* **2011**, *187* (6), 3238–3246. https://doi.org/10.4049/jimmunol.1003336.

(16) Ma, J.; Mo, Y.; Tang, M.; Shen, J.; Qi, Y.; Zhao, W.; Huang, Y.; Xu, Y.; Qian, C. Bispecific Antibodies: From Research to Clinical Application. *Front. Immunol.* **2021**, *12*, 626616. https://doi.org/10.3389/fimmu.2021.626616.

(17) Angal, S.; King, D. J.; Bodmer, M. W.; Turner, A.; Lawson, A. D. G.; Roberts, G.; Pedley, B.; Adair, J. R. A Single Amino Acid Substitution Abolishes the Heterogeneity of Chimeric Mouse/Human (IgG4) Antibody. *Mol. Immunol.* **1993**, *30* (1), 105–108. https://doi.org/10.1016/0161-5890(93)90432-B.

(18) Müller, T.; Winter, D. Systematic Evaluation of Protein Reduction and Alkylation Reveals Massive Unspecific Side Effects by Iodine-Containing Reagents. *Mol. Cell. Proteomics MCP* **2017**, *16* (7), 1173–1187. https://doi.org/10.1074/mcp.M116.064048.

(19) Li, Y.-J.; Rothwarf, D. M.; Scheraga, H. A. Mechanism of Reductive Protein Unfolding. *Nat. Struct. Mol. Biol.* **1995**, *2* (6), 489–494. https://doi.org/10.1038/nsb0695-489.

(20) Kielkopf, C. L.; Bauer, W.; Urbatsch, I. L. Sodium Dodecyl Sulfate–Polyacrylamide Gel Electrophoresis of Proteins. *Cold Spring Harb. Protoc.* **2021**, *2021* (12), pdb.prot102228. https://doi.org/10.1101/pdb.prot102228.

(21) Bass, J. J.; Wilkinson, D. J.; Rankin, D.; Phillips, B. E.; Szewczyk, N. J.; Smith, K.; Atherton, P. J. An Overview of Technical Considerations for Western Blotting

Applications to Physiological Research. *Scand. J. Med. Sci. Sports* **2017**, *27* (1), 4–25. https://doi.org/10.1111/sms.12702.

(22) Morgan, T. E.; Jakes, C.; Brouwer, H.-J.; Millán-Martín, S.; Chervet, J.-P.; Cook, K.; Carillo, S.; Bones, J. Inline Electrochemical Reduction of NISTmAb for Middle-up Subunit Liquid Chromatography-Mass Spectrometry Analysis. *The Analyst* **2021**, *146* (21), 6547–6555. https://doi.org/10.1039/D1AN01184G.

(23) Sjögren, J.; Olsson, F.; Beck, A. Rapid and Improved Characterization of Therapeutic Antibodies and Antibody Related Products Using IdeS Digestion and Subunit Analysis. *The Analyst* **2016**, *141* (11), 3114–3125. https://doi.org/10.1039/C6AN00071A.

(24) Burmeister Getz, E.; Xiao, M.; Chakrabarty, T.; Cooke, R.; Selvin, P. R. A Comparison between the Sulfhydryl Reductants Tris(2-Carboxyethyl)Phosphine and Dithiothreitol for Use in Protein Biochemistry. *Anal. Biochem.* **1999**, *273*, 73–80. https://doi.org/10.1006/abio.1999.4203.

(25) Mthembu, S. N.; Sharma, A.; Albericio, F.; de la Torre, B. G. Breaking a Couple: Disulfide Reducing Agents. *ChemBioChem* **2020**, *21* (14), 1947–1954. https://doi.org/10.1002/cbic.202000092.

(26) Van Der Neut Kolfschoten, M.; Schuurman, J.; Losen, M.; Bleeker, W. K.; Martínez-Martínez, P.; Vermeulen, E.; Den Bleker, T. H.; Wiegman, L.; Vink, T.; Aarden, L. A.; De Baets, M. H.; Van De Winkel, J. G. J.; Aalberse, R. C.; Parren, P. W. H. I. Anti-Inflammatory Activity of Human IgG4 Antibodies by Dynamic Fab Arm Exchange. *Science* **2007**, *317* (5844), 1554–1557. https://doi.org/10.1126/science.1144603.

(27) Montaño, R. F.; Morrison, S. L. Influence of the Isotype of the Light Chain on the Properties of IgG. *J. Immunol.* **2002**, *168* (1), 224–231. https://doi.org/10.4049/jimmunol.168.1.224.

(28) Liu, H.; Chumsae, C.; Gaza-Bulseco, G.; Hurkmans, K.; Radziejewski, C. H. Ranking the Susceptibility of Disulfide Bonds in Human IgG1 Antibodies by Reduction, Differential Alkylation, and LC−MS Analysis. *Anal. Chem.* **2010**, *82* (12), 5219–5226. https://doi.org/10.1021/ac100575n.

(29) Hong, J.; Lee, A.; Han, H.; Kim, J. Structural Characterization of Immunoglobulin G Using Time-Dependent Disulfide Bond Reduction. *Anal. Biochem.* **2009**, *384* (2), 368–370. https://doi.org/10.1016/j.ab.2008.10.012.

(30) Song, Y.; Cai, H.; Tan, Z.; Mussa, N.; Li, Z.-J. Mechanistic Insights into Inter-Chain Disulfide Bond Reduction of IgG1 and IgG4 Antibodies. *Appl. Microbiol. Biotechnol.* **2022**, *106* (3), 1057–1066. https://doi.org/10.1007/s00253-022-11778-5.

(31) Beck, A.; Sanglier-Cianférani, S.; Van Dorsselaer, A. Biosimilar, Biobetter, and Next Generation Antibody Characterization by Mass Spectrometry. *Anal. Chem.* **2012**, *84* (11), 4637–4646. https://doi.org/10.1021/ac3002885.

(32) Beck, A.; Wagner-Rousset, E.; Ayoub, D.; Van Dorsselaer, A.; Sanglier-Cianférani, S. Characterization of Therapeutic Antibodies and Related Products. *Anal. Chem.* **2013**, *85* (2), 715–736. https://doi.org/10.1021/ac3032355.

(33) Dada, O. O.; Rao, R.; Jones, N.; Jaya, N.; Salas-Solano, O. Comparison of SEC and CE-SDS Methods for Monitoring Hinge Fragmentation in IgG1 Monoclonal Antibodies. *J. Pharm. Biomed. Anal.* **2017**, *145*, 91–97. https://doi.org/10.1016/j.jpba.2017.06.006.

(34) Tian, Y.; Han, L.; Buckner, A. C.; Ruotolo, B. T. Collision Induced Unfolding of Intact Antibodies: Rapid Characterization of Disulfide Bonding Patterns, Glycosylation, and Structures. *Anal. Chem.* **2015**, *87* (22), 11509–11515. https://doi.org/10.1021/acs.analchem.5b03291.

(35) Deslignière, E.; Botzanowski, T.; Diemer, H.; Cooper-Shepherd, D. A.; Wagner-Rousset, E.; Colas, O.; Béchade, G.; Giles, K.; Hernandez-Alba, O.; Beck, A.; Cianférani, S. High-Resolution IMS–MS to Assign Additional Disulfide Bridge Pairing in Complementarity-Determining Regions of an IgG4 Monoclonal Antibody. *J. Am. Soc. Mass Spectrom.* **2021**, *32* (10), 2505–2512. https://doi.org/10.1021/jasms.1c00151.

(36) Upton, R.; Migas, L. G.; Pacholarz, K. J.; Beniston, R. G.; Estdale, S.; Firth, D.; Barran, P. E. Hybrid Mass Spectrometry Methods Reveal Lot-to-Lot Differences and Delineate the Effects of Glycosylation on the Tertiary Structure of Herceptin®. *Chem. Sci.* **2019**, *10* (9), 2811–2820. https://doi.org/10.1039/C8SC05029E.

(37) Marcoux, J.; Champion, T.; Colas, O.; Wagner-Rousset, E.; Corvaïa, N.; Van Dorsselaer, A.; Beck, A.; Cianférani, S. Native Mass Spectrometry and Ion Mobility Characterization of Trastuzumab Emtansine, a Lysine-Linked Antibody Drug Conjugate: Native MS and IM-MS for Trastuzumab Emtansine Analysis. *Protein Sci.* **2015**, *24* (8), 1210–1223. https://doi.org/10.1002/pro.2666.

(38) Pacholarz, K. J.; Barran, P. E. Use of a Charge Reducing Agent to Enable Intact Mass Analysis of Cysteine-Linked Antibody-Drug-Conjugates by Native Mass Spectrometry. *EuPA Open Proteomics* **2016**, *11*, 23–27. https://doi.org/10.1016/j.euprot.2016.02.004.

(39) Rose, R. J.; Labrijn, A. F.; van den Bremer, E. T. J.; Loverix, S.; Lasters, I.; van Berkel, P. H. C.; van de Winkel, J. G. J.; Schuurman, J.; Parren, P. W. H. I.; Heck, A. J. R.

Quantitative Analysis of the Interaction Strength and Dynamics of Human IgG4 Half Molecules by Native Mass Spectrometry. *Structure* **2011**, *19* (9), 1274–1282. https://doi.org/10.1016/j.str.2011.06.016.

(40) Rosati, S.; Van Den Bremer, E. T.; Schuurman, J.; Parren, P. W.; Kamerling, J. P.; Heck, A. J. In-Depth Qualitative and Quantitative Analysis of Composite Glycosylation Profiles and Other Micro-Heterogeneity on Intact Monoclonal Antibodies by High-Resolution Native Mass Spectrometry Using a Modified Orbitrap. *mAbs* **2013**, *5* (6), 917–924. https://doi.org/10.4161/mabs.26282.

(41) Debaene, F.; Wagner-Rousset, E.; Colas, O.; Ayoub, D.; Corvaïa, N.; Van Dorsselaer, A.; Beck, A.; Cianférani, S. Time Resolved Native Ion-Mobility Mass Spectrometry to Monitor Dynamics of IgG4 Fab Arm Exchange and "Bispecific" Monoclonal Antibody Formation. *Anal. Chem.* **2013**, *85* (20), 9785–9792. https://doi.org/10.1021/ac402237v.

(42) Nicolardi, S.; Giera, M.; Kooijman, P.; Kraj, A.; Chervet, J.-P.; Deelder, A. M.; van der Burgt, Y. E. M. On-Line Electrochemical Reduction of Disulfide Bonds: Improved FTICR-CID and -ETD Coverage of Oxytocin and Hepcidin. *J. Am. Soc. Mass Spectrom.* **2013**, *24* (12), 1980–1987. https://doi.org/10.1007/s13361-013-0725-7.

(43) Switzar, L.; Nicolardi, S.; Rutten, J. W.; Oberstein, S. A. J. L.; Aartsma-Rus, A.; van der Burgt, Y. E. M. In-Depth Characterization of Protein Disulfide Bonds by Online Liquid Chromatography-Electrochemistry-Mass Spectrometry. *J. Am. Soc. Mass Spectrom.* **2016**, *27* (1), 50–58. https://doi.org/10.1007/s13361-015-1258-z.

(44) Stocks, B. B.; Melanson, J. E. In-Source Reduction of Disulfide-Bonded Peptides Monitored by Ion Mobility Mass Spectrometry. *J. Am. Soc. Mass Spectrom.* **2018**, *29* (4), 742–751. https://doi.org/10.1007/s13361-018-1894-1.

(45) Vanduijn, M. M.; Brouwer, H.-J.; Sanz De La Torre, P.; Chervet, J.-P.; Luider, T. M. Online Electrochemical Reduction of Both Inter- and Intramolecular Disulfide Bridges in Immunoglobulins. *Anal. Chem.* **2022**, *94* (7), 3120–3125. https://doi.org/10.1021/acs.analchem.1c04261.

(46) Pawlowski, J. W.; Carrick, I.; Kaltashov, I. A. Integration of On-Column Chemical Reactions in Protein Characterization by Liquid Chromatography/Mass Spectrometry: Cross-Path Reactive Chromatography. *Anal. Chem.* **2018**, *90* (2), 1348–1355. https://doi.org/10.1021/acs.analchem.7b04328.

(47) Gadzuk-Shea, M. M.; Hubbard, E. E.; Gozzo, T. A.; Bush, M. F. Sample pH Can Drift during Native Mass Spectrometry Experiments: Results from Ratiometric Fluorescence Imaging. *J. Am. Soc. Mass Spectrom.* **2023**, *34* (8), 1675–1684. https://doi.org/10.1021/jasms.3c00147.

(48) Davidson, K. L.; Oberreit, D. R.; Hogan, C. J.; Bush, M. F. Nonspecific Aggregation in Native Electrokinetic Nanoelectrospray Ionization. *Int. J. Mass Spectrom.* **2017**, *420*, 35–42. https://doi.org/10.1016/j.ijms.2016.09.013.

(49) Alexander Harrison, J.; Pruška, A.; Oganesyan, I.; Bittner, P.; Zenobi, R. Temperature-Controlled Electrospray Ionization: Recent Progress and Applications. *Chem. – Eur. J.* **2021**, *27* (72), 18015–18028. https://doi.org/10.1002/chem.202102474.

(50) El-Baba, T. J.; Raab, S. A.; Buckley, R. P.; Brown, C. J.; Lutomski, C. A.; Henderson, L. W.; Woodall, D. W.; Shen, J.; Trinidad, J. C.; Niu, H.; Jarrold, M. F.; Russell, D. H.; Laganowsky, A.; Clemmer, D. E. Thermal Analysis of a Mixture of Ribosomal Proteins by vT-ESI-MS: Toward a Parallel Approach for Characterizing the *Stabilitome*. *Anal. Chem.* **2021**, *93* (24), 8484–8492. https://doi.org/10.1021/acs.analchem.1c00772.

(51) Brown, C. J.; Woodall, D. W.; El-Baba, T. J.; Clemmer, D. E. Characterizing Thermal Transitions of IgG with Mass Spectrometry. *J. Am. Soc. Mass Spectrom.* **2019**, *30* (11), 2438–2445. https://doi.org/10.1007/s13361-019-02292-6.

(52) Moghadamchargari, Z.; Huddleston, J.; Shirzadeh, M.; Zheng, X.; Clemmer, D. E.; M. Raushel, F.; Russell, D. H.; Laganowsky, A. Intrinsic GTPase Activity of K-RAS Monitored by Native Mass Spectrometry. *Biochemistry* **2019**, *58* (31), 3396–3405. https://doi.org/10.1021/acs.biochem.9b00532.

(53) Wang, G.; Abzalimov, R. R.; Kaltashov, I. A. Direct Monitoring of Heat-Stressed Biopolymers with Temperature-Controlled Electrospray Ionization Mass Spectrometry. *Anal. Chem.* **2011**, *83* (8), 2870–2876. https://doi.org/10.1021/ac200441a.

(54) Benesch, J. L. P.; Sobott, F.; Robinson, C. V. Thermal Dissociation of Multimeric Protein Complexes by Using Nanoelectrospray Mass Spectrometry. *Anal. Chem.* **2003**, *75* (10), 2208–2214. https://doi.org/10.1021/ac034132x.

(55) Geels, R. B. J.; Calmat, S.; Heck, A. J. R.; van der Vies, S. M.; Heeren, R. M. A. Thermal Activation of the Co-Chaperonins GroES and Gp31 Probed by Mass Spectrometry. *Rapid Commun. Mass Spectrom.* **2008**, *22* (22), 3633–3641. https://doi.org/10.1002/rcm.3782.

(56) Cong, X.; Liu, Y.; Liu, W.; Liang, X.; Russell, D. H.; Laganowsky, A. Determining Membrane Protein–Lipid Binding Thermodynamics Using Native Mass Spectrometry. *J. Am. Chem. Soc.* **2016**, *138* (13), 4346–4349. https://doi.org/10.1021/jacs.6b01771.

(57) El-Baba, T. J.; Woodall, D. W.; Raab, S. A.; Fuller, D. R.; Laganowsky, A.; Russell, D. H.; Clemmer, D. E. Melting Proteins: Evidence for Multiple Stable Structures upon Thermal Denaturation of Native Ubiquitin from Ion Mobility Spectrometry-Mass Spectrometry

Measurements. *J. Am. Chem. Soc.* **2017**, *139* (18), 6306–6309. https://doi.org/10.1021/jacs.7b02774.

(58) Marchand, A.; Rosu, F.; Zenobi, R.; Gabelica, V. Thermal Denaturation of DNA G-Quadruplexes and Their Complexes with Ligands: Thermodynamic Analysis of the Multiple States Revealed by Mass Spectrometry. *J. Am. Chem. Soc.* **2018**, *140* (39), 12553–12565. https://doi.org/10.1021/jacs.8b07302.

(59) McCabe, J. W.; Shirzadeh, M.; Walker, T. E.; Lin, C.-W.; Jones, B. J.; Wysocki, V. H.; Barondeau, D. P.; Clemmer, D. E.; Laganowsky, A.; Russell, D. H. Variable-Temperature Electrospray Ionization for Temperature-Dependent Folding/Refolding Reactions of Proteins and Ligand Binding. *Anal. Chem.* **2021**, *93* (18), 6924–6931. https://doi.org/10.1021/acs.analchem.1c00870.

(60) Jordan, J. S.; Williams, E. R. Laser Heating Nanoelectrospray Emitters for Fast Protein Melting Measurements with Mass Spectrometry. *Anal. Chem.* **2022**, *94* (48), 16894–16900. https://doi.org/10.1021/acs.analchem.2c04204.

(61) Marchand, A.; Czar, M. F.; Eggel, E. N.; Kaeslin, J.; Zenobi, R. Studying Biomolecular Folding and Binding Using Temperature-Jump Mass Spectrometry. *Nat. Commun.* **2020**, *11* (1), 566. https://doi.org/10.1038/s41467-019-14179-x.

(62) Zhao, P.; Gunawardena, H. P.; Zhong, X.; Zare, R. N.; Chen, H. Microdroplet Ultrafast Reactions Speed Antibody Characterization. *Anal. Chem.* **2021**, *93* (8), 3997–4005. https://doi.org/10.1021/acs.analchem.0c04974.

(63) Giles, K.; Ujma, J.; Wildgoose, J.; Pringle, S.; Richardson, K.; Langridge, D.; Green, M. A Cyclic Ion Mobility-Mass Spectrometry System. *Anal. Chem.* **2019**, *91* (13), 8564–8573. https://doi.org/10.1021/acs.analchem.9b01838.

(64) Scigelova, M.; Green, P. S.; Giannakopulos, A. E.; Rodger, A.; Crout, D. H. G.; Derrick, P. J. A Practical Protocol for the Reduction of Disulfide Bonds in Proteins Prior to Analysis by Mass Spectrometry. *Eur. J. Mass Spectrom.* **2001**, *7* (1), 29–34. https://doi.org/10.1255/ejms.385.

(65) Srzentić, K.; Fornelli, L.; Tsybin, Y. O.; Loo, J. A.; Seckler, H.; Agar, J. N.; Anderson, L. C.; Bai, D. L.; Beck, A.; Brodbelt, J. S.; Van Der Burgt, Y. E. M.; Chamot-Rooke, J.; Chatterjee, S.; Chen, Y.; Clarke, D. J.; Danis, P. O.; Diedrich, J. K.; D'Ippolito, R. A.; Dupré, M.; Gasilova, N.; Ge, Y.; Goo, Y. A.; Goodlett, D. R.; Greer, S.; Haselmann, K. F.; He, L.; Hendrickson, C. L.; Hinkle, J. D.; Holt, M. V.; Hughes, S.; Hunt, D. F.; Kelleher, N. L.; Kozhinov, A. N.; Lin, Z.; Malosse, C.; Marshall, A. G.; Menin, L.; Millikin, R. J.; Nagornov, K. O.; Nicolardi, S.; Paša-Tolić, L.; Pengelley, S.; Quebbemann, N. R.; Resemann, A.; Sandoval, W.; Sarin, R.; Schmitt, N. D.; Shabanowitz, J.; Shaw, J. B.; Shortreed, M. R.; Smith, L. M.; Sobott, F.; Suckau, D.; Toby, T.; Weisbrod, C. R.; Wildburger, N. C.; Yates, J. R.; Yoon, S. H.; Young, N. L.; Zhou, M. Interlaboratory Study for Characterizing Monoclonal Antibodies by Top-Down and Middle-Down Mass Spectrometry. *J. Am. Soc. Mass Spectrom.* **2020**, *31* (9), 1783–1802. https://doi.org/10.1021/jasms.0c00036.

(66) Formolo, T.; Ly, M.; Levy, M.; Kilpatrick, L.; Lute, S.; Phinney, K.; Marzilli, L.; Brorson, K.; Boyne, M.; Davis, D.; Schiel, J. Determination of the NISTmAb Primary Structure. In *ACS Symposium Series*; Schiel, J. E., Davis, D. L., Borisov, O. V., Eds.; American Chemical Society: Washington, DC, 2015; Vol. 1201, pp 1–62. https://doi.org/10.1021/bk-2015-1201.ch001.

(67) Product Information SILuLite SigmaMab K4 Universal Monoclonal Antibody Standard, Human Recombinant, Expressed in CHO Cells, Catalog Number MSQC14. chrome-extension://efaidnbmnnnibpcajpcglclefindmkaj/https://www.sigmaaldrich.com/deepweb/assets/sigmaaldrich/product/documents/226/005/msqc14dat.pdf.

(68) Roux, K. H.; Strelets, L.; Michaelsen, T. E. Flexibility of Human IgG Subclasses. *J. Immunol.* **1997**, *159* (7), 3372–3382.

(69) Cohen, S. L.; Price, C.; Vlasak, J. β-Elimination and Peptide Bond Hydrolysis: Two Distinct Mechanisms of Human IgG1 Hinge Fragmentation upon Storage. *J. Am. Chem. Soc.* **2007**, *129* (22), 6976–6977. https://doi.org/10.1021/ja0705994.

(70) Cordoba, A. J.; Shyong, B.-J.; Breen, D.; Harris, R. J. Non-Enzymatic Hinge Region Fragmentation of Antibodies in Solution. *J. Chromatogr. B* **2005**, *818* (2), 115–121. https://doi.org/10.1016/j.jchromb.2004.12.033.

(71) Campuzano, I. D. G.; Larriba, C.; Bagal, D.; Schnier, P. D. Ion Mobility and Mass Spectrometry Measurements of the Humanized IgGk NIST Monoclonal Antibody. In *ACS Symposium Series*; Schiel, J. E., Davis, D. L., Borisov, O. V., Eds.; American Chemical Society: Washington, DC, 2015; Vol. 1202, pp 75–112. https://doi.org/10.1021/bk-2015-1202.ch004.

# Appendix A: Supporting Information for Chapter 2.

## A1 Calculating Collision Cross Sections (Ω) from Arrival-Time Distributions

This section is adapted from previous descriptions of measurements using this system that incorporates an RF-confining drift cell, including the use of field-dependent measurements to determine Ω and the use of single-field measurements to determine apparent Ω distributions.[1] In this system, the drift voltage can be varied up to 354 V. The centroid of each arrival-time distribution is estimated by fitting that distribution to a Gaussian function using in-house software.[2] For mobility experiments, arrival times were measured using 8 to 10 drift voltages ($V$) ranging from 104 to 354 V. The measured arrival times ($t_A$) include the residence time in the drift cell (the mobility-dependent drift time, $t_d$) as well as the transport time from the exit of the drift cell to the time-of-flight mass analyzer, $t_0$:

$$t_A = t_d + t_0 = \frac{L^2}{KV} + t_0$$

where $L$ is the 25.05 cm length of the drift region. $m/z$-dependent ($t_{m/z}$) transport times and $m/z$-independent ($t_{ind}$) transport times contribute to $t_0$:

$$t_0 = t_{m/z} + t_{ind} = \frac{c\sqrt{m/z}}{1000} + t_{ind}$$

where $c$ represents an instrument-specific parameter, the enhanced duty cycle delay coefficient. Plotting arrival time as a function of reciprocal drift voltage allows the determination of $t_0$ from the y-intercepts of the best-fit lines. The arrival times are corrected for $t_0$. The mobilities of the precursors are determined from the slopes.

$$K = \frac{L^2}{\left[t_A - \left(t_{ind} + \frac{c\sqrt{m/z}}{1000}\right)\right] * V}$$

The collision cross-section, **Ω**, can be calculated from mobility using the Mason-Schamp equation:[3]

$$\Omega = \frac{3ez}{16N}\left(\frac{2\pi}{\mu k_B T}\right)^{1/2}\frac{1}{K}$$

where $e$ is elementary charge, $z$ is the ion's charge state, N is the drift-gas number density, $\mu$ is the reduced mass of the drift gas-ion pair, $k_B$ is the Boltzmann constant, and T is the drift-gas temperature.

The average $t_{ind}$ values of the precursors were used to correct arrival times of the charge-reduced CAPTR products and residual precursor ions. CAPTR-IM was performed with 1.5 Torr He and a voltage drop of 183 V across the drift cell. Cumulative distribution functions (CDF) were calculated for each **Ω** distribution to determine critical values. 10%, 50%, and 90% values of the CDF were used to describe the lower bound, median, and upper bound of the **Ω** distributions, respectively.

**A2 Calculating Similarity Scores**

To quantitatively compare the apparent Ω distributions of Ig1 and IgG4 ions, a Jensen-Shannon distance metric was calculated using the SciPy spatial.distance submodule. We define the similarity score as 1 minus the Jensen-Shannon distance. The Jensen-Shannon distance is the square root of the Jensen-Shannon divergence. For vectors $p$ and $q$:

**Eq. S1**
$$Score = 1 - \left(\frac{D(p\|m)+D(q\|m)}{2}\right)^{0.5}$$

where $m$ is the pointwise mean of $p$ and $q$ and D is the Kullback-Liebler divergence. Log base 2 is used in the calculation of the Kullback-Liebler divergences to bound the score between 0 and 1.[4] A score of 1 signifies that the two distributions are identical. As the score decreases to 0, it

signifies increasing dissimilarity between the distributions being compared. Below is an example of the code implemented to calculate this score for two apparent Ω distributions. Note that the distributions subjected to comparison must be interpolated a common Ω axis. If these distributions are not normalized, scipy.spatial.distance.jensenshannon() will normalize these distributions so that they sum to 1.0 prior to calculating the distance.

```
# Import packages
# python version 3.7.4
# numpy version 1.18.4
# pandas version 0.25.1
# scipy version 1.3.1
In [2]:   import numpy as np
          import pandas as pd
          from scipy.spatial import distance

# Load in Ω distributions
# These distributions were interpolated over a common axis of 1000 points
# from 0 to 125 nm²

In [2]:   ccsd_IgG4 = pd.read_csv('IgG4.csv',
                                  header=None,
                                  index_col=0)
In [3]:   ccsd_IgG1 = pd.read_csv('IgG1.csv',
                                  header=None,
                                  index_col=0)

# Compute Jensen-Shannon Similarity Score
In [4]:   np.round((1-distance.jensenshannon(ccsd_IgG4,ccsd_IgG1, base=2)),
                   decimals=2)
Out [4]:  array([0.8])

# Note that the order in which you input the distributions into
# scipy.spatial.distance.jensenshannon() does not affect the score
In [5]:   np.round((1-distance.jensenshannon(ccsd_IgG1,ccsd_IgG4, base=2)),
                   decimals=2)
Out [5]:  array([0.8])
```

**A3 Additional Discussion of the Ω Values for CAPTR Products with Minimal Activation**

The $\widetilde{\Omega}$ values of all *P*→*C* ions are shown in Figure 3. From native-like conditions, CAPTR was performed on 26+, 25+, and 24+ precursors. The lowest-*C* CAPTR product observed from $^{N}$IgG1 was 11+, and the lowest-*C* CAPTR product observed from $^{N}$IgG4 was 12+. Precursor $\widetilde{\Omega}$ values differed by 4.4% for $^{N}$IgG4 and by 1% for $^{N}$IgG1. Comparing the $^{N}$*P*→12 ions to each other, IgG4 ions differed in Ω by 1.8% and IgG1 ions differed by 1.3%, suggesting a weak dependence on the precursor charge state. All $^{N}$*P*→*C* ions of IgG1 were more compact than their precursor ions. For IgG4, this was only true for the $^{N}$25→*C* ions. The $^{N}$IgG4 24+ precursor was more compact than all of its CAPTR products, and the $^{N}$26→24, 23, 22 ions were larger than the 26+ precursor, whereas the remaining $^{N}$26→*C* products were smaller. The $\widetilde{\Omega}$ values of the most-compact CAPTR product ions were between 1.4 and 2.3% smaller than the corresponding precursor ions for these antibodies. In the case of the $^{N}$24→*C* ions of IgG4 where the precursor was the smallest, the largest product ions ($^{N}$24→19) were only 1.3% larger. IgG4 $^{N}$26→23 ions were the largest of the $^{N}$26→24, 23, 22 ions, but they were less than 1% larger than the precursor. Even for CAPTR product series that were all more compact than their precursor, a decrease in $\widetilde{\Omega}$ was not observed following every CAPTR event. The largest percent decrease in $\widetilde{\Omega}$ observed for a single CAPTR event was around 1% and the largest percent increase was less than 1% for both antibodies. Comparing CAPTR products of the two antibodies, the $^{N}$26→24 and $^{N}$26→23 ions exhibited the largest percent difference in $\widetilde{\Omega}$ (5.4%).

The $\widetilde{\Omega}$ values of both IgG1 and IgG4 $^{N}$*P*→*C* ions appear to be independent of *P* and *C* under these conditions; $\widetilde{\Omega}$ values are similar across the range of charge states observed following CAPTR. For alcohol dehydrogenase, $\widetilde{\Omega}$ values of CAPTR products, relative to those of precursors, ranged from –3.6% to +1.3%.[48] For $^{N}$IgG1, the maximum decrease in $\widetilde{\Omega}$ for a CAPTR

product relative to its precursor was –2.3%. For $^{N}$IgG4, the product $\widetilde{\Omega}$ values span –2.2% to +1.3% relative to their precursors.

From denaturing conditions, 49+ and 47+ precursor ions were subjected to CAPTR; CAPTR mass spectra are shown in Figures S5 and S6. The IgG4 $^{D}49\rightarrow C$ ions exhibited consistently larger $^{DT}\widetilde{\Omega}_{He}$ values than IgG1 for all ions observed (Figure 3). Differences are maximized at lower charge states, with the maximum difference in $\widetilde{\Omega}$ observed for the $^{D}49\rightarrow19$ ions. Percent differences for $\widetilde{\Omega}$ values of IgG4 and IgG1 $^{D}49\rightarrow C$ ions were between 0.5 and 5.9%. The lowest-*C* CAPTR products observed with significant intensity were $^{D}49\rightarrow15$ for IgG1 and $^{D}49\rightarrow16$ for IgG4 with $\widetilde{\Omega}$ values of 93.9 nm$^2$ and 99.9 nm$^2$, respectively. The $\widetilde{\Omega}$ value for IgG1 $^{D}49\rightarrow16$ ions was 95.9 nm$^2$, for comparison. These product ions are significantly larger than any of the $^{N}P\rightarrow15$ or $^{N}P\rightarrow16$ ions, and the decreases in $\widetilde{\Omega}$ for the IgG1 $^{D}49\rightarrow15$ and IgG4 $^{D}49\rightarrow16$ ions relative to their precursors were 21.1% and 16.7% (34 and 33 CAPTR events, respectively). Compaction was observed following most CAPTR events.

Comparing ions generated from different precursors, $^{D}47\rightarrow C$ and $^{D}49\rightarrow C$ ions of IgG1 exhibited similar $\widetilde{\Omega}$ values across all charge states. The maximum percent difference of 2.2% was observed at 47+, indicating minimal dependence on *P*. IgG4 $^{D}47\rightarrow$C arrival-time data was not analyzed. In sum, the $\widetilde{\Omega}$ values of IgG ions generated from denaturing conditions and subjected to CAPTR depended strongly on *C*, and CAPTR of multiple precursor ions of IgG1 suggests that $\Omega$ depends weakly on *P*.

## A4 Additional Results

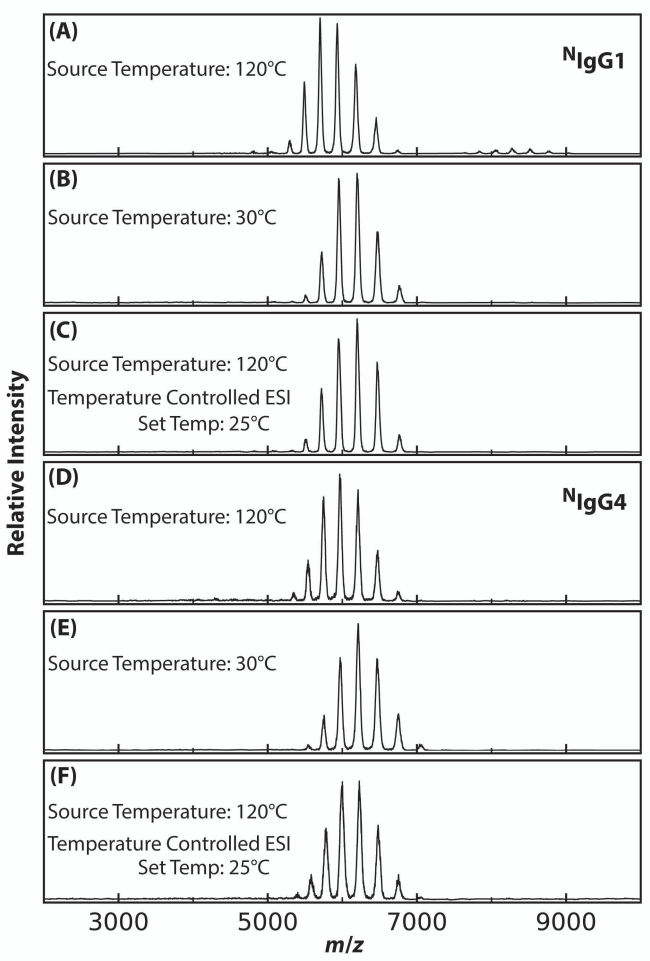


**Figure A1.** Native mass spectra of IgG1 (A, B, and C) and IgG4 (D, E, and F) under different source temperature conditions. (A) and (D) are mass spectra collected with the instrument source temperature set to 120 °C and no temperature control of the electrospray sample. (B) and (E) are mass spectra collected with the instrument source temperature set to 30 °C and no temperature control of the electrospray sample. (C) and (F) are mass spectra collected with the source temperature set to 120 °C and the use of a temperature-controlled nano-electrospray source with its sample temperature set to 25 °C.

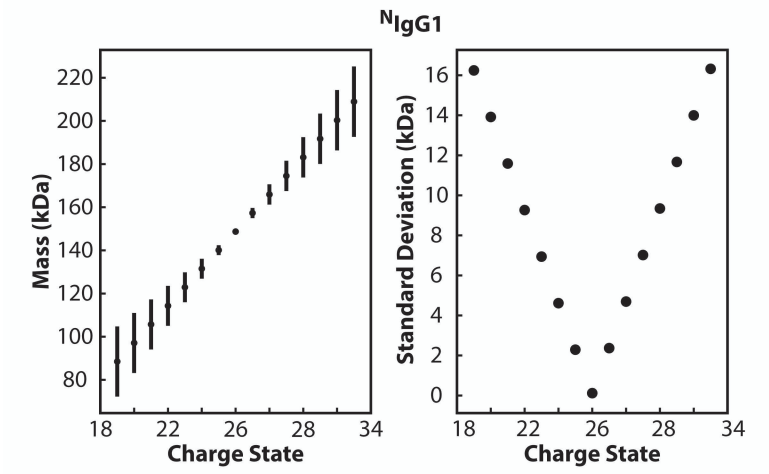


**Figure A2.** Mass and charge state determinations of IgG1 (native-like conditions) by performing CAPTR on the peak centered at 6195 *m*/*z* under minimally activating conditions. The precursor peak was assigned to a series of candidate charge states ranging from 19+ to 33+, and the product ion peaks were then assigned accordingly. The vertical bars on the left-hand plots represent the standard deviations associated with propagating the mass based on the candidate charge-state assignments. Those standard deviations are also shown on the right-hand plot. This analysis shows that the precursor ion had a charge state of 26+. From this analysis, the experimental mass of IgG1 was determined to be 148,714 ± 58 Da at a 95% confidence level.

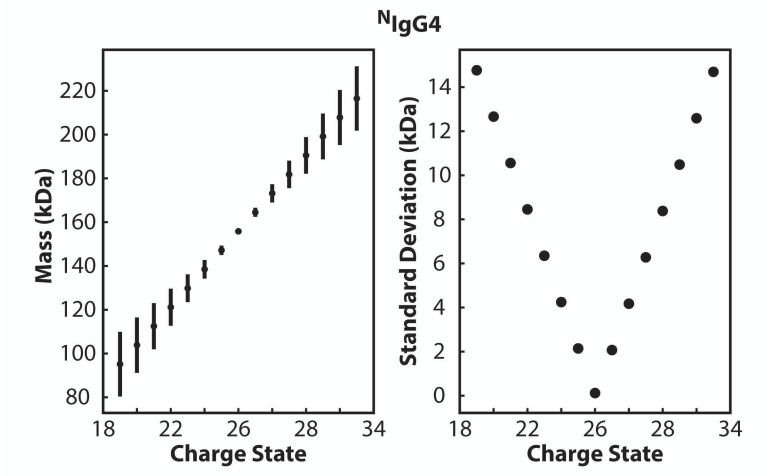


**Figure A3.** Mass and charge state determinations of IgG4 (native-like conditions) by performing CAPTR of the peak centered at 5997 *m*/*z* under minimally activating conditions. The precursor peak was assigned to a series of candidate charge states ranging from 19+ to 33+, and the product ion peaks were then assigned accordingly. The vertical bars on the left-hand plots represent the standard deviations associated with propagating the mass based on the candidate charge-state assignments. Those standard deviations are also shown on the right-hand plot. This analysis shows that the precursor ion had a charge state of 26+. From this analysis, the experimental mass of IgG4 was determined to be 155,826 ± 61 Da at a 95% confidence level.

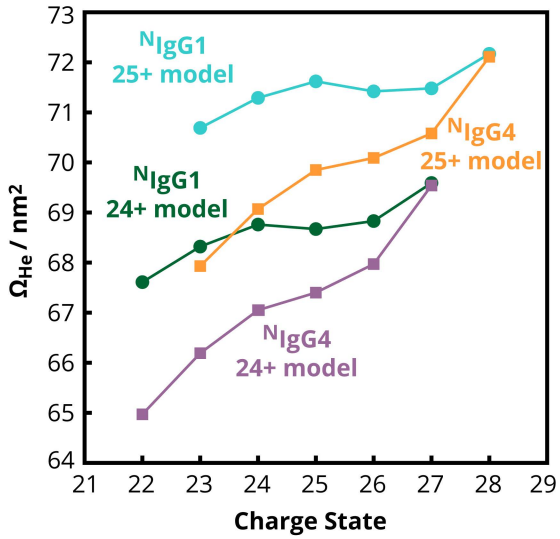


**Figure A4.** The mass and charge state assignments shown in Figure 2 were used to calculate $^{DT}\Omega_{He}$ values for $^{N}$IgG1 (green and blue) and $^{N}$IgG4 (orange and purple) ions generated from native-like conditions. With the correct charge-state assignments of 24+ for $^{N}$IgG1 ions (6195 *m*/*z*) and 25+ for $^{N}$IgG4 ions (6227 *m*/*z*), $^{N}$IgG1 and $^{N}$IgG4 ions of a given charge state exhibit small differences in Ω.

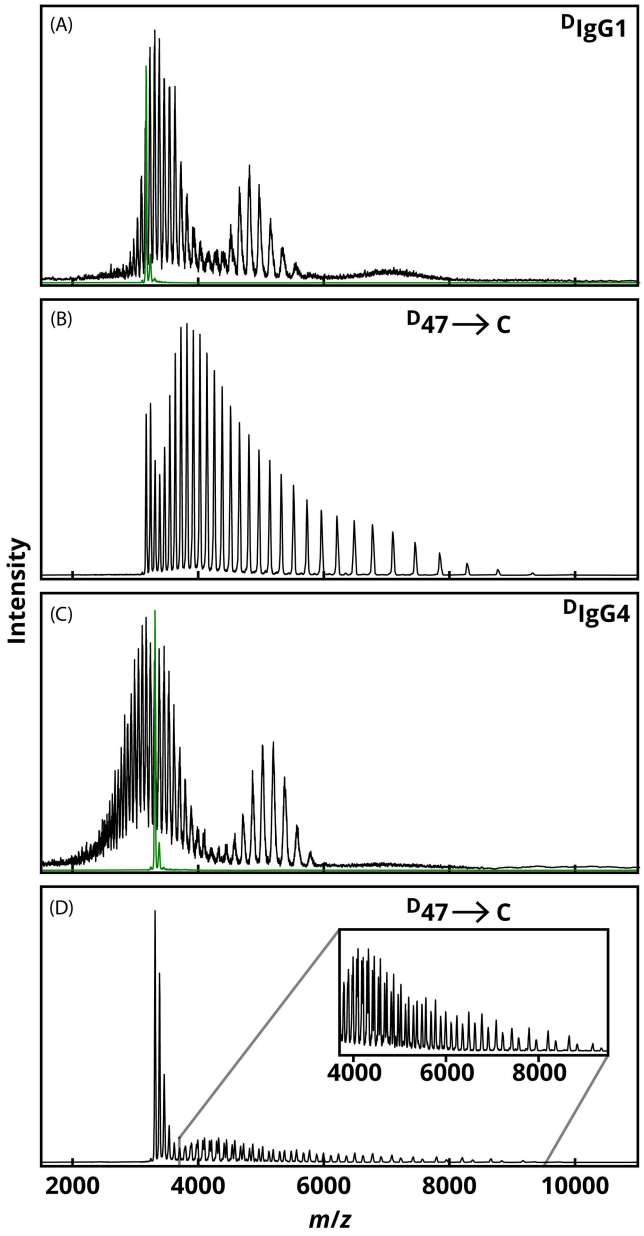


**Figure A5.** Precursor and $^{D}47\rightarrow C$ CAPTR mass spectra of IgGs from denaturing conditions. (A) Mass spectrum of $^{D}$IgG1 ions generated directly by ESI from denaturing solution conditions with the 47+ quadrupole-isolated precursor peak overlayed in green. (B) IgG1 $^{D}47\rightarrow C$ CAPTR mass spectrum. (C) Mass spectrum of $^{D}$IgG4 ions generated directly by ESI from denaturing solution conditions with the 47+ quadrupole-isolated precursor peak overlayed in green. (D) IgG4 $^{D}47\rightarrow C$ CAPTR mass spectrum with zoom inset to see resolved peaks.

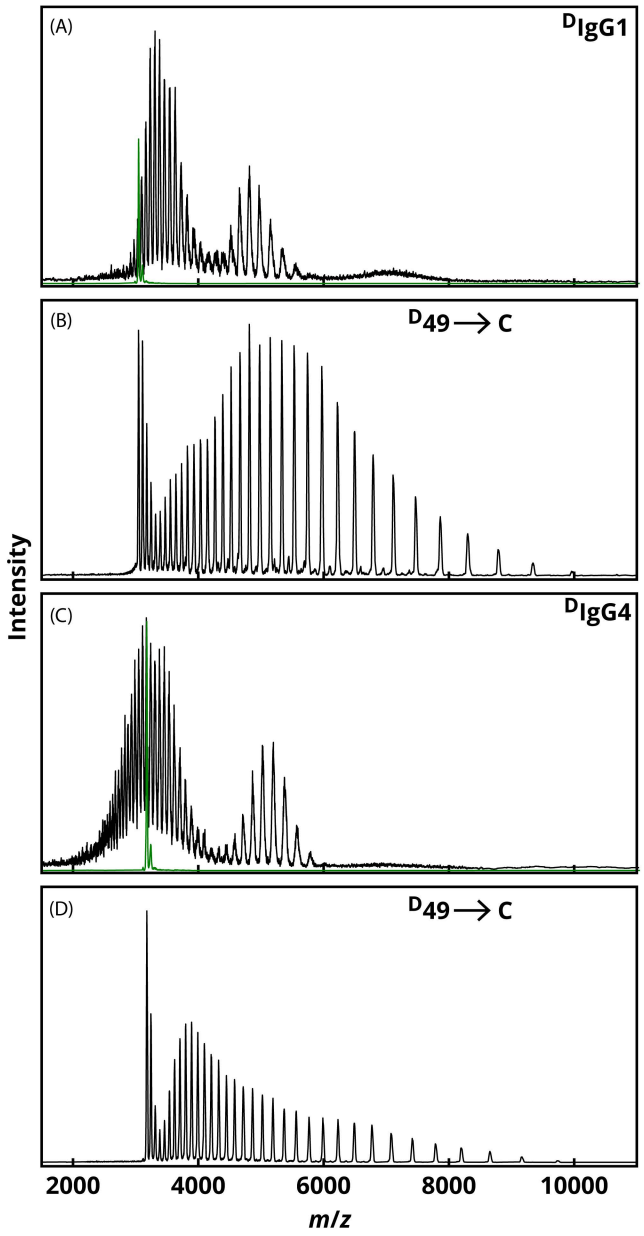


**Figure A6.** Precursor and $^{D}49\rightarrow C$ CAPTR mass spectra of IgGs from denaturing conditions. (A) Mass spectrum of $^{D}$IgG1 ions generated directly by ESI from denaturing solution conditions with the 49+ quadrupole-isolated precursor peak overlayed in green. (B) IgG1 $^{D}49\rightarrow C$ CAPTR mass spectrum. Some additional species become resolved, but they are of low intensity. (C) Mass spectrum of $^{D}$IgG4 ions generated directly by ESI from denaturing solution conditions with the 49+ quadrupole-isolated precursor peak overlayed in green. (D) IgG4 $49\rightarrow C$ CAPTR mass spectrum.

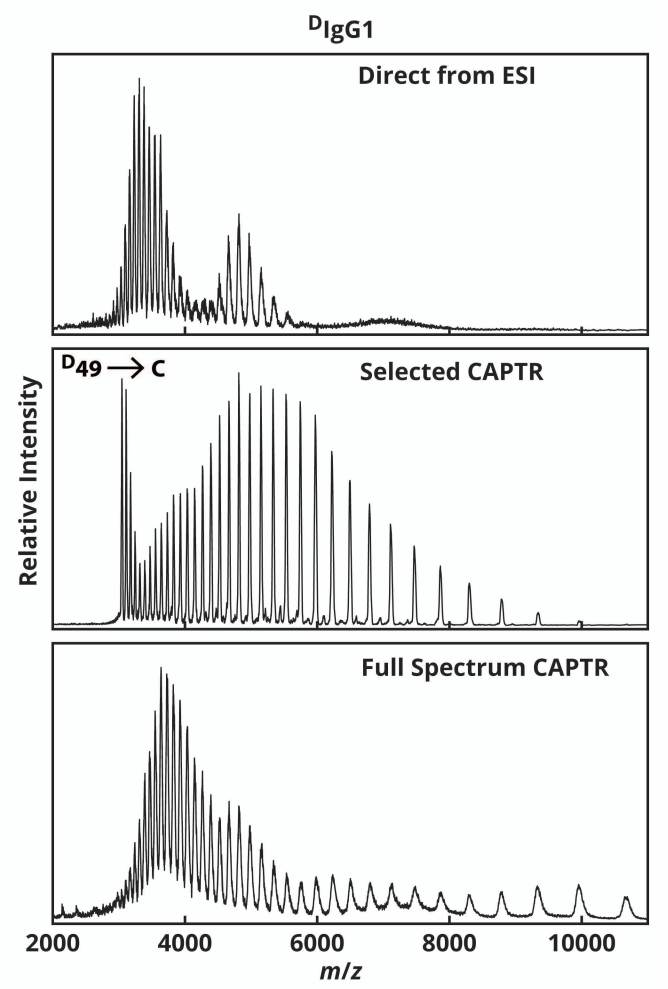


**Figure A7.** Comparing mass spectral resolution of $^{D}$IgG1 ions generated from ESI, quadrupole-selected $^{D}$IgG1 49+ ions subjected to CAPTR ($^{D}$49→*C*), and all $^{D}$IgG1 ions generated from ESI subjected to CAPTR.

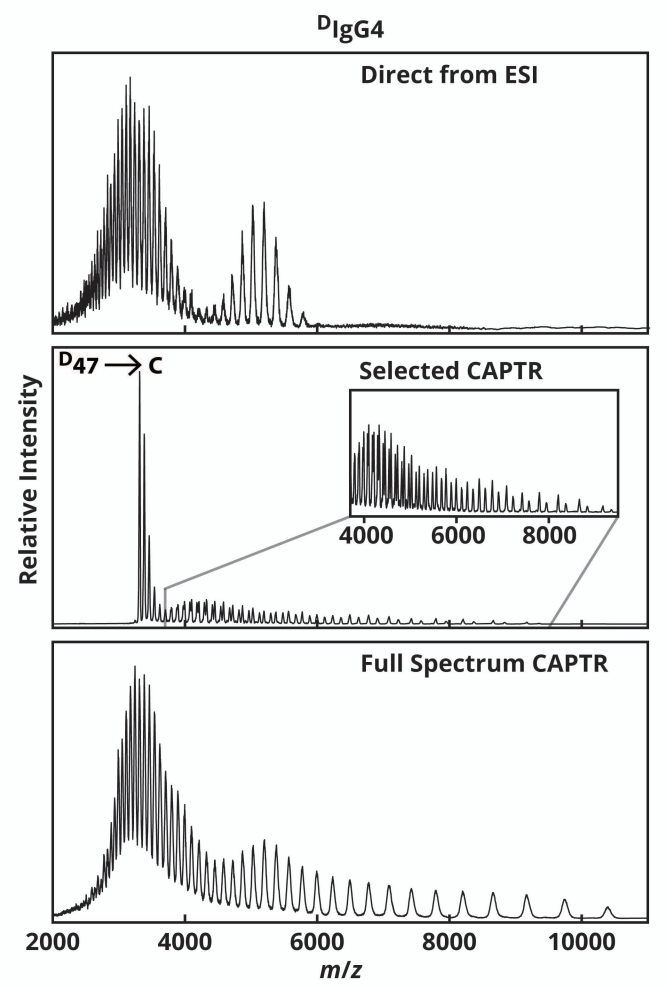


**Figure A8.** Comparing mass spectral resolution of $^{D}$IgG4 ions generated from ESI, quadrupole-selected $^{D}$IgG4 49+ ions subjected to CAPTR ($^{D}$47→*C*), and all $^{D}$IgG4 ions generated from ESI subjected to CAPTR.

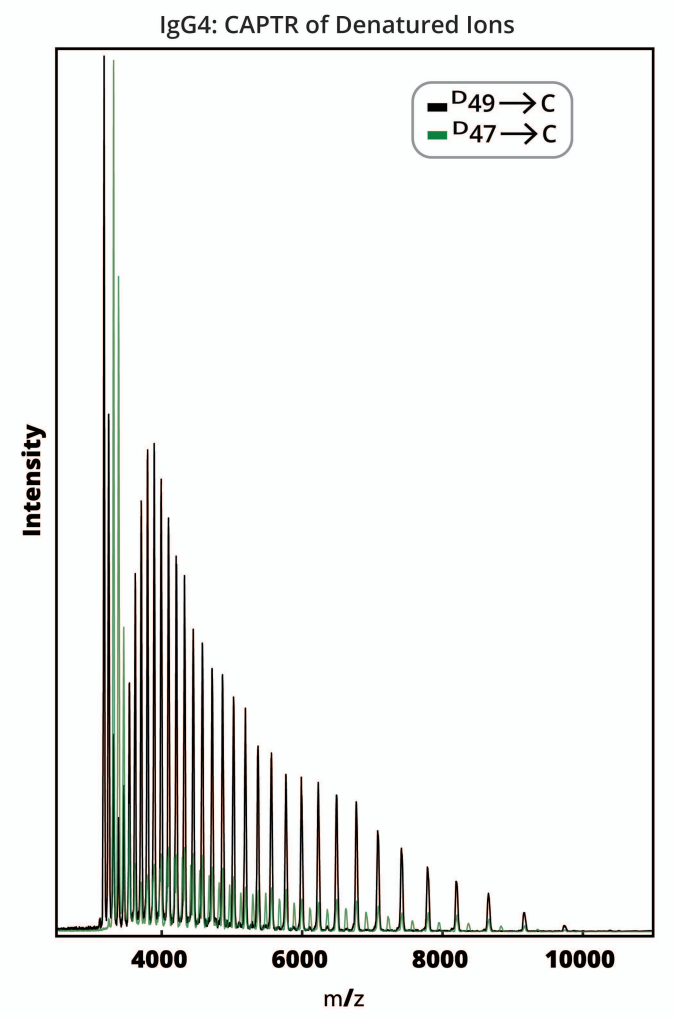


**Figure A9.** Overlaid CAPTR mass spectra of 47+ and 49+ $^{D}$IgG4.

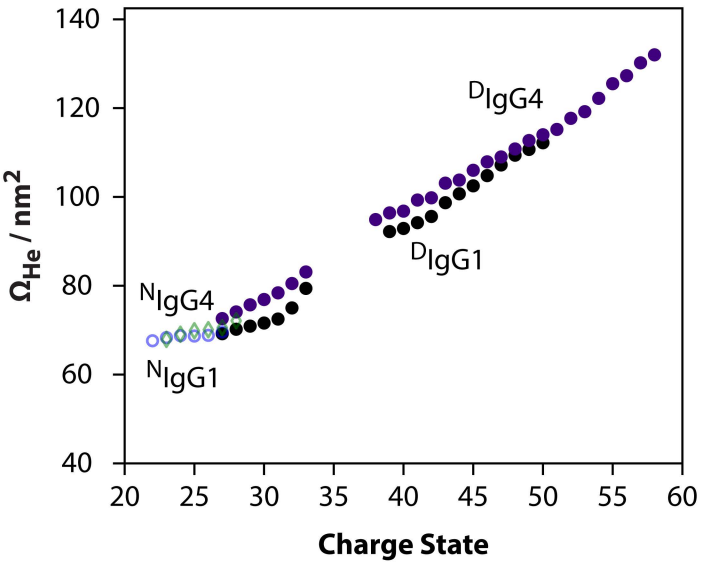


**Figure A10.** Centroid collision cross-section ($^{DT}\Omega_{He}$) values of IgG1 and IgG4 ions generated by electrospray from native-like and denaturing solution conditions, as determined from field-dependent measurements and in-house fitting software. Low intensities of 34+ to 38+ $^{D}$IgG1 ions and 34+ to 37+ $^{D}$IgG4 ions resulted in a significantly increased uncertainty in **Ω**, so they were excluded from analysis. $^{DT}\Omega_{He}$ values for $^{D}$IgG1 and $^{D}$IgG4 ions are similar to native-like ions of the same charge.

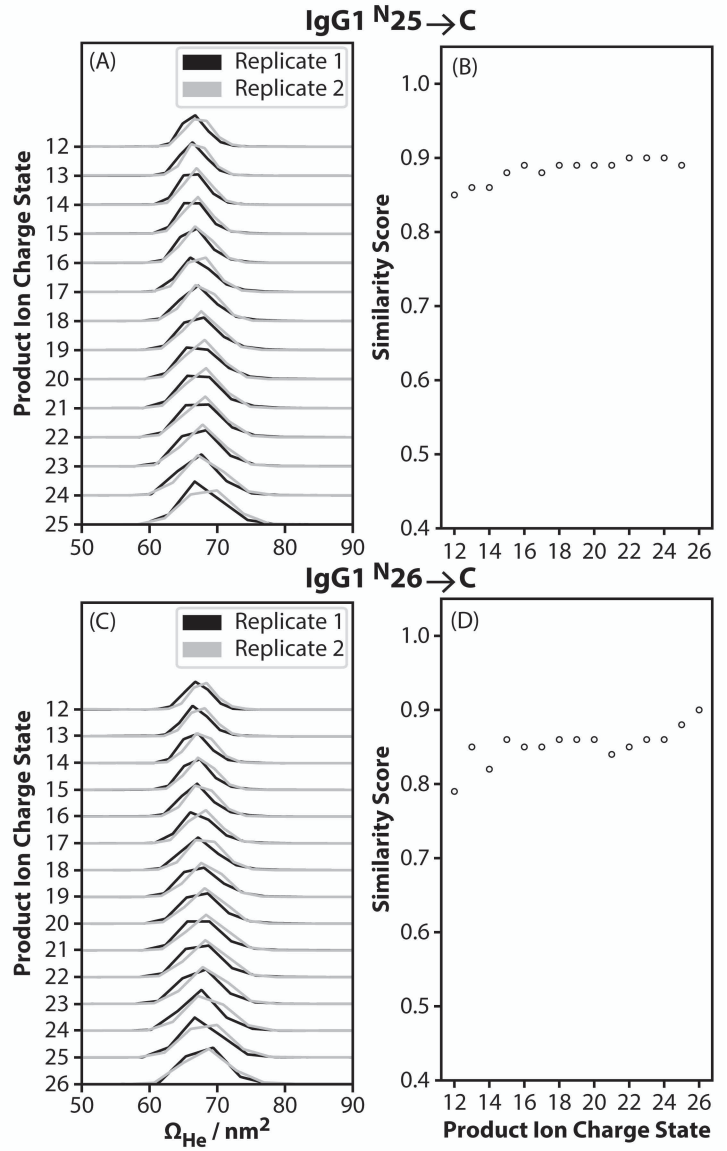


**Figure A11.** On the left, apparent **Ω** distributions of $^{N}25 \rightarrow C$ (A) and $^{N}26 \rightarrow C$ (C) IgG1 ions on different days (25 V sampling cone voltage). On the right, Jensen-Shannon scores comparing apparent **Ω** distributions of $^{N}25 \rightarrow C$ (B) and $^{N}26 \rightarrow C$ (D) IgG1 ions on different days.

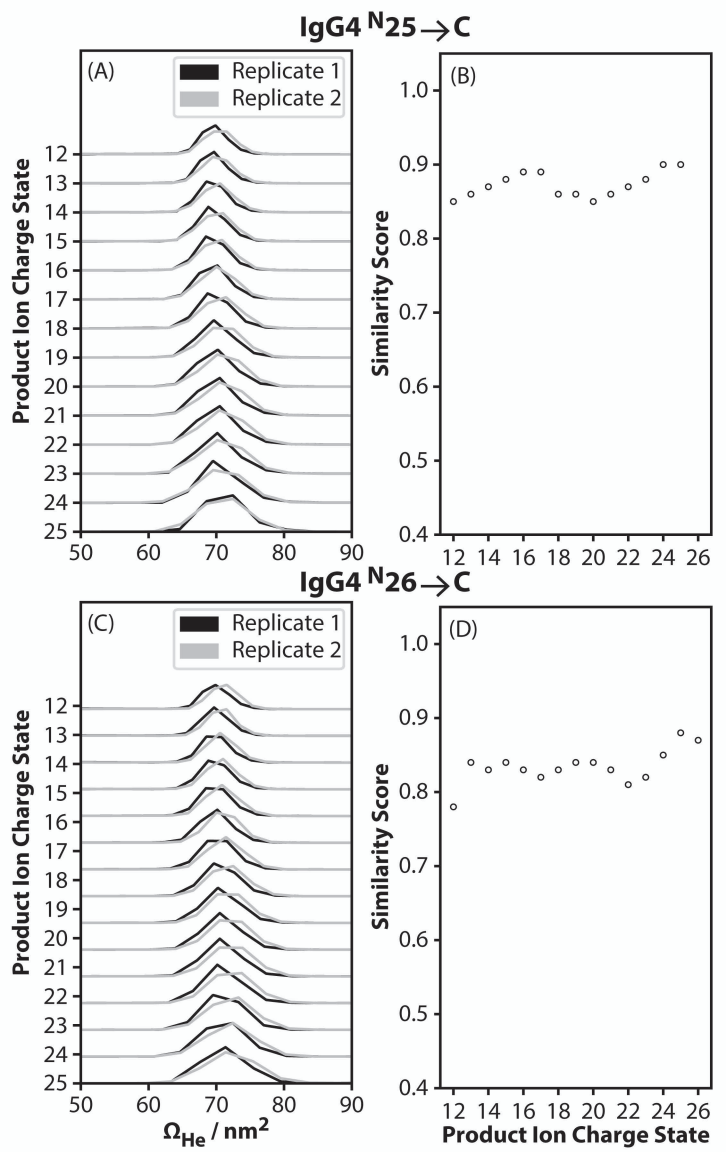


**Figure A12.** On the left, apparent Ω distributions of $^{N}25 \rightarrow C$ (A) and $^{N}26 \rightarrow C$ (C) IgG4 ions on different days (25 V sampling cone voltage). On the right, Jensen-Shannon scores comparing apparent Ω distributions of $^{N}25 \rightarrow C$ (B) and $^{N}26 \rightarrow C$ (D) IgG4 ions on different days.

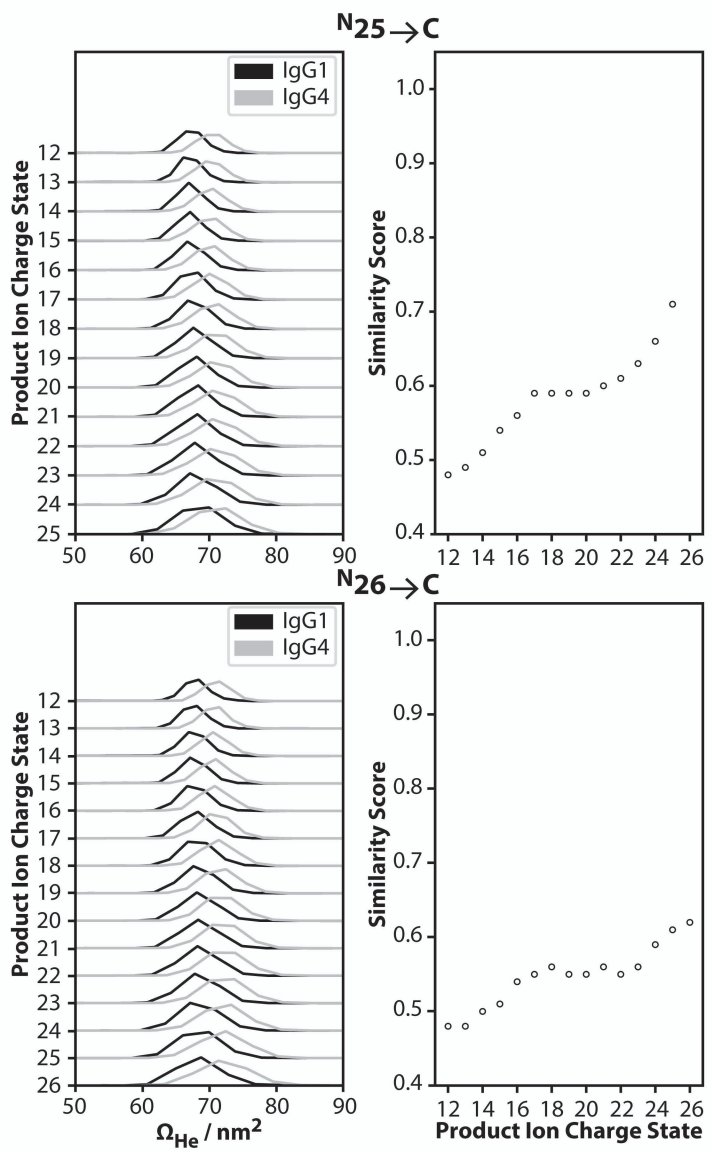


**Figure A13.** On the left, apparent **Ω** distributions of $^{N}25 \rightarrow C$ (A) and $^{N}26 \rightarrow C$ (C) CAPTR product ions of IgG1 and IgG4 (25 V sampling cone voltage). On the right, Jensen-Shannon scores comparing apparent **Ω** distributions of $^{N}25 \rightarrow C$ (B) and $^{N}26 \rightarrow C$ (D) IgG1 and IgG4 ions.

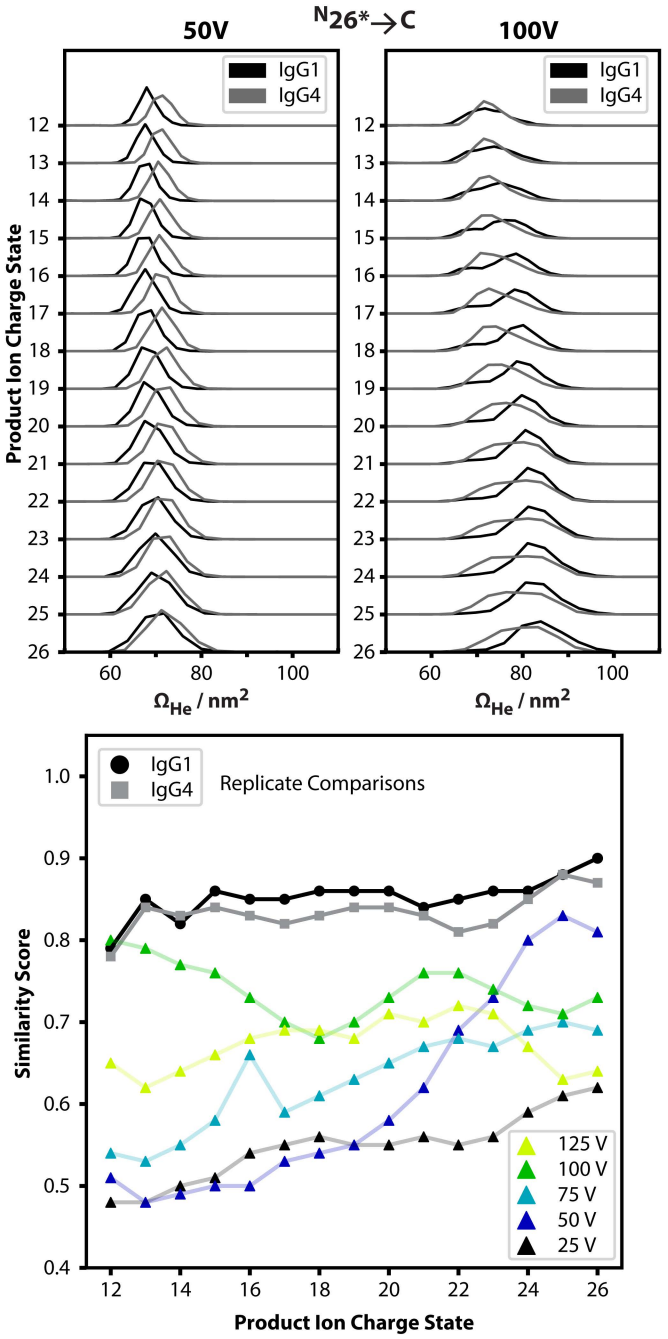


**Figure A14.** (A) and (B) show apparent Ω distributions observed for $^{N}$IgG1 and $^{N}$IgG4 ions 26+ ions subjected to pre-CAPTR activation ($^{N}$26* → *C*) with a sampling cone voltage of 50 V and 100 V, respectively. (C) shows the Jensen-Shannon similarity scores calculated for the comparison of apparent Ω distributions of IgG1 and IgG4 $^{N}$26* → *C* ions for each pre-CAPTR activation voltage tested.

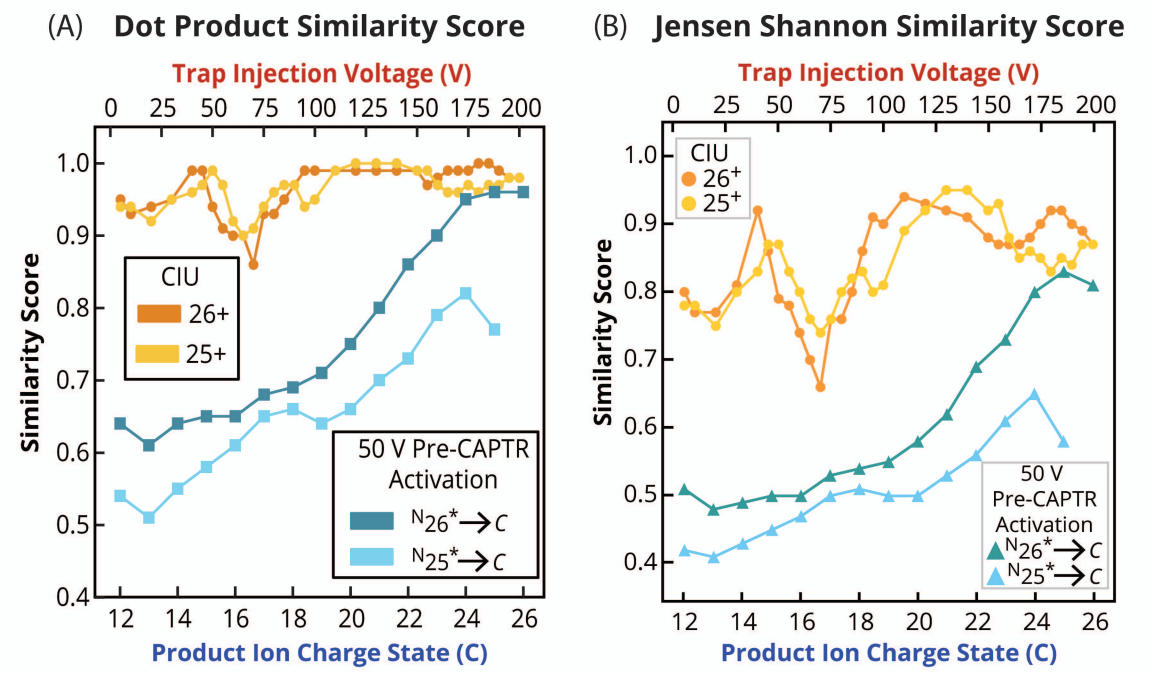


**Figure A15.** Comparison of similarity scoring functions. A and B show the scores of the apparent $^{DT}\Omega_{He}$ distributions of $^{N}$IgG1 and $^{N}$IgG4 CAPTR products and residual precursor (25+ and 26+) ions at 50 V pre-CAPTR activation versus charge state (cool colors), and the scores of apparent DTΩHe distributions of NIgG1 and NIgG4 precursor ions (25+ and 26+) subjected to collision-induced unfolding versus trap injection voltage (warm colors). (A) presents results using a dot product based similarity score reported previously5 and (B) presents results using the Jensen-Shannon similarity score used in this study.

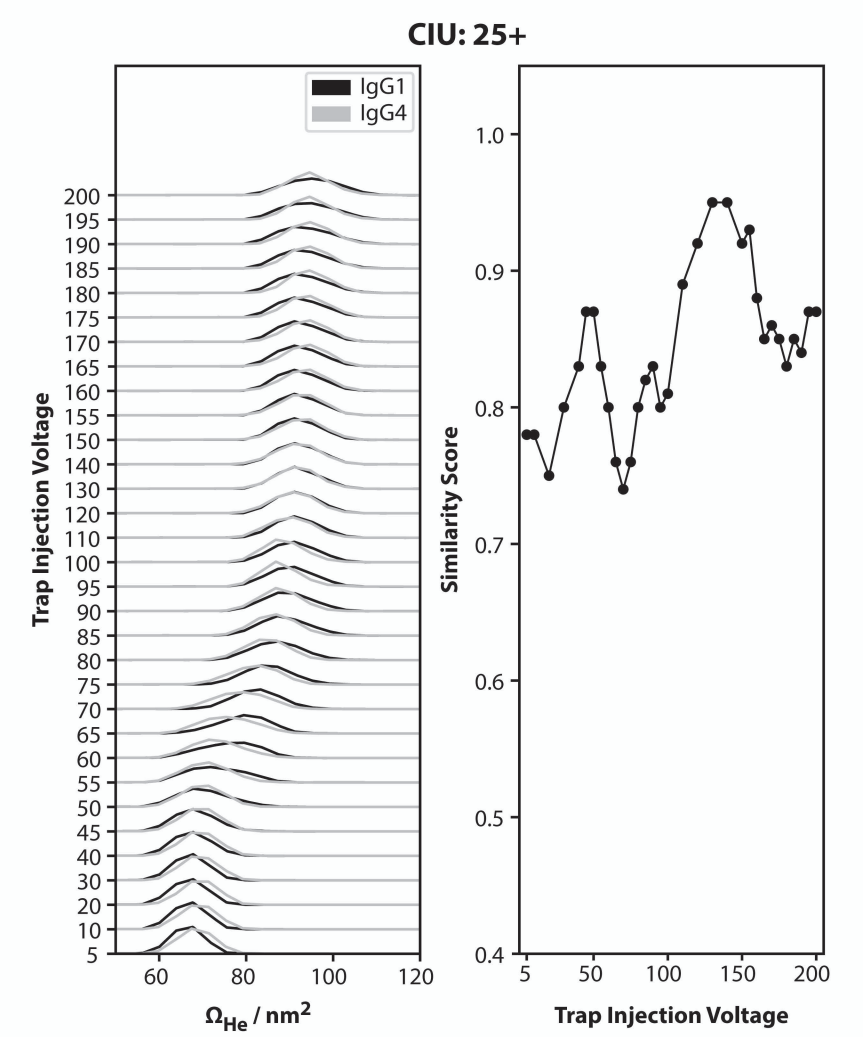


**Figure A16.** (A) Apparent $^{DT}\Omega_{He}$ distributions of $^{N}$IgG1 and $^{N}$IgG4 25+ ions subjected to collision-induced unfolding (CIU) in the trap cell. (B) Corresponding Jensen-Shannon similarity scores for comparison of the apparent $^{DT}\Omega_{He}$ distributions of $^{N}$IgG1 and $^{N}$IgG4 25+ ions at each trap collision voltage.

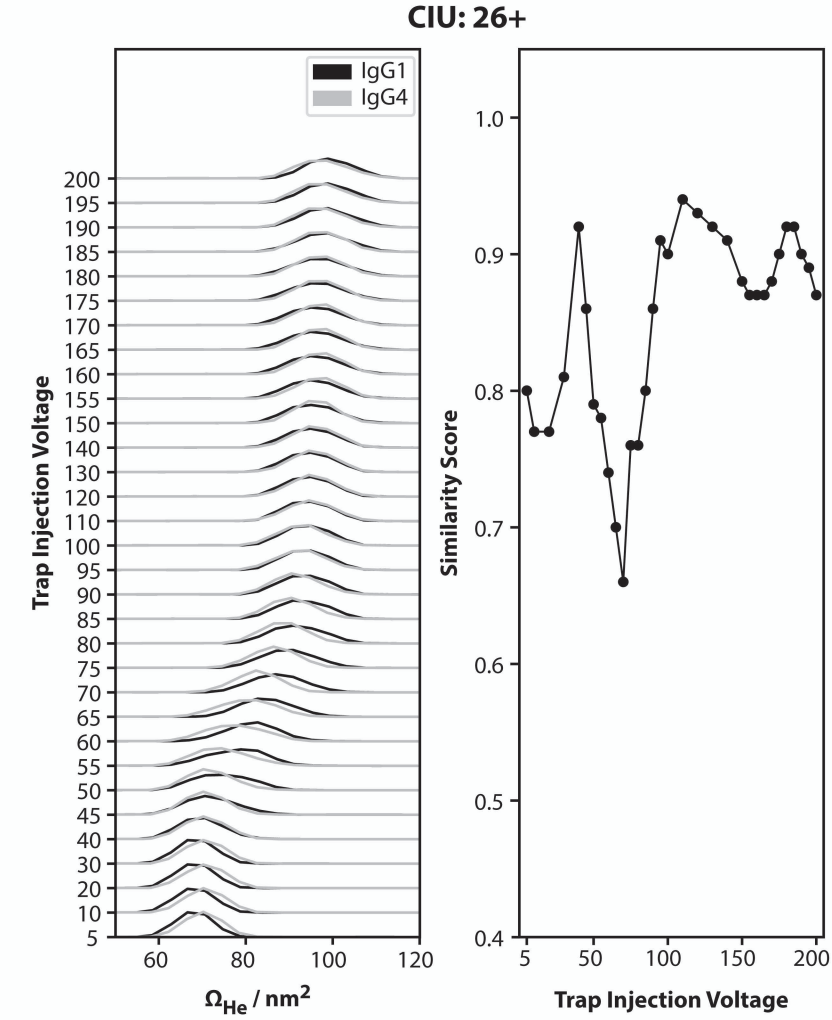


**Figure A17.** (A) Apparent $^{DT}\Omega_{He}$ distributions of $^{N}$IgG1 and $^{N}$IgG4 26+ ions subjected to collision-induced unfolding (CIU) in the trap cell. (B) Corresponding Jensen-Shannon similarity scores for comparison of the apparent $^{DT}\Omega_{He}$ distributions of $^{N}$IgG1 and $^{N}$IgG4 26+ ions at each trap collision voltage.

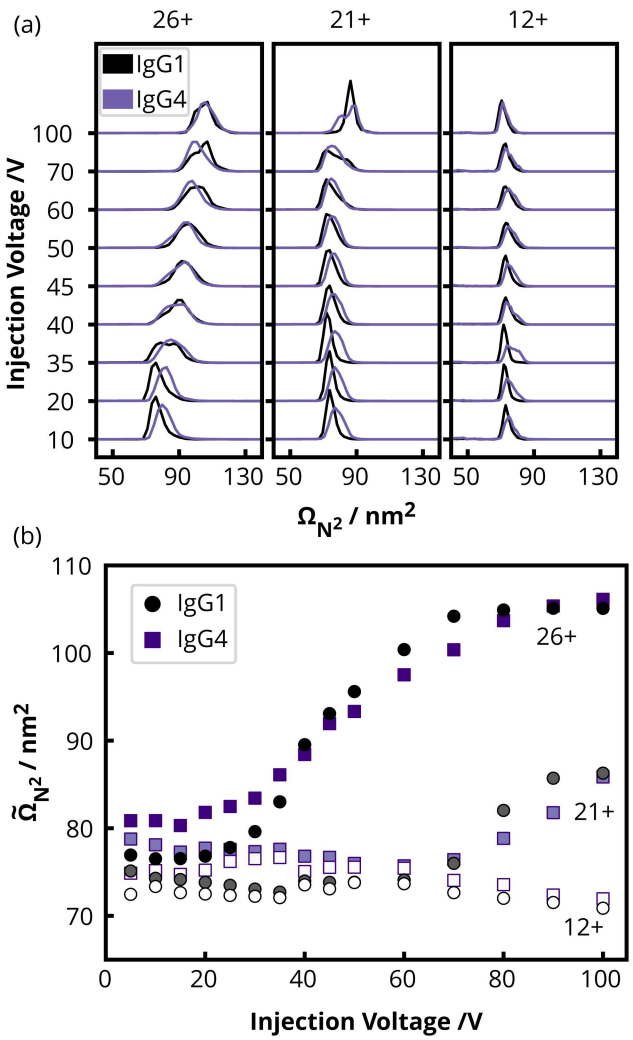


**Figure A18**. Post-CAPTR activation of $^{N}$IgG1 and $^{N}$IgG4. (a) Apparent $^{DT}\Omega_{N_2}$ distributions of $^{N}$26→26*, $^{N}$26→21*, and $^{N}$26→12* ions of IgG1 (black) and IgG4 (light purple) at selected mobility cell injection voltages. (b) $\tilde{\Omega}_{N_2}$ values of $^{N}$26→26*, $^{N}$26→21*, and $^{N}$26→12* ions of IgG1 (black, grey, and white circles) and IgG4 (dark purple, light purple, and white squares) as a function of mobility cell injection voltage.

**A5 References**

(1) Gadzuk-Shea, M. M.; Bush, M. F. Effects of Charge State on the Structures of Serum Albumin Ions in the Gas Phase: Insights from Cation-to-Anion Proton-Transfer Reactions, Ion Mobility, and Mass Spectrometry. *J. Phys. Chem. B* **2018**, *122* (43), 9947–9955. https://doi.org/10.1021/acs.jpcb.8b08427.

(2) Bush, M. F.; Campuzano, I. D. G.; Robinson, C. V. Ion Mobility Mass Spectrometry of Peptide Ions: Effects of Drift Gas and Calibration Strategies. *Anal. Chem.* **2012**, *84* (16), 7124–7130. https://doi.org/10.1021/ac3014498.

(3) Mason, E.; McDaniel, W. *Transport Properties of Ions in Gases*; Wiley, 1988.

(4) Lin, J. Divergence Measures Based on the Shannon Entropy. *IEEE Trans. Inf. Theory* **1991**, *37* (1), 145–151. https://doi.org/10.1109/18.61115.

(5) Hong, S.; Bush, M. F. Collision-Induced Unfolding Is Sensitive to the Polarity of Proteins and Protein Complexes. *J. Am. Soc. Mass Spectrom.* **2019**, *30* (11), 2430–2437. https://doi.org/10.1007/s13361-019-02326-z.

# Appendix B: Supporting Information for Chapter 3.

## B1 Additional Results and Experimental Details

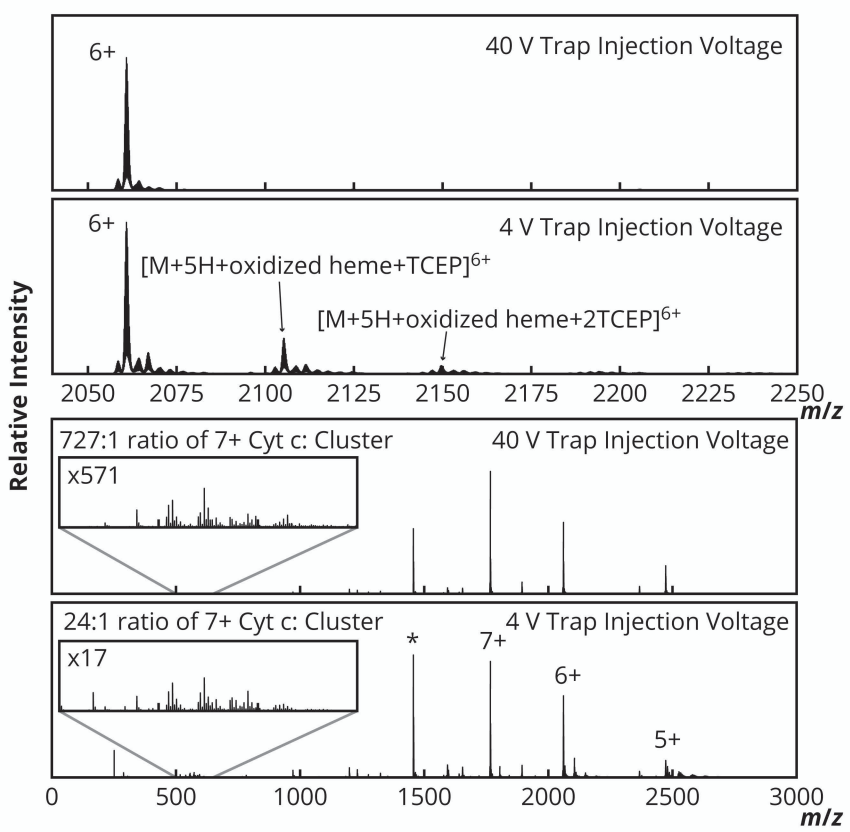


**Figure B1**. Comparison of mass spectra of Cyt *c* in 200 mM ammonium acetate, 1 mM TCEP, at pH 7 with a setting of 4 V of trap injection voltage or 40 V trap injection voltage. The ratios of Cyt *c* to TCEP cluster were calculated using the intensity of the most abundant isotope of the $[M+6H+ \text{ reduced heme}]^{7+}$ Cyt *c* peak and the most intense TCEP cluster peak in the region of 500 to 600 *m*/*z* (573.00 *m*/*z*). This group of TCEP clusters represents combinations of at least 2 TCEP molecules, reduced or oxidized (+O), with charge originating from combinations of protons, potassium, or sodium. The absolute intensity of the 573 *m*/*z* drops from 7.29e3 to 535 with the increased collisional activation, and the adducts of the 6+ Cyt *c* peaks decrease to negligible levels. The sum of the absolute intensity over the *m*/*z* range 2055-2072 (6+ Cyt *c* with no TCEP adducts) increases by 39% with the application of 40 V.

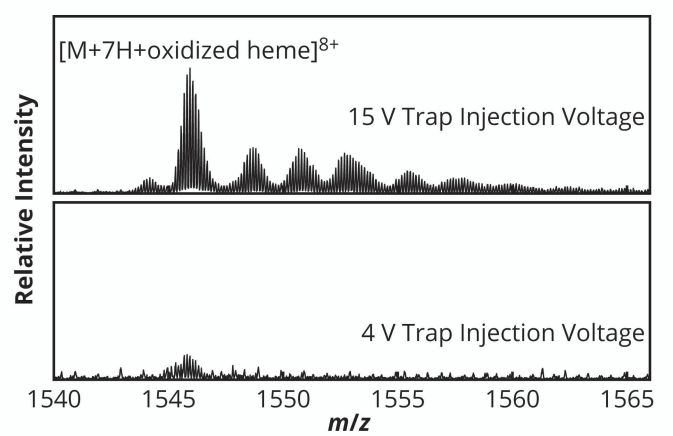


**Figure B2**. Mass spectra of 8+ Cyt *c* in 200 mM ammonium acetate with 1 mM TCEP at pH 6 collected at trap injection voltages of 4 V and 15 V.

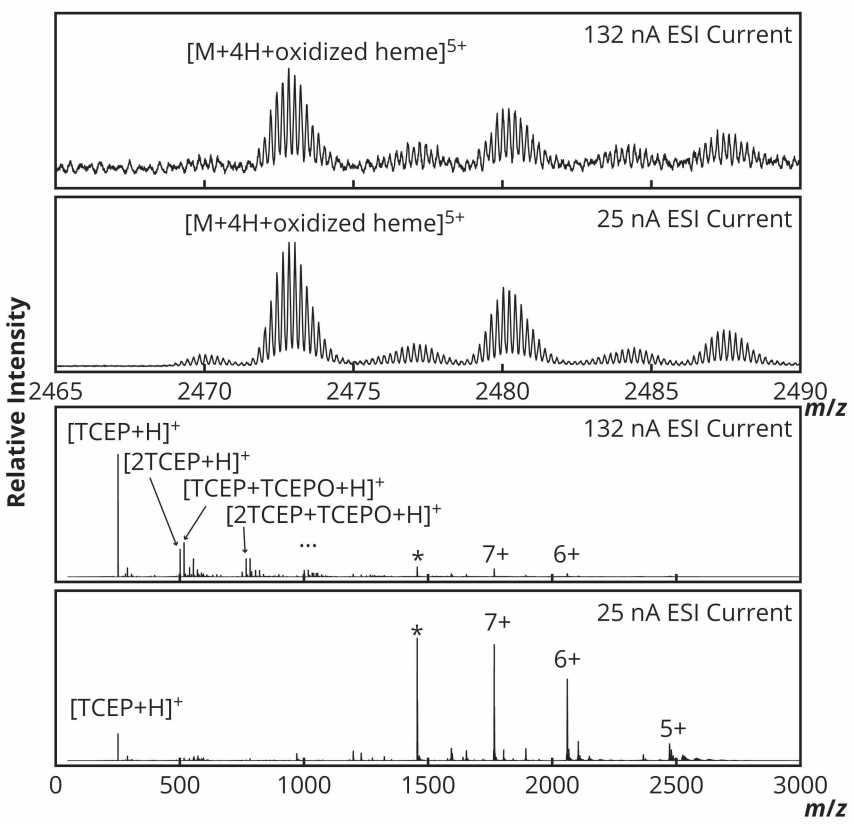


**Figure B3**. Comparison of mass spectra of Cyt *c* in 200 mM ammonium acetate, 1 mM TCEP, at pH 7 electrospray-generated with 25 nA of current or 132 nA of current. TCEPO represents oxidized TCEP.

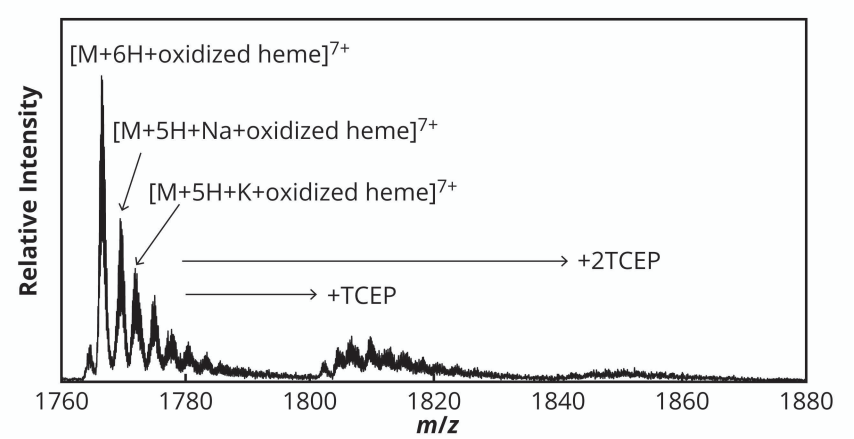


**Figure B4**. Mass Spectra of Cyt *c* prepared in 200 mM ammonium acetate with 50 uM TCEP without pH adjustment, collected on the Synapt G2.

| Charge State of Cytochrome *c* | DTT | βME | TCEP |
|---|---|---|---|
| 5 | 2460-2560 *m*/*z* | 2460-2560 *m*/*z* | 2460-3150 *m*/*z* |
| 6 | 2055-2150 *m*/*z* | 2055-2150 *m*/*z* | 2055-2340 *m*/*z* |
| 7 | 1760-1800 *m*/*z* | 1760-1800 *m*/*z* | 1760-1850 *m*/*z* |
| 8 | 1540-1570 *m*/*z* | 1540-1570 *m*/*z* | 1540-1570 *m*/*z* |
| 9 | 1370-1390 *m*/*z* | 1370-1390 *m*/*z* | Not Observed |
| 10 | 1230-1250 *m*/*z* | Not Observed | Not Observed |

**Table B1**. *m*/*z* ranges extracted for average charge state calculations.

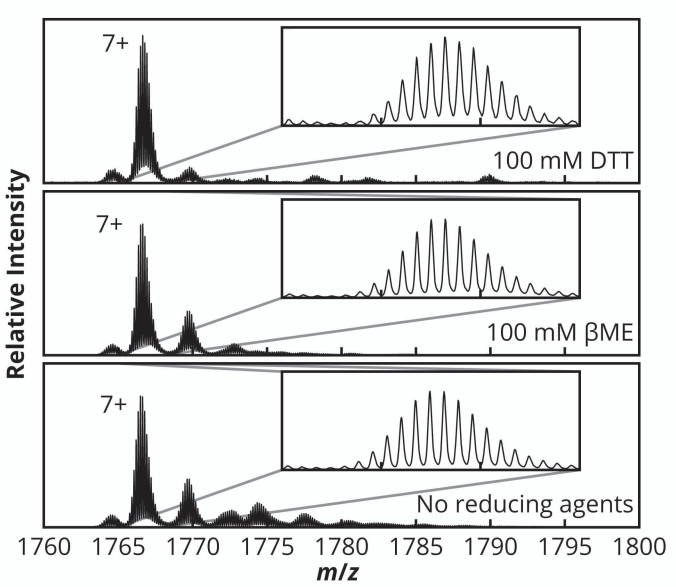


**Figure B5**. Mass spectral results after the addition of 100 mM DTT or 100 mM βME to Cyt *c* in 200 mM ammonium acetate at pH 7. No shifts in the isotope distributions of 7+ Cyt *c* are observed. Both reducing agents may be influencing the presence of salt adducts (Na+, K+) in comparison to the no reducing agent condition. At high concentrations of DTT, a low intensity peak arises at around 1790 *m*/*z* which corresponds to a modification of about 162 Da. It is present at low intensity with all Cyt *c* mass spectral peaks. Intact, reduced DTT has a mass of 154.25 Da. This 162 Da modification is currently unidentified.

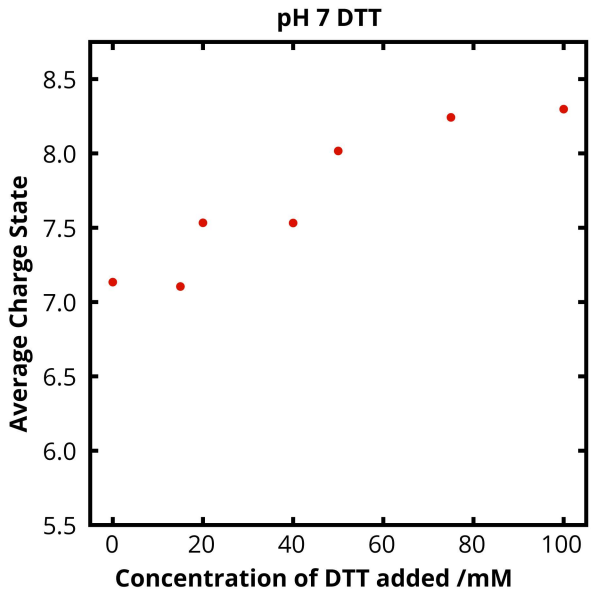


**Figure B6**. Average charge state of Cyc *c* in 200 mM ammonium acetate with various concentrations of DTT at pH 7. This is a replicate of experiments discussed in the main text.

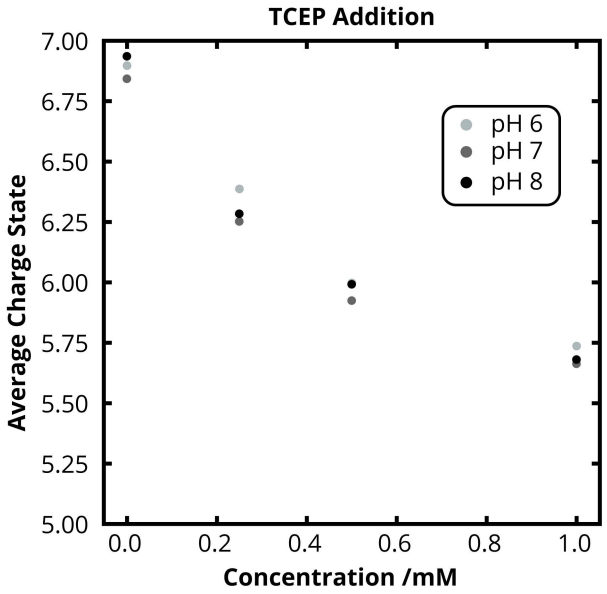


**Figure B7**. Average Charge State of Cyt *c* in 200 mM ammonium acetate with various concentrations of TCEP at pH 6, 7, and 8.

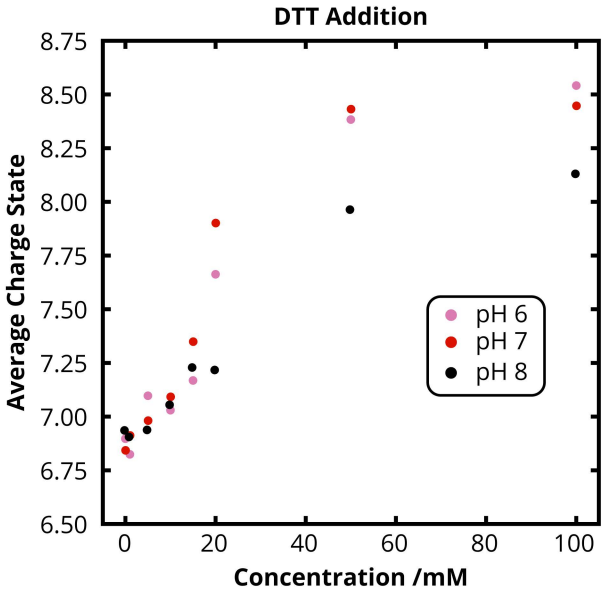


**Figure B8**. Average Charge State of Cyt *c* in 200 mM ammonium acetate with various concentrations of DTT at pH 6, 7, and 8.

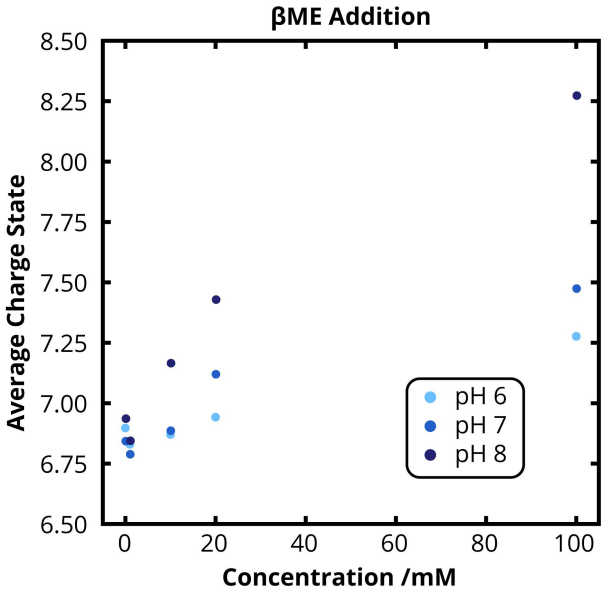


**Figure B9**. Average Charge State of Cyt *c* in 200 mM ammonium acetate with various concentrations of βME at pH 6, 7, and 8.

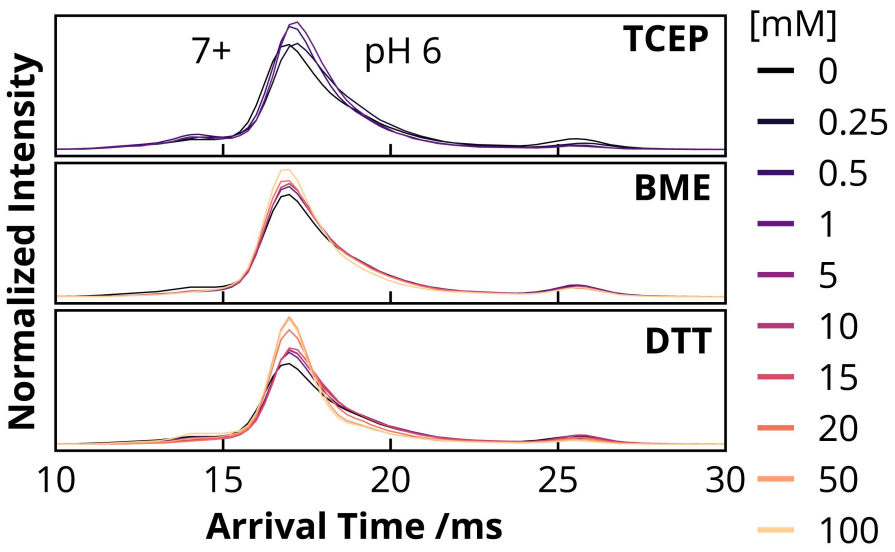


**Figure B10**. Cyclic ion mobility arrival time distributions of 7+ Cyt *c* (1760 to 1800 *m*/*z*) in 200 mM ammonium acetate, pH 6, with and without reducing agents.

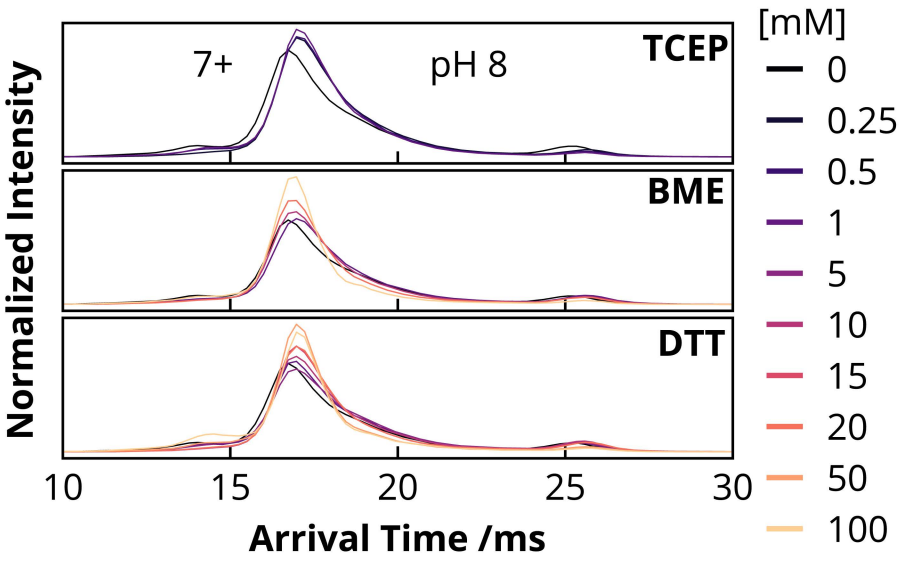


**Figure B11**. Cyclic ion mobility arrival time distributions of 7+ Cyt *c* (1760 to 1800 *m*/*z*) in 200 mM ammonium acetate, pH 8, with and without reducing agents.

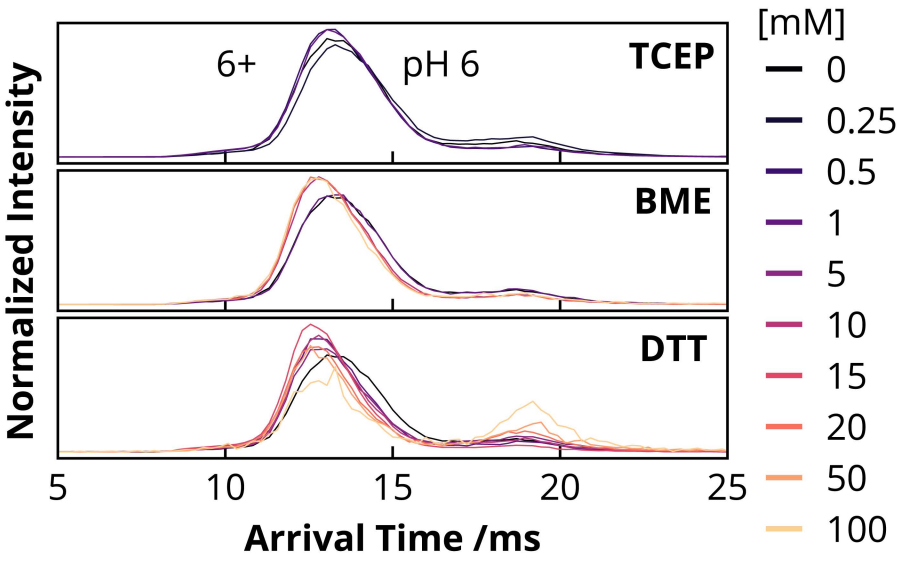


**Figure B12**. Cyclic ion mobility arrival time distributions of 6+ Cyt *c* (1760 to 1800 *m*/*z*) in 200 mM ammonium acetate, pH 6, with and without reducing agents.

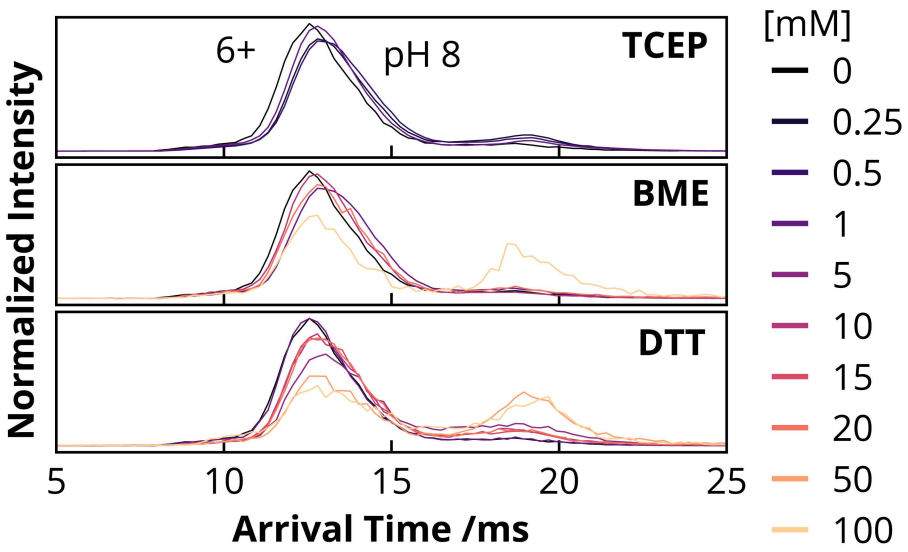


**Figure B13**. Cyclic ion mobility arrival time distributions of 6+ Cyt *c* (1760 to 1800 *m*/*z*) in 200 mM ammonium acetate, pH 8, with and without reducing agents.

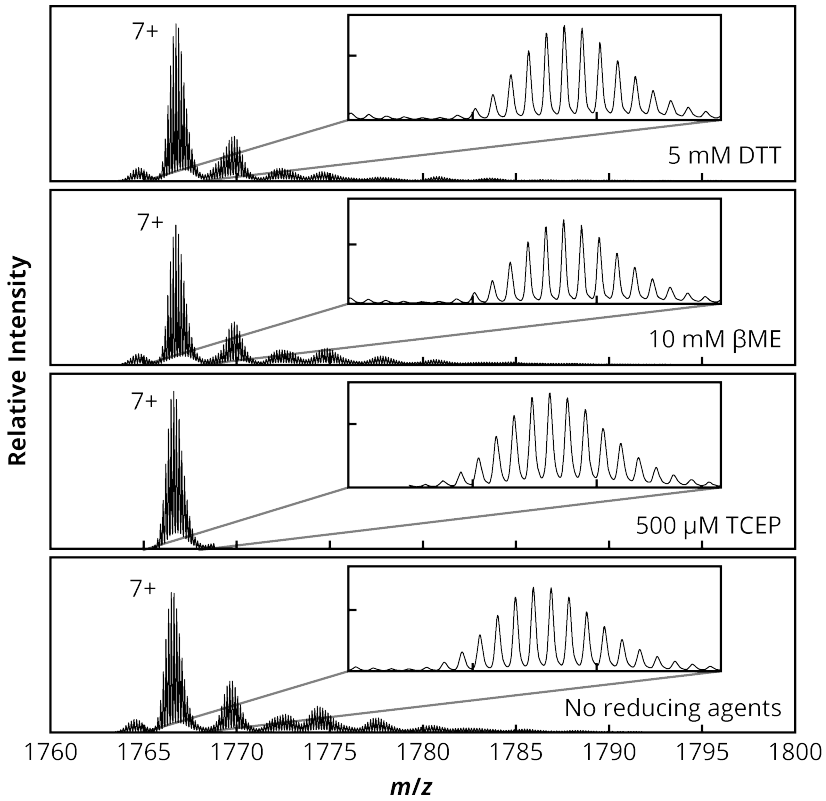


**Figure B14**. Mass spectral results from incubation of Cyt *c* with reducing agents. A minute shift to higher *m*/*z* is observed following incubation with DTT or βME.

# Appendix C: Supporting Information for Chapter 4.

## C1 Additional Results

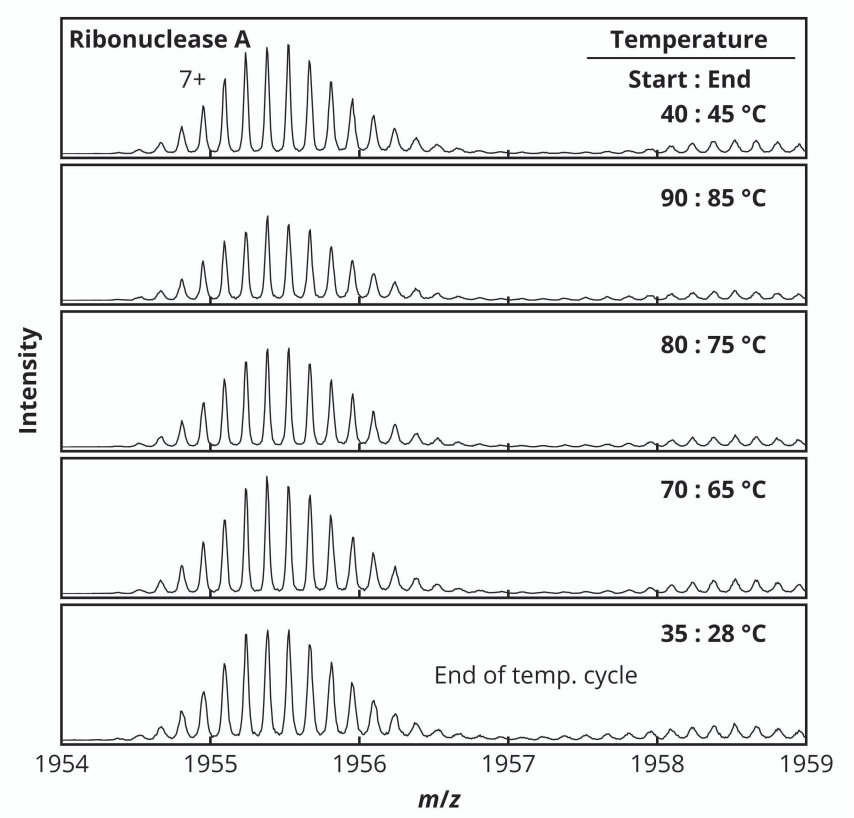


**Figure C1**. Selected spectra of the 7+ species from a ±30 °C $min^{-1}$ temperature cycle of Ribonuclease A (RbA) without reducing agents. Start and end temperatures indicate the range of temperatures over which mass spectra were signal-averaged. No significant changes in the isotope distributions are observed over a temperature cycle in the absence of DTT.

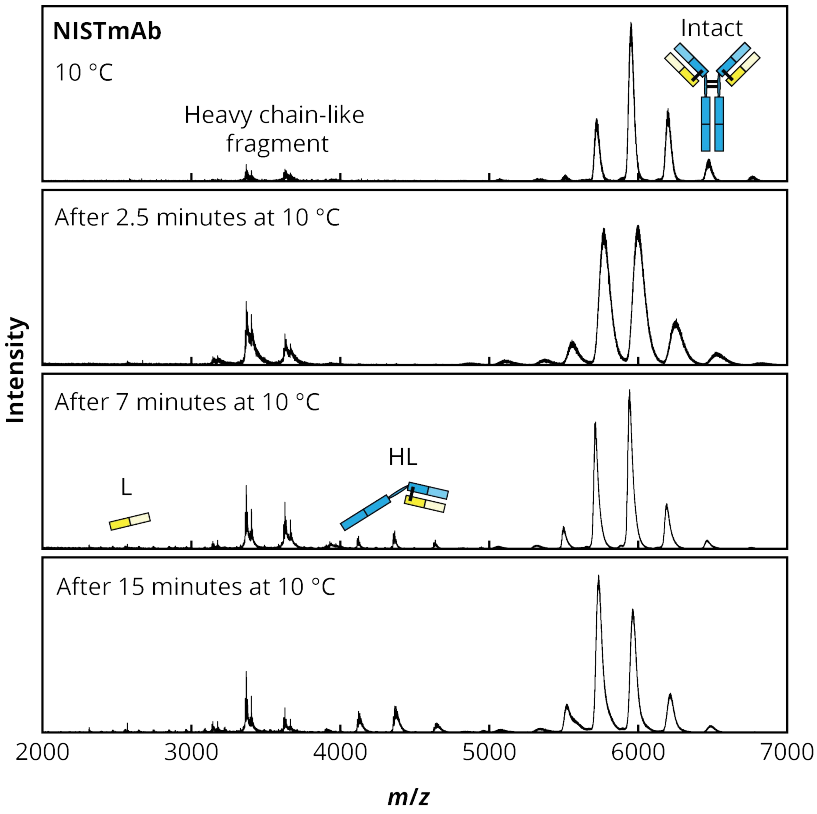


**Figure C2**. Mass spectra (collected on different days) of NISTmAb after incubation at 10 °C in the presence of 2 mM DTT. Compared to temperature cycles performed over 11 minutes (±9 °C $min^{-1}$ from 10 to 65 to 25 °C), disulfide bond reduction is slowed significantly.

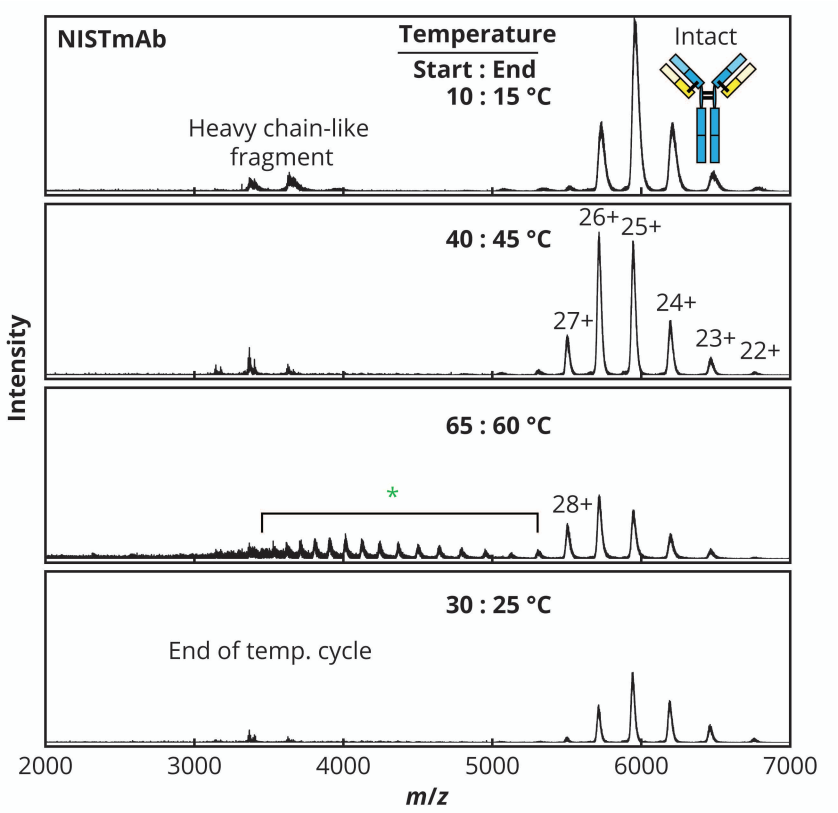


**Figure C3**. Selected spectra from a ±9 °C $min^{-1}$ temperature cycle of NISTmAb in the absence of reducing agents. The y-axis absolute intensity maxima are the same for all four plots so that differences in intensity over the course of the temperature cycle can be appreciated. The green asterisk highlights a region that may correspond to highly charged intact NISTmAb. It is unlikely that these peaks correspond to half mAbs (HL) because no HL is observed at the end of the cycle. The H-like fragment is also observed in the absence of DTT.

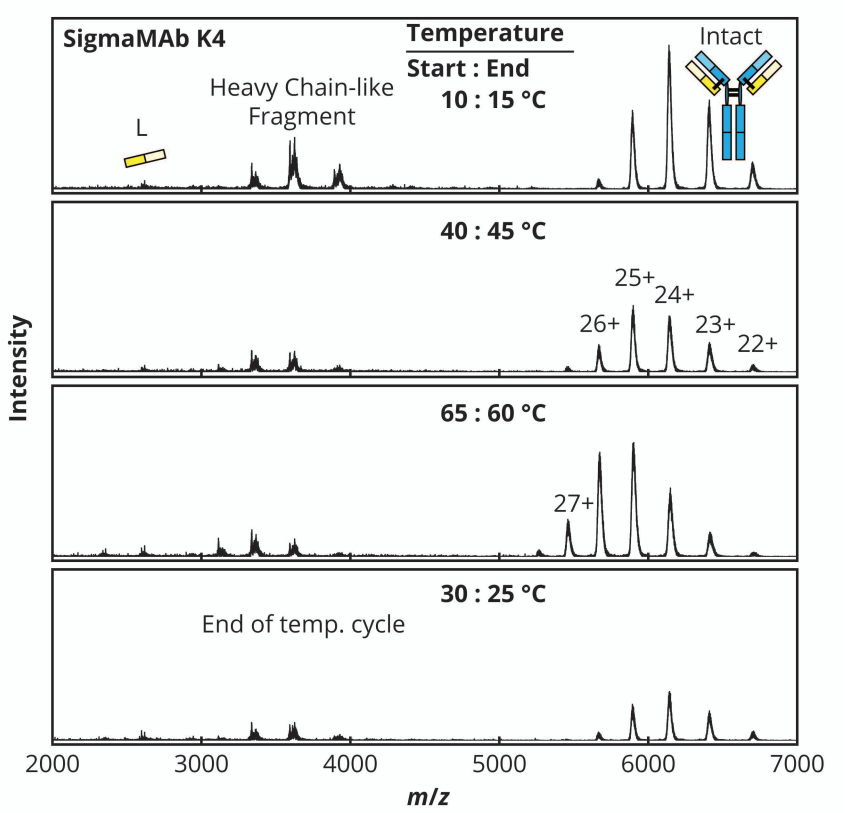


**Figure C4**. Selected spectra from a ±9 °C $min^{-1}$ temperature cycle of SigmaMAb K4 in the absence of reducing agents. The y-axis absolute intensity maxima are the same for all four plots so that differences in intensity over the course of the temperature cycle can be appreciated. L products are observed at low intensity in the absence of reducing agent. The H-like fragment is also observed in the absence of DTT.

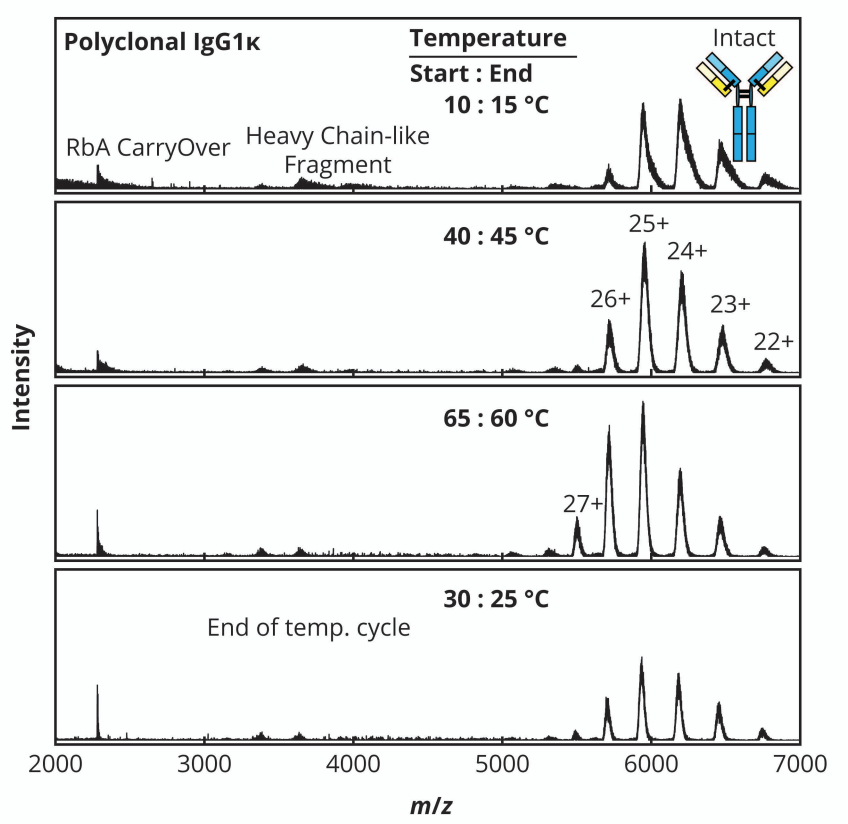


**Figure C5**. Selected spectra from a ±9 °C $min^{-1}$ temperature cycle of polyclonal IgG1κ in the absence of reducing agents. The y-axis absolute intensity maxima are the same for all four plots so that differences in intensity over the course of the temperature cycle can be appreciated. Some RbA carryover from previous runs is visible in the lower *m*/*z* range, but no L or HL products are observed over the course of a cycle in the absence of DTT.

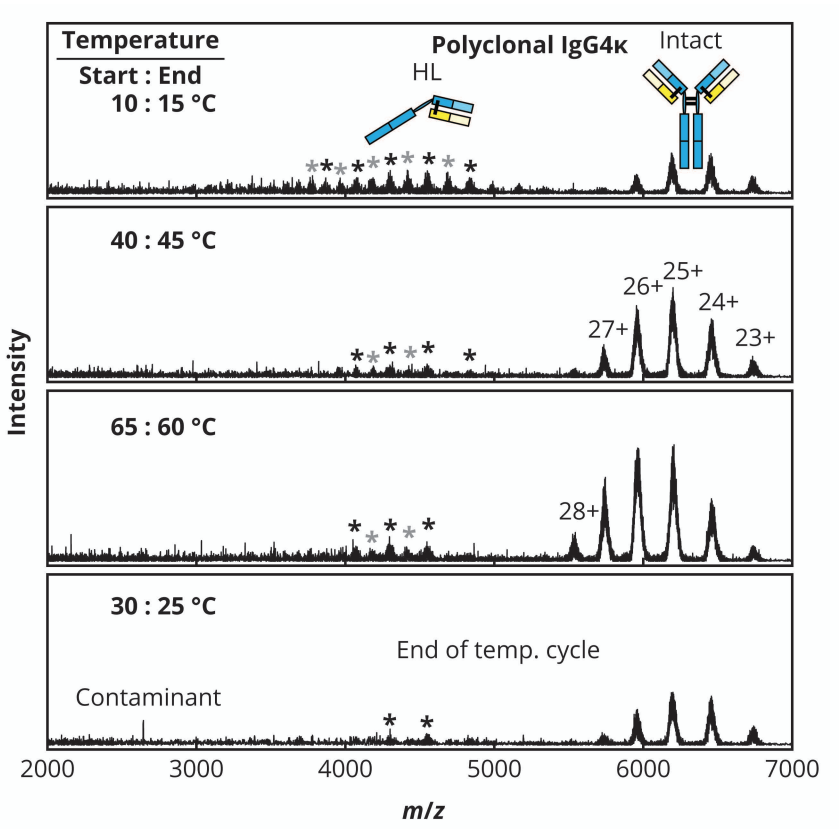


**Figure C6**. Selected spectra from a ±9 °C $min^{-1}$ temperature cycle of polyclonal IgG4κ in the absence of reducing agents. The y-axis absolute intensity maxima are the same for all four plots so that differences in intensity over the course of the temperature cycle can be appreciated. HL products are observed throughout the cycle. *Black asterisks* correspond to the dominant HL (~77,471 Da) and *gray asterisks* correspond to another population of HL products (~79,493 Da).

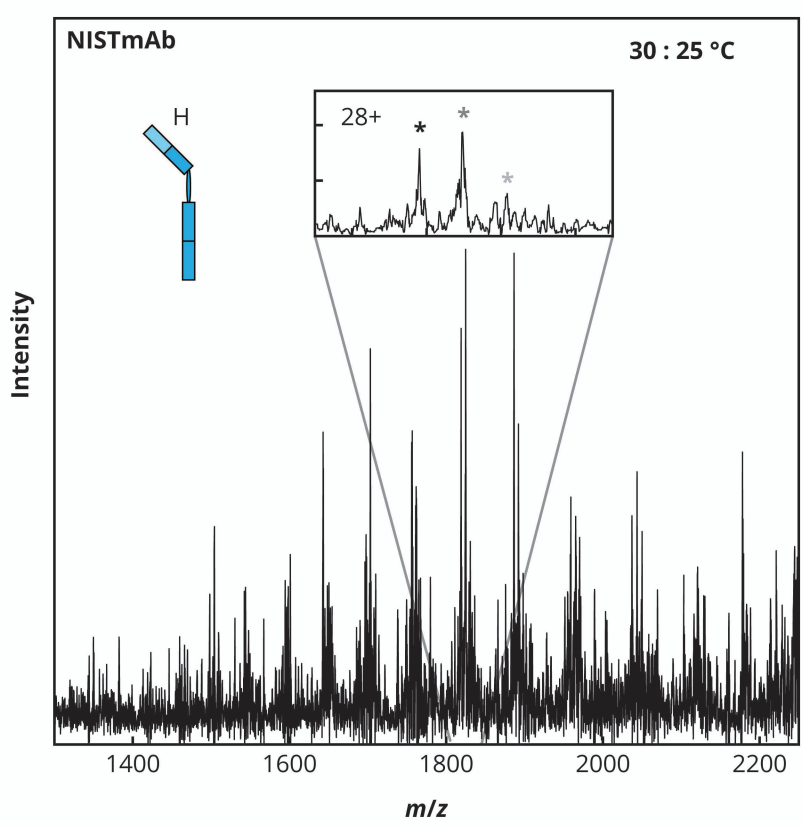


**Figure C7**. Zoom of lower *m*/*z* region at the end of a ±9 °C $min^{-1}$ temperature cycle of NISTmAb in the presence of 2 mM DTT. Higher charge states of H products are observed. The inset shows a zoom of the 28+ charge state with the *black asterisk* corresponding to 50,905 Da, the G0F glycoform, the *medium gray asterisk* corresponding to 51,067 Da, the G1F glycoform, and the *light gray asterisk* corresponding to 51,228 Da, the G2F glycoform.

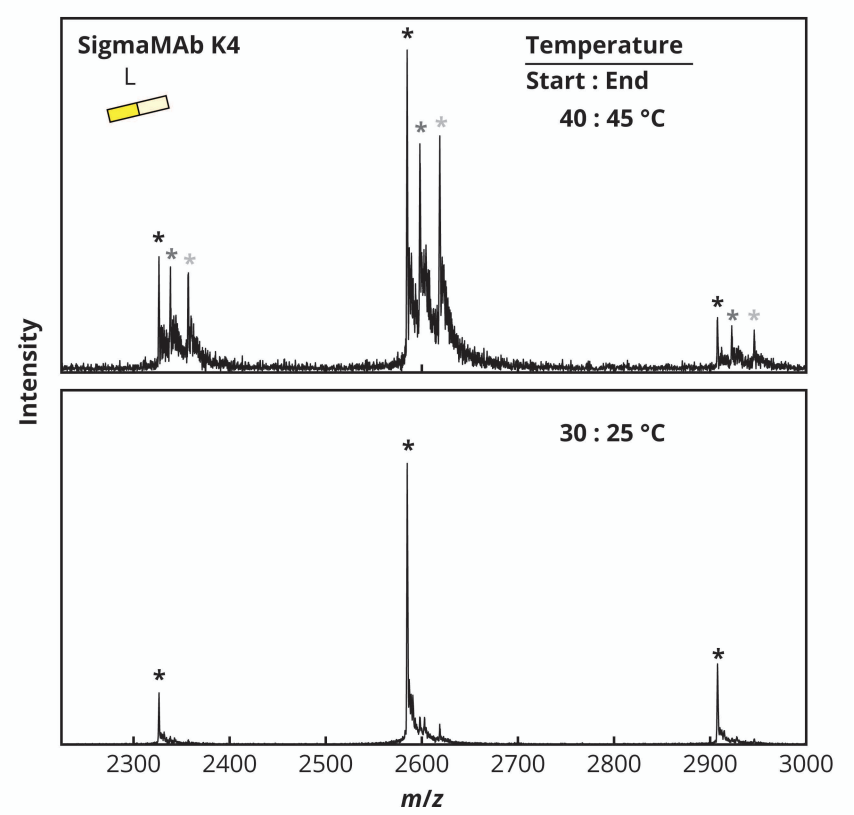


**Figure C8**. Zoom of peaks in the L product region of the mass spectra of SigmaMAb K4 during a ±9 °C $min^{-1}$ temperature cycle in the presence of 2 mM DTT. Additional peaks are observed in the cycle's heating phase, but they diminish over the course of the cycle. *Black asterisks* correspond to the dominant species at 25,254 Da, which agrees well with the predicted mass of the intact L product. *Medium gray asterisks* correspond to 23,272 Da, and *light gray asterisks* correspond to 23,561 Da.

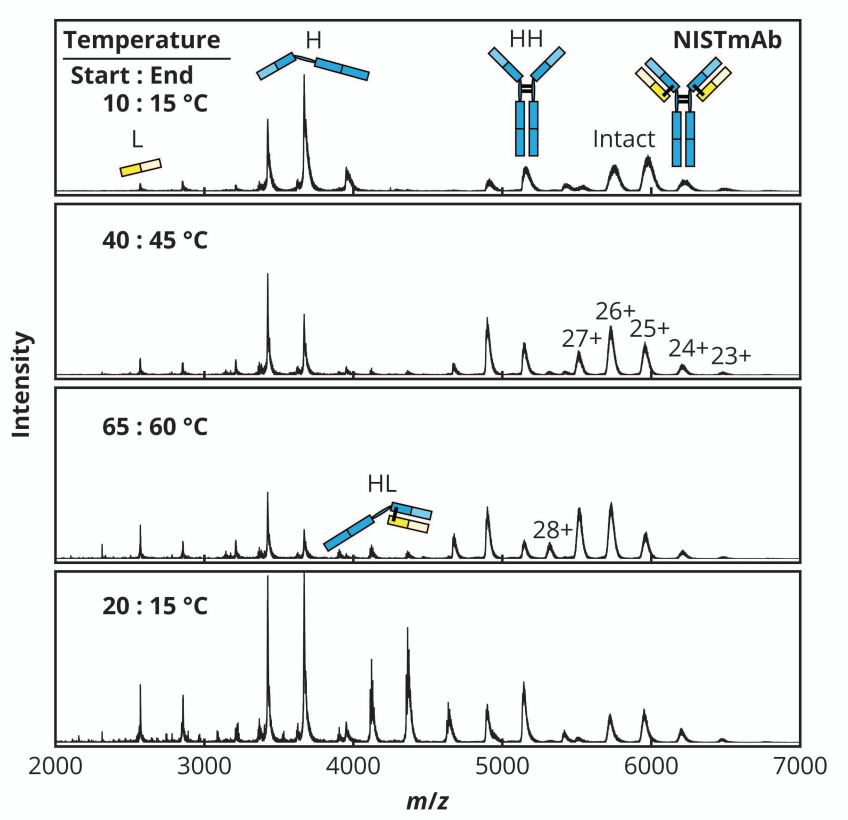


**Figure C9**. Selected spectra from a ±15 °C $min^{-1}$ temperature cycle of NISTmAb in the presence of 2 mM DTT. The HH and H species are present in high intensity and increase in intensity over the course of the temperature cycle. Similar results were not observed in other replicates, but these results show that H and HH products can be ionized and detected. We hypothesize that this sample may have been heated more than other samples by handling prior to insertion into the ptESI source held at 10 °C. These results motivate additional experiments with different temperature programs and DTT concentrations to investigate effects on the resulting reduction profiles.

# Appendix D: Native Mass Spectrometry of Yeast F-Box Protein, Met30

## 1 Introduction

Protein degradation is an important aspect of cellular maintenance and homeostasis, and the ubiquitin-proteosome pathway is one way in which protein degradation is accomplished and regulated.[1] Protein ubiquitination is catalyzed by three enzymes: the E1 ubiquitin-activating enzyme, one of several E2 ubiquitin-conjugating enzymes, and one of many E3 ubiquitin ligases.[2,3] E3 ligases provide substrate specificity in the ubiquitination cascade, and two yeast E3s have been identified as essential, one being $^{SCF}$Met30, or Skp–Cullin–F-box Met30.[2–4] SCF complexes are some of the most well studied Cullin-Ring ligases, which are the largest class of E3 enzymes.[2] SCF complexes are comprised of Skp1 and Cullin-1 (Cdc53) proteins along with an F-box protein that is responsible for the substrate specificity. These proteins form a complex with Rbx1, the RING domain protein that interacts with the E2 conjugating enzyme to facilitate the transfer of ubiquitin to the substrate.[2] Met30 is an F-box protein, and its E3 ligase complex participates in the sulfur perception network in yeast.[5] Met30 selects Met4 for ubiquitination.[5] Met4 is transcriptional activator for the MET genes that affect sulfur uptake and the synthesis of sulfur-containing molecules, like methionine.[5] When yeast is grown in the absence of methionine, $^{SCF}$Met30 does not bind Met4, and Met4 is available to activate genes for methionine synthesis.[5]

The pathway (s) by which $^{SCF}$Met30 senses changes in the concentration of sulfur-containing molecules is still unclear.[6] Several evolutionarily conserved domains have been identified within Met30 that are shared with similar proteins in fungi.[5] The F-box domain is important for interaction with Skp1, and the WD-40 repeat domain is important for substrate recognition.[2,5] A dimerization domain has also been identified which is conserved with other SCF

ligases that form homodimers.[2] Homodimerization of $^{SCF}$Met30 and the conditions thereof have not been clearly demonstrated; however, the dimerization domain of Met30 has been shown to be essential for cell viability.[2] We hypothesized in collaboration with Dr. Ning Zheng that a cofactor, possibly an Fe-S cluster, may provide an explanation for the sulfur perception of $^{SCF}$Met30.

Fe-S clusters are utilized in most living organisms, and are common protein cofactors with diverse roles in energy production, DNA replication and repair, nitrogen fixation, and more.[7,8] Their reactivity with molecules like $O_2$, NO, and free Fe, imparts an ability to sense cellular changes and, in conjunction with proteins, respond to those changes.[8] The goal of this study was to analyze various Met30 complexes using native MS to provide insights into $^{SCF}$Met30 structure and function as an E3 ligase for Met4.

## 2 Methods

Met30 and Skp1 proteins were coexpressed in insect cells and samples were prepared by the Ning Zheng lab at UW. A number of samples were provided that comprised different constructs of wild-type (WT) and mutant Met30 protein. The samples discussed herein were of truncated WT Met30 (180-285), which comprises the F-box motif and an additional conserved region, and a truncated 4A mutant (180-285) in which the following amino acid substitutions were made: C229A, H232A, C237A, C240A. Sequences of Met30 proteins are provided in Figure D1. Samples of WT Met30 (180-285)/Skp1 and 4A Met30 (180-285)/Skp1 were provided in aqueous 20 mM Tris HCl, 200 mM NaCl and 5 mM DTT at pH 8. Samples were buffer-exchanged into a solution containing 200 mM ammonium acetate at pH 7 or pH 8, with and without 5 mM DTT, using a microdialysis device with 2-4 buffer replacements. Native MS was

performed on a modified Waters Synapt G2 HDMS, a Waters QTOF Premier, or a Waters SELECT SERIES Cyclic IMS system.

**WT Met30 (180-285):**

```
        180         190         200         210         220
SGSGGSG KIDFISILPQ ELSLKILSYL DCQSLCNATR VCRKWQKLAD DDRVWYHMCE
        230         240         250         260         270
        QHIDRKCPNC GWGLPLLHMK RARIQQNSTG SSSNADIQTQ TTRPWKVIYR
        280
        ERFKVE
```

**4A Mutant Met30 (180-285):**

```
        180         190         200         210         220
SGSGGSG KIDFISILPQ ELSLKILSYL DCQSLCNATR VCRKWQKLAD DDRVWYHMAE
        230         240         250         260         270
        QAIDRKAPNA GWGLPLLHMK RARIQQNSTG SSSNADIQTQ TTRPWKVIYR
        280
        ERFKVE
```

**Figure D1**. Sequences of WT Met30 F-box construct and 4A Mutant Met30 F-box construct. Amino acids substituted to A in the 4A mutant are highlighted in red. Methionine and additional cysteine residues are bolded.

## 3 Results and Discussion

Initially, samples were exchanged into new solutions with a pH of 7, and samples were analyzed in positive mode on the G2 and QTOF premier instruments. Overall, the native mass spectra of the 4A mutant displayed less homodimerization (4A/Skp1-4A/Skp1) relative to the monomer (4A/Skp1) when compared to native mass spectra of the WT Met30 sample (Figure D2). These results supported experiments performed in the Zheng lab which indicated that the WT may form a dimer in solution. 4A/Skp1 monomer-to-dimer relative abundances were 100:18 versus WT/Skp1 with a ratio of 100:60. No apo peaks for WT/Skp1 homodimers were observed under either condition (with or without 5 mM DTT), but apo peaks for 4A/Skp1 homodimers were observed under both conditions. Larger complexes (more mass relative to predicted apo

masses) were observed with the addition of 5 mM DTT for both samples. This was promising because the addition of DTT was intended to help preserve reducing conditions and help maintain native-like structures. Fe-S clusters can be very susceptible to oxidation.[8] We observed the addition of 63-66 Da in mass relative to apo WT/Skp1 and 123-128 Da for WT/Skp1 homodimers. In addition to the possibility of zinc ions in the sample, we hypothesized that persulfidation could be occurring if Fe-S clusters were degrading due to oxidizing conditions during sample handling.[9,10] Previous work has also shown that Fe-S cluster proteins may be more stable as negative ions,[11] so follow-up experiments were also performed in negative mode. Overall, mass spectra peaks were also broad and difficult to assign, so follow-up experiments aimed to decrease peak width and enhance resolution as well.

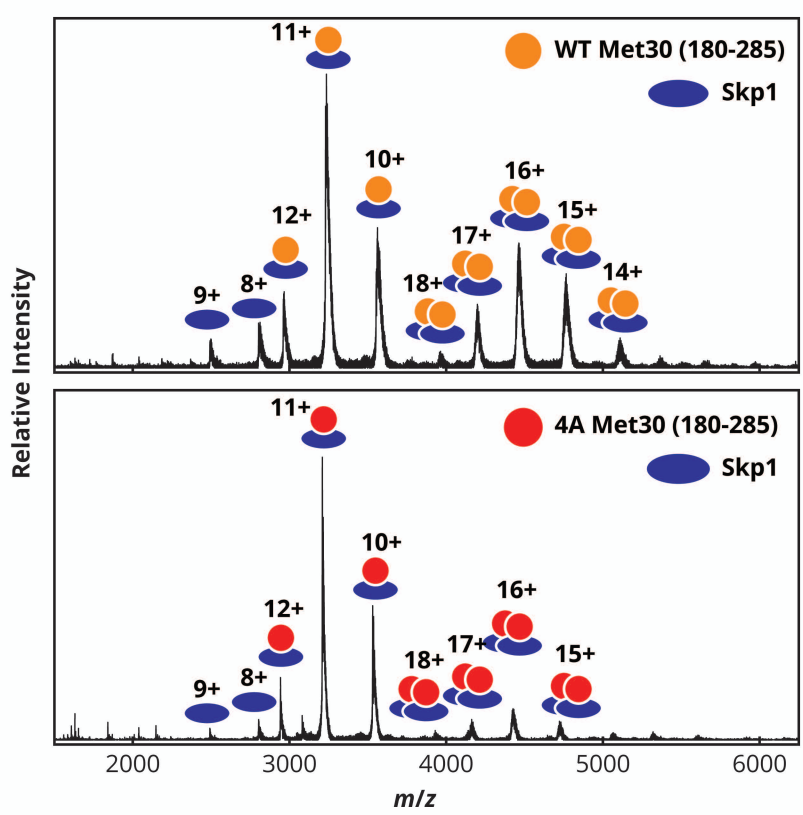


**Figure D2**. Native mass spectra of Met30 samples in 200 mM ammonium acetate, pH 7, in the absence of DTT. These spectra were acquired on the QTOF Premier in positive mode.

Increasing ionic strength of the ammonium acetate solution from 200 mM to 1 M has enhanced resolution of other complexes in native MS by reducing nonspecific adduction. Experiments using 1 M ammonium acetate buffers resulted in destabilization of both WT and 4A complexes, so this method was eliminated as a viable option. All remaining experiments were performed in 200 mM ammonium acetate. The remaining experiments also used ammonium acetate at pH 8, rather than pH 7, to maintain more of the original solution conditions. Additionally, as shown in Ch. 3, the Cyclic instrument resulted in more base level activation of

the complexes compared to the G2 or QTOF premier instruments, so troubleshooting and tuning was performed to enhance the transmission of higher *m*/*z* species and reduce activation.

Native MS of the 4A mutant/Skp1 sample was repeated several times on the Cyclic prior to performing additional experiments on the WT/Skp1 sample. In positive mode, spectra were collected that appeared more similar to those acquired on the G2 under pH 7 conditions. Higher resolution of the 4A Met30 monomer (not in complex with Skp1) was observed as well. With the addition of 5 mM DTT, the peak corresponding to an increase in mass of 62-64 Da relative to apo 4A was absent or diminished (Figure D3). The absence of this peak was also evident for the 4A/Skp1 monomer complex in the presence of DTT. The Skp1 monomer was not affected by the addition of DTT (Figure D4). Resolution of the 4A/Skp1-4A/Skp1 complex peaks appeared to be negatively impacted by the addition of DTT; as observed previously, and the apo peak was observed under both conditions. In negative mode, the 4A monomer was not observed. The 4A/Skp1 monomer complex showed the depletion of the 62-64 Da peak in the presence of DTT, similar to observations in positive mode. The Skp1 monomer was unchanged by the addition of DTT. 4A/Skp1 homodimer peaks were broad. Resolution improved with collisional activation performed in the trap cell, but no clear cofactor or cluster could be assigned in either positive or negative mode.

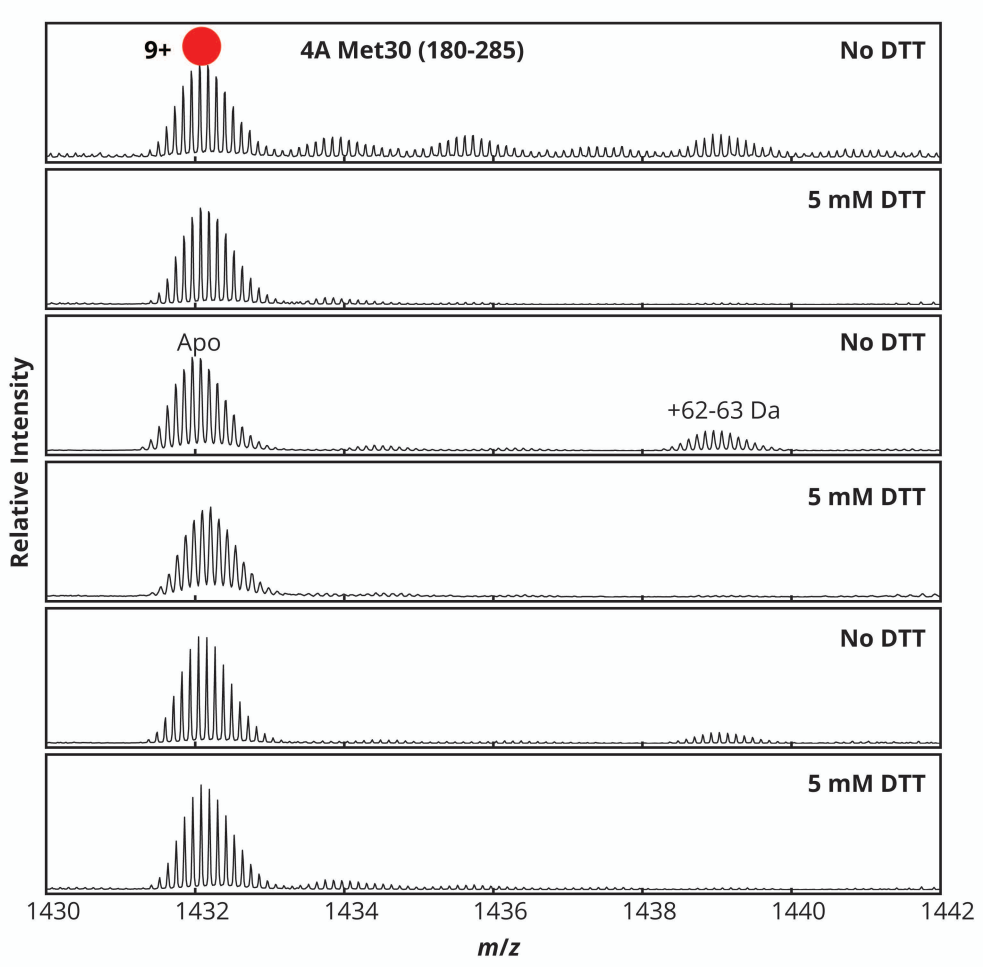


**Figure D3**. Native mass spectra of 4A Met30 (180-285) acquired on the Cyclic instrument in positive mode with supplementary activation. Spectra were collected on different days. Solution conditions were 200 mM ammonium acetate with pH of 8, with and without 5 mM DTT. A view of only the 9+ 4A monomer is shown.

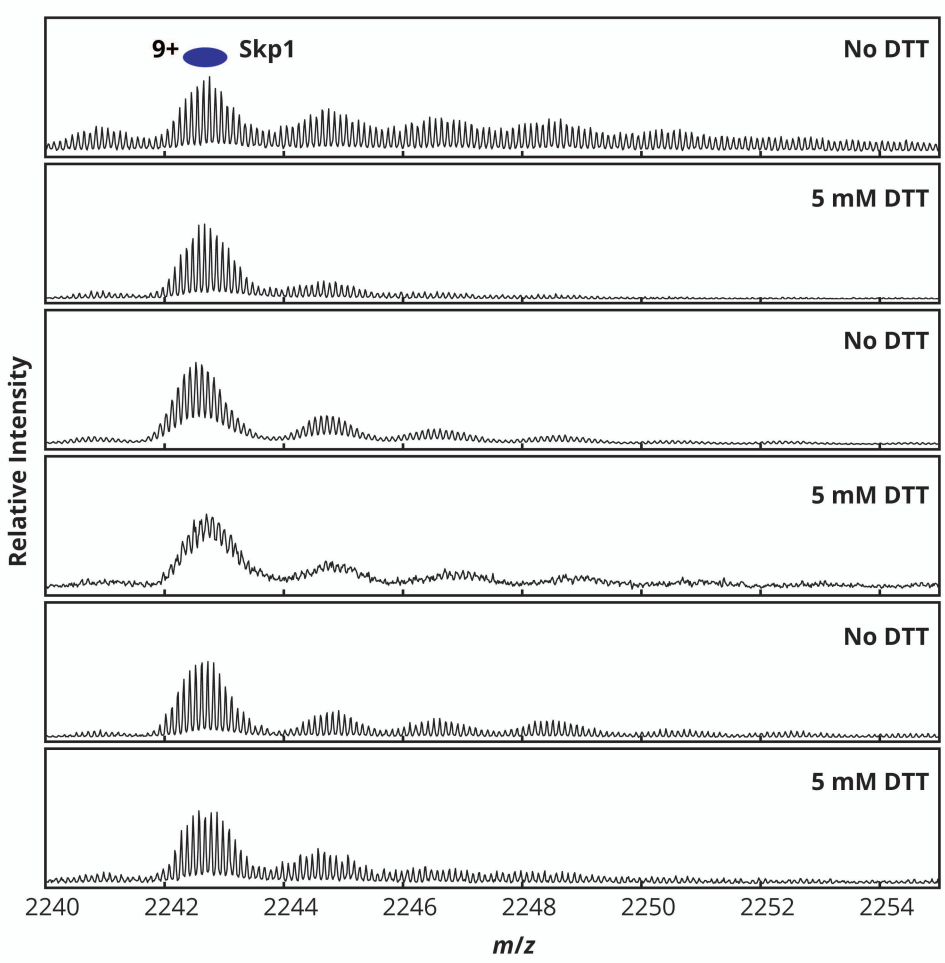


**Figure D4**. Native mass spectra of 4A Met30 (180-285) acquired on the Cyclic instrument in positive mode with supplementary activation. Spectra were collected on different days. Solution conditions were 200 mM ammonium acetate with pH of 8, with and without 5 mM DTT. A view of only the 10+ Skp1 monomer is shown.

In positive mode, the WT monomer displayed a peak that corresponded to 127-128 Da in added mass relative to the apo peak. This modification was diminished with the addition of DTT (Figure D5). A similar modification (129-130 Da) was observed on the WT/Skp1 monomer complex in the absence of DTT and was diminished in the 5 mM DTT sample. Skp1 monomer

peaks were not observed to change with the addition of DTT. The WT/Skp1 homodimer peaks were broad and poorly resolved even with collisional activation. Better resolution was achieved under conditions without DTT, but no cofactor or cluster could be positively identified. In negative mode, the WT monomer was not observed. The WT/Skp1 complex didn't clearly show the depletion of a 127-130 Da modification with the addition of DTT as was observed in positive mode. The Skp1 monomer peaks again looked similar with and without DTT. The WT/Skp1 homodimer peaks were also poorly resolved in negative mode (Figure D6) and were broader with the addition of DTT. Again, no cofactor or cluster could positively be identified.

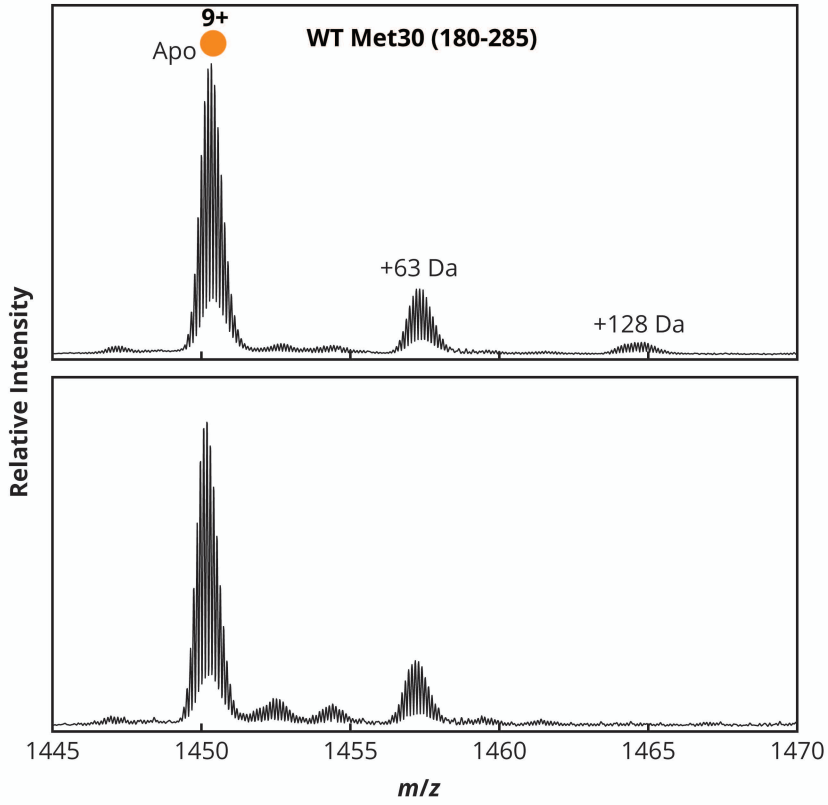


**Figure D5**. Native mass spectra of WT Met30 (180-285) acquired on the Cyclic instrument in positive mode with supplementary activation. Solution conditions were 200 mM ammonium acetate with pH of 8, with and without 5 mM DTT. A view of only the 9+ WT monomer is shown.

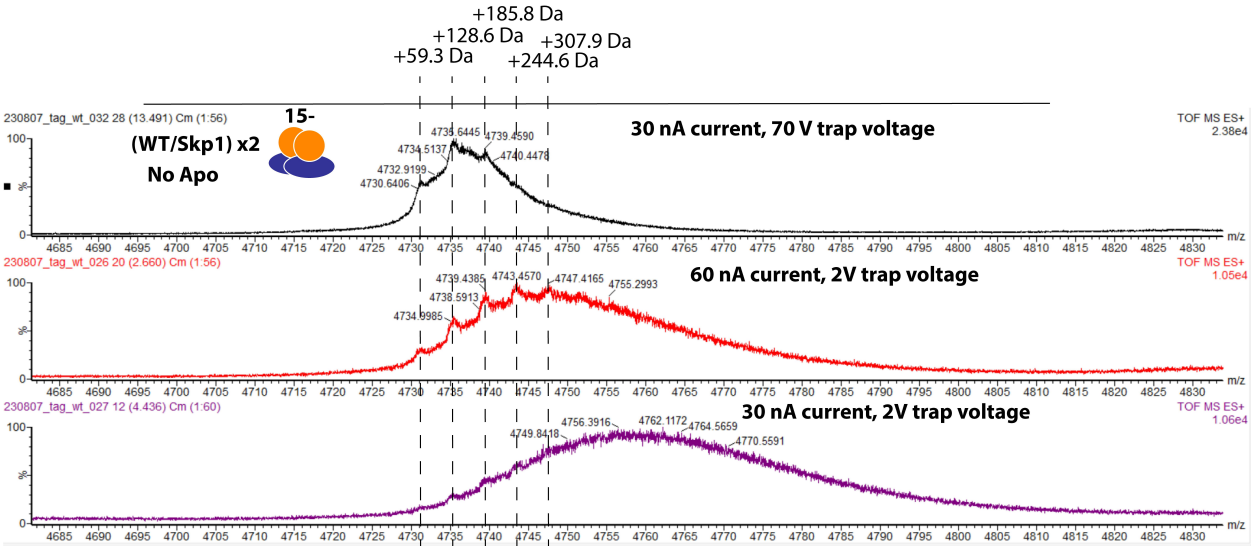


**Figure D6**. Native mass spectra of WT Met30 (180-285) acquired on the Cyclic instrument in negative mode with supplementary activation and electrospray current. Solution conditions were 200 mM ammonium acetate with pH of 8. A view of only the 15- WT/Skp1 homodimer is shown. No apo peak was observed. Added masses are relative to theoretical apo mass.

The colors of the WT samples and the 4A mutant samples were different; the WT sample displayed a brownish-red color and the mutant sample was clear (Figure D7). Ligation of Fe-S clusters has been shown to occur between Fe-S clusters and cysteine and histidine residues,[12] so the 4A substitutions may have prevented the binding of such a cluster and could provide an explanation for the differences in color.

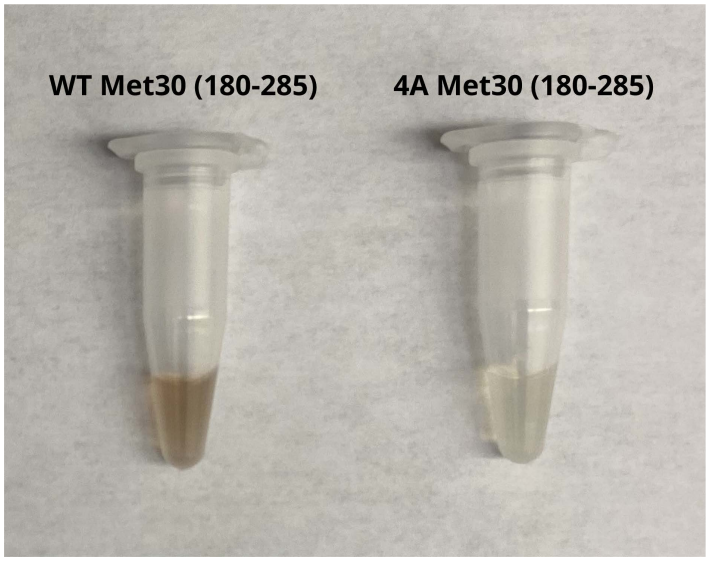


**Figure D7**. Image of WT Met30 (180-285) and 4A Met30 (180-285) samples.

Methionine residues are present in all proteins (WT Met30, 4A Met30, and Skp1). They are also prone to oxidative modification. DTT is ineffective in reducing methionine oxidation, but effective in reducing some oxidative modifications of cysteine residues. We hypothesize that the depletion of peaks corresponding to 62-64 Da modifications of 4A Met30 and 127-130 Da modifications of WT Met30 may correspond to oxidative cysteine modifications. There are three cysteines in the 4A mutant sequence and six cysteines in the WT sequence. Persulfidation is a cysteine modification susceptible to reduction by DTT, but no peaks corresponding to the addition or depletion of a single persulfide modification (+32-34 Da) were observed.

## 4 Future Work

Anaerobic preparations of new Met30 samples are underway in the Zheng lab. Analyses performed under anerobic conditions may reveal clearer information about the presence or absence of Fe-S clusters, as suggested by published protocols for performing native MS on Fe-S

proteins.[8] Mass spectra should continue to be collected in both positive and negative modes for complementary information about the complexes and to maximize stability of Fe-S clusters, if present. Additional heat or activation may enhance resolution of these complexes for more clear assignment. ICP-MS or EPR may be useful in verifying or rejecting the presence of iron or Fe-S clusters in the samples.

## 5 Acknowledgements

This work was supported by the National Science Foundation through award 2203513 from the Division of Chemistry, with partial co-funding from the Division of Molecular and Cellular Biosciences. Thank you to Dr. Ning Zheng and Baiyun Wang and their funding sources for Met30 samples and scientific discussion.

## 6 References

(1) Schwartz, A. L.; Ciechanover, A. Targeting Proteins for Destruction by the Ubiquitin System: Implications for Human Pathobiology. *Annu. Rev. Pharmacol. Toxicol.* **2009**, *49* (1), 73–96. https://doi.org/10.1146/annurev.pharmtox.051208.165340.

(2) Au, W.-C.; Zhang, T.; Mishra, P. K.; Eisenstatt, J. R.; Walker, R. L.; Ocampo, J.; Dawson, A.; Warren, J.; Costanzo, M.; Baryshnikova, A.; Flick, K.; Clark, D. J.; Meltzer, P. S.; Baker, R. E.; Myers, C.; Boone, C.; Kaiser, P.; Basrai, M. A. Skp, Cullin, F-Box (SCF)-Met30 and SCF-Cdc4-Mediated Proteolysis of CENP-A Prevents Mislocalization of CENP-A for Chromosomal Stability in Budding Yeast. *PLOS Genet.* **2020**, *16* (2), e1008597. https://doi.org/10.1371/journal.pgen.1008597.

(3) Finley, D.; Ulrich, H. D.; Sommer, T.; Kaiser, P. The Ubiquitin–Proteasome System of *Saccharomyces Cerevisiae*. *Genetics* **2012**, *192* (2), 319–360. https://doi.org/10.1534/genetics.112.140467.

(4) Thomas, D.; Kuras, L.; Barbey, R.; Cherest, H.; Blaiseau, P.-L.; Surdin-Kerjan, Y. Met30p, a Yeast Transcriptional Inhibitor That Responds to *S* -Adenosylmethionine, Is an Essential Protein with WD40 Repeats. *Mol. Cell. Biol.* **1995**, *15* (12), 6526–6534. https://doi.org/10.1128/MCB.15.12.6526.

(5) Brunson, L. E.; Dixon, C.; LeFebvre, A.; Sun, L.; Mathias, N. Identification of Residues in the WD-40 Repeat Motif of the F-Box Protein Met30p Required for Interaction with Its Substrate Met4p. *Mol. Genet. Genomics* **2005**, *273* (5), 361–370. https://doi.org/10.1007/s00438-005-1137-6.

(6) Sadhu, M. J.; Moresco, J. J.; Zimmer, A. D.; Yates, J. R.; Rine, J. Multiple Inputs Control Sulfur-Containing Amino Acid Synthesis in *Saccharomyces Cerevisiae*. *Mol. Biol. Cell* **2014**, *25* (10), 1653–1665. https://doi.org/10.1091/mbc.e13-12-0755.

(7) Shi, R.; Hou, W.; Wang, Z.-Q.; Xu, X. Biogenesis of Iron–Sulfur Clusters and Their Role in DNA Metabolism. *Front. Cell Dev. Biol.* **2021**, *9*, 735678. https://doi.org/10.3389/fcell.2021.735678.

(8) Crack, J. C.; Le Brun, N. E. Native Mass Spectrometry of Iron-Sulfur Proteins. In *Fe-S proteins: methods and protocols*; Santos, P. C. dos, Ed.; Methods in molecular biology; Humana Press: New York, NY, 2021.

(9) Johnson, K. A.; Verhagen, M. F. J. M.; Brereton, P. S.; Adams, M. W. W.; Amster, I. J. Probing the Stoichiometry and Oxidation States of Metal Centers in Iron−Sulfur Proteins Using Electrospray FTICR Mass Spectrometry. *Anal. Chem.* **2000**, *72* (7), 1410–1418. https://doi.org/10.1021/ac991183e.

(10) Crack, J. C.; Thomson, A. J.; Le Brun, N. E. Mass Spectrometric Identification of Intermediates in the $O_2$ -Driven [4Fe-4S] to [2Fe-2S] Cluster Conversion in FNR. *Proc. Natl. Acad. Sci.* **2017**, *114* (16). https://doi.org/10.1073/pnas.1620987114.

(11) Johnson, K. A.; Verhagen, M. F. J. M.; Adams, M. W. W.; Amster, I. J. Differences between Positive and Negative Ion Stabilities of Metal–Sulfur Cluster Proteins: An Electrospray Ionization Fourier Transform Ion Cyclotron Resonance Study. *Int. J. Mass Spectrom.* **2001**, *204* (1–3), 77–85. https://doi.org/10.1016/S1387-3806(00)00337-7.

(12) Qi, W.; Cowan, J. A. Structural, Mechanistic and Coordination Chemistry of Relevance to the Biosynthesis of Iron–Sulfur and Related Iron Cofactors☆. *Coord. Chem. Rev.* **2011**, *255* (7–8), 688–699. https://doi.org/10.1016/j.ccr.2010.10.016.